Transactions of the ASME

EDITORIAL STAFF
Editor, J. J. JAKLITSCH, JR.
Production Editor, CORNELIA MONAHAN
Editorial Production Assistant, BETH DARCHI

FLUIDS ENGINEERING DIVISION
Technical Editor
FRANK M. WHITE (1981)
Executive Secretary
L. T. NELSON (1981)
Calendar Editor
M. F. ACKERSON

Associate Editors
Fluid Machinery
H. JAMES HERRING (1981)
BUDUGUR LAKSHMINARAYANA (1983)
Fluid Measurements
BHARATAN R. PATEL (1983)
Fluid Mechanics
RICHARD A. BAJURA (1980)
OWEN M. GRIFFIN (1981)
BRIAN E. LAUNDER (1981)
WILLIAM G. TIEDERMAN (1981)
Fluid Transients
DAVID C. WIGGERT (1980)
Polyphase Flow
CLAYTON T. CROWE (1980)
ROBERT L. STREET (1981)
Review Articles
KENNETH E. HICKMAN (1981)

FOREIGN CORRESPONDENTS
Europe and Russia
JACQUES CHAUVIN
Europe and Russia
JOHN H. HORLOCK
India and Middle East
ARUN PRASAD
Japan and China
YASUTOSHI SENOO

POLICY BOARD, COMMUNICATIONS
Chairman and Vice-President
I. BERMAN

Members-at-Large
W. J. WARREN
J. E. ORTLOFF
M. J. RABINS
J. W. LOCKE

Policy Board Representiatives
Basic Engineering, FRED LANDIS
General Engineering, C. F. PHILLIPS
Industry, J. E. ORTLOFF
Power, R. E. REDER
Research, G. P. COOPER
Codes and Stds., L. L. ELDER
Nom. Com. Rep., J. W. LOCKE

Business Staff
345 East 47th St.
New York, N. Y. 10017
(212) 644-7789
Mng. Dir., Publ., C. O. SANDERSON

OFFICERS OF THE ASME
President, CHARLES E. JONES
Exec. Director & Sec'y, ROGERS B. FINCH
Secretary and Treasurer, ROBERT A. BENNETT

The Journal of FLUIDS ENGINEERING (USPS 278-480) is edited and published quarterly at the offices of The American Society of Mechanical Engineers, United Engineering Center, 345 E. 47th St., New York, N. Y. 10017. Cable Address, "Mechaneer," New York. Second-class postage paid at New York, CHANGES OF ADDRESS must be received at Society headquarters seven weeks before they are to be effective. Please send old label and new address. PRICES: To members, $25.00, annually: to nonmembers, $50.00. Single copies, $15.00 each. Add $1.50 for postage to countries outside the United States and Canada. STATEMENT from By-Laws. The Society shall not be responsible for statements or opinions advanced in papers or . . . printed in its publications (B13, Par. 4),

COPYRIGHT © 1980 by The American Society of Mechanical Engineers. Reprints from this publication may be made on condition that full credit be given the TRANSACTIONS OF THE ASME, JOURNAL OF FLUIDS ENGINEERING and the author, and date of publication be stated.

INDEXED by the Engineering Index, Inc.

Journal of Fluids Engineering

Published Quarterly by The American Society of Mechanical Engineers

VOLUME 102 • NUMBER 3 • SEPTEMBER 1980

Announcements and Special Notices

Downloaded 03 Jun 2010 to 171.66.16.159. Redistribution subject to ASME license or copyright; see http://www.asme.org/terms/Terms_Use.cfm

REVIEW—Bluff Body Flows Applicable to Vehicle Aerodynamics

P. W. Bearman
Department of Aeronautics,
Imperial College,
London, England

This paper attempts to review those aspects of bluff body aerodynamics that are relevant to the understanding of vehicle flows. Vehicles often have complex body shapes and are influenced by the proximity of the ground. The effect of the ground is discussed in some detail and results for bluff bodies mounted in wind tunnels above fixed and moving ground planes are presented. It is concluded that drag is little affected by ground proximity and ground representation whereas lift is often sensitive to both. The effect of slanting the base of a bluff body is discussed and the two main flow regimes that result are described. The influence of the wind on vehicle flows is investigated and it is found that vehicle mean flows are sensitive to the turbulence level in the relative wind. Finally numerical prediction methods are considered.

Introduction

This paper is concerned with the aerodynamics of various forms of land transportation: cars, lorries, tractor-trailers, trains, etc., although a bias towards the motor car will be detected. The plan is to concentrate on the more fundamental aspects of vehicle flows and to consider what can be applied from our knowledge of bluff body aerodynamics. As a review it is by no means exhaustive, being strongly influenced by the author's own research interests, and for a comprehensive bibliography readers are referred to Milliken [1].

The vehicle designer requires to know aerodynamic force and moment coefficients as well as more detailed information such as pressure distributions, ventilation and radiator flows, heat transfer rates and aerodynamically generated noise levels. In the literature, for obvious reasons, most attention has been directed towards the question of drag and its reduction and in this review frequent reference will be made to papers presented at a General Motors Symposium [2] entitled "The Aerodynamic Drag Mechanisms of Bluff Bodies and Road Vehicles." However concern for aerodynamic forces is by no means restricted to the fuel consumption problem; they influence stability and handling characteristics and in the design of high speed racing cars the achievement of a large negative lift is all important. Practical considerations often result in a vehicle shape that has substantial areas of separated flow and if the aerodynamic performance is to be improved we require detailed understanding of the various flow phenomena that act together to generate the complex flow field. It is only through this understanding that we shall be able to predict and take advantage of the effects that various geometric changes can make.

First we should ascertain whether there is information available in other fields of aerodynamics that can be applied directly to the vehicle problem. Aeronautical aerodynamics is often thought to be only concerned with the study of attached flows but notable exceptions to this are the flow fields generated by slender delta wings at high angles of incidence (Küchemann [3]) and the flow at the rear of upswept fuselages of transport aircraft (Peake [4]). Both of these flows involve the generation and shedding of discrete vortices and vortices are an important feature of bluff body flow. One of the major application areas of bluff body aerodynamics is in the determination of wind loads on buildings and structures. The major contribution that the study of wind forces on buildings has made is to unravel the roles played by mean shear and turbulence in the approaching flow (Cermak [5]). In the understanding of vehicle flows the wind is only one of a number of influencing factors but we can expect it to be particularly important when making comparisons between results from wind tunnel models and full scale.

A vehicle has a complex aerodynamic shape, its surface being a mixture of attached and separated flow areas, and on the forward part the separated regions may be only limited in extent but vortices can trail back to influence the remainder of the flow field. The flow at the rear of a vehicle is invariably separated and the near wake can contain vortices of any orientation. In addition we have the flow developed by the rotating wheels and the wheel arches, the flow through the engine compartment and the underbody flow. It is the close proximity to the ground and the underbody flow that sets the vehicle apart from other bluff body flows. The boundary condition at the ground is different to that of a building and although the ground effect problem is studied in connection with aircraft it is hopefully never so acute. Hence there is a class of flow peculiar to land vehicles and one which has received comparatively little attention. There is no agreed view, for example, on whether in a wind tunnel test with a fixed model the ground needs to be moving or not. Although there is probably no lack of data on specific vehicle shapes more effort would appear to be needed in identifying the fundamental features, and their interaction, that contribute to a typical vehicle flow.

This paper reviews knowledge on three-dimensional bluff

Contributed by the Fluids Engineering Division for publication in the JOURNAL OF FLUIDS ENGINEERING. Manuscript received by the Fluids Engineering Division, July 23, 1979.

Copyright © 1980 by ASME

Downloaded 02 Jun 2010 to 171.66.16.103. Redistribution subject to ASME license or copyright; see http://www.asme.org/terms/Terms_Use.cfm

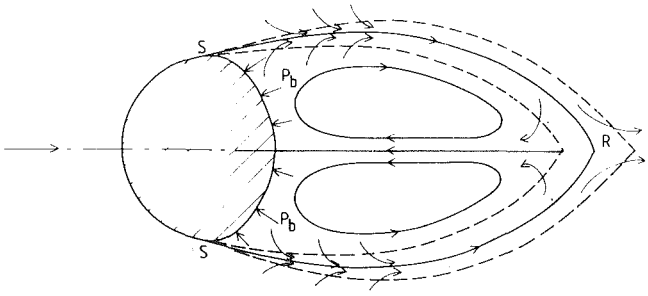

Fig. 1 Sketch of the mean flow in the near wake of an axisymmetric bluff body

body flows and discusses the problem of bringing a body close to a ground plane. However, in addition to fundamental understanding, the vehicle designer will be concerned as much or more with making predictions and prospects for calculating flows around vehicle shapes are discussed.

Axisymmetric Bluff Body Flow

The majority of bluff body research has been conducted on either two-dimensional or axisymmetric shapes; the two most common bodies being the circular cylinder (Morkovin [6], and the sphere (Achenbach [7]). The pair of shear layers that spring from the separtion points on a bluff cylinder are inherently unstable and interact to form strong vortices that are shed alternately from either side of the body at a constant frequency. The regular shedding of strong vortices results in high drag and for cylinders of rectangular cross-section Nakaguchi, Hashimoto, and Muto [8] have reported C_D values as high as 3. Research on two-dimensional cylinders, however, is of limited relevance to vehicles because on highly three-dimensional bodies drag generation is not dominated by the regular shedding of intense vortices. Bluff body flow regimes can be classified in terms of the body aspect ratio, i.e. ratio of larger cross-wind dimension to smaller cross-wind dimension. Substantial departures from two-dimensional type flows are observed when this ratio is as high as 20 and as it is further reduced the flow around the ends increasingly interferes with the regular shedding of vortices and reduces their strength. The drag coefficient of a square section cylinder, for example, is just over two whereas for a cube it is about one.

The main features of the flow around an axisymmetric bluff body are shown in Fig. 1. Separation occurs at S and the growing free shear layer entrains fluid from the wake cavity. This entrainment leads to a reduction of pressure within the near wake and it sets up a recirculating flow field. The pressure difference generated across the shear layer causes it to curve back towards the wake axis. At the point of meeting, R, fluid is returned into the separated region to balance the fluid removed by entrainment, since there can be no net flow out of the near wake. There will be some equilibrium position in the wake where, if the distance to the meeting point R were to lengthen momentarily, the amount entrained would increase and the base pressure would then decrease drawing R back to its original position. The opposite would occur if R were to move closer to the body and thus entrainment acts as a form of feedback to stabilize the near wake bubble. The pressure on the rear face of the body, in the separation region, is found to be approximately uniform and equal to the pressure just outside the boundary layer at separation. Taking as an example a circular disc, the base pressure coefficient, C_{Pb}, is -0.36 whereas on a two-dimensional flat plate $C_{Pb} = -1.2$. (Pressure coefficients are defined as the pressure at a point on a body surface minus ambient static pressure and the result divided by free stream dynamic pressure.) The attached flow region, or forebody, contributes a similar amount to the drag of the disc and the flat plate and the higher drag of two-dimensional bodies results directly from a higher base drag.

Separations from bluff bodies are of two forms; sharp-edged and continuous surface where the boundary layer fails to withstand some critical adverse pressure gradient. In the latter case the flow is more likely to be Reynolds number dependent but at the Reynolds numbers typical of road vehicles most boundary layers at separation will be turbulent and little sensitivity to changing Reynolds number would be expected. The pressure gradient approaching a sharp-edged separation is found to be favorable. On bodies with either kind of separation the resulting flow is likely to be sensitive to turbulence level in the approaching flow.

The angle θ between the shear layer at separation and the free stream direction is an important factor in determining base pressure and hence drag. The table below shows the effect of increasing this angle on axisymmetric bluff body drag. Throughout this review drag coefficients are based on an area equal to the maximimum cross-sectional area of the body normal to the flow direction.

Drag of Cones

θ	C_D
90 deg*	1.15
135 deg	0.8
150 deg	0.5
167 deg	0.4

*Circular Disk

Increasing θ beyond 180 deg is known as boat-tailing and Mair [9] suggests that this is the most effective way of reducing axisymmetric bluff body drag. However there will be some critical boat-tail angle beyond which the flow will separate at the beginning of the tail. Mair [10] carried out experiments on a basic body consisting of a cylindrical portion of diameter d and length 3d with a semiellipsoidal nose of length 1.3d. Various boat-tailed sections were added to this body and he found that the optimum boat-tail angle was $\beta = 22$ deg, where $\beta = \theta - 180$ deg. Mair presented results for the drag reduction effected by the addition of various lengths of afterbody. His results are presented in figure 2 where C_D, which does not include any skin friction drag contribution from the basic body, is plotted against afterbody length l/d. It can be seen that boat-tailing is extremely effective and, although Mair concentrated on tails with l/d greater than 0.5, it is clear that substantial drag reductions can be achieved with shorter tails. He also comments that there is little to be gained in continuing the tail to a point.

It is interesting to note that Mason and Beebe [11] were unable to reduce significantly the base drag of tractor-trailer vehicles by using splitter plates, vanes or base cavities. Another method of reducing drag, however, is to interfere with the mass entrainment feedback mechanism of the near wake by bleeding fluid into the wake across the rear face of the body. Calvert [12] and Sykes [13] show that this can be used to produce some improvement although in any estimate of gains in performance allowance must be made for the power requirements of the bleed system. The use of auxillary air opens up possibilities for using some form of boundary layer control, either by suction or blowing, to maintain attached flow. Practically this could turn out to be more attractive than bleeding out air over a large area of a vehicle rear surface however there is little information available on boundary layer control applied to road vehicles. As our knowledge of vehicle flows is improved the possibilities for using boundary layer control may become more apparent.

The Influence of the Ground on Bluff Body Flow

Althoughh one can learn something of the fundamentals of bluff body flow by studying isolated axisymmetric bodies this family of shapes has only limited relevance to the land vehicle

Downloaded 02 Jun 2010 to 171.66.16.103. Redistribution subject to ASME license or copyright; see http://www.asme.org/terms/Terms_Use.cfm

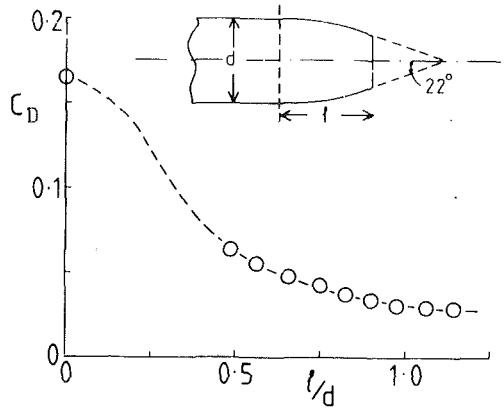

Fig. 2 The effect of boat-tailing on bluff body drag (Mair [10])

problem. When a body is brought into the vicinity of the ground plane it comes under the influence of its image beneath the ground. The image concept, borrowed from potential flow, has much to recommend it in the understanding of the effect of the ground on complex bluff body shapes. To take a simple example, consider a cube with one face normal to the flow and with two other faces parallel with the ground then, as the ground clearance tends to zero, the body will appear as a cuboid with sides in the ratio 2:1:1. Since drag is not sensitive to changing aspect ratio when aspect ratio is near unity we could argue that C_D will change little with ground clearance. The stagnation point will move from the center of the front face towards the bottom edge of the cube as the ground is approached and this will produce different flows on the top and bottom surfaces and thus generate a lift force. Near the ground the flow field may be complicated by the generation and shedding of vorticity with a strong longitudinal as well as transverse component. The presence of longitudinal vortices will destroy the simple picture of the axisymmetric near wake flow presented earlier. Flow fields generated by three-dimensional separations can be extremely complicated and most progress has been made in predicting the comparatively simple separated flow developed over slender delta wings (Smith [14]). General concepts related to flow separation in three dimensions have been presented by Maskell [15] and Lighthill [16].

A problem common to all separated flows is the prediction of the ways in which the viscous and inviscid parts of the flow interact. When a bluff body is brought close to a ground plane, for example, we are often unable to predict the sign of the lift force let alone its magnitude. Consider a circular cylinder; potential flow arguments would suggest that the cylinder should be attracted towards the ground because of the influence of the increased velocity induced between the cylinder and its image. In reality, however, one finds that the effect of the proximity of the ground is to change the boundary layer separation positions such that, in subcritical Reynolds number flow, the upper separation point moves forward of 80 deg and the lower one occurs in the adverse pressure gradient region following the minimum ground clearance position. The resulting flow develops a lift away from the wall (Bearman and Zdravkovich [17]). In the case of a three-dimensional bluff body the effect of the viscous-inviscid interaction on lift force will not be so easily analyzed.

Measurements of forces on various simple bluff body shapes above a ground plane have been made by Carr [18 and 19], George [20], Howell [21 and 22] Fackrell [23] and Anderson [24]. Carr and Howell have investigated the effect of ground clearance on forces and pressure distributions on "vehicles" ranging from sharp-edged cuboids to saloon car bodies, all mounted above a fixed floor. Fackrell studied a wedge-shaped body with fixed separation at the rear, and

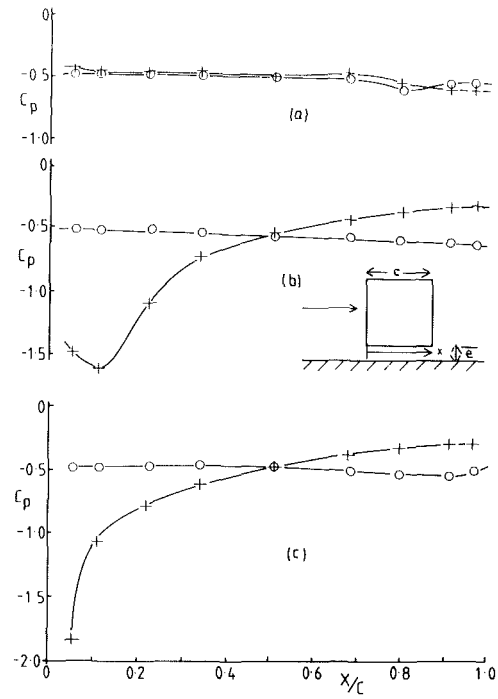

Fig. 3 Pressure distributions on a cube above a moving floor; 0, top surface; +, lower surface. *(a)* $e/c = 1.0$, *(b)* $e/c = 0.11$, *(c)* $= 0.056$.

Anderson made measurements on a cube and both mounted their models above a moving floor. The simple body shapes studied by George, who also made measurements above a moving floor, were a variety of blocks with rounded noses and cut-off tails and with various cambers and tapers. Anderson's results for a cube mounted with one face normal to the flow, and two others parallel with the ground, will be discussed in more detail.

Anderson carried out experiments on a cube of side 23 cm mounted in a tunnel 1.37 m wide by 1.22 m high equipped with a moving floor 0.8 m wide and 1.5 m long. The cube was suspended on struts from a wind tunnel balance which measured lift, drag and pitching moment. 48 pressure tappings were set into the cube surface and these were connected to two remotely controlled pressure switches positioned inside the model. The experiments were conducted at a Reynolds number of 3×10^5, Reynolds number being based on cube side dimension c. The tare forces on the supporting struts were subtracted from the balance readings and the forces and pressures were corrected for the effect of the 3 percent tunnel blockage by the method due to Maskell [25]. The final results were estimated to be accurate to better than 2 percent.

Pressure coefficients measured along the stream-wise centre-lines of the top and bottom surfaces are shown in Fig. 3 for ground clearances $e = 1.0c$, $0.11c$ and $0.056c$ where ground clearance is the height of the bottom surface of the cube above the floor. Results for $e/c = 1.0$ are similar to those measured on a cube far from the ground with the pressure nearly constant along both surfaces. The flow separates at the four front edges of the cube and there is no steady reattachment on the side faces. This is consistent with the flow visualization photographs of Nakaguchi [26] who found that on cuboids, with a square face mounted normal to the flow, no reattachment was observed so long as the length of the cuboid was less than 1.4 times the length of a side on the front face. Figure 3 shows that as the ground was approached the interference field caused a suction peak to develop at the front of the undersurface followed by a pressure recovery towards the base. Surface oil flow patterns confirmed that reattachment occurred on the lower surface and that reattachment

Downloaded 02 Jun 2010 to 171.66.16.103. Redistribution subject to ASME license or copyright; see http://www.asme.org/terms/Terms_Use.cfm

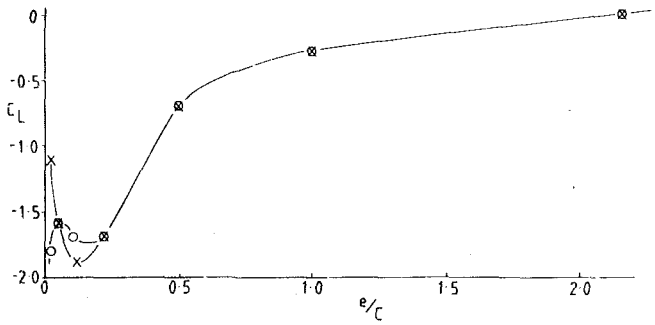

Fig. 4 Variation of lift coefficient on a cube with ground clearance; X, stationary ground; 0, moving ground. *e*, *c* as in Fig. 3.

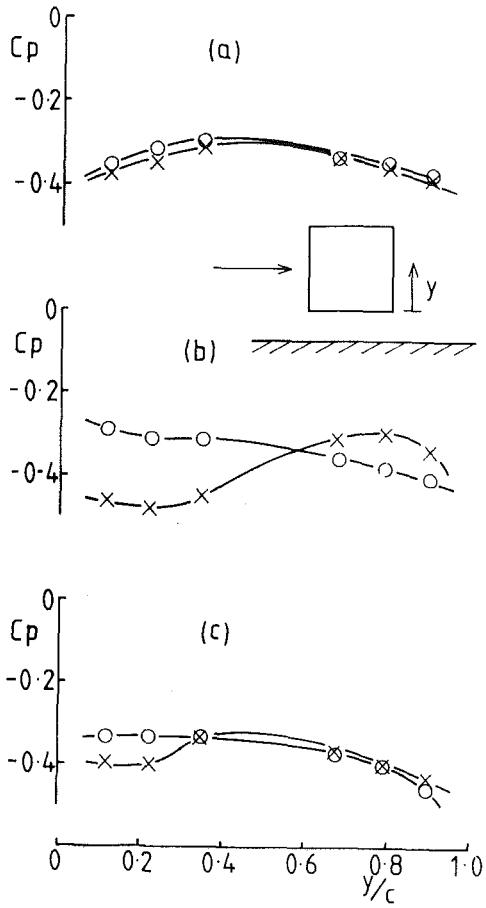

Fig. 5 Base pressure distribution on a cube; X, stationary ground; 0, moving ground. *(a)* e/c = 1.0, *(b)* e/c = 0.11, *(c)* e/c = 0.056.

moved increasingly towards the front as the ground clearance was reduced to almost zero. At the rear the pressure recovered to a value greater than the almost constant pressure along the top surface and thus there is some mechanism within the near wake that sustains a small pressure difference across the rear face.

The pressure results plotted in Fig. 3 suggest that a cube near to a ground plane should experience a negative lift, i.e. a downforce. This is confirmed by the lift coefficient measurements plotted in Fig. 4. Also shown in Fig. 4 are C_L measurements taken with the cube above a stationary floor where the boundary layer thickness, in the absence of the cube, was about 0.09c. The results are remarkably similar for all but the lowest ground clearance tested of 0.028c.

The variation of base pressure down the center line of the rear face of the cube is shown in Figure 5 for $e/c = 1.0$, 0.11 and 0.056 with both a moving and a stationary floor representation. The results with the moving floor, for the smaller ground clearances, show a gradual reduction in base suction as the lower edge is approached. The variation of base suction with a fixed floor is quite different although the mean base pressure appears similar. It was surprising to find the greatest influence of floor representation at the comparatively high ground clearance of 0.11c. The drag coefficient and the base pressure coefficient, averaged across the rear face, are shown plotted against ground clearance in Fig. 6.

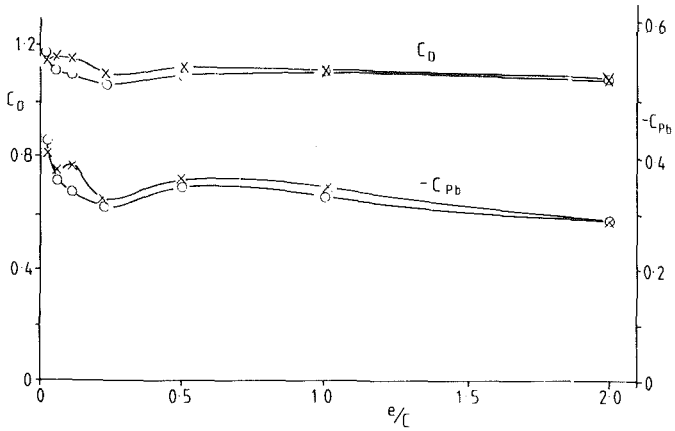

Fig. 6 C_D and average base pressure on a cube versus ground clearance; X, stationary ground; 0, moving ground.

The main conclusions reached from investigating the cube are that reducing ground height generates a downforce and that drag is almost independent of ground clearance. When a body is near the ground we can identify two main flow regions; an outer flow passing over the body and its image and an underbody flow. These two flows must match where they combine in the near wake and the underbody flow has the base pressure as its downstream boundary condition. On the cube the outer flow appears to be mainly responsible for generating the base pressure and setting the drag. The underbody flow requires far more attention than has hitherto been paid to it since changes in this flow can substantially affect the lift and in the case of the cube it causes a reattachment on the undersurface and generates pressures far lower than those measured anywhere else on the body. At low ground clearances the ratio of ground height to body width takes on a small value suggesting that the underbody flow may approach that of a two-dimensional channel flow. Figure 7 shows a photograph of an oil flow pattern on the undersurface of the cube at a ground clearance of 0.056c and with a moving floor. The near two-dimensional nature of the flow is apparent as is the flow reattachment line. The concept of a locally highly constrained gap flow matched to an outer flow has been proposed by Widnall and Barrows [27] to solve for both two and three dimensional flat plate aerofoils at small ground clearances.

Small changes in C_D with ground clearance were also observed by Fackrell [23] and Morel [28] in experiments on idealized vehicle body shapes. However both measured large changes in the lift coefficient as the ground was approached and near the ground Fackrell noted a much greater sensitivity of C_L to small incidence changes. This result is similar to that predicted by potential flow theory for flow over wings near the ground. The lift on Fackrell's wedge-shaped body was sensitive to the ground simulation method used with a stationary ground creating the higher lift. Turner [29] also noted, in experiments on a model automobile in a wind tunnel equipped with a moving ground, that the boundary layer on the fixed ground tends to increase the lift but has negligible effect on other components. A similar effect is just discernible in the measurements of Grunwald [30] on train-like vehicles

Downloaded 02 Jun 2010 to 171.66.16.103. Redistribution subject to ASME license or copyright; see http://www.asme.org/terms/Terms_Use.cfm

Fig. 7 Undersurface flow pattern on a cube with a ground clearance of 0.056c and with the floor moving.

above a moving and fixed ground. On a fixed ground it is impossible to eliminate the influence of the upstream boundary layer and although the boundary layer can be thinned, such that its displacement thickness δ^* is very small, it will still possess non-zero values of $d\delta^*/dx$, $d^2\delta^*/dx^2$, etc. The effect of $d\delta^*/dx$ will be to induce a slight incidence on the flow near the ground and, since C_L becomes much more sensitive to incidence change near the ground, we can expect a measurable increase in lift with a stationary ground. The cube, however, has a negative lift curve slope, i.e. increasing incidence decreases lift and it may be that the cube's insensitivity to ground representation may be a combination of several effects. Thus the need for moving ground simulation depends on body geometry; for example in order to test ground-effect type racing cars in a wind tunnel a moving ground simulation is essential (Wright [31]).

Another bluff body that has been investigated with a moving and a fixed ground is the road wheel. Fackrell and Harvey [32] carried out wind tunnel experiments to measure pressure distributions on a stationary wheel on a fixed ground and a rotating wheel on a moving ground. It is clear from their work that wheel flow can only be modelled correctly with a moving ground.

Base Drag and Vehicle Wakes

Many factors contribute to the drag of a vehicle and if drag is to be minimized all of these need to be considered. Previous discussion has emphasized the importance of the underbody flow and, because of the high relative velocities under a vehicle, it would seem advantageous to maintain the underbody smooth. The outer flow over a vehicle consists of a forebody flow region and a base flow region. Many of the separations occurring over the forebody of a complex three-dimensional shape can be avoided, or at least minimized, by careful design and by developing the body shape in a wind tunnel. Hucho [33] has described a technique of "aerodynamic tuning" whereby drag is significantly reduced by making small changes to a large number of body details. Another kind of tuning, or shear layer conditioning, has been investigated by Roshko and Koenig [34] who have studied the drag of two bodies in tandem. They found that the forebody drag of a blunt-ended circular cylinder, aligned with the flow, could be substantially reduced by placing a suitably-sized disc upstream such that the shear layer separating from the disc attaches on to the front shoulder of the cylinder. This eliminates any separation from the front of the cylinder and the drag of the cylinder forebody and disc combination can be

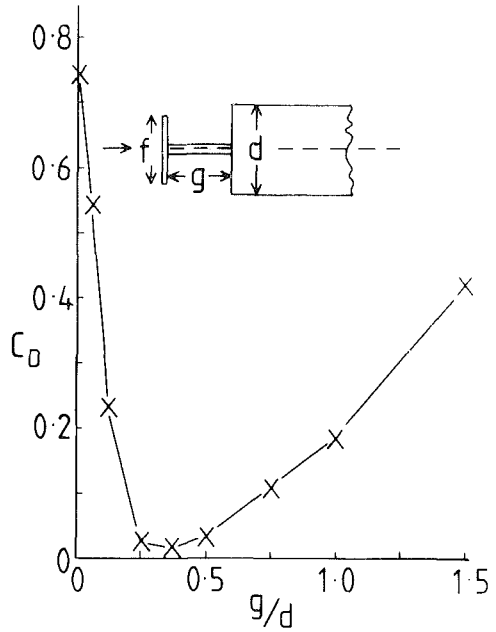

Fig. 8 Effect of gap on forebody drag for $f/d = 0.75$ (Roshko and Koennig [34]).

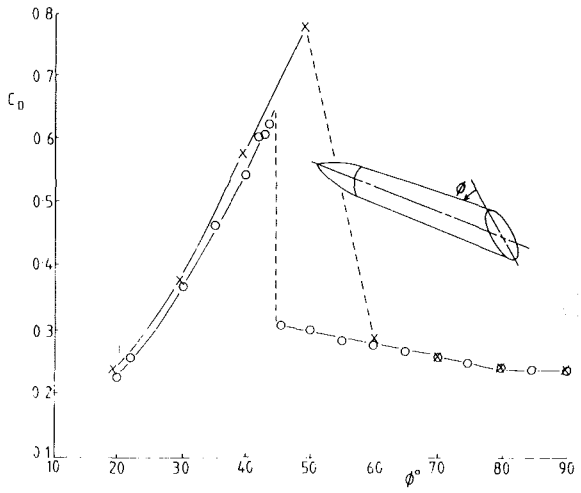

Fig. 9 Drag coefficient of a body with an axisymmetric forebody and slanted base. O, Morel [37]; X, Stuart and Jones [38].

much lower than the forebody drag of the cylinder in isolation, as shown in Fig. 8. Air deflectors to reduce the drag of trucks work on a similar principle. The flow over two circular discs in tandem has been studied by Morel and Bohn [35] and they found that the optimum two disc configuration had a drag 81 percent lower than that of a single disc alone.

The particular body feature that is responsible for the largest contribution to overall aerodynamic drag varies from one vehicle type to another. On trains, for example, wheel and bogie drag is extremely important and skin friction drag is much larger than base drag whereas on saloon cars base drag makes the largest contribution. Thus if the drag of road vehicles is to be reduced to a minimum we need to understand the mechanisms responsible for generating its base drag.

Janssen and Hucho [36] were the first to report the remarkable effect that slanting the base of a three-dimensional bluff body has on its drag. They varied the rear roof angle of a car and found that a drag maximum occurred when the roof was angled at about 30 deg to the horizontal. This discovery led Morel [37] to initiate a programme of research into the general behaviour of slanted bases. Morel's

Downloaded 02 Jun 2010 to 171.66.16.103. Redistribution subject to ASME license or copyright; see http://www.asme.org/terms/Terms_Use.cfm

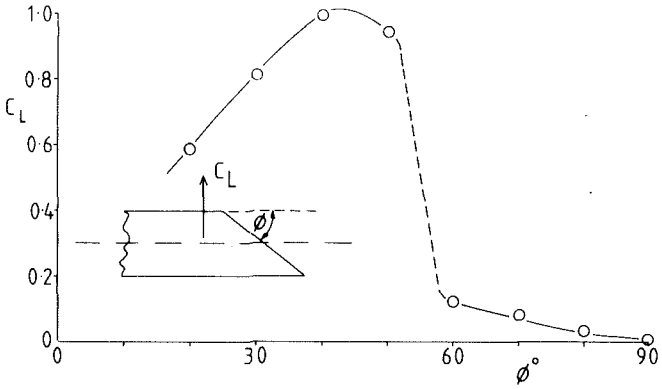

Fig. 10 Effect of base slant angle on lift

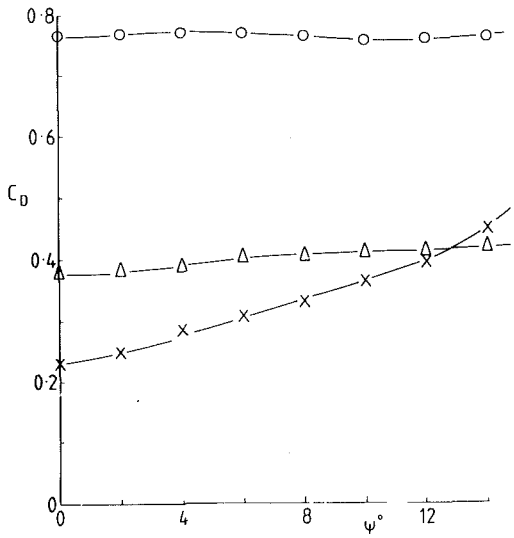

Fig. 11 Effect of yaw angle on the drag of bodies with various slant angle bases. △, $\phi = 30$ deg; 0, $\phi = 50$ deg; X, $\phi = 90$ deg.

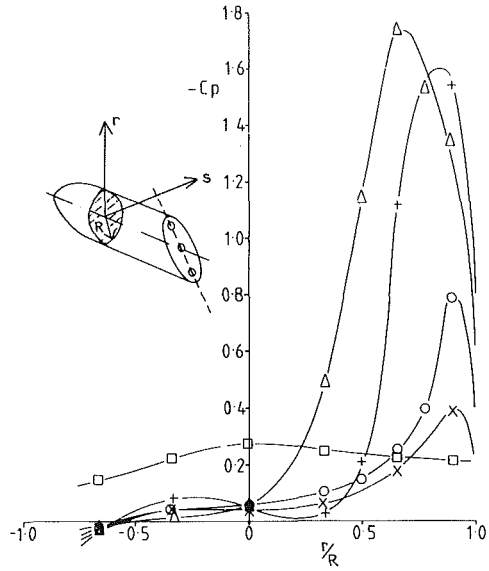

Fig. 12 Pressure distributions measured along a line passing through the furthest upstream point of the base and the base center. X, $\phi = 20$ deg; 0, $\phi = 30$ deg; +, $\phi = 40$ deg; △, $\phi = 50$ deg; □, $\phi = 70$ deg.

measurements of the drag coefficient of an axisymmetric cylinder, aligned with the flow, with a slanted base are reproduced in Figure 9. The slant angle, ϕ, is the angle of the base to the horizontal. Also included in the figure are C_D measurements from Imperial College taken by Stuart and Jones [38] on a similar body shape. Stuart and Jones found the maximum drag to be extremely sensitive to angle of incidence and a small incidence variation could account for the different slant angles for maximum drag shown in the Figure.

Morel described how there are two distinct flow regimes for slanted bases, one appropriate to small angles and another for large angles. At high ϕ vorticity is shed approximately axisymmetrically and a recirculating type wake is set up similar to that described earlier for the disc. On the other hand, below a value of ϕ between 40 and 50 deg, the vorticity is shed in two intense longitudinal vortices that have their origin at the furthest upstream point of the slanted base. The vortices grow, as they trail back down the base, as vorticity is fed in from the boundary layer on the upstream part of the body. The presence of the vortices greatly enhances the lift, as can be seen from Stuart and Jones' results plotted in Fig. 10 (C_L is based on body frontal area). They also found that C_D was insensitive to small yaw angle changes in the twin vortex regime but very dependent on yaw in the recirculating near wake regime as can be seen in Fig. 11, where C_D is referred to wind axes. Sedney [39] has proposed a flow model for the effect of a slanted base on drag that suggests that vortex breakdown is responsible for the sudden change in drag. It should be noted that the flow at small values of ϕ has been examined extensively by aircraft aerodynamicists in connection with the flow around upswept rear fuselages (Peake [4]).

Hoare [40] used the same model as Jones and Stuart, mounted at zero incidence, and measured pressure distributions over bases with various slant angles. Figure 12 shows pressure distributions taken along the center line of the base from a position $r/R = -1.0$ at the furthest downstream point of the base, where r is a distance measured perpendicular to the axis of the forebody and R is the forebody radius. Pressure measurements taken along a line of tappings normal to those used in Fig. 12 are plotted in Fig. 13. The pressure measurements clearly distinguish the two flow regimes with the longitudinal vortices generating intense low pressures and an extremely non-uniform base pressure. Figure 12 shows that the lowest pressures were recorded for $\phi = 50$ deg at a point near to the beginning of the slant. Hoare also investigated the effectiveness of spoilers and strakes, mounted on the base, in alleviating the high base suctions at the critical angle of $\phi = 50$ deg. Pressure measurements taken across the center of the base are shown in Fig. 14 for a spoiler (a) and a pair of strakes (b). The effect of these devices was to reduce the base angle for maximum drag by about 10 deg and to reduce the magnitude of this maximum.

It is clear from the preceding discussion that the slant angle of the base of a vehicle will affect the structure of its wake. In the longitudinal vortex regime it is not known, however, how far these vortices will persist in the wake. It is possible that, since they are moving into a region of rising pressure, that they will burst within a few vehicle lengths. Although a knowledge of vehicle wakes is extremely important to both the problems of predicting the dispersion of exhaust gases and to estimating the interference caused to following vehicles little detailed information seems to be available. In any wind tunnel studies of vehicle wakes the ground plane simulation technique is likely to influence wake development. The pressure distribution on the ground, just behind a vehicle, will show an adverse gradient and on a stationary floor the flow could separate. Eskridge and Hunt [41], have presented theoretical results, based on similarity arguments, that predict for a wind tunnel experiment that the wake of a bluff body above a fixed floor should grow as $(x/d)^{1/2}$ whereas above a moving floor the growth rate is less at $(x/d)^{1/4}$, where x is

Downloaded 02 Jun 2010 to 171.66.16.103. Redistribution subject to ASME license or copyright; see http://www.asme.org/terms/Terms_Use.cfm

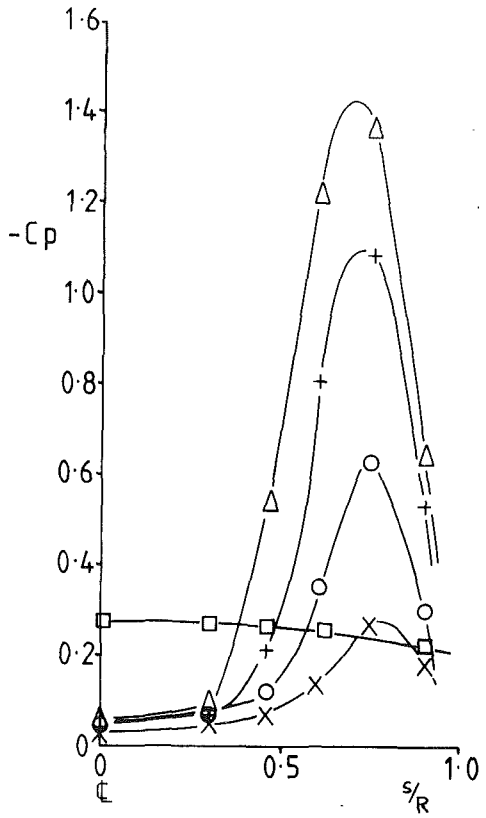

Fig. 13 Pressure distributions measured along a horizontal line pasing through the base center. X, $\phi = 20$ deg; 0, $\phi = 30$ deg; +, $\phi = 40$ deg; △, $\phi = 50$ deg; □, $\phi = 70$ deg.

distance behind the vehicle and d is a typical vehicle dimension. Experiments are being carried out at Imperial College to test this theory. Ahmed and Baumert [42] have measured some time mean velocity and pressure profiles behind estate, fastback and notchback vehicles mounted in a wind tunnel above a fixed floor. Their results are extremely interesting and show how vehicle shape influences the development of longitudinal vortices in the wake. Howell [21] and Ahmed and Baumert [42] have demonstrated that longitudinal vortices are an important feature of vehicle wakes.

The wake flow behind two-dimensional bluff bodies at high Reynolds numbers is dominated by the regular shedding of turbulent vortices but for bluff bodies with aspect ratios near unity the presence of discrete vortices is not so well documented. Achenbach [7] has shown that a sphere sheds vortex loops at a regular frequency but how important these are to the forces generated on the sphere is not clear. Similarly Calvert [43] has shown that a disc has a preferred wake frequency and that the energy at this frequency increases as the disc is inclined to the flow. However there is very little information available on the unsteady structure of the wake of a three-dimensional bluff body moving close to a ground plane.

The Influence of the Wind on the Flow Round Vehicles

Land vehicles are exposed to the natural wind and their aerodynamic performance is affected by both the wind's mean velocity and its turbulence structure. During the travelling life of a vehicle it will, on average, experience a relative air flow at some small angle of yaw. By combining wind speed and direction statistics with vehicle journey data some average yaw angle can be calculated (Cooper [44]). Whilst many vehicle forebody shapes appear reasonably streamlined to a head on wind a fairly modest angle of yaw can cause separations from longitudinal edges and sharply

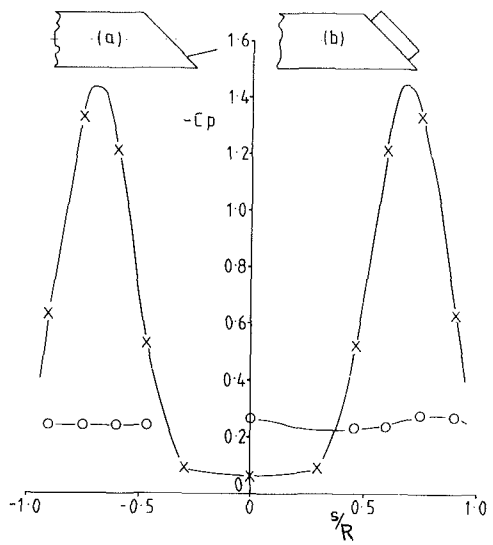

Fig. 14 Effect of a spoiler, *(a)*, and strakes, *(b)*, on the pressure distribution measured along a horizontal line passing through the base center for $\phi = 50$ deg. X, plain base; 0, with device added.

rounded sides which can substantially increase the drag. Thus there is no point in modifying a vehicle's shape to reduce its straight ahead drag if in the process the drag at small angles of yaw is increased. A yawed wind can also affect handling and stability and, in the case of long vehicles such as trains, can cause a large side force on the leading vehicle (Cooper [45]).

An aspect of the problem of the interaction of the natural wind with vehicles which has been less fully discussed is that of the effect of atmospheric turbulence. Near the ground there are turbulent eddies with scales comparable with the size of a vehicle and these can interact with the body flow field and may affect boundary layer growth, separation, reattachment and wake development. Thus turbulence can have a large influence on the mean flow and the mean loading and it is wrong to assume that the only effect of gusts is to generate unsteady forces. A vehicle will experience turbulence from different terrains, embankments, cuttings, bridges and from other vehicles. The relative turbulence intensity, defined as the r.m.s. of wind fluctuations divided by mean relative wind can take on any value, depending on the magnitude and direction of the wind. The relative turbulence intensity experienced by a vehicle driving into a head wind is $\sqrt{\bar{u}^2}/(V+U)$ where U is mean wind speed at say the top of the vehicle, V vehicle speed and $\sqrt{\bar{u}^2}$ is the r.m.s. of horizontal wind speed fluctuations. In open terrain the value of $\sqrt{\bar{u}^2}/U$ is around 0.2, and if the wind speed is as high as a third of the vehicle speed then the turbulence level relative to the vehicle would be 0.05. Higher turbulence levels are likely to be encountered when one vehicle is travelling in the wake of another but for the purposes of this discussion 0.05 will be taken as a typical value.

The effect of free stream turbulence on bluff body flows is reviewed by Bearman [46] and it is concluded that, in the majority of cases, mean forces are sensitive to variations in turbulence intensity but that changing turbulence scale has little influence. The fact that turbulence reduces the critical Reynolds number of a circular cylinder has led some to take the erroneous view that turbulence is equivalent to an increase in Reynolds number. However turbulence also affects the flow around bodies with sharp-edged separation, its primary effect being to accelerate the growth rate of free shear layers. The more rapidly growing shear layers entrain extra fluid from inside the separated region and the pressure reduces further causing the shear layer curvature to rise. This can lead to reattachments on downstream surfaces which were not present in smooth flow.

Downloaded 02 Jun 2010 to 171.66.16.103. Redistribution subject to ASME license or copyright; see http://www.asme.org/terms/Terms_Use.cfm

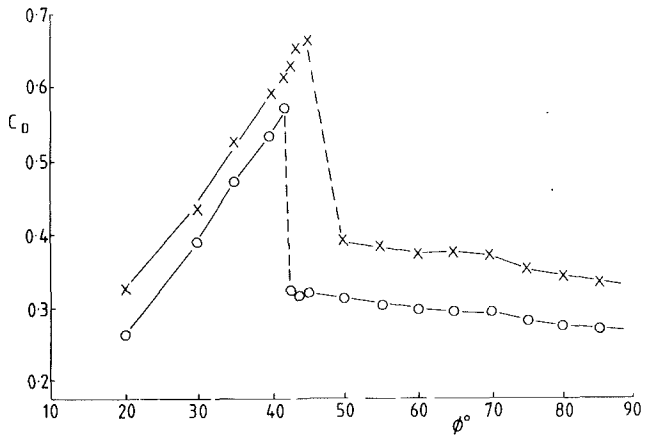

Fig. 15 Effect of turbulence on the drag of bodies with slanted bases (Morel [25]). 0, smooth flow; X, turbulent flow with $\sqrt{\bar{u}^2}/U = 0.06$.

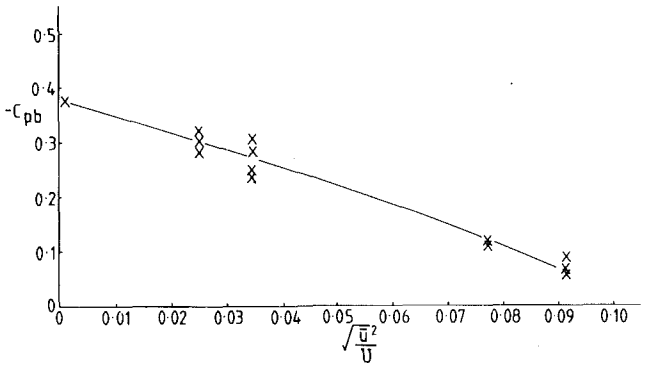

Fig. 16 Base pressure coefficient on a cube versus turbulence intensity, $\sqrt{\bar{u}^2}/U$

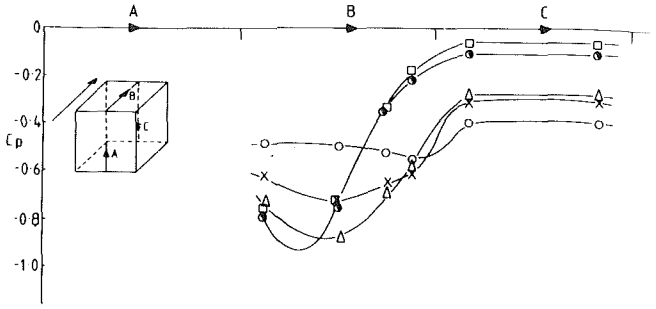

Fig. 17 Pressure distributions on a cube in turbulent flow, 0, smooth flow, $\sqrt{\bar{u}^2}/U < 0.005$; X, $\sqrt{\bar{u}^2}/U = 0.025$; △, $\sqrt{\bar{u}^2}/U = 0.035$; ⊕, $\sqrt{\bar{u}^2}/U = 0.078$; □, $\sqrt{\bar{u}^2}/U = 0.092$.

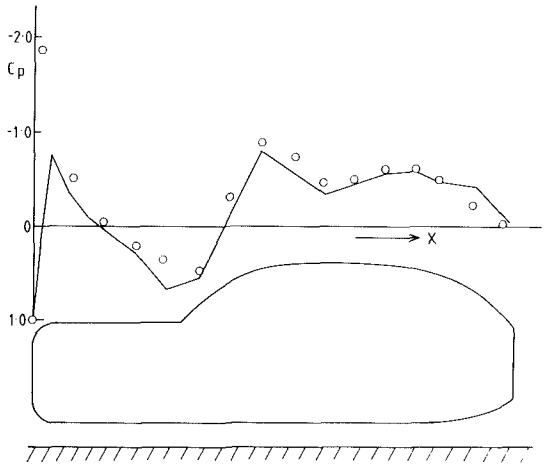

Fig. 18 Pressure distribution along the center line of the top surface of a car model. 0, wind tunnel measurement; ——, Stafford's calculation method.

There is very little information available on the effect of turbulence on vehicle-like shapes near the ground and results will only be presented for two simple bluff body shapes free of ground effect. Morel [28] repeated his measurements of C_D on a cylindrical body with a slanted base in a turbulent flow of intensity 0.06 and with a longitudinal scale equal to roughly half the forebody diameter. His results are presented in Fig. 15 and it can be seen that at all slant angles turbulence increased the drag. The increased drag was primarily felt as an additional base drag. Martin [47] has investigated the effect of turbulence on the drag of a cube with one face normal to the flow and her measurements of base pressure coefficient, C_{P_b}, versus $\sqrt{\bar{u}^2}/U$ are shown in Fig. 16. Here we see an opposite effect to that of the Morel body with increasing turbulence decreasing base drag. Pressure distributions on a side face of the cube are plotted in Fig. 17 and it can be seen that increasing turbulence level decreases the pressure just downstream of separation but that a presure recovery occurs towards the rear edge as the flow attempts to reattach. The base pressure is now higher than it would have been if the flow had been smooth. It can be anticipated from these results that the influence of turbulence on the drag of cuboids will depend critically on cuboid depth. Although it is always dangerous to make generalizations concerning turbulence it would appear that well designed bodies with separation occurring at the rear are likely to have their drag coefficients increased by the wind whereas as box-type vehicles will have them decreased. An interesting feature of the cube measurements is that although the integral scale of the longitudinal component of the turbulence was varied from 0.1 to 1.2 times the cube dimension the results showed little influence of changing scale.

Numerical Prediction Methods

The possibility of having a prediction method that can generate flow patterns and pressure distributions on any vehicle shape to a high degree of accuracy is of course extremely attractive to a designer. It means that unsuitable body shapes can be discarded at an early stage and the effect of improvements on more promising shapes can be quickly assessed. The question is not whether numerical methods are desirable, however, but, for complex three-dimensional bluff shapes, how long will it be before they approach the accuracy of wind tunnel testing. Fortunately my task is to review present knowledge and I need not be drawn into any speculation on future developments, however the requirement to predict pressures all over a car body to an accuracy of a few per cent of free stream dynamic pressure would seem a stringent one.

Hirt and Ramshaw [48] have discussed the possibilities of using numerical methods to solve the Navier-Stokes equations for flow over three-dimensional bluff bodies. They show sample calculations using finite difference techniques and go on to describe the limitations of such methods. The capacity of present day computers limits the Reynolds number at which calculations can be made to a few hundred and turbulence can only be introduced through the use of fairly crude turbulence models. On the coarse scale used it is impossible to represent boundary layers and free shear layers with sufficient accuracy and separation positions have to be assumed. In their long range projections for complex 3D bluff body calculations Hirt and Ramshaw see computer improvements failing to meet the needs of calculators using presently available methods and they turn towards improvements in

Downloaded 02 Jun 2010 to 171.66.16.103. Redistribution subject to ASME license or copyright; see http://www.asme.org/terms/Terms_Use.cfm

calculation methods and procedures as being the most promising area for advance.

Much of the flow about a bluff body is irrotational and although viscosity is responsible for generating vorticity over a body surface it plays a much smaller role once that vorticity is shed. A technique that has achieved some uncertain success in modelling high Reynolds number flow around two-dimensional bluff bodies is the method of discrete vortices. Here separating shear layers are discretized into a number of point vortices and calculation proceeds from time $t=0$, with small point vortices injected into the flow near separation points until some stable solution is achieved. These methods are reviewed by Clements and Maull [49] and in principle can be extended to complex 3D shapes although the computing requirements may prove prohibitive. Leonard [50] has carried out calculations on a simple 3D shape, the sphere, using vortex filaments and obtained a drag coefficient appropriate to a subcritical Reynolds number. Separation position has to be specified in his method and since he choose a position appropriate to a subcritical Reynolds number the solution is consistent.

The viscous-inviscid interaction about a vehicle sets up a flow field outside the boundary layer and wake that can in principle be solved by potential flow methods. In two dimensions bluff body potential flow can be solved by free streamline or wake source methods provided the base pressure and separation positions are known (Bearman and Fackrell [51]). Potential flow about 3D bluff bodies is complicated in general by the presence of longitudinal vorticity in the wake. To calculate flow over streamlined 3D lifting bodies surface singularity methods are widely used where the surface is represented by a large number of panels over which a suitable distribution of singularities is spread. Ahmed and Hucho [52] and Stafford [53] have extended these methods to calculate the potential flow over road vehicle shapes. Ahmed and Hucho overcame the problem of correctly representing the wake by first carrying out flow visualization studies of a similar body in a wind tunnel and then panelling the wake surface as if it were part of the body. Stafford [53] represented his vehicle by vortex elements and at the assumed separation position these were allowed to trail back parallel to infinity. In addition he introduced a suitably sized source inside the body to represent the effect of the wake. A comparison of the pressure distribution measured along the center line of the top surface of a car model in a wind tunnel and calculated using Stafford's method [54] is shown in Figure 18.

A way ahead for the surface singularity methods, which have the advantage that they can represent body detail to a fair accuracy, would be to combine such a calculation with accurate predictions of boundary layer growth, using probably yet to be developed turbulent boundary layer calculation methods, and some better physical modelling of the wake. The latter step awaits an improved understanding of road vehicle near wake flows. It can be concluded that the way ahead for all of these methods is not going to be easy and it would appear that wind tunnels will continue to fulfill a useful role for many years to come.

References

1 Milliken Jr., W. F., "Aerodynamic Research Plan for Automotive-Type Vehicles," Oct. 1977, Milliken Research Associates, Inc., Williamsville, N.Y., USA.

2 Sovran, G., Morel, T., and Mason Jr., W. T., ed., *Aerodynamic Drag Mechanisms of Bluff Bodies and Road Vehicles,* Plenum Press, New York, 1978.

3 Küchemann, D., *Aerodynamic Design of Aircraft,* Pergamon, Oxford, 1978, pp. 351–373.

4 Peake, D. J., "Controlled and Uncontrolled Flow Separations in Three Dimensions," National Aeronautical Establishment, Ottawa, Aeronautical Report LR591, 1976.

5 Cermak, J. E., "Aerodynamics of Buildings," *Annual Review of Fluid Mechanics,* Vol. 8, 1976, pp. 75–106.

6 Morkovin, M. V., "Flow Around a Circular Cylinder–A Kaleidoscope of Challenging Fluid Phenomena," *Symposium on Fully Separated Flows,* ASME, 1964.

7 Achenbach, E., "Vortex Shedding from Spheres," *J. Fluid Mech.,* Vol. 62, 1974, pp. 209–221.

8 Nakaguchi, H., Hashimoto, K., and Muto, S., "An Experimental Study on Aerodynamic Drag of Rectangular Cylinders," *J. of the Japan Soc. of Aeronautical and Space Sciences,* Vol. 16, 1968, pp. 1–5.

9 Mair, W. A., "Drag-Reducing Techniques for Axi-Symmetric Bluff Bodies," *Aerodynamic Drag Mechanisms of Bluff Bodies and Road Vehicles,* General Motors Research Laboratories Symposium, Sept. 1976.

10 Mair, W. A., "Reduction of Base Drag by Boat-tailed Afterbodies in Low Speed Flow," *Aero. Quart.,* Vol. 20, 1969, pp. 307–320.

11 Mason Jr., W. T., and Beebe, P. S., "The Drag Related Flow Field Characteristics of Trucks and Buses," *Aerodynamic Drag Mechanisms of Bluff Bodies and Road Vehicles,* General Motors Research Laboratories Symposium, Sept. 1976.

12 Calvert, J. R., "The Separated Flow behind Axially Symmetric Bodies," Ph.D. dissertation, University of Cambridge, 1967.

13 Sykes, D. M., "The Effect of Low Flow Rate Gas Ejection and Ground Proximity on Afterbody Pressure Distribution," *Proceedings of 1st Symposium on Road Vehicle Aerodynamics,* City University, London, 1969.

14 Smith, J. H. B., "A Review of Separations in Steady, Three-Dimensional Flow," AGARD CP-168, May 1975.

15 Maskell, E. C., "Flow Separation in Three Dimensions," Royal Aircraft Establishment, Aero, Rept. 2565, Nov. 1955.

16 Lighthill, M. J., "Attachment and Separation in Three-Dimensional Flow," *Laminar Boundary Layers,* Ed. L. Rosenhead, Oxford Univ. Press, 1963, pp. 72–82.

17 Bearman, P. W., and Zdravkovich, M. M., "Flow Around a Circular Cylinder Near a Plane Boundary," *J. Fluid Mech.,* Vol. 89, 1978, pp. 33–47.

18 Carr, G. W., "The Aerodynamics of Basic Shapes for Road Vehicles. Part 1: Simple Rectangular Bodies," MIRA Report No. 1968/2, 1968.

19 Carr, G. W., "The Aerodynamics of Basic Shapes for Road Vehicles. Part 2: Saloon Car Bodies," MIRA Report No. 1968/9, 1968.

20 George, A. R., "Aerodynamics of Simple Bluff Bodies Including Effects of Body Shape, Ground Proximity and Pitch," *Aerodynamics of Transportation,* ASME Symposium, Niagara Falls, June 1979.

21 Howell, J. P., *Force and Wake Characteristics of Simple Bluff Bodies in Ground Proximity,* Ph.D. dissertation, City University, London, 1977.

22 Howell, J., "Force and Wake Characteristics of Simple Bluff Bodies in Ground Proximity, *Aerodynamics of Transportation.* ASME Symposium, Niagara Falls, June 1979.

23 Fackrell, J. E., "The Simulation and Prediction of Ground Effect in Car Aerodynamics," Imperial College, I.C. Aero. Report 75-11, Nov. 1975.

24 Anderson, H. L., *Investigation of the Forces on Bluff Bodies Near the Ground,* M.Sc. dissertation, Department of Aeronautics, Imperial College, 1977.

25 Maskell, E. C., "A Theory of the Blockage Effects of Bluff Bodies and Stalled Wings in a Closed Wind Tunnel," Aero. Res. Counc. R.&M. No. 3400, 1965.

26 Nakaguchi, H., "Recent Japanese Research on Three-Dimensional Bluff Body Flows Relevant to Road-Vehicle Aerodynamics," *Aerodynamic Drag Mechanisms of Bluff Bodies and Road Vehicles,* General Motors Research Laboratories Symposium, Sept. 1976.

27 Widnall, S. E., and Barrows, T. M., "An Analytic Solution for Two and Three-Dimensional Wings in Ground Effect," *J. Fluid Mech.,* Vol. 41, 1970, pp. 769–792.

28 Morel, T., "Aerodynamic Drag of Bluff Body Shapes Characteristic of Hatch-Back Cars," SAE Paper 780280; also *SAE Transactions,* 1978.

29 Turner, T. R., "Wind-Tunnel Investigation of a 3/8 Scale Automobile Model over a Moving-Belt Ground Plane," NASA Tech. Note TN D-4229, 1967.

30 Grunwald, K. J., "Aerodynamic Characteristics of Vehicle Bodies at Crosswind Conditions in Ground Proximity," NASA Tech. Note TN D-5935, 1970.

31 Wright, P., Lotus Cars Ltd., Private Communication.

32 Fackrell, J. E., and Harvey, J. K., "The Aerodynamics of an Isolated Road Wheel," *Proceedings of the Second AIAA Symposium on Aerodynamics of Sports and Competition Automobiles,* Vol. 16, May 1974.

33 Hucho, W.-H., "The Aerodynamic Drag of Cars, Current Understanding, Unresolved Problems and Future Prospects," *Aerodynamic Drag Mechanisms of Bluff Bodies and Road Vehicles,* General Drag Mechanisms of Bluff Bodies and Road Vehicles, General Motors Research Laboratories Symposium, Sept. 1976.

34 Roshko, A., and Koenig, K., "Interaction Effects on the Drag of Bluff Bodies in Tandem," *Aerodynamic Drag Mechanisms of Bluff Bodies and Road Vehicles,* General Motors Research Laboratories Symposium, Sept., 1976.

35 Morel, T., and Bohn M., "Flow Over Two Circular Disks in Tandem," ASME JOURNAL OF FLUID ENGINEERING, Vol. 102, 1980, pp. 104–111.

36 Janssen, L. J., and Hucho, W.-H., "Aerodynamische Formoptimierung der Type VW-Golf and VW-Scirocco," *Kolloquium ueber Industrie-Aerodynamik,* Aachen, Part 3, 1974, pp. 46–49.

37 Morel, T., "The Effect of Base Slant on the Flow Pattern and Drag of Three-Dimensional Bodies with Blunt Ends," *Aerodynamic Drag Mechanisms*

Downloaded 02 Jun 2010 to 171.66.16.103. Redistribution subject to ASME license or copyright; see http://www.asme.org/terms/Terms_Use.cfm

of Bluff Bodies and Road Vehicles, General Motors Research Laboratories Symposium, Sept. 1976.

38 Stuart, A. D., and Jones, A. T., *The Drag of an Upswept Rear Fuselage,* Undergraduate Project, Department of Aeronautics, Imperial College, 1977.

39 Sedney, R., "A Flow Model for the Effect of a Slanted Base on Drag," *Aerodynamics of Transportation,* ASME Symposium, Niagara Falls, June 1979.

40 Hoare, G. T., *Pressure Measurements on Upswept Afterbodies,* Undergraduate Project, Department of Aeronautics, Imperial College, 1978.

41 Eskridge, R. E., and Hunt, J. C. R., "Highway Modelling. Part 1: Prediction of Velocity and Turbulence Fields in the Wake of Vehicles," To be published in the Journal of Applied Meteorology, 1979.

42 Ahmed, S. R., and Baumert, W., "The Structure of the Wake Flow behind Road Vehicles," *Aerodynamics of Transportation,* ASME Symposium, Niagara Falls, June 1979.

43 Calvert, J. R., "Experiments on the Flow Past an Inclined Disk," *J. Fluid Mech.,* Vol. 29, 1967, pp. 691–703.

44 Cooper, K. R., "A Wind Tunnel Investigation into the Fuel Savings Available from the Aerodynamic Drag Reduction of Trucks," National Research Council of Canada, DME/NAE Quarterly Bulletin No. 1976(3), 1976.

45 Cooper, R. K., "The Effect of Cross Winds on Trains," *Aerodynamics of Transportation,* ASME Symposium, Niagara Falls, June 1979.

46 Bearman, P. W., "Some Effects of Free-Stream Turbulence and the Presence of the Ground on the Flow Around Bluff Bodies," *Aerodynamic Drag Mechanisms of Bluff Bodies and Road Vehicles,* General Motors Research Laboratories, Sept. 1976.

47 Martin, L. J., "The Effect of Turbulence on the Flow around a Cube," M.Sc. dissertation, Department of Aeronautics, Imperial College, 1977.

48 Hirt, C. W., and Ramshaw, J. D., "Proespects for Numerical Simulation of Bluff-Body Aerodynamics," *Aerodynamic Drag Mechanisms of Bluff Bodies and Road Vehicles,* General Research Laboratories Symposium, Sept. 1976.

49 Clements, R. R., and Maull, D. J., "The Representation of Sheets of Vorticity by Discrete Vortices," *Prog. Aerospace Sci.,* Vol. 16, 1975, pp. 129–146.

50 Leonard, A., "Simulation of Unsteady Three-Dimensional Separated Flows with Interacting Vortex Filaments," *Aerodynamic Analyses Requiring Advanced Computers,* NASA SP-347, 1975, pp. 925–937.

51 Bearman, P. W., and Fackrell, J. E., "Calculation of Two-Dimensional and Axi-Symmetric Bluff Body Potential Flow," *J. Fluid Mech.,* Vol. 72, 1975, pp. 229–241.

52 Ahmed, S. R., and Hucho, W.-H., "The Calculation of the Flow Field Past a Van with the Aid of a Panel Method," SAE Paper No. 770390, 1977.

53 Stafford, L. G., "A Numerical Method for the Calculation of the Flow Field Around a Motor Vehicle," *Advances in Road Vehicle Aerodynamics,* reported by BHRA Fluid Engineering, Paper No. 11, 1973.

54 Stafford, L. G., Private Communication, 1979.

Downloaded 02 Jun 2010 to 171.66.16.103. Redistribution subject to ASME license or copyright; see http://www.asme.org/terms/Terms_Use.cfm

Straight-Walled, Two-Dimensional Diffusers—Transitory Stall and Peak Pressure Recovery

J. Ashjaee

J. P. Johnston
Mem. ASME.

Department of Mechanical Engineering,
Stanford University,
Stanford, Calif. 94305

Straight-walled, two-dimensional diffusers of large aspect ratio were investigated experimentally for the purpose of studying the regime of incipient transitory stall, the location of the geometry of peak diffuser pressure recovery. Twelve symmetric diffusers of constant nondimensional length ($L/W_1 = 15$) with total included angles ranging from 4 to 24 degrees, covering attached, intermittently detaching, and unsteady detached flows were examined. Tests were run at one inlet blockage, $2\delta_1/W_1 = 0.027$, and at an inlet Reynolds number of $U_1W_1/\nu = 2.2 \times 10^5$ with air flow at low inlet Mach number. Pressure recovery and flow direction intermittency were obtained along the diffuser walls. An objective comparison of the UIM method of Ghose and Kline and an improved prediction method [Appendix] was performed with respect to these new experimental data. Some new conclusions are drawn concerning the nature of the flow in the vicinity of peak pressure recovery.

Introduction

Transitory stall in diffusers is a class of internal flow that is naturally unsteady and very difficult to predict. In these intrinsically unsteady flows, maximum (peak) pressure recovery at constant diffuser length-to-width ratio, L/W_1, is achieved as transitory stall starts to develop, and, consequently, prediction methods for this regime of flow are applicable in the design of diffusers of optimum geometry.

Transitory stall, along with the other flow regimes in diffusers, was first recognized as a result of flow visualization experiments. Numerous contributions have been made to this topic; among the most useful ones for two-dimensional geometries are the diffuser flow regime studies of Fox and Kline [1] and the pressure-recovery charts developed by Reneau, et al. [2]. Many attempts to compute mean quantities of the flow have been made; a few of the most recent ones are [3], [4], and [5]. The UIM method by Ghose and Kline [5] is very promising. Indeed, a modified (but unpublished) version of the UIM developed by Ghose is sufficient if mean pressure recoveries in the neighborhood of C_p^* are desired. Recently, some new and revealing experiments have been carried out by Layne and Smith [6] which quantitatively indicate the magnitudes of the flow unsteadiness generated by transitory stall.

The purpose of our paper is to present a recent study on the local wall static pressure coefficient, $C_p(S)$, the overall pressure recovery, C_p, the flow-direction intermittency, γ_p, and an improved prediction method based on the UIM method [5]. These new data on C_p have a low experimental uncertainty ($\pm$ .003 at 20:1 odds) compared to earlier systematic data in which uncertainty is typically greater than $\pm$ 0.02, a fact which has improved our ability to evaluate the prediction methods. In addition, a new instrument, the thermal tuft [7], is used to determine the flow direction intermittency along the diffuser walls. The latter data allow the accurate location of flow detachment (separation) points, the knowledge of which is also of considerable value in the evaluation of prediction method accuracy and applicability.

Experimental Apparatus

Figure 1 illustrates the diffuser tunnel. A low-noise, airfoil-bladed, centrifugal fan draws air from the plenum chamber through high-efficiency filters and forces it through a vaned, double-expansion diffuser and into the return circuit. The exit plenum and the filter box are made of 3/4 in. plywood covered on the inside by 1 in. sound-absorbing material to diminish sound reflectivity and, hence, to reduce the sound-flow interactions. The fan is driven by an adjustable-speed motor which is controlled by a very stable feedback system. The combined system gives the desired operational range: continuously adjustable air velocity of 12-50 m/s at the test section inlet. The double-expansion diffuser is made of 3/4 in. plywood and is vaned with 1/16 inch thick aluminum plates to enable it to yield a high pressure recovery. The return circuit (60×54 cm^2 area) is made of 1/2 in. plywood, which is braced externally for stiffness. The double-expansion diffuser and the return circuit are covered on the inside by 1/2 inch sound-absorbing material. All three 90° corners in the tunnel circuit are vaned with airfoil-shaped aluminum vanes perforated on the convex side and filled with fiberglass in order to further reduce acoustic wave transmission through the circuit. The screen-pack and honeycomb were designed following recommendations found in the current literature [8]. Five precision mesh screen (58 mesh with 0.1 mm wire diameter) with a solidity (blocked area/frontal area) of 41.0

Contributed by the Fluids Engineering Division of The American Society of Mechanical Engineers and presented at the Winter Annual Meeting, New York, N.Y., December 2-7, 1979. Manuscript received by the Fluids Engineering Division, April 23, 1979.

Copyright © 1980 by ASME

Downloaded 02 Jun 2010 to 171.66.16.103. Redistribution subject to ASME license or copyright; see http://www.asme.org/terms/Terms_Use.cfm

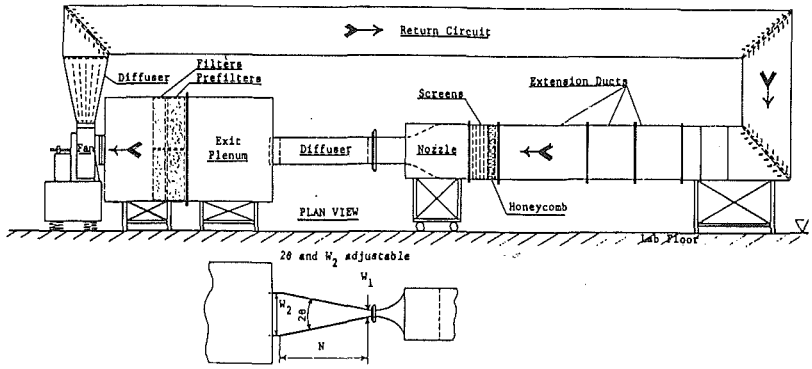

Fig. 1 Diffuser test apparatus

percent are installed on frames at 5.1 cm intervals. Immediately upstream of the screens is a "honeycomb" made of 24070 plastic milk straws (4 mm diameter and 14.6 cm length), carefully packed in close array. The tunnel is designed so that the filter box, the fan, and the return circuit are permanently fixed relative to the laboratory floor. Extension ducts in lengths up to 244 cm are inserted between the honeycomb and the upstream duct in order to accomodate various lengths of inlet and/or exit tail pipes.

The diverging (side) walls of the test section are 114.3 cm long so that, with the inlet width of 7.62 cm, the length-to-inlet-width ratio of the diffuser (L/W_1) is 15:1. The inlet aspect ratio of the diffuser is 4:1. The side-walls of the diffuser have short, flexible sections at both inlet and outlet planes, so that 2θ may be adjusted to arbitrary angles up to approximately 26°. The small changes in axial length that accompany variation of wall angle are accommodated by short, parallel, side-wall segments at the diffuser exit plane. These segments are free to slide through a rectangular, adjustable hole in the upstream wall of the exit plenum box. The diffuser walls are made of 1/2 in. thick plexiglass to allow for flow visualization.

Figure 2 shows some details of the inlet configuration. Complete analytic description of the diffuser wall geometry is provided in Fig. 2(*b*) [15]. The 34 cm long inlet duct, with its boundary layer trips, assures the development of identical turbulent boundary layer on all four walls at the inlet station, Station 1, located at a distance $S/W_1 = -1.15$ upstream of the diffuser throat. The diffusing section comprises the region $0 < S/W_1 < 15$, and values of S/W_1 greater than 15 represent locations in the short, parallel-walled exit section.

In the descriptions to follow, the side walls, or diverging walls, refer to the diffuser walls set at equal angles $\theta_A = \theta_B$ so that $2\theta = \theta_A + \theta_B$. The parallel walls bounding the side walls are often denoted as end walls. Both side walls and one end wall are provided with wall static pressure taps and instrument ports.

Experimental Results

Inlet mean velocity profiles, in $u^+ - y^+$ coordinates, are shown in Fig. 3. These profiles are measured with a traversing impact tube (tip O.D. = 0.071 cm) and wall static taps at six different spanwise positions, four on one side wall (wall *A*)

Nomenclature

a = local distance from the fictitious source in a source-like core flow model

C_p = pressure coefficient, $(p-p_1)\Big/\frac{\rho}{2}u_{e_1}^2$

h = diffuser height

H = boundary layer shape factor, δ^*/Θ

L = diffuser length

$\mathfrak{L}$ = effective flow width (Fig. A-1)

p = mean static pressure at wall

S = distance along the wall (see Fig. 2)

u = mean velocity in the streamwise direction

u_e = velocity at edge of boundary layer

u_β = wake amplitude

u_τ = friction velocity, (sign τ_w) $\sqrt{|\tau_w|/\rho}$

u_∞ = free-stream velocity

u^+ = nondimensional u, u/u_τ

W = diffuser width

Z = distance from mid-span of diverging walls

y = distance normal to the wall

y^+ = nondimensional y, $y|u_\tau|/\nu$

α = local wall angle

γ_p = flow direction intermittency at a point in wall layer (100 % always downstream)

δ = boundary layer thickness

δ^* = boundary layer displacement thickness

θ = wall angle of divergence

2θ = total included angle between diffuser walls; $\theta_A + \theta_B$

Θ = boundary layer momentum thickness

ν = kinematic viscosity

ρ = mass density

τ = shear stress

Subscripts

1 = diffuser inlet station ($S/W_1 = -1.15$)

2 = outlet station ($S/W_1 = 15.98$)

w = wall

A = wall A (diverging wall of the diffuser)

B = wall B (diverging wall of the diffuser)

p = parallel wall of the diffuser (end-wall)

Downloaded 02 Jun 2010 to 171.66.16.103. Redistribution subject to ASME license or copyright; see http://www.asme.org/terms/Terms_Use.cfm

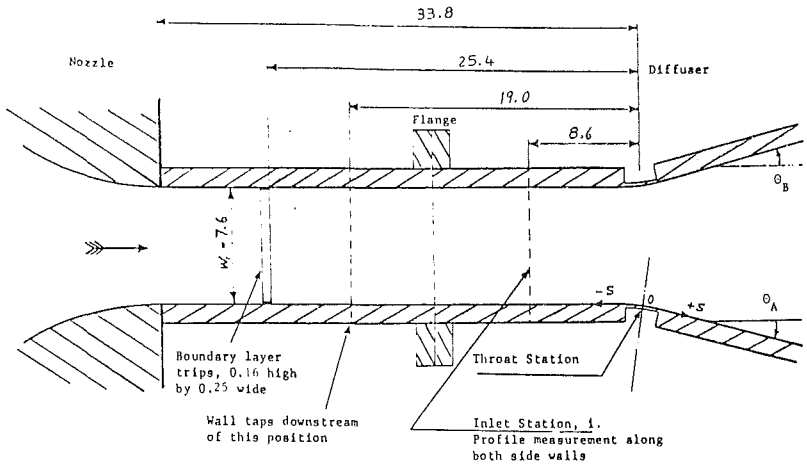

Fig. 2 Inlet geometry (parallel walls 30.5 cm apart). All dimensions in centimeters.

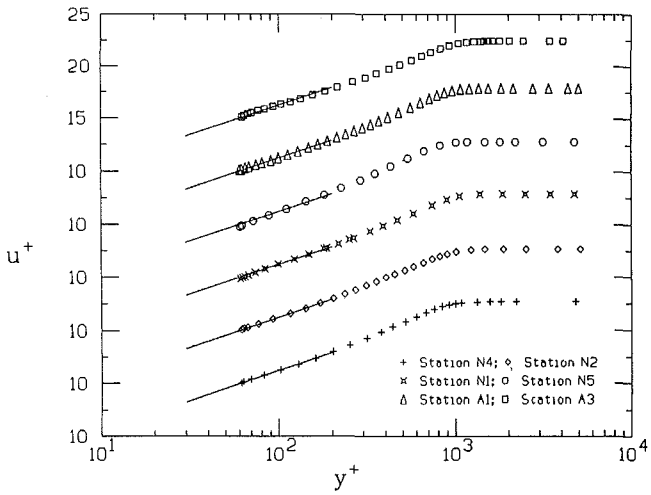

Fig. 3 Inlet velocity profiles, Station 1. Uncertainty in $u^+ = \pm 0.3$ (20:1 odds)

and two on the opposite wall (wall B). Inlet boundary layers on the two end walls are the same as those on the side walls. The spanwise distance between side-wall probe ports is 4.44 cm. The measured velocities have been corrected for the effect of velocity gradient, after Young and Maas [9]. No other corrections have been applied. However, in calculating shear velocity, u_τ, and boundary layer integral parameters, a few points affected by wall proximity have been excluded from the data set. A method [10] of fitting the data in the logarithmic region of the velocity profile has been used to calculate u_τ for each profile, as shown by the lines ($u^+ = 5.62 \log y^+ + 5.0$) in Fig. 3. The mean (average) integral parameters for the six measured profiles, as well as the deviations from the mean, are given in Table 1 before and after the corrections [9] were made. In order to account for sublayer effects below $y^+ = 50$, Coles' integrals for a standard sublayer [11] have been employed in calculating the boundary layer thicknesses δ_1^* and Θ_1 reported in Table 1.

For the series of tests reported in this paper, inlet free-stream velocity $u_{e_1} = 46.6 \pm 0.3$ m/s, inlet Reynolds number $u_{e_1} W_1/\nu = 2.2 \times 10^5$, and inlet blockage $2\delta_1^*/W_1 = 0.027$ were held constant. As shown in Fig. 3 and Table 1, the inlet profiles are those of a normal, flat-plate, turbulent boundary layer. Tables of experimental data on inlet velocity profiles, as well as on C_p and γ_p measurements, are provided in Ref. [15].

Mean wall-static pressure recovery measurements are shown in Fig. 4. Symmetric diffusers of L/W_1 of 15 have been tested at 12 values of 2θ. The last two data points in each set (values of S/W_1 greater than 15) reside in the parallel-walled tailpipe. In order to obtain stable and accurate average readings of the pressure transducer output, long integration times, up to several minutes in highly unsteady cases, were used.

For diffusers with angles up to $2\theta = 8$ deg, measurements did not show any difference in the mean static pressure recovery distributions along the two side walls; however, as transitory stall begins to develop, pressures on the side walls become distinguishably different, a sure sign of asymmetry in the mean flow pattern. This asymmetry is seen in Fig. 4 for $2\theta = 9$ deg (only near the exit station), and it becomes more evident for higher opening angles. With exceptionally symmetric side-wall angles, as established in these experiments ($|\Delta\theta| = |\theta_A - \theta_B| < 0.01$ degrees), there is no way to tell in advance which side wall will be the stalled wall. For the data set shown in Fig. 4, the stalled wall is wall A at $2\theta = 10$, 18, 20, and 24 deg, but the stall lies on wall B for $2\theta = 9$, 12, 14, and 16 deg. It is possible to cause the stall to switch sides, in which case the pressure coefficients interchange so that the former values of C_p on wall A are accurately reproduced on wall B, and vice versa. In fact, the flow occasionally shifted from one wall to the other, without our assistance, in a phenomenon we called the "stall switch." This is not a rapid flipping motion; rather, it occurs sporadically at long time

Table 1 Boundary layer integral parameters at inlet

Integral Parameter	Uncorrected		Corrected	
	Mean	Deviation	Mean	Deviation
δ_1, B. L. Thickness (in.)	0.337	.036	0.338	.036
δ_1^*, Displacement Thickness (in.)	0.039	.002	0.040	.002
Θ_1, Momentum Thickness (in.)	0.029	.002	0.030	.002
$H_1 = \delta_1^*/\theta_1$, Shape Factor	1.335	.018	1.348	.019

Downloaded 02 Jun 2010 to 171.66.16.103. Redistribution subject to ASME license or copyright; see http://www.asme.org/terms/Terms_Use.cfm

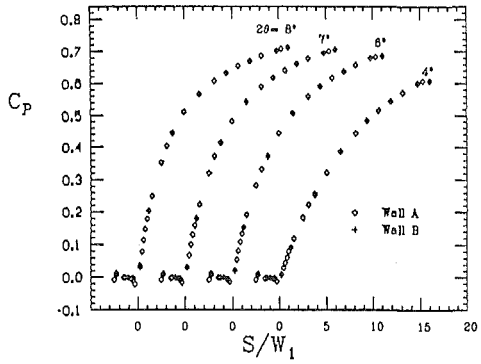

(1.) Unstalled flow: 2θ = 4, 6, 7, 8 deg

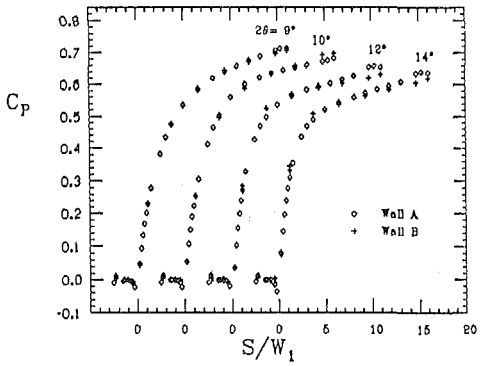

(2.) Transitory stall: 2θ = 9, 10, 12, 14 deg

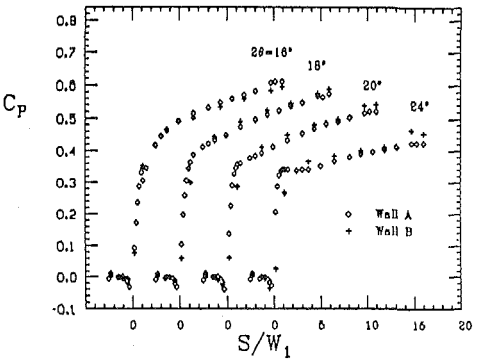

(3.) Large transitory stall: 2θ = 16, 18, 20, 24 deg

Fig. 4 Wall static pressure coefficients as a function of distance along the wall. Uncertainty in C_p = ± 0.003 (20:1 odds)

intervals, many minutes or even hours apart. "Stall switch" was commonly observed at opening angles about 16 deg, where large transitory stall prevails.

Figure 5 illustrates the overall static pressure recovery coefficient, $C_{p_{\text{overall}}} = (p_2 - p_1)/1/2\,\rho u_{e_1}^2$, as a function of the opening angle. Exit pressure, p_2, was measured at outlet, Station 2, which was established in the short tailpipe at S/W_1 = 15.98, 7.5 cm downstream of the end of the diffuser. Because of the asymmetry in the mean flow pattern discussed previously, the overall pressure recovery coefficient data in the transitory stall regime are shown to have two slightly different values. The line fit to the upper curve corresponds to conditions on the unstalled wall, which may be *A* or *B*. Peak pressure recovery occurs in the vicinity of 2θ = 9 deg with a value of $C_p^* = 0.715$.

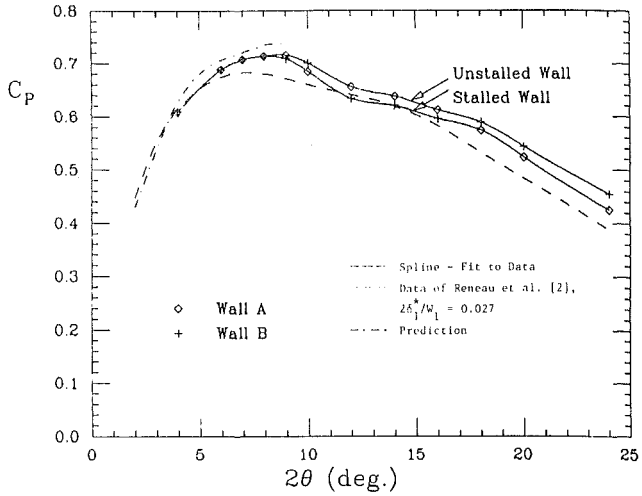

Fig. 5 Overall static pressure recovery coefficient as a function of opening angle. $2\delta_1^*/W_1$ = 0.027. Uncertainty in C_p = ± 0.003 (20:1 odds) for new data.

The lower, dashed curve in Fig. 5 is interpolated from the older data of Reneau et al. [2] at an equivalent value of inlet blockage, $2\delta_1^*/W_1 = 0.027$. The shapes of the old and new curves are very similar, although the older data appear to give slightly lower C_p values in the transitory stall regime.

The uncertainty in experimental values of C_p in our data is quite low compared to the uncertainty in older works. At odds of 20:1, we estimate that the uncertainty (using the method of [12]) in our measured C_p values is ± 0.003. With such a low uncertainty, there is no doubt that the bump in the overall C_p curve in the region of transitory stall regime is real. This bump exists, although it was not noticed or was masked by the uncertainty band of the data in older works. A flow subregime change may well be responsible for such a behavior of the overall C_p curve. The dot-dashed curve in Fig. 5 represents the predicted values for the overall pressure recovery coefficient. Discussion of these predictions follows.

Figures 6 through 9 give some new insight into the phenomena of unsteady separation and transitory stall. Here, experimental results on the flow direction intermittency very near the wall are reported. Denoted by γ_p, intermittency is defined here as the fraction of the time that the flow in the wall layers is in the downstream (forward) direction. Distribution of γ_p along the diffuser walls has been measured for four symmetric diffusers of L/W_1 = 15 operating in the neighborhood of peak pressure recovery (2θ = 8, 9, 10 and 12 deg). The inlet conditions, as mentioned earlier, are not changed. The instrument used, the thermal tuft (or wall-flow-direction probe), was developed for this purpose and is completely explained in reference [7].

Transitory Detachment (TD), Intermittent Transitory Detachment (ITD), and Incipient Detachment (ID) in Figs. 6 through 9 are defined to correspond to 50, 20, and 1 percent reverse flow, respectively. It is believed that detachment (separation), defined as the location where the time-average value of the wall shear stress goes to zero, will be very close to the TD point obtained with our thermal tuft probe.

In Fig. 8 for 2θ = 10 deg, as well as in Fig. 9 for 2θ = 12 deg, results are presented for two separate experimental runs corresponding to the two cases where the stalled region has been established on either side wall *A* or on side wall *B*. Although the separation phenomenon is highly sensitive to minute asymmetries, there is little difference between the results from two runs, since the wall goemetry is very symmetric. Measurement on the opposite (unstalled) wall in each case indicates that there is no reverse flow present on that wall. In Fig. 8, it is readily observed that the separation

Downloaded 02 Jun 2010 to 171.66.16.103. Redistribution subject to ASME license or copyright; see http://www.asme.org/terms/Terms_Use.cfm

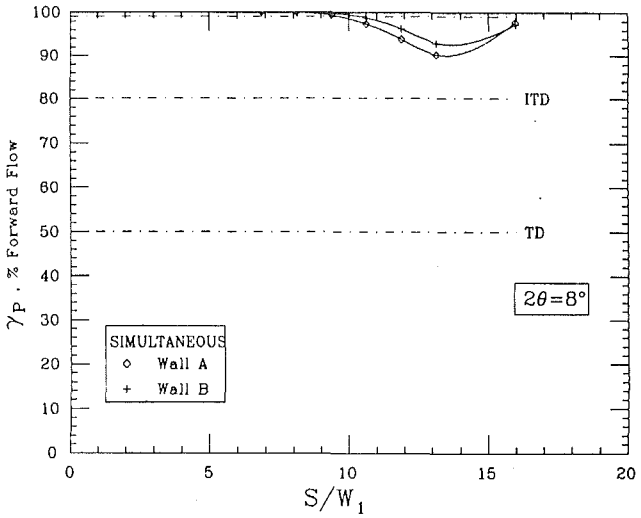

Fig. 6 Flow direction intermittency along diffuser wall, 2θ = 8 deg. Uncertainty in γ_p = ± 1 percent (20:1 odds).

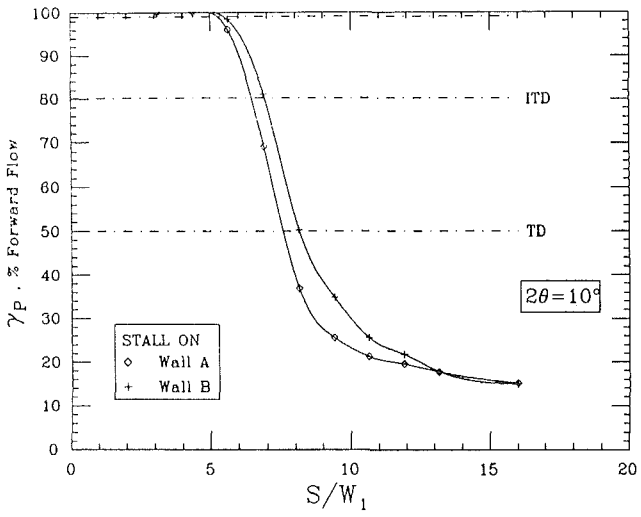

Fig. 8 Flow direction intermittency along diffuser wall, 2θ = 10 deg. Uncertainty in γ_p = ± 1 percent (20:1 odds).

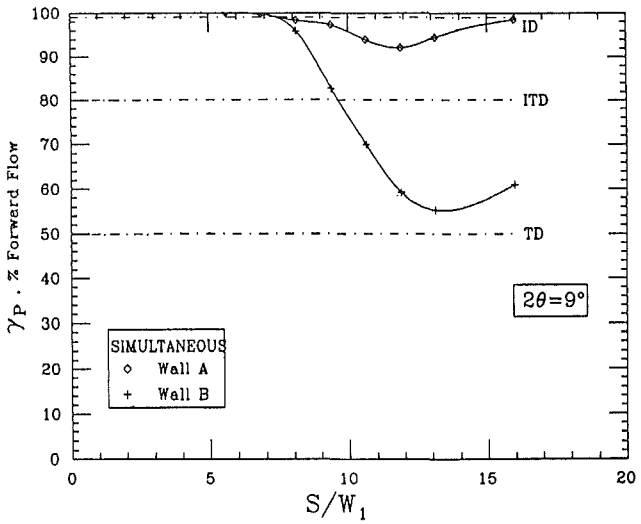

Fig. 7 Flow direction intermittency along diffuser wall, 2θ = 9 deg. Uncertainty in γ_p = ± 1 percent (20:1 odds).

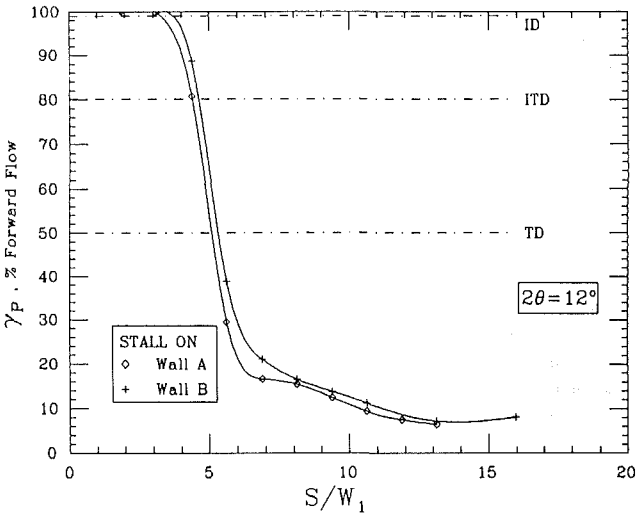

Fig. 9 Flow direction intermittency along diffuser wall, 2θ = 12 deg. Uncertainty in γ_p = ± 1 percent (20:1 odds).

phenomenon covers a significant portion of the diffuser's wall, and that the locations of IT, ITD, and TD are widely separated. Under larger adverse pressure gradients, however, ID, ITD, and TD are closer to each other (cf. Fig. 9).

Figure 7 illustrates a phenomenon that has not been observed or documented before. As seen in this figure, the two walls of the diffuser undergo some degree of reverse flow in the same experiment; the differences in the γ_p curves show that the process is not symmetric on the two side walls. Measurements on wall A show only a small amount of backflow is present on this wall, while wall B, on the other hand, is on the verge of detachment. Experiment on γ_p distribution for 2θ = 8 deg revealed a pattern analogous to that of 2θ = 9 deg (see Fig. 6).

Long time averages have also been employed in measurement of γ_p. The estimated uncertainty in γ_p values is ± 1 percent at 20:1 odds. There is some spanwise variation at each S/W_1 station. The data shown here are taken on the spanwise center plane, midway between end walls.

Computational Method and Results

Figure 10 gives the predicted values for C_p, along with the experimental data for four different opening angles. Experimentally determined locations of ID, ITD, and TD are also shown in this figure. The dotted curves represent the prediction of the Unified Integral Method (UIM) developed by Ghose and Kline [5]. The solid curves represent the present code [unpublished] which, indeed, is a modified version of the UIM and is described briefly in the Appendix. In addition to fixing minor bugs found in the UIM code, we have included in the present method the blockage effect of the end walls and the effects of viscous sublayer on the relationships between integral parameters of the turbulent boundary layer. The core model and the three-dimensionality correction have also been improved.

Unlike the original UIM, the present method assumes that the boundary layers on each diffuser wall may be treated separately. However, since the boundary layers near detachment become sensitive to small changes in the pressure gradinet, this method, which uses a 1-D core model along with separate side-wall boundary layers, has not proven too fruitful for detaching flows; the equation set becomes very stiff near detachment. Still, for attached flows, separate treatment of the side-wall boundary layers allows one to specify distinct initial conditions on each wall and look at diffusers of asymmetric geometry ($\theta_A \neq \theta_B$). Furthermore, using identical initial conditions for the two side walls, when

Downloaded 02 Jun 2010 to 171.66.16.103. Redistribution subject to ASME license or copyright; see http://www.asme.org/terms/Terms_Use.cfm

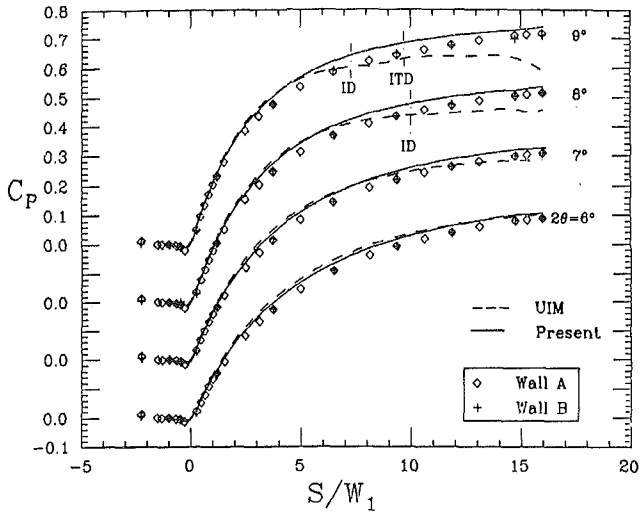

Fig. 10 Comparison of the UIM and the present code predictions with respect to experimental data. Uncertainty in C_p = ± .003 (20:1 odds).

the geometry and conditions are symmetric, the method is equivalent to treating the side-wall boundary layers as similar. In Fig. 10, major improvement in prediction has been achieved for 2θ = 8 deg and 2θ = 9 deg by avoiding premature detachments resulting from neglect of the end-wall effects.[1] The end-wall blockage effect would become even more important for inlet aspect ratios less than 4. Its effect is to relieve pressure gradient and delay side-wall detachment.

The differences between the current predicted values and the experimental data, we believe, are mainly due to the missing normal stress term in the momentun integral equation [13] and possibly to the corner flow effects. It should also be mentioned that no constants borrowed from the original UIM have been tuned for this report. This task should be carried out after proper modeling of the normal stress term and possibly the inclusion of blockage effect of the corners.

Conclusions

At this point, we want to emphasize several points that the reader may find revealing. Some of these conclusions are tentative and require further investigation.

1. The uncertainty in the experimental values of C_p is very low — less than half the size of symbols in Fig. 4. For opening angles above 8 deg, small differences in pressure gradients acting along the two side walls (A and B) are observed in Fig. 4. Prior to detachment, the adverse pressure gradient is higher for the stalled wall. However, downstream of detachment, the situation reverses; the pressure gradient on the stalled wall relaxes more than the gradient on the unstalled wall. As a result, the cross-stream pressure gradient changes sign in the vicinity of the detachment point. This configuration of pressure gradient implies that slight two-dimensionality in the core flow field is an important feature in the establishment of the detachment location. The core flow two-dimensionality probably needs to play a role in proper modeling for the computation of the early stages of transitory stall.

2. Peak pressure recovery occurs when both side walls still show some degrees of unsteady reverse flow. The overall pressure recovery starts to fall off as soon as a zone of strong reverse flow is found solely on one side wall. Computations, as well as experiments, suggest that mean-wall shear stress does not drop to zero anywhere, on either wide wall at peak pressure recovery. In other words, time-mean, two-dimensional detachment (separation) first occurs near the diffuser exit at or after C_p^*.

3. In the case of diffusers with symmetric inlet conditions, the UIM method [5] and similar methods [3, 4] are successful in predicting diffuser flows up to geometries of peak pressure recovery; they depend on the assumption that the boundary layers on the two diverging walls are nearly identical. Our data confirm this assumption. However, just beyond C_p^* the flow near the walls becomes quite asymmetrical, and predictions using the original UIM deteriorate. Two-dimensionality may have to be introduced in the core flow model and separate side-wall boundary layers allowed, if good predictions are to be obtained beyond peak C_p (see No. 1, above). On the other hand, recent preliminary work in our lab (Bardina, Lyrio, and Kline) suggests that the UIM method with a one-dimensional core can be extended all the way to full stall if proper regard is taken of the physical and asymptotic limits inherent in the original method.

4. For attached flows, computed local C_p values are slightly too large. This is consistently seen in results by all the methods. We believe that omission of the normal stress term in the boundary layer equations is the major cause of this error, as shown by improved results obtained in preliminary attempts to include the normal stress effects following suggestions in [2].

5. The spontaneous "stall switch" phenomenon has been observed for the first time, as far as we know. This may occur only when extreme symmetry in the diffuser wall geometry exists, but this remains to be tested.

Acknowledgment

This research was supported by the Office of Naval Research under a grant from Project SQUID.

References

1 Fox, R.W., and Kline, S.J., "Flow Regime Data and Design Methods for Curved Subsonic Diffusers," ASME *Journal of Basic Engineering*, Vol. 84, Sept. 1962, pp. 303–312.

2 Reneau, L.R., Johnston, J.P., and Kline, S.J., "Performance and Design of Straight, Two-Dimensional Diffusers," PD-8, Sept. 1964, Thermosciences Division, Dept. of Mechanical Engineering, Stanford University.

3 Moses, H.L., and Chappell, J.R., "Turbulent Boundary Layers in Diffusers Exhibiting Partial Stall," ASME *Journal of Basic Engineering*, Vol. 89, No. 3, Sept. 1967, pp. 655–665.

4 Bower, W.W., "An Analytical Procedure for the Calculation of Attached and Separated Subsonic Diffuser Flows," AIAA Paper 74-1173, 1974.

5 Ghose, S., and Kline, S.J., "The Computation of Optimum Pressure Recovery in Two-Dimensional Diffusers," ASME JOURNAL OF FLUIDS ENGINEERING, Vol. 100, No. 4, Dec. 1978, pp. 419–426.

6 Smith, C.R., and Layne, J.L., "An Experimental Investigation of Flow Unsteadiness Generated by Transitory Stall in Plane-Wall Diffusers," *Proceedings, Joint Symposium on Design and Operation of Fluid Machinery*, Vol. 1, Ft. Collins, Colo., June 1978, pp. 167–176.

7 Eaton, J.K., Jeans, A.H., Ashjaee, J., and Johnston, J.P., "A Wall-Flow-Direction Probe for Use in Separating and Reattaching Flows," ASME JOURNAL OF FLUIDS ENGINEERING, Vol. 101, No. 3, Sept. 1979, pp. 364–366.

8 Loehrke, R.I., and Nagib, H.M., "Control of Free Stream Turbulence by Means of Honeycombs: A Balance between Suppression and Generation," ASME JOURNAL OF FLUIDS ENGINEERING, Vol. 98, No. 3, Sept. 1976, pp. 342–353.

9 Young, A.D., and Maas, J.N., "The Behavior of a Pitot-Tube in a Transverse Pressure Gradient," A.R.C., RVM 1770.

10 Bertelrud, Arild, "Measurements on Three-Dimensional Swept Wing at Low Speeds, Part II," Report 131, The Aeronautical Research Institute of Sweden, 1977.

11 Coles, D.E., and Hirst, E.A., editors, *Computations of Turbulent Boundary Layers—1968 AFOSR-IFP-Stanford Conference*, Vol. 2, Thermosciences Division, Dept. of Mechanical Engineering, Stanford University, 1969.

12 Kline, S.J., and McClintock, F.A., "Describing Uncertainties in Single-Sample Experiments," Mechanical Engineering, Jan. 1953, pp. 3–8.

13 Simpson, R.L., and Collins, M.A., "Prediction of Turbulent Boundary

[1] Ghose, too, included the end walls in his calculation in an unpublished version of the UIM. Similar improvements are noted here, too.

Downloaded 02 Jun 2010 to 171.66.16.103. Redistribution subject to ASME license or copyright; see http://www.asme.org/terms/Terms_Use.cfm

Layers in the Vicinity of Separation," *AIAA Journal*, Vol. 16, Apr. 1978, pp. 289–290.

14 Schlichting, H., *Boundary Layer Theory*, 6th ed., McGraw-Hill, 1968, pp. 651–652.

15 Ashjaee, J., and Johnston, J.P., "Transitory Stall in Diffusers," Report submitted to Project SQUID, June 1979.

APPENDIX

Governing Equations and Computational Method

The method of prediction presented here is based on the Unified Integral Method (UIM) of Ghose and Kline. See Ref. [5] for details of the UIM. In this calculation, we assume that the boundary layers growing on the end walls are identical.

Development of Equations. *Relationships between turbulent boundary layer integral parameters.* Using Coles' velocity profile, modified to permit representation of reverse flow ($\kappa = 0.41$, $\hat{C} = 2.05$),

$$u = \frac{u\tau}{\kappa}\left[\ln\frac{y|u_\tau|}{\nu} + \hat{C}\right] + \frac{u_\beta}{2}\left(1 - \cos\frac{\pi y}{\delta}\right)$$

and integrals for standard sublayer [11],

$$\int_0^{y_1^+} u^+ dy^+ = \phi_1; \int_0^{y_1^+} {u^+}^2 dy^+ = \phi_2$$

where $y_1^+ = 50$, $\phi_1 = 540.6$, and $\phi_2 = 6546$, the following relationships between the boundary layer integral parameters can be obtained upon proper integration across the layer:

$$\delta^* = y_1 - \frac{\phi_1 \nu}{u_\infty} + \frac{u_\beta}{u_\infty}\left(\frac{\delta}{2} - y_1\right) + \frac{u_\tau}{\kappa u_\infty}\left(y_1 \ln\frac{y_1}{\delta} + \delta - y_1\right) \tag{A-1a}$$

$$\theta = \lambda_1 + \lambda_2 + \lambda_3 + \lambda_4 + \lambda_5$$

where $y_1 = y_1^+ \nu/|u_\tau|$ and

$$\lambda_1 = \frac{\nu\phi_1}{u_\infty} - \frac{\nu u_\tau \phi_2}{u_\infty^2} + \frac{u_\beta}{u_\infty}\left(\frac{\delta}{2} - \frac{y_1}{2} - \frac{\delta}{2\pi}\sin\frac{\pi y_1}{\delta}\right)$$

$$\lambda_2 = \frac{u_\tau}{\kappa u_\infty}\left(y_1 \ln\frac{y_1}{\delta} + \delta - y_1\right) \tag{A-1b}$$

$$\lambda_3 = \left(\frac{u_\beta}{u_\infty}\right)^2\left(\frac{3}{8}y_1 - \frac{3}{8}\delta + \frac{\delta}{2\pi}\sin\frac{\pi y_1}{\delta} + \frac{\delta}{16\pi}\sin\frac{2\pi y_1}{\delta}\right)$$

$$\lambda_4 = \left(\frac{u_\tau}{\kappa u_\infty}\right)^2\left(2y_1 - 2\delta - 2y_1\ln\frac{y_1}{\delta} + y_1\ln^2\frac{y_1}{\delta}\right)$$

$$\lambda_5 = \frac{u_\beta u_\infty}{\kappa u_\infty^2}\left[y_1 - \delta - y_1\ln\frac{y_1}{\delta} - \frac{\delta}{\pi}\sin\frac{\pi y_1}{\delta}\ln\frac{y_1}{\delta} + \frac{\delta}{\pi}Si\left(\frac{\pi y_1}{\delta}\right) - \frac{\delta}{\pi}\mathrm{Si}(\pi)\right]$$

$$Si(z) = -\int_z^\infty \frac{\sin t}{t}\,dt,\ Si(\pi) = 1.85193$$

Since $y_1/\delta << 1$, the following approximations were used for simplification:

$$\sin\frac{\pi y_1}{\delta} \approx \frac{\pi y_1}{\delta};\ \sin\frac{2\pi y_1}{\delta} \approx \frac{2\pi y_1}{\delta};\ \text{and}$$

$$Si\left(\frac{\pi y_1}{\delta}\right) \approx \frac{\pi y_1}{\delta}.$$

Near and after detachment, sublayer integrals are removed (ϕ_1, ϕ_2, $y_1 \to 0$) and the equations (A-1) reduce to those in UIM, i.e.,

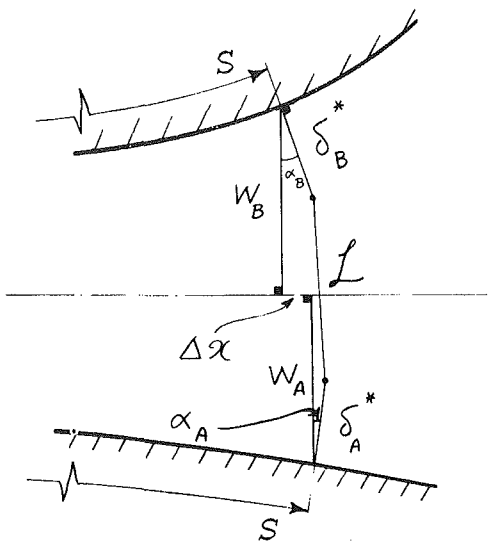

$$\delta^* = \frac{\delta}{u_\infty}\left(\frac{u_\beta}{2} + \frac{u_\tau}{\kappa}\right),$$

$$\phi = \delta^* - \frac{\delta}{u_\infty^2}\left(\frac{3}{8}u_\beta^2 + 1.58949\frac{u_\beta u_\tau}{\kappa} + \frac{2u_\tau^2}{\kappa^2}\right)$$

Viscid/Inviscid Interaction. From Fig. A-1, the following relation can be derived for the effective two-dimensional flow area ($\mathcal{L}$ • 1):

$$\mathcal{L}^2 = \delta_A^{*2} + \delta_B^{*2} + W^2 + \Delta x^2 - 2W(\delta_A^* \cos\alpha_A + \delta_B^* \cos\alpha_B) + \Delta x(\delta_A^* \sin\alpha_A - \delta_B^* \sin\alpha_B) + 2\delta_A^*\delta_B^* \cos(\alpha_A + \alpha_B) \tag{A-2a}$$

where $W = W_A + W_B$ and α_A and α_B are the local wall angles. For symmetric two-dimensional flows, (A-2a) reduces to

$$\mathcal{L} = W - 2\delta^* \cos\alpha.$$

When end-wall effects are included, the continuity equation is written as

$$Q = u_\infty(h - 2\delta_p^*)\mathcal{L} = \text{constant}$$

or

$$\frac{d}{ds}\{u_\infty(h - 2\delta_p^*)\mathcal{L}\} = 0 \tag{A-2b}$$

The Momentum Integral Equation. This equation is written in the following form:

$$\frac{d\Theta}{dS} = \mathrm{sign}(u_\tau)\left(\frac{u_\tau}{u_\infty}\right)^2 - (2+H)\frac{\Theta}{u_\infty}\frac{du_\infty}{dS} - T \tag{A-3}$$

where T is the three-dimensionality correction for a converging or diverging stream and is written, following Schlichting [14], as

$$T = \frac{1}{u_\infty^2}\int_0^\delta (u_\infty - u)\frac{\partial w}{\partial z}\bigg|_{z=0} dy = \frac{\Theta}{a}$$

where a is the distance from the fictitious source origin. It can be shown that, for the diverging (side) walls of the diffuser,

$$T_A \approx -\left(\frac{2\Theta_A}{h - 2\delta_p^*}\right)\frac{d\delta_p^*}{dS}$$

$$T_B \approx -\left(\frac{2\Theta_B}{h - 2\delta_p^*}\right)\frac{d\delta_p^*}{dS}$$

Downloaded 02 Jun 2010 to 171.66.16.103. Redistribution subject to ASME license or copyright; see http://www.asme.org/terms/Terms_Use.cfm

and, for the parallel (end) walls,

$$T_P \approx \frac{\Theta_p}{\mathfrak{L}} \left(\alpha_A + \alpha_B - \frac{d\delta_A^*}{dS} - \frac{d\delta_B^*}{dS} \right)$$

The Entrainment Equation. This equation employs the same model as in UIM.

$$\frac{1}{u_\infty} \frac{d}{dS} [u_\infty (\delta - \delta^*)] = 10\tau_{\max}/\rho u_\infty^2 \qquad \text{(A-4)}$$

Method of Solution. Equations (A-1), (A-3), and (A-4) are first reduced to two equations for each separate boundary layer (i.e., *A*, *B*, and *P*) with $d\delta^*/dS$ and du_τ/dS as primary variables for that wall. This set combined with (A-2) forms a system of 7 linear equations in 7 unknowns: du_∞/dS, $d\delta_A^*/dS$, $du_{\tau A}/dS$, $d\delta_B^*/dS$, $du_{\tau B}/dS$, $d\delta_p^*/dS$ and $du_{\tau p}/dS$. This set is first decoupled and then solved using an ordinary differential equation solver.

Downloaded 02 Jun 2010 to 171.66.16.103. Redistribution subject to ASME license or copyright; see http://www.asme.org/terms/Terms_Use.cfm

and, for the parallel (end) walls,

$$T_P \approx \frac{\Theta_p}{\mathfrak{L}} \left(\alpha_A + \alpha_B - \frac{d\delta_A^*}{dS} - \frac{d\delta_B^*}{dS} \right)$$

The Entrainment Equation. This equation employs the same model as in UIM.

$$\frac{1}{u_\infty} \frac{d}{dS} [u_\infty (\delta - \delta^*)] = 10 \tau_{\max} / \rho u_\infty^2 \qquad \text{(A-4)}$$

Method of Solution. Equations (A-1), (A-3), and (A-4) are first reduced to two equations for each separate boundary layer (i.e., *A*, *B*, and *P*) with $d\delta^*/dS$ and du_τ/dS as primary variables for that wall. This set combined with (A-2) forms a system of 7 linear equations in 7 unknowns: du_∞/dS, $d\delta_A^*/dS$, $du_{\tau A}/dS$, $d\delta_B^*/dS$, $du_{\tau B}/dS$, $d\delta_p^*/dS$ and $du_{\tau p}/dS$. This set is first decoupled and then solved using an ordinary differential equation solver.

DISCUSSION

C. R. Smith.[1] The authors are to be complemented on a fine piece of experimental work examining a particularly difficult and complex fluid dynamic phenomena. They have gone to great lengths to develop a carefully controlled experiment which has allowed them to establish a very reliable set of pressure recovery data. In addition, their employment of their thermal tuft has provided a better understanding and categorization of the time-averaged separation behavior experienced by the diverging walls of a two-dimensional diffuser. This paper also benefits by the inclusion of a complementary prediction technique which appears to function quite nicely for geometries operating up to and including peak pressure recovery. This is a very nice addition to the diffuser literature.

There are, however, two points which could use some additional clarification by the authors. The first is with regard to the observed stall switch phenomena, which I might point out has been observed and commented on in three previous studies examining various aspects of transitory stall [16, 17, 18]. It has been my experience that such stall switching is a strong function of the diffuser exit conditions, and can be controlled by modification of the exit plenum geometry. It would be helpful to know if the authors examined the effects of the exit plenum geometry (and the subsequent change in flow patterns within the plenum) and if so, what effect they noted on the stall switch behavior.

My second point is with regard to the quoted uncertainty for C_p. The authors state that the uncertainty in C_p was $\delta C_p = \pm 0.003$. This would yield a relative uncertainty of $\delta C_p / C_p = 0.42$ percent at $C_p{}^* = 0.715$. However, they quote a value for δu_{e_1} which yields a relative uncertainty of $\delta u_{e_1}/u_{e_1} = 0.64$ percent. Now, an uncertainty analysis of C_p for propagation effects yields:

$$\frac{\delta C_p}{C_p} = \left[\left(\frac{\delta \Delta p}{\Delta p} \right)^2 + \left(\frac{\delta \rho}{\rho} \right)^2 + 2 \left(\frac{\delta u_{e_1}}{u_{e_1}} \right)^2 \right]^{1/2}$$

(where $\Delta p = p_2 = p_2$)

This implies that

$$\frac{\delta C_p}{C_p} > \sqrt{2} \frac{\delta u_{e_1}}{u_{e_1}} = 0.91 \text{ percent}$$

This value would indicate that δC_p should be more on the order of $\pm$ 0.007 to $\pm$ 0.008 when the uncertainty of the pressure measurement and density are accounted for. Could the authors comment on this apparent discrepancy, and clarify their method for determining δC_p?

[1] Professor, Department of Mechanical Engineering and Mechanics, Lehigh University, Bethlehem, Pa. 18015

Additional References

16 Layne, J. L., and Smith, C. R., "An Experimental Investigation of Inlet Flow Unsteadiness Generated By Transitory Stall in Two-Dimensional Diffusers," Tech. Rept. CFMTR 76-4, Thermal Sciences and Propulsion Center, School of M.E., Purdue Univ., Aug. 1976.

17 Waitman, B. A., Reneau, L. R., and Kline, S. J., "Effects of Inlet Conditions on Performance of Two-Dimensional Diffusers," Rept. PD-5, Dept. of M.E., Stanford Univ., Aug. 1960.

18 Reid, E. G., "Performance Characteristics of Plane-Wall, Two-Dimensional Diffusers," NACA TN 2888, Feb. 1953.

Authors' Closure

The authors wish to thank Professor Smith for his interest and comments and offer the following clarification in reply.

The spontaneous stall switch phenomenon we referred to differs, we believe, from previous observations. This effect is neither a rapid flipping motion as mentioned in [16], nor is it caused by external disturbances. Our experiments revealed that such a motion occurs only in a particular, narrow subregion of the transitory stall regime [19]. However, the back and forth motion of stall between the two walls seen in [16], appears to have occurred within the same subregion. This indicates that the two observations may be essentially of the same phenomenon. On the other hand, we found that inlet conditions have a much stronger effect on the stall switching than exit conditions.

With regard to the quoted uncertainty in C_p, the discrepancy Professor Smith has found stems from his use of an inappropriate value of δu_{e_1}. As described in the text, the inlet velocity, was kept within 46.6 $\pm$ 0.3 m/s for the whole *series of tests* reported in this paper. Within a set, individual experiments (profile of C_p [S/W_1] at each opening angle), the relative uncertainty for inlet dynamic pressure was no more than $\pm$ 0.2 percent. It would have been possible to keep the tunnel conditions for the whole test series to this low level of uncertainty, but this refinement is totally unnecessary.

Additional Reference

19 Ashajee, J., and Johnston, J. P., "Subsonic Turbulent Flow in Plane-Wall Diffusers: Peak Pressure Recovery and Transitory Stall," Report PD-21, Thermosciences Division, Mechanical Engr. Dept., Stanford University.

Copyright © 1980 by ASME

Downloaded 02 Jun 2010 to 171.66.16.103. Redistribution subject to ASME license or copyright; see http://www.asme.org/terms/Terms_Use.cfm

Effect of Wake-Type Nonuniform Inlet Velocity Profiles on First Appreciable Stall in Plane-Wall Diffusers

K. F. Kaiser

Manager,
Turbochargers,
Cummins Engine Company,
Columbus, Ind. 47201

A. T. McDonald

Professor,
Fluid Mechanics Group,
School of Mechanical Engineering,
Purdue University,
West Lafayette, Ind.

The combustor diffuser in a gas turbine engine must accept a high-speed, unsteady, distorted flow from the engine compressor. It must deliver flow to the combustor with minimum loss in total pressure and minimum velocity profile distortion. Both pressure recovery and outlet flow distortion characteristics of diffusers must be considered in design tradeoffs. The purpose of this investigation was to study the effects of nonuniform inlet velocity profiles on the inception of stall in two-dimensional plane-wall diffusers. Centrally-located "wake-type" inlet velocity profiles were chosen to simulate the flow conditions at the inlet of a combustor diffuser. The inlet distortion was characterized by dimensionless wake strength and wake width parameters. The experiments were performed on an open surface water table to make flow visualization possible. A centerline or pocket-type stall, such as previously reported in swirling flows, was observed for sufficiently severe inlet profile distortion. A new definition of first appreciable stall, based on a fraction of the exit area stalled, was introduced to characterize stalls which did not occur on a solid surface.

Introduction

Background. In a typical gas turbine engine, air leaving an axial flow compressor passes through a diffuser before entering the combustor. Flow at the inlet of the combustor diffuser is distorted by wall boundary layers and blade wakes. Bulk-flow pulsations may be transmitted through the compressor from the inlet. Often the mean velocity is not parallel to the diffuser centerline because of residual swirl. Therefore the inlet velocity profile of an actual combustor diffuser may have

(1) thick wall boundary layers,
(2) a central region of highly momentum deficient fluid,
(3) unsteady flow, and
(4) mean velocity not parallel to the centerline of the diffuser.

Combustor efficiency is affected by the velocity profile at the exit plane of the diffuser. The overall engine cycle efficiency depends on the pressure rise through the diffuser. Maximum pressure rise normally occurs when some stall exists in a diffuser. Therefore the optimum combustor diffuser design may involve a tradeoff between pressure rise and exit velocity profile distortion. Both performance and flow regime data are needed to design diffusers.

Because some stall is present in high performance diffusers, theoretrical analyses have been of limited success. Solutions to current design problems are based largely on experimental data.

Purpose. The purpose of this investigation was to study the effect of steady centrally-located "wake-type" inlet velocity profiles, with the mean velocity parallel to the diffuser throat, on the inception of stall in a two-dimensional plane-wall diffuser. Inlet profiles with high velocity regions near the walls and a centrally-located low velocity region are chosen to simulate one of the important features of the inlet velocity profile to a combustor diffuser.

Literature Review

The majority of diffuser research has been experimental because optimum recovery normally occurs with some stall in the diffuser. Although the amount of diffuser data in the literature is enormous, work has been devoted primarily to cases where the inlet velocity profile is steady and uniform over a core region outside the boundary layer. Accomplishments include:

(1) classification of the regimes of flow [1, 2] (see Fig. 1),
(2) the construction of performance maps [3, 4], and
(3) performance correlations based on inlet blockage [5].

Waitman, Reneau, and Kline [6] investigated the effect of inlet conditions on performance of plane-wall diffusers. Specifically they looked at the effect of thickening the inlet boundary layer, increasing the inlet turbulence intensity, and creating a single momentum deficient region located both

Contributed by the Fluids Engineering Division of THE AMERICAN SOCIETY OF MECHANICAL ENGINEERS and presented at the Winter Annual Meeting, New York, N.Y., December 2-7, 1979. Manuscript received by the Fluids Engineering Division, April 12, 1979.

Copyright © 1980 by ASME

Downloaded 02 Jun 2010 to 171.66.16.103. Redistribution subject to ASME license or copyright; see http://www.asme.org/terms/Terms_Use.cfm

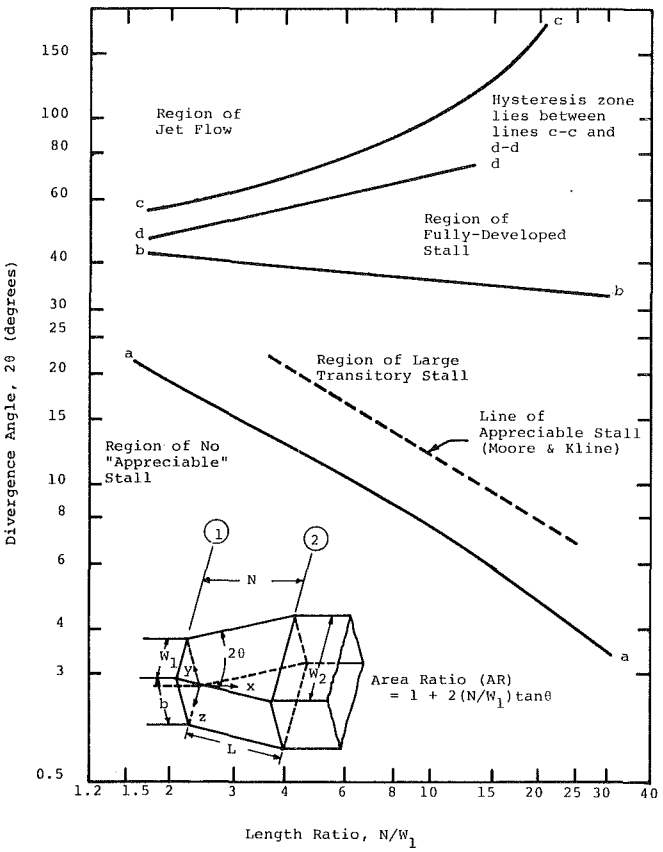

Fig. 1 Geometry and flow regime map for two-dimensional plane-wall diffusers with uniform inlet flow [2]

symmetrically and unsymmetrically. The general conclusions of their investigation were:

(1) As the inlet boundary layer thickened the pressure recovery decreased.

(2) The pressure recovery increased with increasing turbulence intensity.

(3) Centrally-located momentum deficient regions increased the pressure recovery.

(4) Changes in flow regime depend strongly on the type of obstruction and its location.

Wolf and Johnston [7] also studied the effect of nonuniform inlet velocity profiles on flow regimes and performance in plane-wall diffusers. They did not obtain enough systematic flow regime data to quantify a change in the line of first appreciable stall but could draw these qualitative conclusions:

(1) Diffusers with nonuniform inlet velocity profiles having a momentum deficient region near one or both of the walls (unifirm shear, jet flow and step shear) shifted lines a-a and b-b downward appreciably. This downward shift was also accompanied by a decrease in pressure recovery.

(2) Diffusers with centrally-located wake inlet velocity profiles (Fig. 2) developed a central stall in the core region for sufficiently large area ratios.

(3) Diffusers with a centrally-located wake inlet velocity profile have increased performance above that measured for diffusers with irrotational inlet core velocity profiles and equal boundary-layer blockage.

Tyler and Williamson [8] performed a series of experiments with conical and annular diffuser geometries using inlet velocity profile distortion created by cross flow at the inlet section. The performance of the conical diffusers decreased slightly as inlet blockage increased to a value of $B_1 \simeq 0.1$ and then increased dramatically. Values of pressure recovery coefficient (C_p) as large as 3.0[1] were measured for an inlet blockage fraction of $B_1 = 0.68$.

All pressure recovery coefficients for the annular diffusers tested were less than unity; they decreased continuously as inlet blockage was made more severe. The differing trends between the conical and annular data were attributed to differences in frictional losses. These are larger in an annular diffuser because the wetted area is greater than that of a conical diffuser.

Horlock and Lewis [9] showed analytically that nonuniformities in the velocity profile of an incompressible inviscid flow through a diverging duct become accentuated according to the expression

$$\frac{u}{\bar{u}} = (AR)^2 \left(\frac{u_1}{\bar{u}_1}\right) \tag{1}$$

Although the above expression depends on the same variables as the data correlation developed by Sovran and Klomp [5], the functional relationship is quite different. Horlock and Lewis only verified the analytical prediction for small area ratios.

None of the prior experimental work included systematic determination of flow regime behavior for diffusers with nonuniform inlet velocity profiles. As stated in reference [11], "Diffuser performance and flow conditions (i.e. stall state) are strongly coupled so knowledge of flow conditions is absolutely necessary in interpretation of performance theory and data."

[1] The definition of recovery coefficient was based on uniform inlet flow. The actual flux of kinetic energy for any distorted inlet profile exceeds $1/2\rho\bar{u}_1^2$. Therefore C_p can exceed unity for such flows.

Nomenclature

A = cross-sectional area
AR = area ratio, A/A_1
b = depth of diffuser passage
B = blocked-area fraction, $\frac{1}{A}\int^A \left(1 - \frac{u}{u_{max}}\right) dA$
C_p = pressure-recovery coefficient, $(p_2 - p_1)/\bar{q}_1$
Cp,i = pressure-recovery coefficient for an ideal, one-dimensional flow, $1 - 1/(AR)^2$
L = wall length of diffuser
N = axial length of diffuser
p = static pressure
q = dynamic pressure based on mass-averaged velocity, $1/2\rho\bar{u}^2$
Re = Reynolds number, $\bar{u}_1 w_1/\nu$
u = axial velocity component
W = width of diffuser cross-section
x,y,z = coordinates (Fig. 1)
Δ = wake width parameter (equation (2))
θ = divergence half-angle
λ' = wake strength parameter, u_{max}/u_{defect}
ν = kinematic viscosity
ρ = fluid density

Subscripts

defect = minimum value in a wake-type profile
max = maximum value at a cross-section
1 = inlet condition
2 = exit condition

Superscript

$-$ = average value over a cross-section

Downloaded 02 Jun 2010 to 171.66.16.103. Redistribution subject to ASME license or copyright; see http://www.asme.org/terms/Terms_Use.cfm

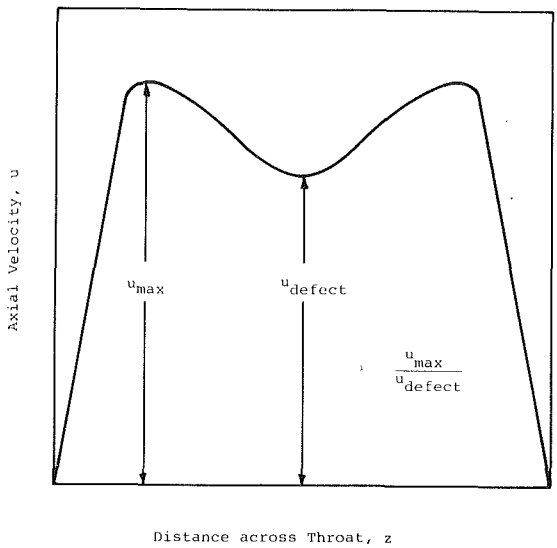

Fig. 2 Centrally-located wake-type inlet velocity profile

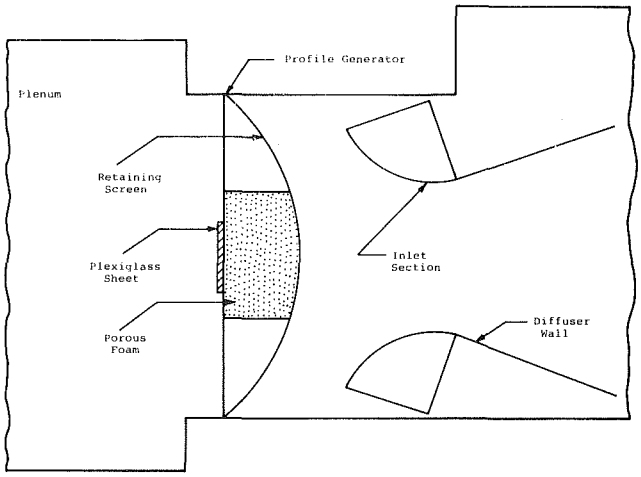

Fig. 3 Details of diffuser inlet section with wake-type velocity profile generator

Experimental Apparatus

Water Table. The experimental program was conducted on a water table [12]. Water was recirculated through the inlet and test section shown schematically in Fig. 3. The flow rate was controlled by submerged exit weirs (not shown in Fig. 3) designed to minimize air entrainment.

The inlet throat width of the diffuser was held constant at approximately 77 mm. Water depth was maintained for all tests at about 356 mm. Average inlet velocities ranged between about 0.27 and 0.35 m/s. The corresponding Reynolds numbers based on throat width were between 21,000 and 27,000.

A boundary-layer trip was used to obtain a turbulent boundary layer at the diffuser inlet. A brass rod was formed into a "U" shape to trip boundary layers on the floor and the converging walls of the inlet section. The smallest diameter rod which would produce a turbulent boundary layer was 64 mm, located 125 mm upstream from the diffuser throat.

The test section consisted of two inlet contraction quadrants to which extensions were added to form the desired diffuser geometry.

Wake Profile Generators. The objective of this program was to study the effect of wake-type inlet velocity profiles on the location of first appreciable stall. A wake profile can be generated by placing a solid object upstream from the diffuser inlet. However, a solid body often causes vortex shedding, resulting in an unsteady inlet velocity profile.

Vortex shedding is caused by instabilities in the location of the separation points on a solid object. The pressure field around the object is affected by fluctuations in the separated region behind the object. Hence, if the separated flow behind the object is stabilized, the unsteadiness and resultant vortex shedding are eliminated.

Several approaches were tried before the best solution was found. A piece of porous foam was placed on the downstream side of a solid plate to stabilize the separated flow region behind the plate. Flow visualization downstream showed that vortex shedding was eliminated and the wake profile was steady. The magnitude of the wake profile was varied by changing the axial distance between the wake generator and the throat of the diffuser.

Instrumentation. A total head tube was used for all quantitative measurements. The measurement end of the stainless steel tube was formed into a rectangular shape with a 0.5 mm thickness perpendicular to the wall.

The distribution of dynamic head was measured by feeding the output of the total head tube into one side of a differential pressure transducer, and the static pressure (obtained from a tap in the table bed) into the other side of the transducer. The transducer output was read using an integrating digital voltmeter.

The signal were integrated over a 30-second time interval to obtain average values. The procedure was repeated four times for each velocity measurement to insure reproducibility.

Flow Visualization. A fine streak line of dye could be injected manually either on the wall or into the flow field using a hypodermic syringe fitted with a long needle. The flow direction and the size of a stalled region could be determined by observing the movement of the resulting dye trace. Observations of the stall for each geometry was repeated 10 to 12 times because the size of the stall pattern was time-dependent.

A continuous dye injection system was used for some unsteady stall situations since it allowed a more accurate estimation of the size of the stalled region.

Estimate of Experimental Uncertainty

The change from one flow regime to another actually covers a continuous spectrum of flow states such as that found in the transition process between laminar and turbulent pipe flow. The boundaries of a transitory stall are particularly difficult to quantify since the flow is unsteady. Nevertheless, an error analysis has been carried out [13]. The estimated uncertainty of each class of experimental measurement is listed in Table 1.

Table 1 Uncertainties in experimental measurements

Measured quantity	Estimated uncertainty (± percent)
Velocity	5.1
Area ratio	2
Nondimensional length	1
Stall size	20

Results

Uniform Inlet Velocity Profiles. Inlet velocity profiles were measured with no diffuser attached to the inlet section. Several checks were made with diffusers in place to verify this procedure.

Flow uniformity at the inlet was checked by measuring

Downloaded 02 Jun 2010 to 171.66.16.103. Redistribution subject to ASME license or copyright; see http://www.asme.org/terms/Terms_Use.cfm

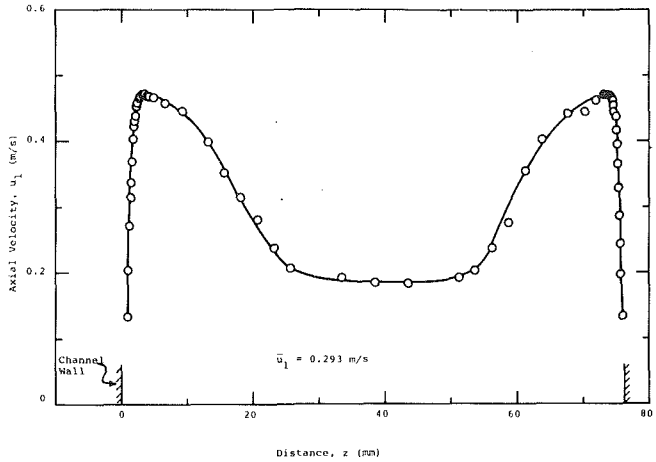

Fig. 4(*a*) Typical wake-type inlet velocity profile (λ_1 = 2.58)

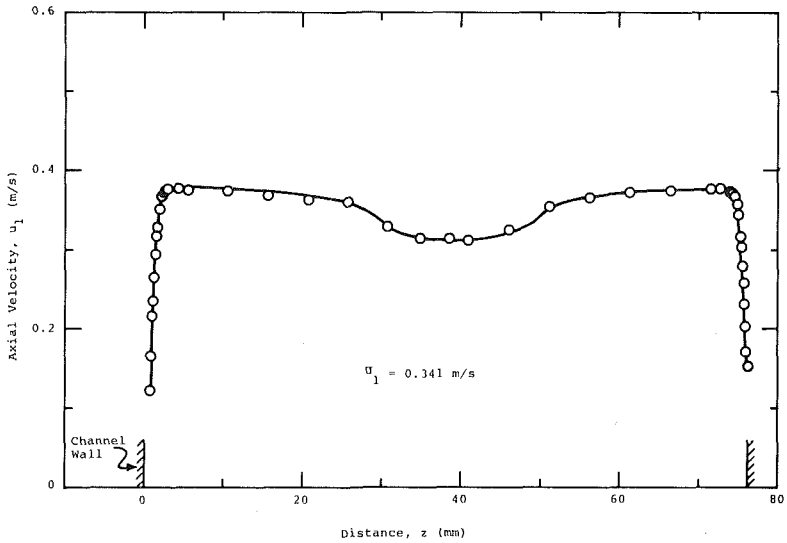

Fig. 4(*b*) Typical wake-type inlet velocity profile (λ_1 = 1.2)

velocity profiles at three heights above the table bed. As an additional check, a vertical traverse was made on the centerline. The only significant variations in velocity were near the floor and the surface.

Wake Inlet Velocity Profiles. The vertical uniformity of one wake inlet profile was checked by measuring inlet velocity profiles at three locations above the channel floor. Each of the remaining wake profiles was also checked at several vertical locations on the channel center line. Complete data, tabulated in reference [13], showed negligible variation with depth for the measured profiles.

Wake inlet velocity profiles were characterized by two parameters. The dimensionless wake strength parameter, λ_1, is defined as the ratio of the maximum to the minimum values of velocity that occur at a cross-section. The profile with λ_1 = 1.1 was the weakest wake that could be generated with the experimental setup and the profile with λ_1 = 2.58 was the strongest.

Because wake strength was varied by changing the axial location of the wake profile generator (Fig. 3), there was some variation in width of the tested wakes. The wake width parameter was defined as

$$\Delta_1 \equiv \frac{W_{0.95}}{W_1} \tag{2}$$

where $W_{0.95}$ is the width of the central momentum-deficient region, measured at the point where $u = 0.95\, u_{max}$. Measured values of Δ_1 are shown in Table 2.

Table 2 Wake strength and wake width parameters for inlet velocity profiles investigated

Wake strength parameter, λ_1	Wake width parameter, Δ_1
1.10	0.19
1.20	0.37
1.30	0.55
1.40	0.53
1.65	0.54
2.00	0.75
2.58	0.78

Representative data for two typical inlet velocity profiles are presented in Fig. 4.

First Appreciable Stall. The line of first appreciable stall was defined by Fox and Kline [2] as the condition at which stall (reversed flow) covered 20 percent of the height of one diverging wall at the exit plane. This definition is applicable as long as the flow stalls on one of the diverging walls. Wake inlet profiles frequently cause stall along the diffuser centerline at the exit plane. Therefore a new definition was needed for first appreciable stall.

When first appreciable stall was present on a diverging wall for uniform inlet flow, approximately 3 percent of the exit

Downloaded 02 Jun 2010 to 171.66.16.103. Redistribution subject to ASME license or copyright; see http://www.asme.org/terms/Terms_Use.cfm

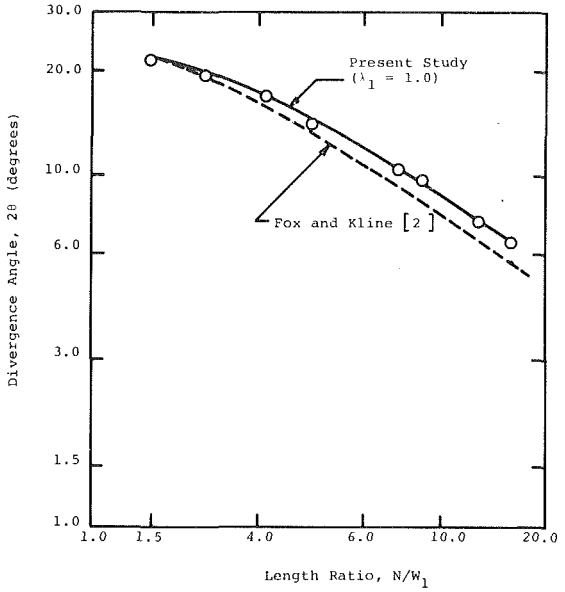

Fig. 5 Line of first appreciable stall for uniform inlet conditions

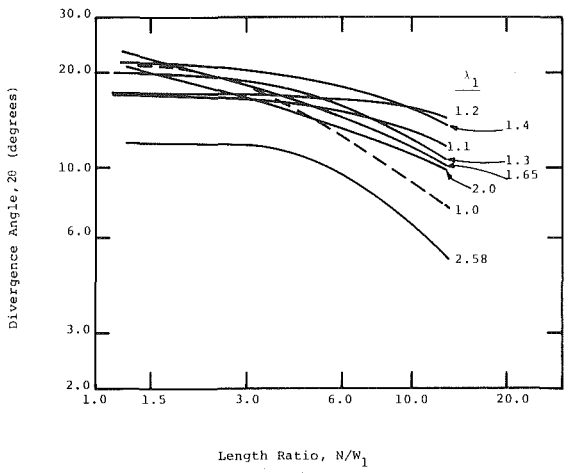

Fig. 6 Lines of first appreciable stall for nonuniform inlet conditions

area was stalled. Therefore the definition of Fox and Kline (based on wall stall height) was altered to one based on stalled area. All first appreciable stalls determined with nonuniform inlet conditions were based on the criterion that stall occupies 3 percent of the exit area. In all centerline stalls the width of the stalled region changed but the height remained approximately constant. For a center-line stall, 3 percent of the exit area stalled corresponded to a region stalled flow occupying about 20 percent of the channel depth.

After the flow conditions were adjusted to produce the desired inlet velocity profiles, a diffuser was installed in the test facility. Then the divergence angle (2θ) was increased slowly until first appreciable stall occurred. This procedure was repeated for 8 diffusers at each inlet condition.

The line of first appreciable stall obtained for uniform inlet flow is presented in Fig. 5. The line of first appreciable stall as determined by Fox and Kline [2] is also included for comparison. Agreement between this facility and that of Fox and Kline is acceptable.

Experimental results for the location of the line of first appreciable stall for the seven wake inlet velocity profiles are presented in Fig. 6. Four different stall patterns were observed:

(1) Stall began in the corner and spread out on the floor and up the wall simultaneously. When first appreciable stall was attained, a triangular stall pattern existed. There was no apparent wall preference; an artifical disturbance would shift the stall from one diverging wall to the other.

The fluid in the stalled region washed in and out periodically. The period of the flow reversal decreased with the length of the diffuser. As a consequence, it was difficult to determine the point of first appreciable stall for very short diffusers.

(2) Stall developed at the surface on one of the diverging walls. It extended from the surface approximately 20 percent down the wall. The stalled region was very chaotic and definitely three dimensional.

(3) Stall developed at the surface in the center of the diffuser, and extended 20 percent down into the flow. The stalled region was chaotic and three-dimensional. The position of the stall was neutrally stable; if the flow were artifically distributed, the stall could be shifted to the right or left wall. However, the flow still stalled from the surface down and began at the center when the flow was started again.

(4) A pocket of stall built up around the center line. The flow was not stalled along the floor or surface. The stalled region extended only a short distance laterally from the centerline. (The distance varied with area ratio.)

When center-line stalls were present, they were always transitory; the stall pocket pulsed into and out of the diffuser. The center-line stall moved into the diffuser a maximum of approximately 50 mm. When a center-line stall moved toward the diffuser throat, fluid was expelled from the centeral region. This expelled fluid was forced into the unstalled region, where it caused the unstalled fluid to accelerate. The opposite process occurred when the center-line stall moved toward the diffuser exit plane. The fluid seemed to enter and leave the stalled region from the sides and the bottom. The entire process appeared analogous to moving a solid object into and out of the diffuser. Thus, a very small center-line stall caused the entire flow at the exit plane to become unsteady. The most severe wake profile caused the flow to stall earlier than in the uniform inlet flow case. As the wake profiles became less severe, the inception of stall was delayed. For the weakest wake profile ($\lambda_1 = 1.1$), the flow stalled sooner than for the case where $\lambda_1 = 1.2$. This behavior should be expected because as λ_1 approaches 1.0, the line of first appreciable stall must approach that obtained with uniform inlet flow.

Pocket stalls have been observed in swirling flows in conical diffusers [15]. However, this is believed to be the first observation of a pocket stall in a nonswirling flow. Wolf and Johnston [6] observed a center-line stall but did not indicate whether or not it was a pocket stall.

Analysis and Discussion

Stall behavior may be explained qualitatively by considering the effects of adverse pressure gradients and viscous forces. Viscous forces would cause lateral diffusion of momentum, thus tending to attenuate nonuniformities in the inlet profile. Since a center-line stall was observed in numerous cases, the effect of viscosity must not be dominant for this type of stall.

Inviscid Prediction Technique. An inviscid flow model was derived by Wolf and Johnston [7], who used the continuity and Bernoulli equations along with the definition of C_{pi}. The complete derivation is presented in [7] and]13]. The technique predicts the exit velocity profile and the value of C_{pi} for a given nonuniform inlet velocity profile.

The prediction scheme is limited to nonuniform, steady inviscid inlet flows. Therefore the wall boundary layers of the inlet velocity profiles were neglected by assuming that the

Downloaded 02 Jun 2010 to 171.66.16.103. Redistribution subject to ASME license or copyright; see http://www.asme.org/terms/Terms_Use.cfm

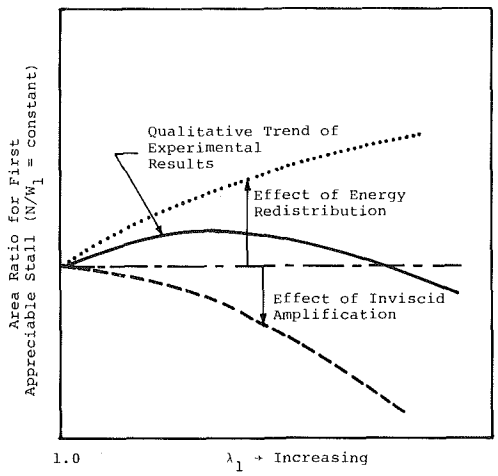

Fig. 7 Qualitative behavior of area ratio for first appreciable stall with increasing inlet distortion, for constant nondimensional length

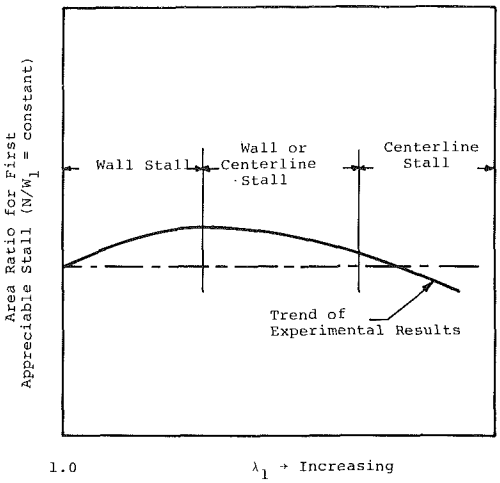

Fig. 8 Qualitative behavior of stall as a function of inlet velocity profile distortion

velocity from the wall to the point of maximum velocity was equal to the maximum velocity.

The results were in general agreement with those of [7]: center-line stall was predicted to occur earlier for more severely distorted inlet profiles (details are given in [13]. The earlier stall results both because the initial defect is larger, and because it is amplified more rapidly. The qualitative trend is shown in Fig. 7.

The predicted area ratios agree reasonably well with the experimental values over a portion of the line of first appreciable stall if the inlet wake profile is "sufficiently severe." Thus, the inviscid prediction technique could prove to be valuable once its limitations are determined by comparing predicted results with more experimental data.

Proposed Explanation of Stall. Two interacting mechanisms determine the type of stall that will occur in a diffuser with a wake-type inlet flow:

(1) inviscid amplification
(2) energy redistribution

One of the following stall patterns is produced, depending on the relative strength of these two effects:

(1) Centerline Stall - Inviscid ampification dominates over energy redistribution.
(2) Centerline or Wall Stall - Inviscid amplification and energy redistribution are equally important.
(3) Wall Stall - Energy redistribution dominates over inviscid amplification.

The trend of the experimental results for constant nondimensional length is shown by the solid line in Fig. 7. For moderate λ_1, stall is delayed to larger area ratio. As λ_1 is increased, the area ratio at stall passes through a maximum and then decreases. For very distorted profiles, the area ratio for first stall decreases below the value for uniform inlet flow.

The observed effects on area ratio for first appreciable stall can be explained plausibly in terms of energy redistribution and inviscid amplification. The kinetic energy content of a wake-type inlet profile is greater than that of a uniform profile, and the kinetic energy is also redistributed toward the walls. This higher energy would tend to delay the onset of wall stall to larger area ratios, as shown qualitatively by the dotted curve in Fig. 7.

As the inlet profle distortion is increased, inviscid amplification of the distortion also increases, as shown in Fig. 7. At large values of λ_1, inviscid distortion dominates, causing the trend of area ratio at stall first to level off and then fall.

The expected type of stall behavior for various values of inlet distortion is shown in Fig. 8. These suggested trends may be used to explain the experimental results.

Centerline stalls were observed for inlet profiles with λ_1 = 2.58, 2.0 and 1.65. Thus, the inviscid amplification was apparently the dominant mechanism for these profiles. Both center line wall stalls occurred for inlet profiles with λ_1 = 1.4, 1.3 and 1.2 Energy redistribution and inviscid amplification were probably about equally important for these profiles. Only wall stalls occurred for the inlet profile with λ_1 = 1.1. The area ratio for stall with this profile was larger than for λ_1 = 1.0, indicating the effect of energy redistribution.

Pressure Recovery. In the present study, only the line of first appreciable stall was determined. Performance information is also required for diffuser design.

Performance cannot be measured (in practice) on a free surface water table. A few measurements of performance with inlet distortion were made by Wolf and Johnston [7]. Their results, combined with the present results suggest that a slightly distorted wake-type inlet velocity profile may be beneficial for performance. However, creation of a wake-type inlet velocity profile to increase performance is an unlikely remedy, owing to the losses incurred in generating the profile [16].

Conclusions

Several conclusions may be drawn from this experimental study of two-dimensional, plane-wall diffusers with wake-type inlet velocity profile distortions:

(1) Diffusers with distorted inlet velocity profiles exhibit stall behavior quite different from that found in diffusers with uniform inlet profiles.
   (*a*) The area ratio for first appreciable stall shift toward larger area ratio for moderate inlet profile distortion, and then is reduced as distortion becomes severe.
   (*b*) A centerline "pocket" stall develops if the inlet flow is severely distorted.
(2) Inlet distortion effects on location of first appreciable stall can be explained qualitatively by considering inviscid amplification and energy redistribution. For slightly distorted inlet profiles, wall stall is delayed by energy added to the layers near the wall. For severely distorted inlet profiles, inviscid amplification dominates and center-line stall occurs.
(3) Available data do not permit prediction of performance with confidence for diffusers with distorted inlet flows.
(4) Flow regime data presented in this paper are for fairly

Downloaded 02 Jun 2010 to 171.66.16.103. Redistribution subject to ASME license or copyright; see http://www.asme.org/terms/Terms_Use.cfm

broad wakes at the diffuser inlet. Further study may be required before the conclusions presented are generalized to the interesting practical case of narrow wakes, such as those generated by compressor blades.

References

1 Moore, C. A., and Kline, S. J., "Some Effects of Vanes and of Turbulence on Two-Dimensional Wide-Angle Subsonic Diffusers," NACA TN 4080, 1958.

2 Fox, R. W., and Kline, S. J., "Flow Regime Data and Design Methods for Curved Subsonic Diffusers," Report PD-6, Thermosciences Division, Mechanical Engineering Department, Stanford University, Stanford, Calif. 1960.

3 Kline, S. J., "On the Nature of Stall," ASME *Journal of Basic Engineering,* Vol. 81, No. 3, Sept. 1959, pp. 305–320.

4 McDonald, A. T., and Fox, R. W., "An Experimental Investigation of Incompressible Flow in Conical Diffusers," *International Journal of the Mechanical Sciences,* Vol. 8, No. 2, Feb. 1966, pp. 125–139.

5 Sovran, G., and Klomp, E. D., "Experimentally Determined Optimum Geometries for Rectilinear Diffusers with Rectangular, Conical or Annular Cross-Section," *Fluid Mechanics of Internal Flow,* G. Sovran, ed., Elsevier Publishing Company, New York, 1967, pp. 270–319.

6 Waitman, B. A., Reneau, L. R., and Kline, S. J., "Effects of Inlet Conditions on Performance of Two-Dimensional Diffusers," ASME *Journal of Basic Engineering,* Vol. 83, No. 2, Sept. 1961, pp. 349–360.

7 Wolf, S., and Johnston, J. P., "Effects of Nonuniform Inlet Velocity Profiles on Flow Regimes and Performance in Two-Dimensional Diffusers," ASME *Journal of Basic Engineering,* Vol. 91, No. 3, Sept. 1969, pp. 462–474.

8 Tyler, R. A., and Williamson, R. G., "Diffuser Performance with Distorted Inflow," *Proceedings of the Institution of Mechanical Engineers,* Vol. 182, 3D, 1967–1968, pp. 1–11.

9 Horlock, J. H., and Lewis, R. I., "Shear Flows in Straight-Sided Nozzles and Diffusers," *International Journal of the Mechanical Sciences,* Vol. 2, No. 4, Apr. 1961, pp. 251–266.

10 Moses, H. L., and Chappell, J. R., "Turbulent Boundary Layers in Diffusers Exhibiting Partial Stall," ASME Paper No. 66-WA/FE-14, 1966.

11 Carlson, J. J., Johnston, J. P., and Sagi, C. J., "Effects of Wall Shape on Flow Regimes and Performance in Straight, Two-Dimensional Diffusers," ASME *Journal of Basic Engineering,* Vol. 89, No. 1, Mar. 1967, pp. 151–160.

12 Swift, R. J., "Design and Construction of a Water Table for the Study of High Reynolds Number Diffuser Flows," M.S. thesis, School of Mechanical Engineering, Purdue University, West Lafayette, Ind., Jan. 1972.

13 Kaiser, K. F., "The Effect of a Class of Nonuniform Inlet Velocity Profiles on First Appreciable Stall in Two-Dimensional Plane Wall Diffusers," Ph.D. thesis, School of Mechanical Engineering, Purdue University, West Lafayette, Ind., May 1973.

14 Reneau, L. R., Johnston, J. P., and Kline, S. J., "Performance and Design of Straight, Two-Dimensional Diffusers," Report PD-8, Mechanical Engineering Department, Stanford University, Stanford, Calif., 1964.

15 Sarpkaya, T., "Vortex Breakdown in Swirling Conical Flows," AIAA Paper No. 71-52, Jan. 1971.

16 McDonald, A. T., Fox, R. W., and Van Dewoestine, R. V., "Effects of Swirling Flow on Pressure Recovery in Conical Diffusers," *AIAA Journal,* Vol. 9, No. 10, Oct. 1971, pp. 2014–2018.

Downloaded 02 Jun 2010 to 171.66.16.103. Redistribution subject to ASME license or copyright; see http://www.asme.org/terms/Terms_Use.cfm

W. Tabakoff

Y. Sheoran

K. Kroll

Department of Aerospace Engineering
and Applied Mechanics,
University of Cincinnati,
Cincinnati, Ohio 45221

Flow Measurements in a Turbine Scroll

A study was conducted to determine experimentally the flow behavior in the combined scroll nozzle assembly of a radial inflow turbine. Hot film anemometry technique was used to measure the flow velocity in the scroll.

Introduction

In recent years there have been considerable interest in the study of small radial gas turbines to improve their performance characteristics. Most of the research work has been concentrated on turbine rotors, since it was considered to have the main effect on turbine efficiency. Recent research works have shown the need for new design techniques in the turbine scroll and guide vanes in order to improve the turbine performance.

At the present time the scroll designs are still based on one dimensional flow calculations. Guide vane blades are merely designed to give the required flow turning angle. The inlet velocity distribution has been assumed to be uniform from one guide vane to another. Such an assumption is not realistic; a variation in the inlet velocity distribution exists and depends mainly on the scroll and the guide vane blade effects.

Scroll Effect on Guide Vane Inlet Velocity Variation. The three dimensional flow behavior in the scroll affects the nozzle inlet flow properties. A circumferential variation in the flow properties and lateral velocity components result from the secondary flow effects on the scroll discharge.

Boundary layer build-up on scroll side walls has a blocking effect in the scroll passage. Consequently, each vane will have different inlet conditions, especially the inlet mass flow and the inlet flow incidence.

The secondary flow in the scroll results from the nonequilibrium between the pressure and the centrifugal forces in the boundary layers on the scroll side walls. Nonuniformities in the flow properties at the scroll inlet also result in secondary flow. This effect is similar to the secondary flow in cascade passages and pipe bends. The secondary flow consists mainly of vortices, whose strength increases along the scroll, causing a circumferential variation in the flow parameters. This is another factor that leads to different inlet flow conditions in each guide vane channel.

Additional weak vortices are created in the scroll passage due to the flow discharge to the guide vanes. Such vortices are similar to the corner vortices, but are not stationary. They depend on the geometry of the scroll and nozzle entrance arrangements.

A new analysis which describes the flow behavior in combined scroll-nozzle assembly of radial inflow turbines is reported by Hamed, et al. [1]. This analysis provides a better understanding of the mutual interaction effects of the flow in scroll-nozzle assembly. In a different but parallel investigation, Hamed, et al. [2] are presenting the solution for nonviscous three dimensional scroll flow which determines the velocity components in the scroll cross sectional planes. Very few experimental measurements of the flow in the scroll can be found in the literature. Reference [3] reports a detailed experimental and analytical study of the losses in both the vaned and vaneless regions of a radial inflow turbine nozzle. To be able to confirm the analytical investigations reported in references [1] and [2], an experimental investigation was undertaken.

Research Scroll Facility. The scroll facility at the University of Cincinnati, Department of Aerospace Engineering and Applied Mechanics, was used in this program. The test facility was designed to incorporate a complete nonsymmetrical radial inflow turbine scroll for testing using cold air. The present phase of experimental investigation was concerned with the measurement of the through flow velocities at different scroll cross sections. It is hoped that with this data a better understanding of the flow behavior in the scroll will be obtained. The scroll used was nonsymmetric circular type with nozzle stator annulus consisting of 13 untwisted vanes.

Experimental Investigation

Frame of Reference. A schematic diagram of the scroll is shown in Fig. 1. In the flow analysis of such a scroll, it is more convenient to define two cylindrical coordinate systems. The machine coordinate system (R,ϕ,Z) is a fixed frame of reference with its Z axis as the machine shaft axis of the impeller. For the machine axes, the $\phi = 0$ line is tangent to the flat side of the scroll as shown in Fig. 1. This set condition will be used for the purpose of discussion of the results. For the convenience of handling the experimental data in a certain scroll section, it is necessary to define a local axes system

Contributed by the Fluids Engineering Division of THE AMERICAN SOCIETY OF MECHANICAL ENGINEERS *and presented at the Winter Annual Meeting, New York, N.Y., December 2-7, 1979. Manuscript received by the Fluids Engineering Division, May 10, 1979.*

Copyright © 1980 by ASME

Downloaded 02 Jun 2010 to 171.66.16.103. Redistribution subject to ASME license or copyright; see http://www.asme.org/terms/Terms_Use.cfm

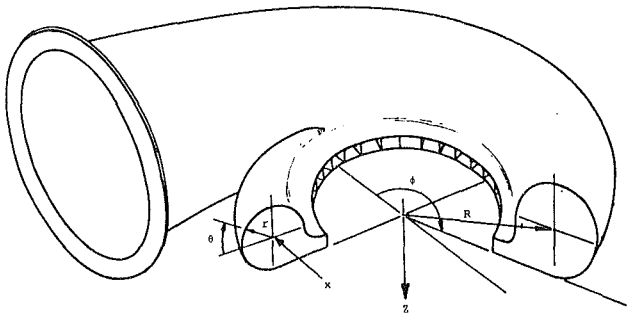

Fig. 1 Scroll schematic diagram

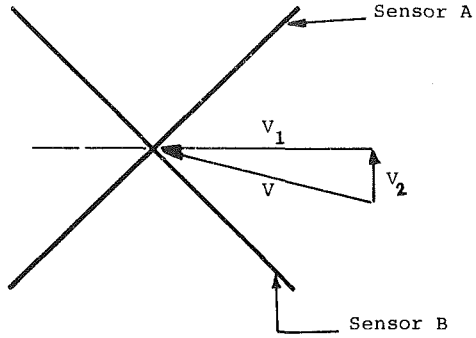

Fig. 2 Hot film probe configuration with respect to the measured velocity

(r,θ,x) which is attached to the center of any particular scroll cross section under investigation. In this system, the x-axis is zero in the plane of the cross-section and is normal to this plane. Note that in the machine coordinate systems, the tangential direction at the center of any section coincides with the x-axis on the scroll cross section (the so-called through flow velocity direction).

Measurement Technique. In this study a hot film anemometry technique was used to measure the flow velocities in the scroll. Two types of x-probes were used [4]. The two-dimensional x-probe consists of two sensors mounted perpendicular to each other as shown in Fig. 2. This probe measures two components of velocity V_1 and V_2 in the plane formed by the two sensors. The velocity components with respect to the sensor output voltage are given by the following equations:

$$V_1 = 0.707\,K\,(A+B)$$
$$V_2 = 0.707\,K\,(A-B)$$

where A = linearized output voltage from sensor A,
B = linearized output voltage from sensor B,
K = the proportionality constant between sensor output voltage caused by the velocity component normal to the sensor.

Hence, appropriately orienting the sensor elements, one can measure any two desired velocity components; the tangential velocity and the through flow velocity, or the radial and through flow velocity. By using the two types of probes, where one component of velocity is measured twice and hence gives a method of checking the results, one can build up the three components of velocity in this plane. Unfortunately, the tangential and radial velocity directions are ambiguous if measured this way, therefore they will be excluded from this report.

Probe Mount and Flow Measurement. The plan view of the scroll is shown in Fig. 3, with the corresponding three cross sections where the measurements were taken. A special design was made to mount the probes in scroll sections 1 and 2. A slit was cut in the top outer quadrant of the scroll. Around this slit, two races were welded to allow a spring steel strip to move in an arc on teflon sealed races, thereby sealing the flow leakage. An adapter was welded to a hole in the spring steel to receive and hold the probe in place, or allow a probe traversing mechanism to be mounted on it. In this way, the hot film probe could be easily lowered into the measuring cross section from the outer scroll wall to any radial location as shown with shaded area in Fig. 4. By the use of gear teeth fixed on one of the races and gear mounted on a potentiometer pod fixed to the traversing mechanism, the angular location of the probe was very accurately plotted on the x-axis while the probe output was continuously plotted on the y-axis by the use of a x-y plotter.

In order to be able to survey a larger portion of the scroll cross section a better technique was used in section 3. Figure 4 shows the seven probe locations. Specially designed probe ports were welded at discrete angular locations which allowed the probes to survey the complete cross section 3. The probes were mounted onto a traversing mechanism which continuously moved the probe into cross section along radial lines. The probe traverse mechanism was electrically driven to reduce experimentation time and human error. This movement was also monitored by a potentiometer, hence making it possible to continuously measure the velocity profiles along these radial lines.

Scroll Geometry. Since curvilinear flow channels with variable cross-sections offer no characteristic length,

Nomenclature

A = voltage output from the hot film probe sensor A
B = voltage output from the hot film probe sensor B
C = proportionality constant for equation (1)
d = distance along a cross-section diameter (meters)
Δd = increment along the section diameter (meters)
n = exponent in equation (1)
R = radial distance between the machine center ($Z=0$), and the local scroll cross seciton center
R' = projected radius (Fig. 13)
r = radius of the scroll cross-section
(R/r) = relative radius
R,ϕ,Z = machine coordinate system
r,θ,x = local scroll cross section coordinate system
r_{RV} = correlation coefficient of the least square fit between radius of curvature and through flow velocity
V_1,V_2 = two normal components of velocity vector measured by the hot film probe
ΔV = increment in velocity corresponding to the increment in diameter Δd
α = angle made by the radius of curvature R of the scroll cross-section center to the horizontal plane ($Z=0$).
ν = kinematic viscosity of the air in the scroll, (s/m^2).

Subscripts

1,2,3 = refer to the three scroll sections at which the measurements are made.

Downloaded 02 Jun 2010 to 171.66.16.103. Redistribution subject to ASME license or copyright; see http://www.asme.org/terms/Terms_Use.cfm

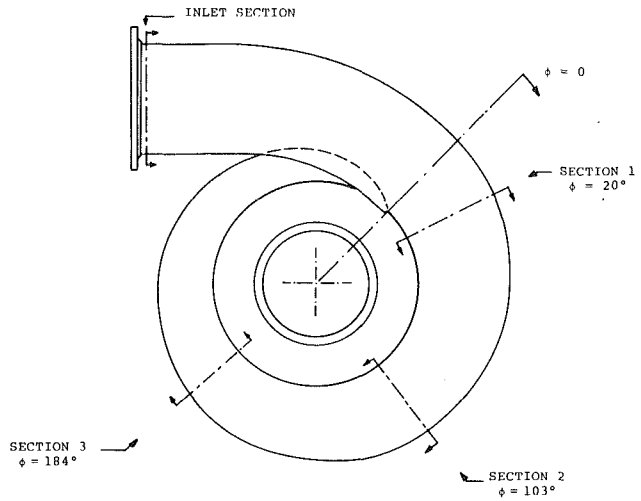

Fig. 3 Plan view of the scroll

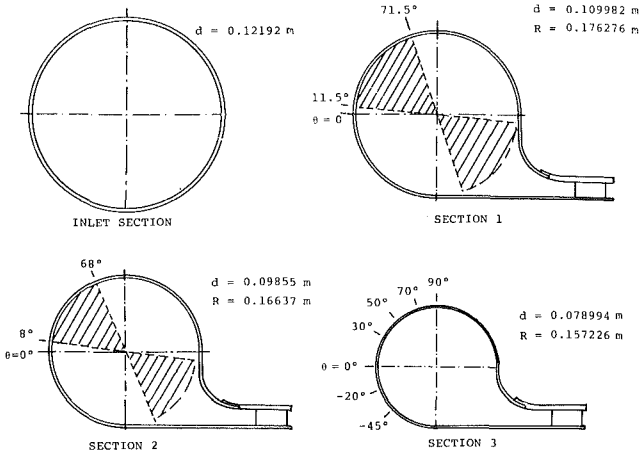

Fig. 4 Measurement sections of the scroll showing flow sampling regions and port location

Reynolds number ($\bar{V}d/\nu$) alone based on the average velocity $\bar{V}$ of steady flow ceases to be a criterion of describing the flow, as it is used for straight pipe flow [5]. However, a simple dimensional analysis carried out suggests that such flow can be geometrically and dynamically compared by defining two nondimensional numbers, namely: ($\rho Q/\mu d$) and R/d where Q is the volume flow rate. The first nondimensional number, under certain conditions can be defined as a local Reynolds number based on the section diameter d and the average section velocity $\bar{V}$. The second number is a ratio of the radius of curvature of the center line of the scroll section to the diameter of the scroll cross-section (Fig. 1) [6].

Figure 3 shows the three scroll section locations. The first section is at ϕ = 20 deg, the second at ϕ = 103 deg and the third at ϕ = 184 deg. Table 1 is provided to establish the geometry of the scroll being investigated. The second column in Table 1 lists the radius of curvature, $R' = R\cos\alpha$, projected on a z = constant surface. Consequently, the last column is a relative ratio based on the projected radius R'. The relative radius (R/r) values for the three scroll sections where the measurements were performed are as follows: Section 1, R/r = 3.21; Section 2, R/r = 3.38; and Section 3, R/r = 4.10. These three values may be used for comparing the flow properties of any other scroll which has the same relative radius.

Table 1

ϕ (degree)	$R' = R\cos\alpha$ (meters)	d (meters)	R'/r
0	0.177038	0.113538	3.125
45	0.172212	0.105156	3.28
90	0.167894	0.096012	3.51
135	0.164338	0.087376	3.77
180	0.157988	0.0762	4.17
225	0.1524	0.06477	4.65
270	0.144526	0.0508	5.71
315	0.136144	0.034544	8.0
359	0.119126	0.004064	66.7

Results and Discussion

The cold air flow enters the scroll inlet section from a plenum chamber via a short convergent nozzle. At the scroll inlet section the flow had a laminar axisymmetric velocity profile. For all the measurements, the velocity at the center of the inlet section was 41.15 m/s (135 ft/s), and the mass flow rate was maintained at 0.454 kg/s (1 lb/s). The turbine rotor was modified in such a way that the blades were removed and only the rotor hub was used in its place. Examining the flow field in section 3 which was surveyed completely, one can

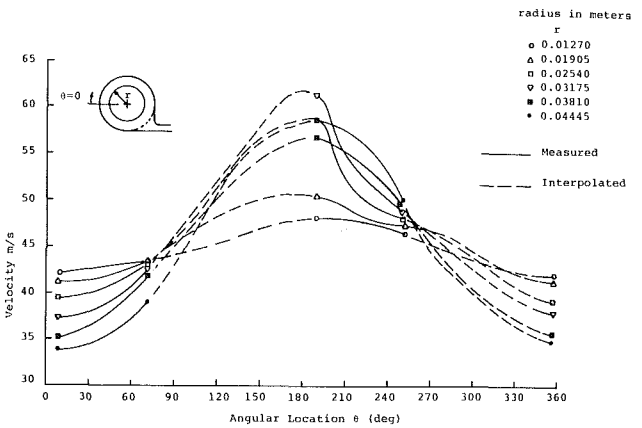

Fig. 5 Through flow velocity profile along concentric circles of various radii in section 1

observe that the velocities vary continuously in the entire circular cross-section.

Since the flow measurements were made in two sectors of each of the circular cross sections 1 and 2 (Fig. 4), the flow contours were generated in the following manner. Based on the observation of flow behavior in section 3, Figs. 5 and 6 were drawn. These show the through flow velocity profiles along concentric circles at various radii. The solid lines indicate the continuously measured velocity while the dotted lines indicated the interpolated velocities.

From the inspection of Figs. 5 and 6, one can see that they compare remarkably well with the flow trend in section 3 as shown in Fig. 7. It is interesting to see that the flow behavior for small radius, r = 0.00254 m does not vary too much from the average value. On the other hand, the flow along a large radius r = 0.02794m starts with a low velocity value at 30 deg then increases to a maximum around 180 deg, and then decreases back to a low value of around 340 deg. For all other radius circles, the flow has intermediate velocity values.

Figures 8, 9, and 10 show the through-flow velocity profiles measured along section diameters at several angular locations starting with respect to the outer wall and the horizontal (θ = 0 deg). These profiles are essentially linear, except for a noticeable bend in some profiles of section 2. The final velocities are found to have an uncertainty of ± 4.42 percent with 20:1 odds. The velocity profiles of section 2 at θ = 0 deg, θ = 50 deg and θ = 135 deg are compared with the corresponding results of the theoretical analysis of reference [7]. This comparison is reproduced in Fig. 11. It is worthy to note that the scroll used in the experiment had nozzles, while

Downloaded 02 Jun 2010 to 171.66.16.103. Redistribution subject to ASME license or copyright; see http://www.asme.org/terms/Terms_Use.cfm

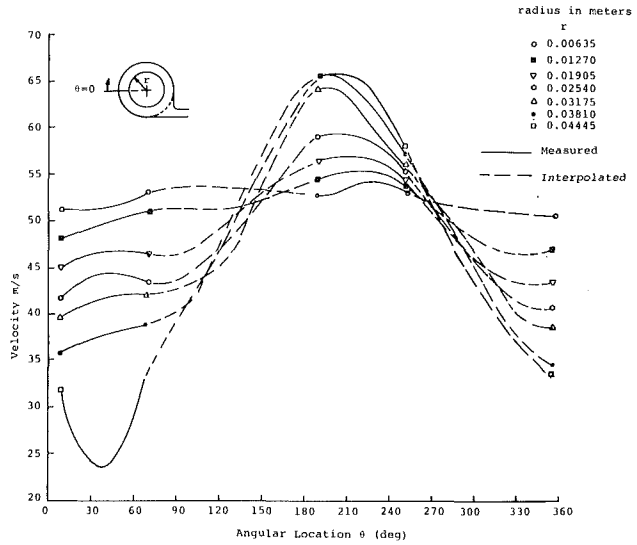

Fig. 6 Through flow velocity profile along concentric circles of various radii in section 2

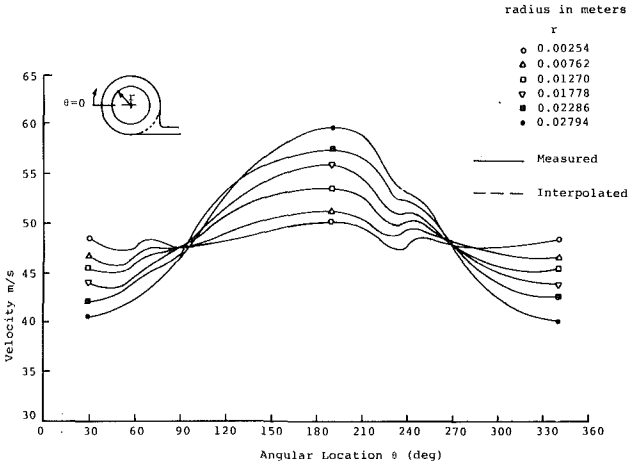

Fig. 7 Through flow velocity profile along concentric circles of various radii in section 3

the scroll used in the theoretical analysis was vaneless. This could account for the difference in velocities in Fig. 11. The slopes of the least square fits of these profiles are easily calculated. It can be represented by the ratio of $\Delta V/\Delta d$. These slopes are plotted as a function of the angular location θ in Fig. 12. If the profiles are considered along diameters originating from the outside wall (i.e., for $\theta = 90$ deg to -90 deg) then the slopes are all positive. Figure 12 implies that the most sharply inclined profiles lie along the diameters locations at $\theta_1 = 10$ deg, $\theta_2 = 6$ deg, and $\theta_3 = 8$ deg, corresponding to sections 1, 2 and 3, respectively.

Figure 13 shows the relative positions of the three sections with respect to the machine axis. The radius of curvature R from the center of the scroll section makes an angle α to the scroll horizontal ($Z = 0$). A table attached to this figure shows the radii of curvature and the corresponding alphas of the three sections 1, 2, and 3. Comparing θ_1, θ_2 and θ_3 from Fig. 12 with α_1, α_2, and α_3 from Fig. 13, one can observe that the thetas deviate slightly from the alphas. In addition, the highest velocities in each case occurred near the inside walls of the cross section, obviously influenced by the position of the nozzles. This trend is clearly seen in Fig. 14 which shows the through-flow velocity contours in each of the three sections. This behavior suggests a tendency towards free vortex type of

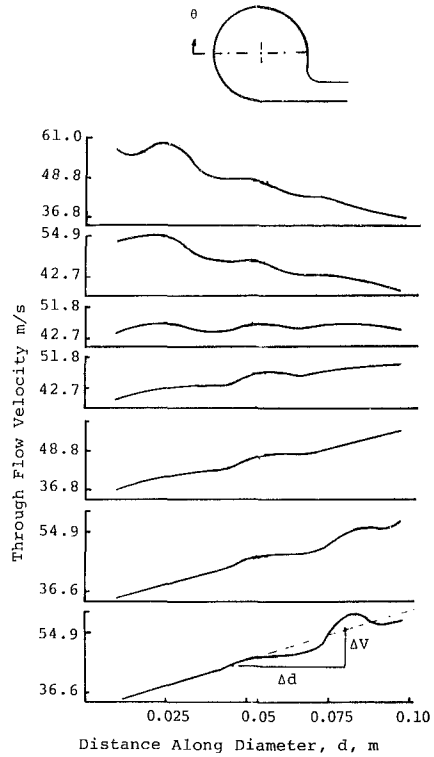

Fig. 8 Through flow velocity profiles along section diameters at various angular locations in section 1

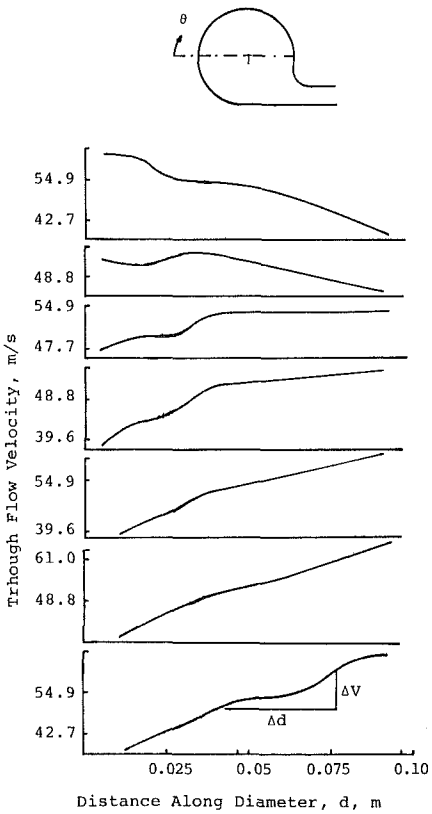

Fig. 9 Through flow velocity profiles along section diameters at various angular locations in section 2

flow with respect to the center of the machine. The contour lines of the through flow velocity in Fig. 14 are obtained by normalizing the local measured velocities with respect to the

Downloaded 02 Jun 2010 to 171.66.16.103. Redistribution subject to ASME license or copyright; see http://www.asme.org/terms/Terms_Use.cfm

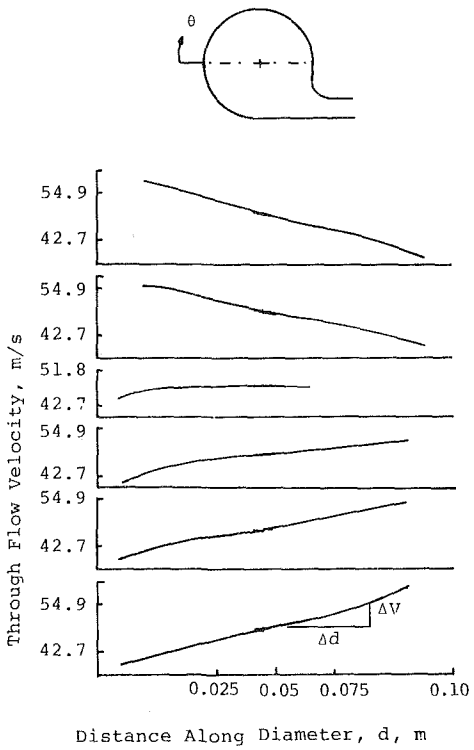

Fig. 10 Through flow velocity profiles along section diameters at various angular locations in section 3

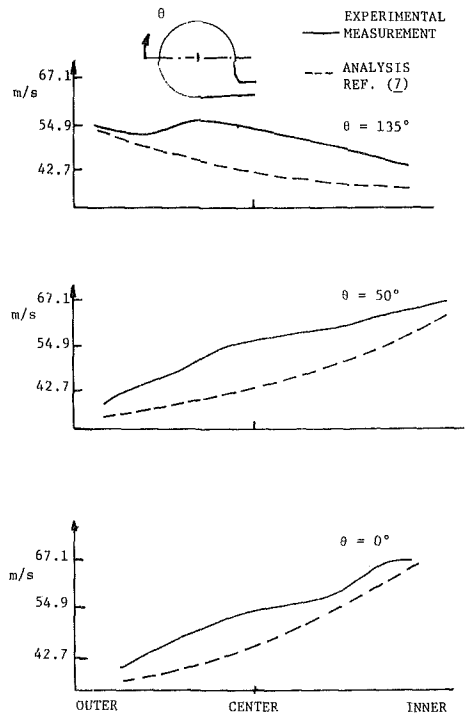

Fig. 11 Comparison of experimental measurements with the analysis of reference [7] for θ = 0, 50 and 135 deg

scroll inlet center velocity of 41.14 m/s. To be able to compare the obtained data with a free vortex flow, it is conventient to plot the measured velocity data on a log-log scale as a function of machine radius, R, as shown in Fig. 15. A least square curve fit of the form

$$V = C\,R^n \tag{1}$$

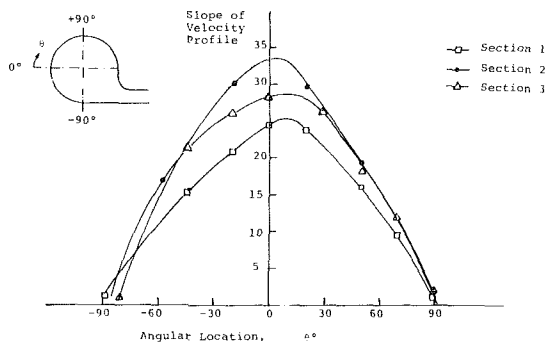

Fig. 12 Slope variations of the through flow velocity profiles along section diameters as a function of the angular locations as shown in Figs. 8, 9, and 10

is fitted through these data points. This produces a straight line. The coefficient C, the exponent n, and the correlation coefficient r_{RV} are tabulated in Table 2.

Table 2

Section	C	n	r_{RV}
1	7.8634	−1.0041	0.972
2	2.6377	−1.6205	0.96
3	6.6759	−1.00616	0.96

The correlation of the least square fit, r_{RV}, for all the sections is very good. For sections 1 and 3, the flow is very nearly to free vortex. However, in the section 2, the flow deviates slightly from the free vortex behavior. In all cases, the exponent "n" is negative, which shows that the higher velocity flow will occur close to the center of the machine. The scatter of the data points about the least square fit governed by equation (1) is due to three main factors: first, due to the position of the nozzle with respect to the center of the section (x = 0, r = 0); secondly, due to the position of the section from the tongue of the scroll ϕ = 0; and thirdly, due to the position of the center of the scroll cross section with respect to the center of the machine.

Figure 16 shows the normalized through flow velocity contours with the estimated secondary flow directions in the three cross sections. It appears that four spiral cross flow motions are present. These are directed (approximately) along the diameter of sharpest inclined velocity profile towards the outer wall of the turn and along the side wall towards the outer wall. The inlet length of the scroll up to the first nozzle ϕ = 0 is like a curved pipe (Fig. 3) and this should tend to move the high velocity flow towards the outer side of the inlet pipe [8]. This trend would be reversed as soon as the first nozzle is encountered. This type of behavior could account for the ripples in the contour of the first section (Fig. 14, Section 1). These ripples and consequently the secondary flow seem to decrease further downstream as shown in the same figure by the sections 2 and 3. The magnitudes of the cross flow velocities in the local tangential and local radial directions were measured, and are of the order of 25 and 6 percent of the through flow velocities, respectively.

Uncertainty Analysis. The hot film sensors were calibrated each time the sensors were used for a day of data taking. A limited sample uncertainty analysis of Kline and McCintock [9] was used on the linearized output of the anemometer. The final velocities are found to have an uncertainty of ±4.42% with 20:1 odds. This is shown as an uncertainty band attached to one particular value on the velocity profiles of Figs. 8, 9, and 10. The fixed errors are due to the change in temperature of the environment during measurement from those at calibration. This is taken care of by applying a temperature compensation calculation on the final output velocities.

Downloaded 02 Jun 2010 to 171.66.16.103. Redistribution subject to ASME license or copyright; see http://www.asme.org/terms/Terms_Use.cfm

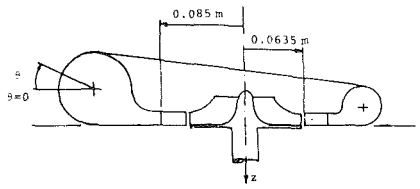

SECTION	R	r	α
1	0.2115 m	0.06596 m	18.15°
2	0.1996 m	0.059 m	17.5°
3	0.1875 m	0.04572 m	15°

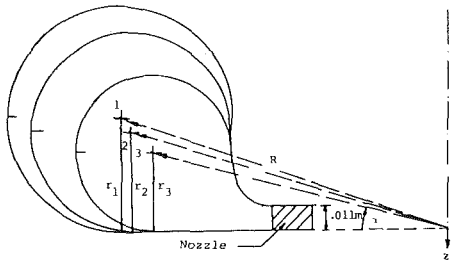

Fig. 13 Relative poisition of three sections with respect to the machine axis

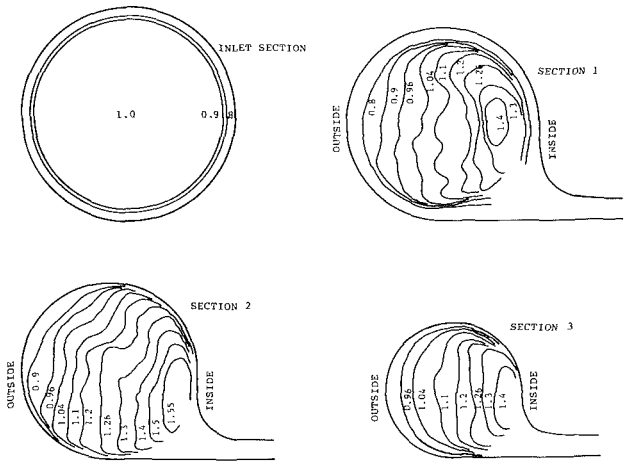

Fig. 14 Contours of through flow velocity, relative to 41.15 m/s the core velocity of the inlet section

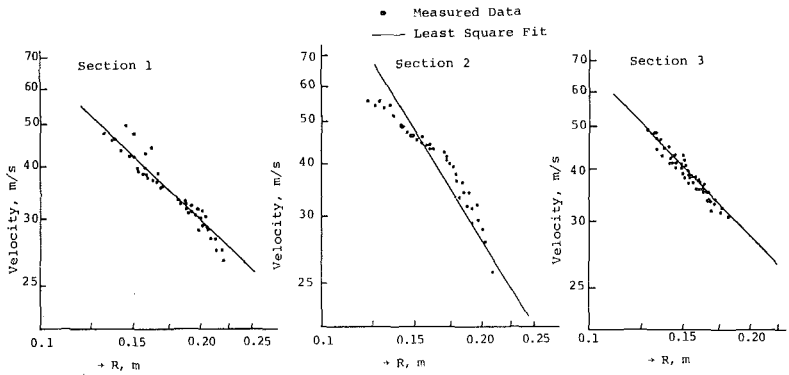

Fig. 15 Least square fit of through flow velocity variation with respect to the machine radius

Downloaded 02 Jun 2010 to 171.66.16.103. Redistribution subject to ASME license or copyright; see http://www.asme.org/terms/Terms_Use.cfm

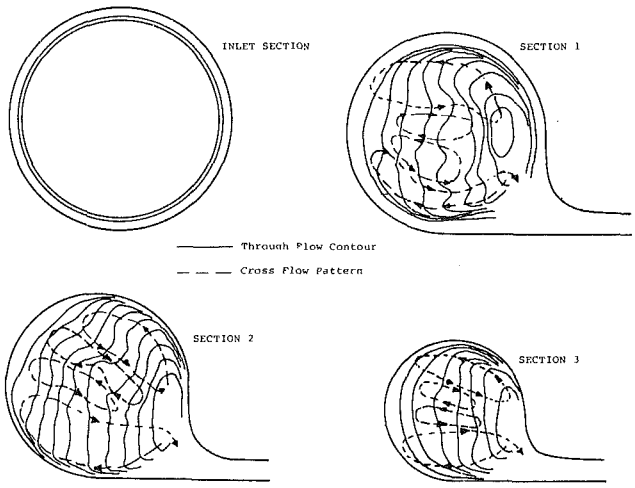

Fig. 16 Through flow velocity contours with estimated cross flow patterns in the three sections

Acknowledgment

The authors wish to acknowledge the helpful discourse provided by Dr. Arthur J. Glassman from NASA Lewis Research Center, Cleveland, Ohio. This research work is sponsored by NASA Grant No. NSG 3066, Lewis Research Laboratory, Cleveland, Ohio.

References

1 Hamed, A., Baskharone, E. and Tabakoff, W., "A Flow Study in Radial Inflow Turbine Scroll-Nozzle Assembly," ASME JOURNAL OF FLUIDS ENGINEERING, Mar. 1978, Vol. 100, pp. 31-36.

2 Hamed, A., Abdallah, S., and Tabakoff, W., "Flow Study in the Cross Sectional Planes of a Turbine Scroll," AIAA Paper No. 77-714, AIAA 10th Fluid and Plasma Dynamics Conference, Albuquerque, New Mexico, June 27-29, 1977.

3 Khalil, I.M., Tabakoff, W., and Hamed, A., "Losses in Radial Inflow Turbines," ASME JOURNAL OF FLUIDS ENGINEERING, Sept. 1976, Vol. 98, pp. 364-373.

4 Thermo Systems, Inc., "Anemometer Catalog," CAT/FORM 6560375.

5 Stepanoff, A.J., *Centrifugal and Axial Flow Pumps. Theory, Design and Application*, Wiley, 1967.

6 Ito, H., "Pressure Losses in Smooth Pipe Bends," ASME *Journal of Basic Engineering*, Vol. 81, Mar. 1960.

7 Hamed, A. and Baskharone, E., "Analysis of Three Dimensional Flow in a Turbine Scroll," ASME Paper presented at the 1979 Winter Annual Meeting, New York City.

8 Rowe, M., "Measurement and Computations of Flow in Pipe Bends," *Journal of Fluid Mechanics*, Vol. 43, Part 4, 1970, pp. 771-783.

9 Kline, S.J. and McClintock, F.A., "Describing Uncertainties in Single-Sample Experiments," *Mechanical Engineering*, Jan. 1953, p. 3.

Downloaded 02 Jun 2010 to 171.66.16.103. Redistribution subject to ASME license or copyright; see http://www.asme.org/terms/Terms_Use.cfm

A. Hamed
E. Baskharone

Department of Aerospace Engineering
and Applied Mechanics,
University of Cincinnati,
Cincinnati, Ohio 45221

Analysis of the Three-Dimensional Flow in a Turbine Scroll

The present analysis describes the three dimensional compressible inviscid flow in the scroll and the vaneless nozzle of a radial inflow turbine. The solution to this flow field, which is further complicated by the geometrical shape of the boundaries, is obtained using the finite element method. Symmetric and nonsymmetric scroll cross sectional geometries are investigated to determine their effect on the general flow field and on the exit flow condiitons.

Introduction

The flow field in the nonrotating passages of a radial inflow turbine is very complicated. This is evidenced by the experimental measurements of references [1] and [2]. While the existing quasi-three-dimensional flow solution techniqes [3–6] are applicable to radial inflow turbine rotors, the analytical solutions of the flow field in a turbine scroll have been limited by grossly simplifying assumptions. The scroll flow field is usually studied using the assumption of one dimensional flow and conservation of the mass and angular momentum [7 and 8]. In a previous study [9], the authors investigated the two dimensional flow field in a scroll, vaned nozzle assembly. The effect of the through flow velocity profile on the cross velocity components, was reported in reference [10] for two different scroll geometries. Although more insight into the scroll flow was possible through these two studies, they do not provide together a quasi-three-dimensional solution. The actual three dimensional scroll geometry must be considered because of the dependence of the through velocity profile on both the cross-sectional geometry and the location of the scroll section. In this paper the finite element method is used to compute the three dimensional inviscid flow field in a vaneless scroll-nozzle assembly of a radial inflow turbine.

Analysis

The three dimensional irrotational flow field is formulated in terms of the velocity potential function ϕ, with the velocity vector $\bar{V}$, expressed in terms of ϕ as follows:

$$\bar{V} = \nabla \phi \tag{1}$$

The equation of conservation of mass, in terms of the velocity potential, for steady state is given by:

$$\nabla \cdot (\rho \nabla \phi) = 0 \tag{2}$$

Using the thermodynamic relations for a perfect gas, the compressible flow density, ρ, is determined from the following equation

$$\rho = \rho_o \left[1 - \frac{\gamma - 1}{2} \left(\frac{\nabla \phi}{C_o}\right)^2\right]^{1/\gamma - 1} \tag{3}$$

where

$$C_o = \sqrt{\gamma R T_o} \tag{4}$$

Analytical solutions to this flow field are not possible and no numerical solutions were obtained using finite difference methods because of the complexity of the scroll boundary shape. The finite element method is more suitable for this type of problem because of its ability to handle complicated boundary shapes.

The Finite Element Method. The three basic steps involved in the finite element method are the domain discretization, the integral statement of the problem and the local approximation of the function in each element [11 through 15]. The unknown velocity potential solution is approximated in each element by:

$$\phi^e = [N]\{\phi\}^e \tag{5}$$

where $\{\phi\}^e$ is the column vector of the potential function values, ϕ_i, at the nodes of the element e, and $[N]$ is the row vector of the interpolation functions, N_i.

Using the Galerkin method, the weighted average of the error resulting from the substitution of equation (5) into equation (2) is required to vanish over the domain D. In addition, the weighting functions are the same as the interpolation functions N_i, leading to the following equation:

$$\int_D N_i \nabla \cdot (\rho \nabla \phi)\, dv = 0 \tag{6}$$

The Boundary Conditions. Applying Green's theorem to equation (6), leads to the following relation, which involves the boundary conditions:

$$\int_D \nabla N_i \cdot (\rho \nabla \phi)\, dv = \int_{\partial D} N_i \rho \nabla \phi \cdot \vec{ds} \tag{7}$$

The right-hand side of equation (7) represents the weighted average of the mass flow across the boundary ∂D. The mass flux, $\rho(\partial\phi/\partial n)$, should therefore be specified across all the solution domain boundaries. The boundary conditions can be expressed as follows:

$$\rho \frac{\partial \phi}{\partial n} = f \tag{8}$$

where $f = 0$ on the solid boundaries;
$f = f_0$ at inlet; and
$f = f_3$ at exit.

Contributed by the Fluids Engineering Division of THE AMERICAN SOCIETY OF MECHANICAL ENGINEERING and presented at the Winter Annual Meeting, New York, N.Y., December 2-7, 1979. Revised manuscript received by the Fluids Engineering Division, May 29, 1980.

Copyright © 1980 by ASME

Downloaded 02 Jun 2010 to 171.66.16.103. Redistribution subject to ASME license or copyright; see http://www.asme.org/terms/Terms_Use.cfm

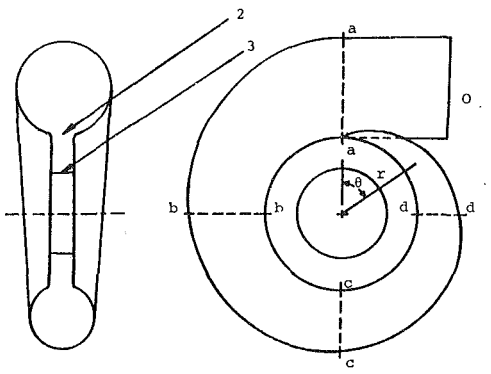

Fig. 1 Schematic of a turbine scroll and station designations

The designations of the various stations used in the analysis and the results, are shown in Fig. 1.

Finite Element Equations. Equation (7) holds for the entire solution domain and also for an arbitrary finite element e. When the potential function representation ϕ^e within the element, as given by equation (5), is substituted in the left-hand side of equation (7), we obtain the following element equation:

$$\int_{D_e} \nabla N_i \cdot (\rho \nabla [N]\{\phi\}^e)\, dv = \int_{\partial D_e} N_i \rho \frac{\partial \phi}{\partial n}\, ds \tag{9}$$

The surface integral on the right-hand side is to be evaluated only when the surface increment "ds" is on the boundary, since the contribution of any two neighboring elements cancel each other.

In the present analysis, the simplest four node linear tetrahedral elements are used, in which case, the equation for the approximation of the potential function in each element is given by:

$$\phi^e = \sum_1^4 N_i \phi_i \tag{10}$$

The notation used in the above equation has been previously explained in connection with equation (5). Equation (9) for a finite element, can be written in this case as follows:

$$\int_{D_e} \rho \left[\frac{\partial N_i}{\partial x}\frac{\partial N_j}{\partial x} + \frac{\partial N_i}{\partial y}\frac{\partial N_j}{\partial y} + \frac{\partial N_i}{\partial z}\frac{\partial N_j}{\partial z} \right] \phi_j\, dv = \int_{\partial D_e} N_i \rho \frac{\partial \phi}{\partial n}\, ds \tag{11}$$

The repeated subscript "j" indicates summation from $j=1$ to $j=4$.

Assembling the equations for all the elements in the flow field results in a set of algebraic equations which can be written in the following form:

$$[K]\{\phi\} = \{F\} \tag{12}$$

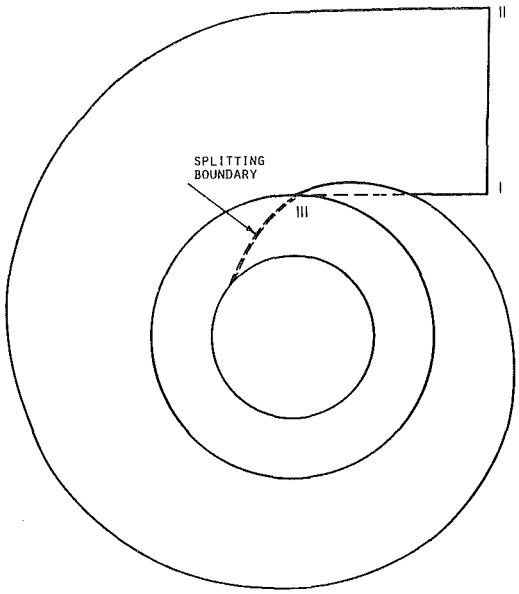

Fig. 2 Conversion of the solution domain from doubly to simply connected

where $[K]$ is the stiffness matrix of coefficients, and $\{\phi\}$ is the column vector of unknown potential functions. The load vector $\{F\}$ is dependent on the specified boundary conditions.

Geometrical Considerations. The complicated flow domain geometry causes two streams with different histories to meet at the scroll tip, resulting in a nonunique potential function distribution. The two streams correspond to the fluid particles entering the scroll at the points I and II of Fig. 2. They join each other later at the point III, from the upper and lower sides of the scroll lip. This complication which is a direct result of the domain multiconnectivity required special handling in both the problem formulation and the numerical solution. A jump in the value of the velocity potential was allowed across a cut of infinitesimal width, which starts at the scroll lip and extends to station 3, at exit as shown in Fig. 2. The jump in the value of the potential function represents an additional unknown which is determined in the numerical solution. The requirement of the continuity of the velocity field represents the matching condition across the infinitesimal cut width. The value of the jump is not specified externally, but is rather determined automatically by the solution procedure. This new approach is described and discussed in more details by the authors in reference [16]. The additional matching condition, in the now singly connected solution domain destroys the symmetry and bandedness of the stiffness matrix. The method of reference [18] was used for solving the resulting set of equations.

Results and Discussion

A computer program was developed which discretizes the

Nomenclature

D = the solution domain
f = the value of the normal flux at the boundary
$\{F\}$ = the load vector
$[K]$ = the stiffness matrix
L = characteristics length of the scroll inlet cross section
n = the normal to the boundary
$\{N\}$ = the column vector of the elements interpolation functions
q = flow velocity magnitude
s = the surface area
v = the volume
$\bar{V}$ = velocity vector
θ = azimuthal angle
ρ = flow density
ϕ = the velocity potential

Subscripts

0 = refer to inlet conditions
3 = refer to exit conditions
e = refer to a finite element
i = refer to variables at the node i

Superscripts

e = associated with the finite element
$*$ = associated with the non-dimensional parameters.

Downloaded 02 Jun 2010 to 171.66.16.103. Redistribution subject to ASME license or copyright; see http://www.asme.org/terms/Terms_Use.cfm

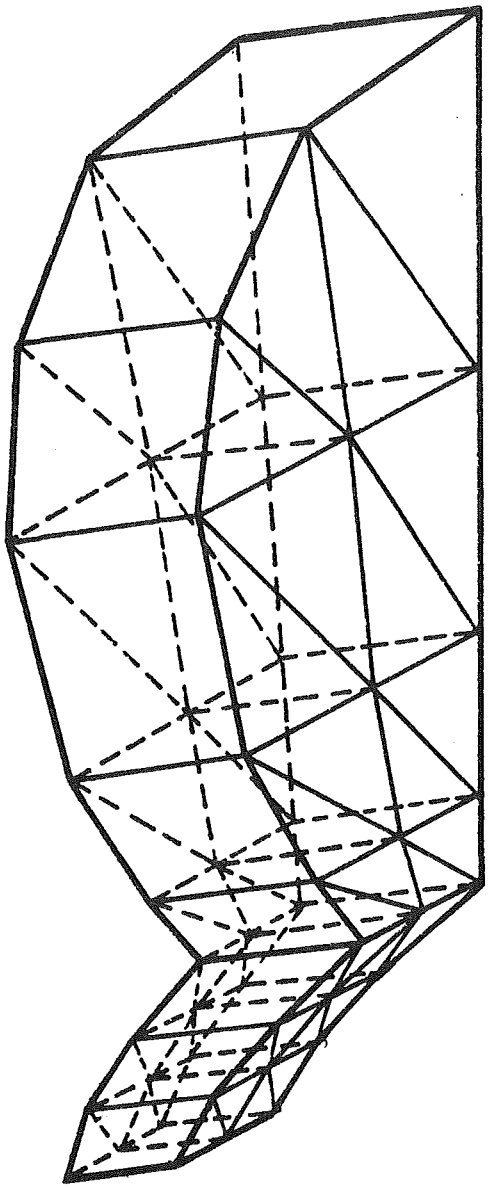

Fig. 3 Finite element discretization schematic

solution domain, generates the stiffness matrix, and solves the resulting set of equations. The input to the program includes geometric data such as the scroll area variation, and the diameters at the exit station 3 and station 2 at inlet to the vaneless nozzle. A given operating condition, corresponds to a particular mass flow rate, in the program input which is used to determine the inlet mass flux f_0. The corresponding exit mass flux, f_3, is determined according to the requirement of conservation of mass between the inlet station 0, and the exit station 3 of Fig. 1. The latter should be placed far enough in the radially inward direction such that its location does not influence the rest of the scroll flow field.

The solution domain is divided into a number of continuous nonoverlapping tetrahedral finite elements. The complete three dimensional discretization model is hard to depict, especially with the large number of nodal points and elements, 828 and 2772 respectively. The discretization model followed a pattern similar somewhat to the one we used earlier in a two dimensional study [9], with forty stations along the flow path. Thirty-six of these stations, separated from each other by 10 degrees in the circumferential direction, were placed in the scroll. A schematic of the discretized solution domain between two successive stations is shown in Fig. 3. The number

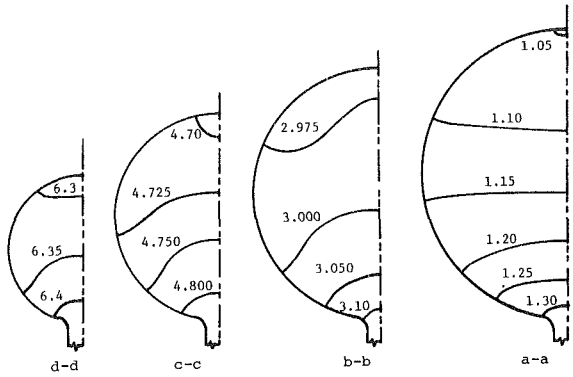

Fig. 4 Potential function distribution in the symmetric scroll cross sections

of nodal points started with 24 at the stations close to the scroll inlet and reduced gradually to 15 along the flow path maintaining the same number of nodal points in the nozzle portion at all stations. The remaining four stations representing the difference between 40 and 36 were placed in the scroll inlet neck portion, each with 14 nodal points.

Numerical results are presented for two cases representing symmetric and nonsymmetric scroll cross-sections. The geometry of the nonsymmetric scroll was similar to that of reference [1]. In both symmetric and nonsymmetric scroll cases, the scroll cross sectional area varied linearly around the circumference, starting with 0.11 meter initial cross-section diameter at a-a. In the vaneless nozzle portion the diameters D_2 and D_3 were equal to 0.170 and 0.127 meters, respectively and the distance between the two end walls was 0.011 meter. Figures 4 and 5 show the potential function distribution in four of the scroll cross sections which are located at 90 deg azimuthal angles intervals for the symmetric and nonsymmetric cases respectively. the nondimensional potential function in these figures is defined as:

$$\phi^* = \frac{\phi - \phi_0}{q_0 L}$$

where ϕ_0 and q_0 refer to the values of the potential function and the flow velocity magnitude at the inlet station, and L refers to the scroll cross section characteristic length, at the same station. It can be seen that the flow potential contour pattern in the scroll cross section does not change appreciably along the circumference after $\theta = 90$ deg. The potential function distribution in the vaneless nozzle is shown in Fig. 6 for the symmetric case at the plane of symmetry. It can be seen from the figure that in spite of the jump in the value of the potential function at $\theta = 0$, its derivatives are continuous. Since the axial velocity component is negligible in this region, these contours provide a good indication of the flow direction.

Most of the experimental studies of the flow in radial inflow turbines, have been concerned with flow measurements in the turbine rotor. Very few investigators attempted to measure experimentally the flow velocities in the scroll, and up till now they have been limited to surveys at the station proceeding the rotors [2 and 7]. Experimental measurements of the through flow velocity at three scroll cross sections are presented by Tabakoff and Sheoran [1] in a companion paper. Although their measurements were obtained in a scroll followed by nozzle vanes, they will be used for comparison with our computed results since they represent the only available experimental data of this type. Figures 7 and 8 show a comparison between the experimental measurements and the computed values of the through flow velocity in a cross section located at $\theta = 103°$. The through flow velocity was measured along several lines passing through the scroll cross

Downloaded 02 Jun 2010 to 171.66.16.103. Redistribution subject to ASME license or copyright; see http://www.asme.org/terms/Terms_Use.cfm

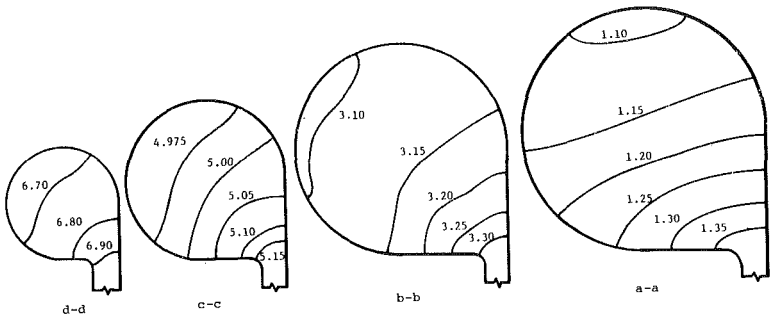

Fig. 5 Potential function distribution in the nonsymmetric scroll cross sections

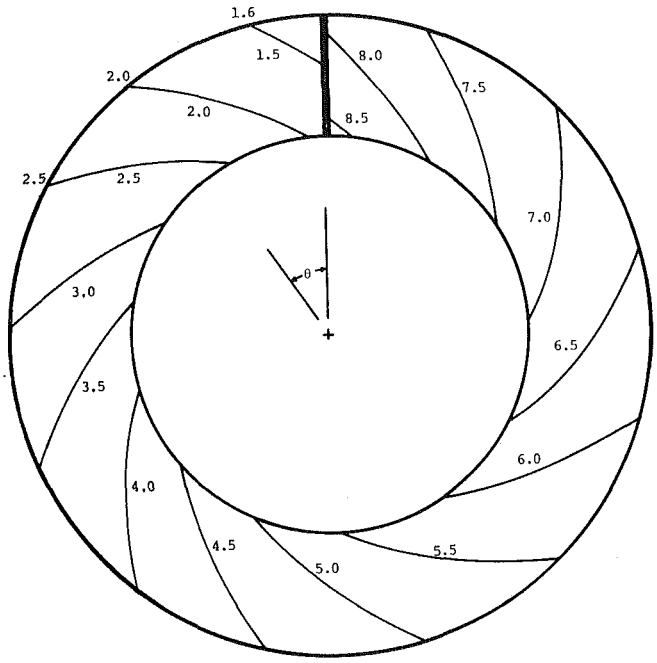

Fig. 6 Potential function distribution in the vaneless nozzle

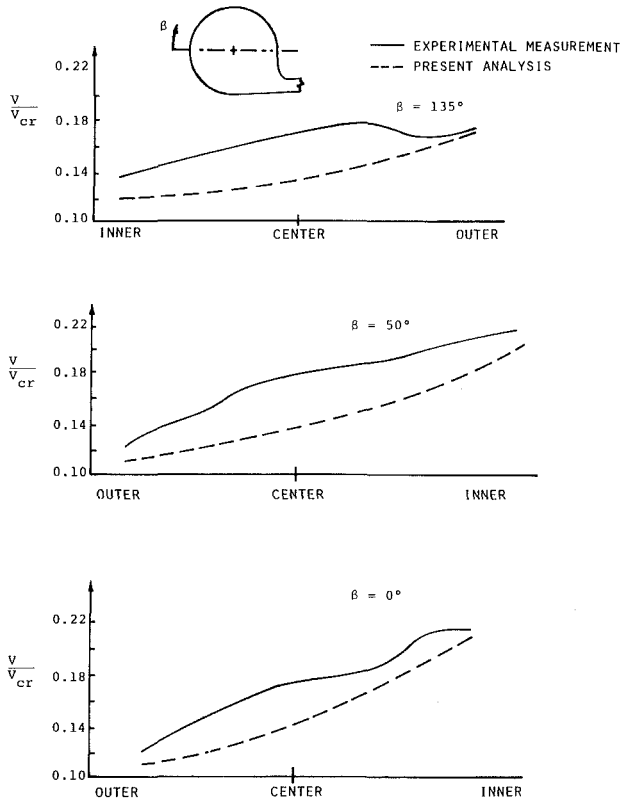

Fig. 7 Comparison with the experimental measurements at θ = 103 deg

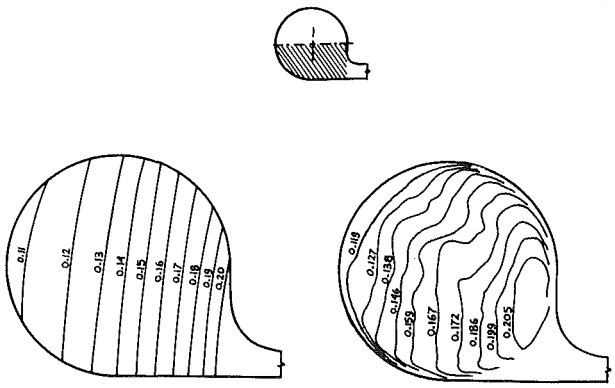

Fig. 8 The through flow velocity profile (V/V_{cr}) at θ = 103 deg

sectional center at $\beta = 0, 45, 135$ deg, [1], as indicated in Fig. 7. The higher values of the measured through flow velocities compared to those computed can be attributed to the blockage effect of the nozzle blades and the boundary layers. Both computed and measured through flow velocity profiles are shown in Fig. 8. It can be seen from this figure that the agreement between the theoretical and experimental results is very close in one half of the scroll section which is shaded in the schematic. The effects of secondary flow and viscosity which were not included in our analysis can cause the differences in the other half. The conditions at the scroll exit, which are important in evaluating the turbine performance, fall in the first half with the closer agreement.

The variation in the flow direction at the scroll exit is shown for the two cross sectional geometries in Fig. 8. It can be seen from this figure that the flow angles which are referred to the radial direction are larger in the case of a nonsymmetric scroll. These results are helpful in evaluating the effect of the scroll geometry on the turbine performance. The lower peak efficiency of turbines with vaneless nozzles is attributed to the flow angle variations around the rotor periphery, shown in Fig. 9. In the case of radial inflow turbines with vaned nozzles, the stator blades provide the desired flow guidance. Even in this case, the circumferential variation in the flow angles, at the scroll exit, results in different nozzle blades incidence angles. If the variation is large enough to cause their operation far from their design point, the performance of the turbine nozzles will be affected. The scroll exit flow angle measurement of reference [7] could not be used for comparison, since the corresponding scroll geometrical data was not provided.

Downloaded 02 Jun 2010 to 171.66.16.103. Redistribution subject to ASME license or copyright; see http://www.asme.org/terms/Terms_Use.cfm

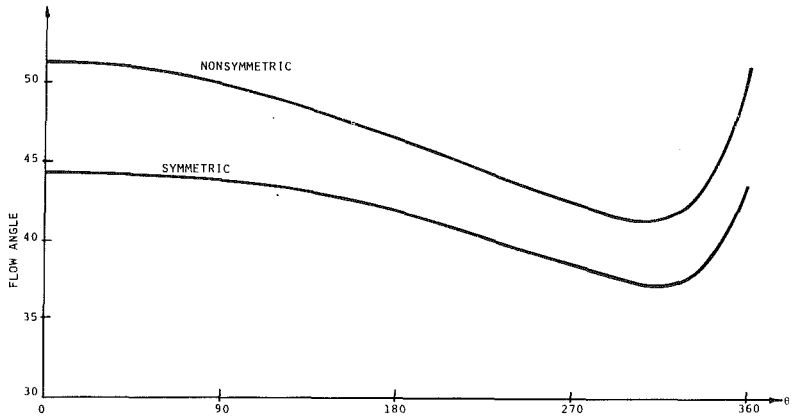

Fig. 9 Flow angle distribution at the scroll exit

Conclusion

A numerical method is presented for solving the three dimensional inviscid flow field in a radial inflow turbine scroll. The computed results compare favorably with the limited amount of flow measurements available. The results of the presented analysis can be very useful to the turbine designer since they provide the variation in the flow velocity magnitude and direction at exit from the scroll. This information is very valuable in evaluating the effect of the scroll geometry on the performance of the subsequent turbine component, and consequently on the overall turbine performance. Experimental flow measurements are very difficult to obtain in the turbine scroll, and, to the authors' knowledge, this is the only theoretical study of the complicated three dimensional flow field in this turbine component.

Acknowledgment

This research work is sponsored by NASA Grant No. NSG 3066, Lewis Research Laboratory, Cleveland, Ohio.

References

1 Tabakoff, W., Sheoran, Y., and Kroll, K., "Flow Measurements in a Turbine Scroll," ASME Paper presented at the 1979 Winter Annual Meeting, New York City, in the Symposium on Flow in Primary, Non-Rotating Passages in Turbomachines.

2 Khalil, I. M., Tabakoff, W. and Hamed, A., "Losses in Radial Inflow Turbines," ASME JOURNAL OF FLUIDS ENGINEERING, Sept. 1976, pp. 364-373.

3 Novak, R. A. and Hearsey, R. M., "A Nearly Three-Dimensional Intrablade Computizing System of Turbomachinery," ASME JOURNAL OF FLUIDS ENGINEERING, Mar. 1977, pp. 154-166.

4 Bosman, C. and El-Shaarawi, M. A. I., "Quasi-Three-Dimensional Numerical Solution of Flow in Turbomachines," ASME Paper No. 76-FE-23, 1976.

5 Katsanis, T., and McNally, D., "Revised Fortran Program for Calculating Velocities and Streamlines on the Hub-Shroud Mid-channel Stream Surface of an Axial-, Radial-, or Mixed-Flow Turbomachine or Annular Duct," NASA TND-3430, 8431, 1977.

6 Katsanis, T., "Fortran Program for Calculating Transonic Velocities in a Blade-to-Blade Stream Surface of a Turbomachine," NASA TND-5427, 1969.

7 Bhinder, F. S., "Investigation of Flow in the Nozzleless Spiral Casing of a Radial Inward-Flow Gas Turbine," *Proc. Insn. Mech. Engrs.*, Vol. 184, Part 3G (11), 1969-1970, pp. 66-71.

8 Wallace, F. J., Baines, N. C., and Whitfield, A., "A Unified Approach to the One-Dimensional Analysis and Design of Radial and Mixed Flow Turbines," ASME Paper No. 76-GT-100, 1976.

9 Hamed, A., Baskharone, E. and Tabakoff, W., "A Flow Study in Radial Inflow Turbine Scroll-Nozzle Assembly," ASME JOURNAL OF FLUIDS ENGINEERING, Vol. 100, Mar. 1978, pp. 31-36.

10 Hamed, A., Abdallah, S., and Tabakoff, W., "Radial Turbine Scroll Flow," AIAA Paper No. 77-714, presented to the AIAA 10th Fluid and Plasma Dynamics Conference, Albuquerque, NM, June 27-29, 1977.

11 Conner, J.J., and Brebbia, C.A., *Finite Element Technique for Fluid Flow,* Butterworth & Co., 1976.

12 Shen, S., "Finite Element Methods in Fluid Mechanics," *Annual Review of Fluid Mechanics,* Vol. 9, 1977, pp. 421-445.

13 Huebner, K., *The Finite Element Method for Engineers,* John Wiley and Sons, 1975.

14 Norrie, D.H., and de Vries, V., *The Finite Element Method Fundamentals and Applications,* Academic Press, 1973.

15 Zienkiewicz, O.C., *The Finite Element Method in Engineering Science,* McGraw-Hill, 1971.

16 Baskhrone, E. and Hamed, A., "A New Approach in Cascade Flow Analysis Using the Finite Element Method," AIAA Paper No. 80-0389, 1980.

17 Gupta, S.K. and Tanji, K.K., "Computer Program for Solution of Large, Sparse, Unsymmetric Systems of Linear Equations," *Int. J. Num. Mech. Engrg.*, Vol. 11, No. 8, 1977, pp. 1251-1259.

Downloaded 02 Jun 2010 to 171.66.16.103. Redistribution subject to ASME license or copyright; see http://www.asme.org/terms/Terms_Use.cfm

Investigation of a Reattaching Turbulent Shear Layer: Flow Over a Backward-Facing Step

J. Kim[1]
S. J. Kline
J. P. Johnston

Department of Mechanical Engineering
Stanford University
Stanford, Calif.

Incompressible flow over a backward-facing step is studied in order to investigate the flow characteristics in the separated shear-layer, the reattachment zone, and the redeveloping boundary layer after reattachment. Two different step-heights are used: $h/\delta_s = 2.2$ and $h/\delta_s = 3.3$. The boundary layer at separation is turbulent for both cases. Turbulent intensities and shear stress reach maxima in the reattachment zone, followed by rapid decay near the surface after reattachment. Downstream of reattachnent, the flow returns very slowly to the structure of an ordinary turbulent boundary layer. In the reattached layer the conventional normalization of outer-layer eddy viscosity by $U_\infty \delta^*$ does not collapse the data. However, it was found that normalization by $U_\infty(\delta - \delta^*)$ does collapse the data to within ± 10% of a single curve as far downstream as $x/x_R \approx 2$, the last data station. This result illustrates the strong downstream persistence of the energetic turbulence structure created in the separated shear layer.

Introduction

Separation of turbulent flows has received a great deal of attention because of its practical importance; nevertheless, it is still far from well understood. Relatively little effort, moreover, has been allocated to flow downstream of separation, and even less to that downstream of reattachment. In many real flows, separation of a boundary layer is followed downstream by reattachment of the separated layer to a solid surface. Understanding the characteristics of reattachment and the redeveloping boundary layer, therefore, becomes a significant problem in engineering applications (e.g., diffuser flows, flows over aircraft wings). In addition, separation and reattachment of a turbulent shear-layer provides a basic flow situation against which many existing theories and models of turbulence can be tested and possibly improved.

The separation-reattachment process is characterized by a complex interaction between the separated shear-layer and the adjacent flow. The most important changes in interaction condition depend on whether the flow is laminar or turbulent at separation and at reattachment. Three different flow regimes are possible: (1) laminar-laminar, where the boundary layer flow is laminar at both separation and reattachment; (2) laminar-turbulent, where flow is laminar at separation and turbulent at reattachment; and (3) turbulent-turbulent, where flow is turbulent at both separation and reattachment. The present experiment belongs to category (3).

Flow over a backward-facing step was used in this study because of its simple geometry. The separation point is fixed by a sharp corner with this geometry. Hence the process of separation-reattachment can be examined without any complexities resulting from motion of the separation point.

Because of the practical importance of predicting base pressure of bluff bodies moving with high speed (such as bullets and coasting missiles), aeronautics researchers have long been interested in the flow over a backward-facing step. Due to the nature of the field, however, much of the work has been done in supersonic flow, where the central problem becomes the shockwave boundary layer interactions. A relatively limited number of studies in low-speed flow over a backward-facing step exists in the literature (see references [1 to 11]. A brief review of the main characteristics of most of the flows and those of some other related flows investigated in the above studies can be found in reference [12].

The purpose of the present study are

- to investigate flow characteristics in the separated shear layer, the reattachment zone, and the redeveloping boundary layer downstream of reattachment;
- to increase understanding of the separation-reattachment process; and
- to obtain new experimental data that may be used to develop computational models.

Experimental Facility

The wind tunnel used in this experiment was the same as that used by Chui and Kline [13], except for the filter box and test section. The filter box described in Hussain and Reynolds [14] was used to insure a supply of clean air needed for hot-wire measurements.

The end of the tunnel was shaped to form a contraction nozzle of ratio 18 to 1. The end of the nozzle was 7.62 cm (3 inches) wide and 60.96 cm (24 in.) high. A new test section

[1] Present address: NASA-Ames Research Center, Moffett Field, Calif.

Contributed by the Fluids Engineering Division of THE AMERICAN SOCIETY OF MECHANICAL ENGINEERS and presented at the Winter Annual Meeting, New York, N.Y., December 2-7, 1979. Manuscript received by the Fluids Engineering Division, April 2, 1979.

Copyright © 1980 by ASME
Downloaded 02 Jun 2010 to 171.66.16.103. Redistribution subject to ASME license or copyright; see http://www.asme.org/terms/Terms_Use.cfm

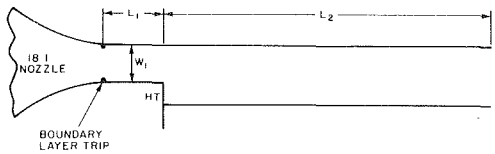

W_1 = INLET WIDTH 3 in. (7.62 cm)
L_1 = INLET LENGTH 12 in. (30.48 cm)
L_2 = TEST SECTION 92 in. (233.68)
HT = ADJUSTABLE STEP HEIGHT 0–8 in. (0–20.32 cm)

Fig. 1 Schematic of test section

was built and attached to the tunnel. The dimensions of the test section are shown in Fig. 1. At the beginning of the inlet, boundary layer trips were placed on each side wall. The trips were carefully machined from phenolic strips to assure that the tripped bounary layer remained two-dimensional.

Pressure was measured by a manometer and a transducer. A Combist micromanometer, using 0.82 s.g. oil with an uncertainty of ± 0.013 mm of water, was used as the standard for pressure measurement. A Validyne DP45 variable reluctance differential pressure transducer, with a diaphragm rating for a maximum pressure of 25.4 mm of water (250 NT/m^2), was calibrated against the micromanometer and used for most of the pressure measurements. The calibration curve of the transducer was checked several times during a run; it was found to be stable and linear within ± 0.025 mm of water.

Since there was a pressure gradient across the shear layer, static pressure variation normal to the wall was also measured. A tubular static pressure probe was made out of 3.18 mm stainless steel tubing. The probe was calibrated against a wall pressure tap in the region where there was no pressure gradient normal to the wall. Total pressure was measured by a C-shaped impact probe made of a 25-gauge (0.51 mm O.D.) hypodermic tubing. This probe was calibrated against a United Sensor and Control Corporation type KA kiel probe.

Thermo-Systems, Inc. (TSI) Model 1050 constant-temperature anemometers together with TSI Model 1052 polynomial linearizers were used as the basic anemometer systems. A TSI Model 1076 RMS meter was used for measurement of turbulence intensities, and multiplications were performed by a DISA Model 52B25 Turbulence Processor to obtain Reynolds shear stress, $\overline{u'v'}$. A TSI Model 1243 boundary layer x-probe of 4-micron, platinum-coated tungsten wire was used for turbulence measurement. This probe was calibrated at the centerline of the channel at the reference point (x = -15.24 cm[2]), where the velocity is uniform across the central region of the channel; the calibration was performed each time before the measurement to minimize the effect from the variation of the ambient temperature of the tunnel.

A special unit was designed and built to measure the intermittency directly. A description of the unit can be found in Kim, et al. [12]. As a qualification test, intermittency of a flat-plate turbulent boundary layer was measured and compared with that obtained by Fiedler and Head [15]. The two results were in good agreement.

Experimental Conditions

The experiment was performed with two different step-heights, 3.81 cm (1.5 in.) and 2.54 cm (1 in.), which are labeled REF and STEP-1, respectively. These step-heights gave aspect ratios (step span to height, b/h) of 16 and 24, respectively, which are higher than the value 10 recommended by de Brederode and Bradshaw [7] as the minimum to assure two-dimensionality of flow in the central region, away from the end-wall bondary layers. The reference dynamic pressure, measured in the inviscid core at the reference point, was kept the same for both experiments at a value of 20.3 mm of water. The reference speed, therefore, varied slightly, depending upon atmospheric conditions in the laboratory. The typical reference speed was 18.2 m/s, with a variation less than 0.15 m/s throughout the experiment. The velocity profile at the reference point (x = -15.24 cm) was that of an equilibrium turbulent flat-plate profile, and the boundary layer displacement thickness at that point was 1.04 mm for both experiments. Reynolds number based on the momentum thickness at separation (x = 0) was about 1.3×10^3.

Experimental Results

Tufts and a mixture of oils were used to visualize the flow field and to determine the reattachment zone. Only a small part of the separated flow (about one step-height length in the middle of the recirculating zone) at $x/h \approx 3$ was found to be steady. Most of the recirculating zone contained unsteady flow, even though it is often called the "dead air zone." Near reattachment, flow was highly unsteady and the tufts moved forward and backward continuously, indicating the variation of the instantaneous reattachment length. The mean distance to reattachement was found to be $x_R/h = 7 \pm 1$. A series of still photographs of the tufts revealed the instantaneous reattachment length was not a straight line across the span; however, it was a straight line in the mean, as indicated by wall oil-flow visualization. This might be indicative of the existence of a three-dmensional spanwise structure near reattachment, but this suggestion was not investigated in detail (see reference [16] for further study).

The wall-static pressure on the step side of the channel for

[2] The step location, x = 0.

Nomenclature

b = channel height (span)
C_p = static pressure coefficient
h, HT = step height
l = turbulent mixing length
p = static pressure
Re_θ = Reynolds number based on θ, $U_\infty \theta/\nu$
U, u = mean velocity in x-direction
u' = turbulent fluctuation in x-direction
u_τ = wall shear velocity $(\tau_w/\rho)^{1/2}$
u^+ = u/u_τ
v' = turbulent fluctuation in y-direction
W_1 = inlet channel width
x = coordinate in streamwise direction
y = coordinate normal to the wall
y^+ = yu_τ/ν
γ = intermittency of turbulence
δ = boundary layer thickness
δ^* = displacement thickness
θ = momentum thickness
ν = kinematic viscosity
ν_T = eddy viscosity
τ = turbulent shear stress $(= -\rho\overline{u'v'})$

Subscripts

s = value at separation
R = value of reattachment
o = reference condition (x = − 15.24 cm)
∞ = free-stream value

Downloaded 02 Jun 2010 to 171.66.16.103. Redistribution subject to ASME license or copyright; see http://www.asme.org/terms/Terms_Use.cfm

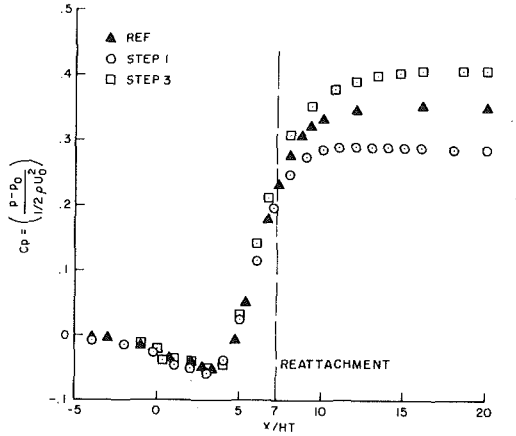

Fig. 2 Step-side pressure distributions for different step-heights

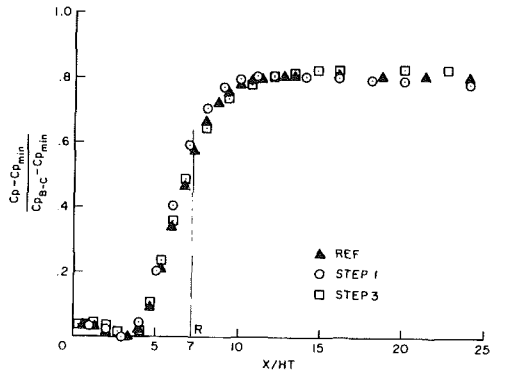

Fig. 3 Normalized pressure coefficients

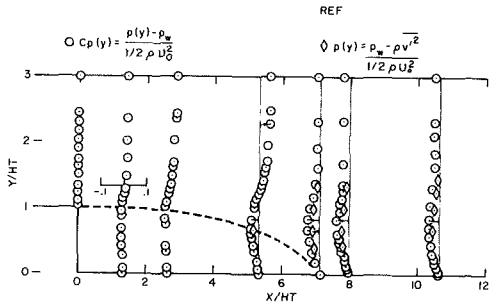

Fig. 4 Static pressure variation across the channel

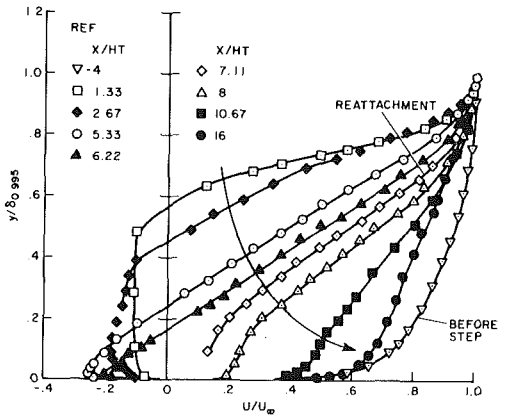

Fig. 5 Velocity profiles on the step-side: U/U_∞ versus y/δ

three different step-heights is shown in Fig. 2.[3] In this figure, the static pressure is plotted in the form of the pressure coefficient,

$$C_p = \frac{p - p_0}{\frac{1}{2}\rho U_0^2} \tag{1}$$

where p_0 and U_0 are the reference pressure and the free stream velocity, respectively, measured at x = - 15.24 cm. The streamwise distance x measured along the surface has its origin, $x = 0$, at the step and is non-dimensionalized by the step heights. Pressure increases for a short distance beyond the reattachment; the final pressure recovery is a function of downstream channel width. In an attempt to normalize the variations due to the different channel widths. A new normalized pressure coefficient was defined as

$$C_p = \frac{C_p - C_{p_{\min}}}{C_{p_{B-C}} - C_{p_{\min}}} \tag{2}$$

where $C_{p_{B-C}}$ is the Broda-Carnot pressure coefficient.[4] The normalizaton (2) reduces the data to a single curve, as shown in Fig. 3.

The static pressure variation across the channel is shown for the REF case in Fig. 4. The static pressure data were not corrected for turbulence effect because the effect of turbulence on the static pressure reading is not well understood. In order to show the variation of the static pressure normal to the surface, the pressure coefficient was defined as

$$C_p(t) = \frac{p(y) - p_w}{\frac{1}{2}\rho U^2_0} \tag{3}$$

where p_w is the static pressure on the surface at a given streamwise location.

The mean velocity profiles on the step-side of the channel are shown in Fig. 5. The parts of the velocity profiles in the recirculating region were obtained by placing the total pressure probe with its mouth facing the direction of local mean flow. This procedure will of course not give true reversed velocity if the flow changes its direction during the measurement, and in fact the flow changes its direction continuously near reattachment. No attempt to correct for this effect was made in the present experiment,[5] and the experimental uncertainty[6] (20:1 odds) in the measurements of the region of reversed flow was estimated to be about 10% of the measured values. In Fig. 6, the mean velocity profiles downstream of reattachment are plotted in terms of the non-dimensionalized variables, u^+ versus y^+. Wall shear stress, u_τ, was determined by the "cross-plot" method.[7] (Wall shear stresses measured by a Preston tube did not differ more than 5 percent from the value obtained by this method.)

Turbulence profiles along the channel are shown in Fig. 7.

[3] Data for STEP-3, the 7.62 cm step-height, were provided by J. Eaton, using the same apparatus and technique.

[4] $C_{p_{B-C}} \triangleq 2 \frac{1}{AR}\left(1 - \frac{1}{AR}\right)$,

Where AR is the area ratio between upstream and downsteam of the channel.

[5] Such measurements are being pursued in a later study by J. Eaton, to be reported separately.

[6] The experimental uncertainties were estimated following the procedure of Kline and McClintock [17].

[7] The wall shear stress is found by forcing data points to match the logarithmic profile ($u^+ = (1/0.41 \cdot \ln y^+ + 5.0)$ over the range of y^+ of 50 to 170. See Schraub and Kline [18] for details.

Downloaded 02 Jun 2010 to 171.66.16.103. Redistribution subject to ASME license or copyright; see http://www.asme.org/terms/Terms_Use.cfm

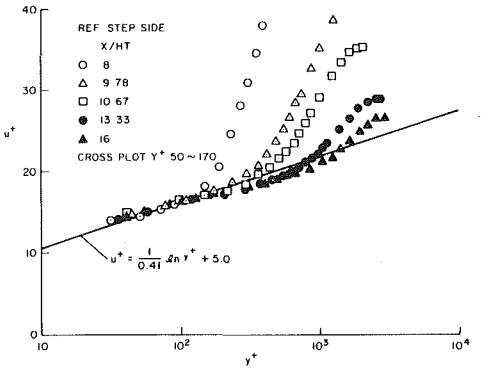

Fig. 6 Mean velocity profiles (step-side): y^+ versus u^+

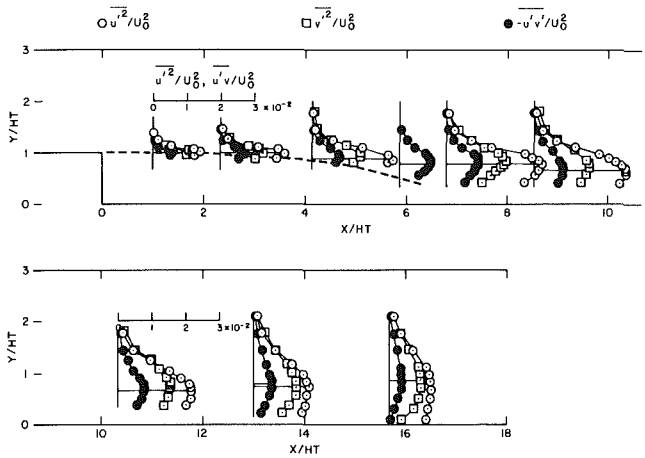

Fig. 7 Turbulent profiles along the channel (REF) (Tabulated data are available in reference [12])

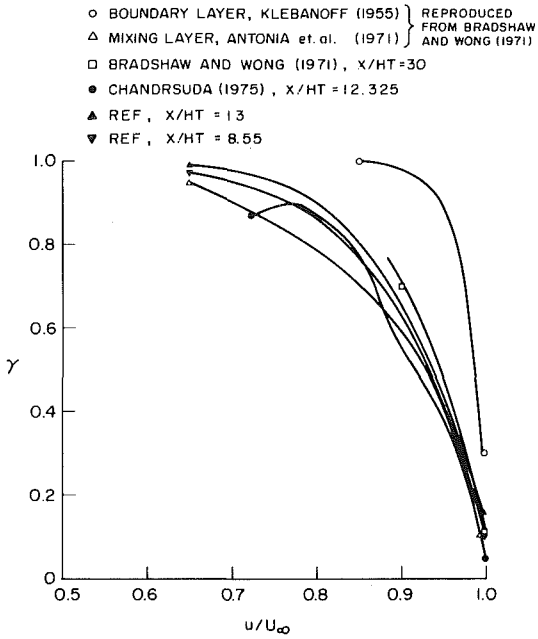

Fig. 8 Comparison of profiles of intermittency

The turbulence measurements were not made in the regions where significant errors were expected, due to signal rectification as a result of the directional insensitity of the hot-wire. At the lowest point of transverse in the figure, $\sqrt{\overline{u'^2}}/U$ was about 40 percent and $\sqrt{\overline{u'^2}_{\max}}/U$ was about 30 to 40 percent. The estimated experimental uncertainties of $\overline{u'^2}$, $\overline{v'^2}$, and $\overline{u'v'}$ were less than 10 percent of the measured values in the region where $\sqrt{\overline{u'^2}}/U$ was less than 0.2, while the uncertainties were about 20 percent when $\sqrt{\overline{u'^2}}/U$ was about 0.4

Intermittency, γ, was measured using $d/dt(u'v')$ as a criterion function. After Bradshaw and Murlis [19], the "signal-or-derivative" approach is used to separate turbulent and nonturbulent flow—that is, flow is declared to be turbulent if either the signal or its derivative exceeds a preset threshold (see Kim, et al. [12] for details). Intermittency profiles of a mixing layer, the redeveloping boundary layer downstream of reattachment, and an ordinary turbulent boundary layer are shown in Fig. 8.

Discussion of Experimental Results

The general flow characteristics hardly changed for the two different step-heights. The effect of change in Reynolds number over a limited range was negligible; this is consistent with previous results obtained by Tani, et al. [1], Abbott and Kline [3], and Chandrsuda [9]. This finding is in constrast to the case of laminar separation with laminar reattachment or laminar separation, where transition does not occur near the step edge. In these cases, flow depends on the step-height and Reynolds number, as observed by Moore [2] and Goldstein et al. [5].

At least for narrow channels where $W_1/h \approx 1$,[8] the values of mean reattachment length $x_R/h = 7 \pm 1$ seem to be universal when flow is turbulent at separation or when the transition to turbulence occurs very close to separation. The flow near reattachment is unsteady, however, and the instantaneous reattachment point is not fixed but moves around within a range. Hence, it seems more appropriate to refer to it as a reattachment "zone" rather than a reattachment point. Since the reattachment length is related directly to the entrainment rate, this suggests that entrainment in the mixing layer does not take place at a uniform rate, but fluctuates. Note that a higher entrainnment rate results in a smaller reattachment length, and vice versa. This is consistent with the observation that distance to reattachment may be quite long for laminar-laminar cases.

As mentioned previously, normalization using a parameter $\hat{C}_p$ reduces the wall pressure data to a single curve. Hence the correlation can be used for an estimation of the pressure recovery of similar geometries, since $C_{p_{B-C}}$ is known for a given geometry and $C_{p_{\min}}$ varies only slightly.

Static pressure increases beyond reattachment, as shown in Fig. 3. This effect can be explained by evaluating the x-momentum equation on the surface; this yields a balance between pressure force and shear force. That is,

$$\frac{1}{\rho}\frac{\partial p}{\partial x} = \frac{\partial \tau}{\partial y} \tag{4}$$

where τ is the total shear stress. In the zone of reattachment this requires positive $\partial p/\partial x$, because the shear stress rises from a typical boundary layer value to a typical mixing layer value near the surface.

The variation of the static pressure across the channel (see Fig. 4) has two causes: the streamline curvature and the high turbulence intensity. The effect of turbulence on the pressure

[8] Examination of other cases (see reference [12] for $\mathrm{Re}_{\theta_s} \gtrsim 1000$ and strong to overwhelming perturbation ($\delta_s < h$) shows that distance to reattachment also depends upon channel width to step-height, W_1/h. For channels like ours ($W_1/h \approx 1$), $x_R \approx 7$, but for very wide channels ($W_1/h \approx 10$), shorter reattachment lengths are typical, e.g., $x_R/h \approx 5.5$ to 6.0. This effect is believed to result from viscid-inviscid flow outside the reattaching shear geometry changes which affect the inviscid flow outside the reattaching shear layer more than they affect the turbulence structure itself.

Downloaded 02 Jun 2010 to 171.66.16.103. Redistribution subject to ASME license or copyright; see http://www.asme.org/terms/Terms_Use.cfm

can be obtained form the y-momentum equation. With the usual boundary layer approximation to the Navier-Stokes equation, but including the turbulence term, the y-momentum equation reduces to

$$\frac{\partial p}{\partial y} = -\frac{\partial}{\partial y}\rho\overline{v'^2} \tag{5}$$

or

$$p(y) = p_w - \rho\overline{v'^2} \tag{6}$$

The y-variation of the static pressure coefficent due to the turbulent fluctuations then becomes

$$C_p(y) = \frac{p(y) - p_w}{\frac{1}{2}U_0^2} = -2\frac{\overline{v'^2}}{U_0^2} \tag{7}$$

This effect is shown by the diamond-shaped points in Fig. 4. Near reattachment a large portion of the cross-term variation of static pressure appears to be caused by the turbulent fluctuations. At $x/h = 7.1$, for example, the maximum variation of $C_p(y)$ is about 6 percent of $(1/2)\rho U_0^2$; of this, 4 percent appears to be caused by the turbulent normal stress, $\rho\overline{v'^2}$. Far downstream of reattachnent, most of the variation is accounted for by the turbulence effect.

The mean velocity profiles shown in Fig. 5 exhibit the typical features of flow over a backward-facing step. The velocity profile before the step is that of an ordinary turbulent boundary layer with shape factor $H = \delta^*/\theta = 1.4$. The magnitude of reversed velocities in the recirculating flow is on the order of 10 to 20 percent of U_0; this result agrees with Tani, et al. [1] and Chandrsuda [9]. The maximum reversed velocity measured is about 25% of free-stream velocity. Downstream of reattachment, the velocity profile returns toward the ordinary turbulent boundary layer. The inner part of the profile relaxes rather quickly, while the outer part requires a surprisingly long distance. The rapid increase of the velocity near the surface downstream of reattachment and the slow response of the layer away from the surface produce an appreciable decrease in mean-velocity gradient in the region above $y^+ \approx 100$. This results in a marked dip in the data below the universal inner-layer profile, this logarithmic law, as shown in Fig. 6, indicating that the flow here is not in local equilibrium. It appears that the local wall-shear velocity, u_τ, which is used as an inner-layer scaling in the local equilibrium flow, is no longer the proper inner velocity scale throughout the layer, since only the velocity very close to the surface adjusts rapidly to the sudden change of the boundary condition, i.e., the reattachment. The velocity away from the surface, on the other hand, responds slowly to the change, causing the dip below the log-law.

The lower velocity gradient is rather puzzling, as pointed out by Bradshaw and Wong [6], since the local equilibrium formula,

$$\frac{\partial U}{\partial y} = \frac{(\tau/\rho)^{1/2}}{\kappa y} \tag{8}$$

would give a velocity gradient even higher than the logarighmic value $(\tau_w/\rho)^{1/2}/\kappa y$ obtained from the log-law in the region $y/\delta < 0.2$, and the formula should hold, since τ is increasing away from the surface. They suspected that the turbulent length scale in the region may not be κy, but rather that it will increase much more rapidly with y. The turbulent mixing length was obtained from the results of the present experiment and is shown in Fig. 9. The mixing length is found to be much larger than κy at $y/\delta < 0.2$. This is understandable, because part of the separated shear layer, which

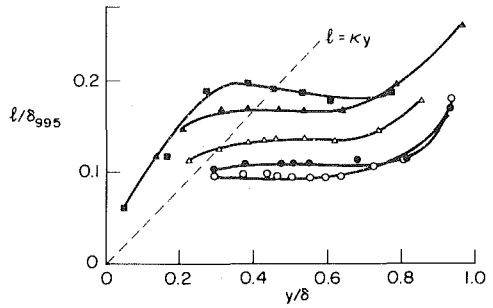

Fig. 9 Turbulent mixing length downstream of reattachment -- REF

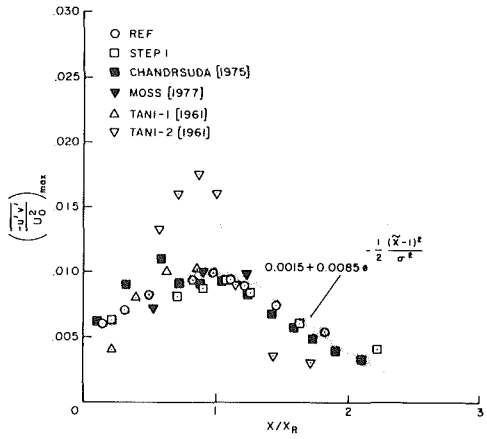

Fig. 10 Distribution of maximum shear stress

has a larger mixing length than the usual attached layer value near the surface, comes very close to the surface as the flow proceeds through reattachment. Therefore, the turbulent length scale can be very large, very close to the surface, even though it decreases to zero at the surface. The result is a mean-velocity gradient lower than that predicted by equation (8), and hence the dip in u^+ below the log-law, as shown in Fig. 6.

The lines which denote the locations of maximum turbulent energy and shear stress coincide with the dividing streamline initially; they deviate outward as the reattachment is approached. Downstream of reattachment near the surface, strong, local, longitudinal rates of strain, $\partial U/\partial x$, increase $\overline{v'^2}$ and $\overline{w'^2}$ and decrease $\overline{u'^2}$. Because of this effect, the difference in the magnitude between $\overline{u'^2}$ and $\overline{v'^2}$ decreases downstream of reattachment. The area between profiles of $\overline{u'^2}$ and $\overline{v'^2}$ in Fig. 7 represents

$$\int_0^\delta (\overline{u'^2} - \overline{v'^2})\, dy,$$

whose streamwise gradient appears in the momentum integral equation. It is apparent that

$$\frac{\partial}{\partial x}\int_0^\delta (\overline{u'^2} - \overline{v'^2})\, dy$$

is not negligible near reattachment. The measurements of the present experiment do not allow accurate quantitative evaluation of this term; however, it should be included in the momentum integral equation if this equation is used for analysis.

The maximum values of turbulent intensities and shear stress have a consistent trend, i.e., a monotonic increase toward a peak value at a station very close to reattachment, followed by a rapid decay downstream of reattachment suggesting a significant change in the structure of the shear layer. At $x/h = 15.67$, the shear stress drops to less than half its value at reattachment. The streamwise variation of the

Downloaded 02 Jun 2010 to 171.66.16.103. Redistribution subject to ASME license or copyright; see http://www.asme.org/terms/Terms_Use.cfm

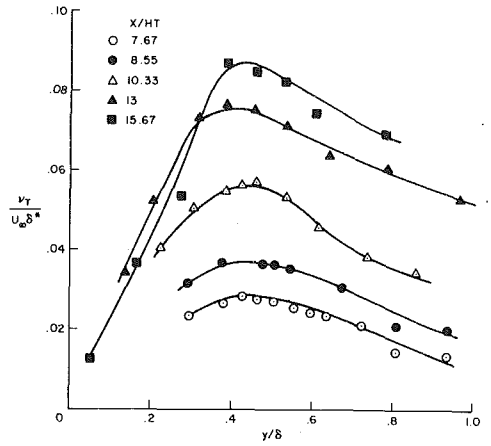

Fig. 11 Nondimensionalized eddy viscosity (REF) using typical correlation

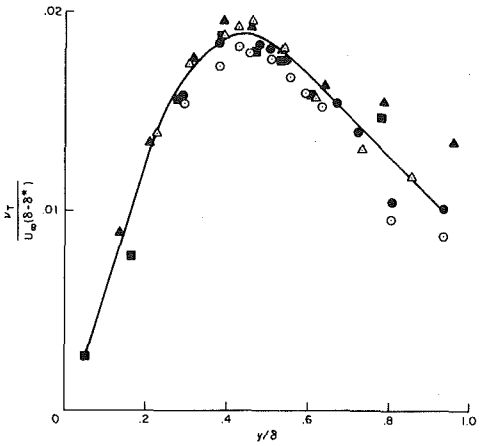

Fig. 12 Nondimensionalized eddy viscosity (REF) using new correlation

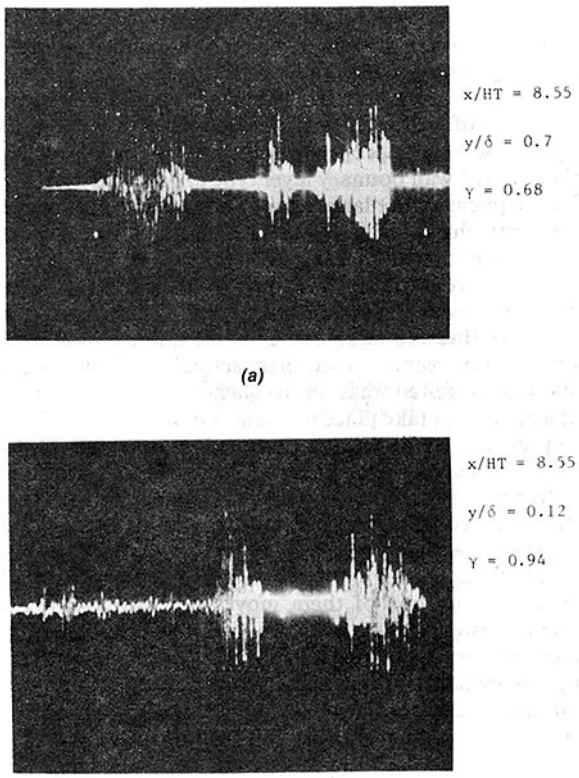

Fig. 13 Photographs of $d/dtu'v'$ from oscilloscope fall

maximum shear stress from different experiments is shown in Fig. 10. $\bar{x}$, defined as x/x_R, is used as the abscissa in order to normalize the variation in the reattachment length. Except for the case of Tani-2, it is seen that the data can be approximated fairly well by a Gaussian curve, drawn such that it has a maximum value of $(-\overline{u'v'}/U_0^2)_{max} = 0.1$ at reattachment and approaches a value of $(-\overline{u'v'}/U_0^2)_{max} = 0.0015$ far downstream of reattachment. This correlation has been used successfully in the computation of the flow over a backward-facing step [12].

The eddy viscosity, defined as $\nu_T = -\overline{u'v'}/(dU/dy)$, is shown in Fig. 11 for the attached flow downstream of reattachment. The eddy viscosity is non-dimensionalized in terms of $U_\infty \delta^*$, the method typically used for attached boundary layers close to equilibrium. This procedure usually colllapses the eddy viscosities in the outer 80 percent of the layer into a nearly universal curve which varies only slightly with pressure gradients. It is apparent in Fig. 11 that this type of collapse does not occur downstream of reattachment. A new non-dimensionalization was therefore formed in terms of $U_\infty (\delta - \delta^*)$, as shown in Fig. 12. (Note that the regression line is drawn through the data as a visual aid.) The result of this new nondimensionalization looks quite satisfactory. It is universal to within the experimental uncertainty. The failure of the conventional correlation is due to the unusual nature of the redeveloping boundary layer downstream of reattachment. In most flow, δ^* increases as U_∞ decreases, so that $U_\infty \delta^*$ tends to remain unchanged. Downstream of reattachment, however, both U_∞ and δ^* decrease and consequently $\nu_T/U_\infty \delta^*$ increases. The new scaling length $(\delta - \delta^*)$, increases downstream of reattachment; it seems to be an appropriate choice for a new characteristic length. Computational results using this correlation have been very satisfactory in predicitng flows downstream of reattachment (see reference [12]).

The characteristics of the outer-layer structure, which is dominated by large turbulent eddies, can be compared to those of other turbulent shear flows by examining the intermittency profiles. Intermittency profiles of different shear flows are shown in Fig. 8. The profiles of the reattaching flow lie between those of the free mixing layer and the ordinary turbulent boundary layer, and they develop very slowly toward the profile of an ordinary boundary layer. The outer layer of reattaching flow is dominated by large and energetic eddies typical of free shear layer flow. These eddies have a relatively long lifetime and carry the "history effect" of the upstream flow. Hence the outer layer takes a relatively long time to return to the ordinary structure of a turbulent boundary layer. Fig. 8 manifests the slow return to the ordinary structure.

The criterion function used for the intermittency measurements, i.e., $d/dt(u'v')$. was monitored through an oscilloscope during the measurement. Typical results are shown in Fig. 13. The characteristic of intermittent turbulent flow is seen in the first figure, which was taken at the outer edge of the shear layer at $x/h = 8.55$ and $y/\delta = 0.7$. The intermittency at this point was about 0.6. The lower picture was taken at $x/h = 8.55$ and $y/\delta = 0.12$. Note that $x/h = 8.55$ is downstream of but close to reattachment. Two different structures are seen in the signal at $y/\delta = 0.12$; they seem to represent two different turbulent flows (measured intermitendency was close to 1.0). The bigger spikes have the same structure as the approaching shear layer; however, the small spikes seems to be the structure of the normal boundary layer. This structure (that is, a signal which is intermittent between two different forms of turbulence) contrasts sharply

Downloaded 02 Jun 2010 to 171.66.16.103. Redistribution subject to ASME license or copyright; see http://www.asme.org/terms/Terms_Use.cfm

with the intermittency of an ordinary boundary layer, which is intermittent between turbulent and non-turbulent zones of fluid. It appears that this might be the reason for the rapid decay of $-\overline{u'v'}$ and other time-averaged turbulent intensities downstream of reattachment, since, through the time-averaged process, the properties of the free shear layer type and those of the wall bounary layer type are averaged out.

What happens to the large eddies in the approaching shear layer at reattachment is not yet clear. Bradshaw and Wong [6] suggested that the large eddies are torn into two parts at reattachment, resulting in a significant decrease in the turbulent length scale downstream of reattachment. Another possibility is that the large eddies move alternatively downstream and upstream, rather than actually splitting. Chandrsuda [9] suggested that both phenonmena seems to be possible, and both take place in a random fashion. The results of the present experiment, e.g., unsteady movements of tufts near the reattachment zone and the structure of $d/dt(u'v')$ downstream of reattachment, seem to support the hypothesis of alternating eddies; the probe downstream of reattachment should see the large spikes in Fig. 13 *continuously,* if the large eddies in the approaching shear layer were torn in two at reattachment and one of them moves downstream of reattachment. However, the evidence presented here does not exclude the hypothesis of splitting, nor of the existence of both phenomena. All that can be said at this point about the fate of large eddies is that it is unlikley that the splitting is the only phenomenon that takes place at reattachment.

Summary

Measurements were made in a low-speed flow over a backward-facing step. Although the instruments used in his study prevented extensive measurements in the recirculating flow (and also included a rather high experimental uncertainty), the present experimental study shows several features of the complex separation/reattachment process and the redeveloping boundary layer. Turbulent intensities and shear stress reach maxima in the reattachment zone, followed by rapid decay near the surface after reattachment. The very high time-averaged values of $\overline{u'v'}$ followed by the rapid decay downstream seem to be caused by the intermittent structure of the turbulence downstream of reattachment. Downstream of reattachment, the flow returns very slowly to the structure of an ordinary turbulent boundary layer. In the inner layer, the rapid adjustment of the velocity profile close to the surface causes a low mean-velocity gradient and, consequently, the dip below, the universal log-law. Eddy viscosity normalized by $\nu_T/U_\infty(\delta-\delta^*)$ is reduced to a single curve downstream of reattachment; however, the usual normalization using $\nu_T/U_\infty\delta^*$ does not collapse the data.

References

1 Tani, I., M. Iuchi, and H. Komodo, "Experimental Investigation of Flow Separation Associated with a Step or Groove," Report No. 364, 1961, Aeronautical Research Institute, University of Tokyo.

2 Moore, T. W. F., "Some Experiments on the Reattachment of a Laminar Boundary Layer Separating from a Rearward-Facing Step on a Flat Plate Aerofoil," *Journal of Royal Aeronautical Society,* Vol. 64, 1960, pp. 668-672.

3 Abbott, D. E., and S. J. Kline, "Theoretical and Experimental Ivestigation of Flow over Single and Double Backward-Facing Steps," MD-5, June 1961, Thermosciences Division, Dept. of Mechanical Engineering, Stanford University.

4 Mueller, T. J., and J. M. Robertson, "A Study of Mean Motion and Turbulence Downstream of a Roughness Element," *Proceedings of the First Southeastern Conference on Theoretical and Applied Mechaincs,* Galinberg, Tenn., 1962.

5 Goldstein, R. J., V. L. Eriksen, R. M. Olson, and E. R. G. Eckert," Laminar Separation, Reattachment, and Transition of Flow over a Downstream-Facing Step," *Journal of Basic Engineering,* Vol. 92, No. 4, 1970, pp. 732-741.

6 Bradshaw, P., and F. Y. F. Wong, "The Reattachment and Relaxation of a Turbulent Shear Layer," *Journal of Fluid Mechanics,* Vol. 52, Part 1, 1972, pp. 113-135.

7 de Brederode, U., and P. Bradshaw, "Three-Dimensional Flow in Nominally Two-Dimensional Separation Bubbles. I. Flow Behind a Rearward-Facing Step," IC Aero Report 72-19, 1972, Imperial College of Science and Technology.

8 Rothe, P. H., and J. P. Johnston, "The Effects of System Rotation on Separation, Reattachment, and Performance in Two-Dimensional Diffusers," PD-17, 1975, Thermosciences Division, Dept. of Mechanical Engineering, Stanford University.

9 Chandrsuda, C., "A Reattaching Turbulent Shear Layer in Incompressible Flow," Ph.D. thesis, 1975, Dept. of Aeronautics, Imperial College of Science and Technology.

10 Moss, W. D., S. Baker, and L. J. S. Bradbury, "Measurements of Mean Velocity and Reynolds Stresses in Regions of Recirculating Flow," presented at Symposium on Turbulent Shear Flows, Pennsylvania State University, 1977.

11 Etheridge, D. W., and P. H. Kemp, "Measurements of Turbulent Flow Downstream of a Rearward-Facing Step," *Journal of Fluid Mechanics,* Vol. 86, Part 3, 1978, pp. 545-566.

12 Kim, J., S. J. Kline, and J. P. Johnston, "Investigation of Separation and Reattachement of a Turbulent Shear Layer: Flow over a Backward-Facing Step," MD-37, 1978, Thermosciences Division, Dept. of Mechanical Engineering, Stanford University.

13 Chui, G. K., and S. J. Kline, "Investigation of a Two-Dimensional, Fully Stalled Turbulent Flow Field," MD-19, 1967, Thermosciences Division, Dept. of Mechanical Engineering, Stanford University.

14 Hussain, A. K. M., and W. C. Reynolds, "The Mechanics of a Perturbation Wave in Turbulent Shear Flow," FM-6, 1970, Thermosciences Division, Dept. of Mechanical Engineering, Stanford University.

15 Fielder, H., and M. R. Head, "Intermittency Measurements in Turbulent Boundary Layer, *Journal of Fluid Mechanics,* Vol. 25, Part 4, 1966, pp. 719-735.

16 Eaton, J. K., J. P. Johnston, and A. H. Jeans, "Measurements in a Reattaching Turbulent Shear Layer," presented at the Second Symposium on Turbulent Shear Flows," July 2-4, 1979, Imperial College of Science and Technology, London, England.

17 Kline, S. J., and. A. McClintock, "Describing Uncertainty in Single-Sample Experiments," Mechanical Engineering Department, Stanford University, Jan. 1953.

18 Schraub, F. A., and S. J. Kline, "A Study of the Structure of the Turbulent Boundary Layer with and without Longitudinal Pressure Gradients," MD-12, March 1965, Thermosciences Division, Dept. of Mechanical Engineering, Stanford University.

19 Bradshaw, P., and J. Murlis, "On the Measurement of Intermittency in Turbulent Flow," IC Aero Report 74-04, March 1974, Dept. of Aeronautics, Imperial College of Science and Technology, London, England.

Downloaded 02 Jun 2010 to 171.66.16.103. Redistribution subject to ASME license or copyright; see http://www.asme.org/terms/Terms_Use.cfm

Transonic Inlet Flow Calculations Using a General Grid-Generation Scheme[1]

L. T. Chen
Research Scientist.

D. A. Caughey[2]
Consultant.

McDonnell Douglas Research Laboratories,
McDonnell Douglas Corporation,
St. Louis, Mo. 63166

Finite difference solutions for transonic flowfields about engine inlet nacelles are obtained by combining a general grid-generation scheme with a previously developed general solver for transonic potential flowfields (1). The grid-generation scheme is similar to Thompson's method, but uses simpler equations to solve for the mesh coordinates. An extrapolated relaxation procedure is used to obtain improved convergence of the transonic solution to small residuals. Results obtained for flowfields with embedded supersonic regions both outside and inside the inlets compare well with experimental results.

Introduction

The transonic flowfield about a nacelle must be determined to predict both the drag associated with the engine inlet and the aerodynamic properties at the entry face of the compressor. Because of the increasing complexity of inlet designs for advanced fighter and transport aircraft, a general, flexible method capable of treating arbitrary geometries is desirable.

After Murman and Cole originated the idea of type-dependent differencing to solve the transonic small disturbance equation [2] and other investigators (for example, references [3-6]) extended it to solve the full potential equation, relaxation methods have been extensively used to compute transonic potential flowfields about engine inlets. Colehour [6] transformed the equation to the complex potential plane of the incompressible flow through the inlet, introducing the incompressible streamlines and potential lines as independent variables. This transformation is attractive because it is boundary-conforming and orthogonal, and the flow direction is always nearly parallel to a coordinate direction in the transformed plane. However, the method introduces a spurious singularity that forces the compressible and incompressible stagnation points to coincide. Arlinger [7] used a sequence of conformal mappings to generate a rectangular computational domain in which the governing equation was solved. Caughey and Jameson [8] solved the same problem using a sequence of simpler transformations and studied ways to accelerate the iterative scheme used to solve the difference equations.

The methods presented in references [6—8] perform a global transformation of the governing equation, a tedious task which frequently results in complicated equations. Reyhner [9, 10] followed the alternative approach of solving the full potential equation in a Cartesian mesh. An interpolation scheme is used to treat the body boundary condition. Because of the variety of mesh-surface intersections that must be considered, especially in three-dimensional problems, the complexity of the program logic becomes a major drawback to the application of this method.

Chen and Caughey [1, 11] developed a scheme which locally transforms the governing equation, similar to the finite volume methods suggested by Caughey and Jameson [12, 13]. This use of purely local coordinate transformations completely uncouples the grid-generation step from the solution of the governing equation in any body-oriented coordinate system, enabling the method to be appleid to rather general geometries. In reference [1], a mapping technique was used to generate the required computational mesh. The meshes generated by any analytical method are limited to certain applicable geometries. In order to improve and extend the work of reference [1] to more general problems, a general grid-generation method will be presented.

It was found in reference [1] that the convergence rate of the relaxation solution depends not only on the mesh size but also on the mass flow ratio. In order to obtain covergent solutions for the flowfields inside nacelles at high mass-flow ratios, an extrapolated relaxation scheme (8) is applied to accelerate the relaxation process.

Numerical results have been obtained for flowfields with embedded supersonic regions both inside and outside the nacelle, and compared with experimental data. Solutions for flowfields with embedded supersonic regions inside the inlet are sensitive to any numerical inaccuracy because the flow is nearly choked; such solutions could not be obtained by the methods of reference [1]. The meshes used in reference [1] were highly distorted near the hub surface and at downstream infinity inside the nacelle. With the present improved mesh-generation scheme, this difficulty is overcome.

[1] This work was supported by the McDonnell Douglas Independent Research and Development Program.

[2] Permanent Address: Cornell University, Sibley School of Mechanical and Aerospace Engineering, Ithaca, N.Y.

Contributed by the Fluids Engineering Division of THE AMERICAN SOCIETY OF MECHANICAL ENGINEERS and presented at the Winter Annual Meeting, New York, N.Y., December 2-7, 1979. Manuscript received by the Fluids Engineering Division, April, 1979.

Copyright © 1980 by ASME

Downloaded 02 Jun 2010 to 171.66.16.103. Redistribution subject to ASME license or copyright; see http://www.asme.org/terms/Terms_Use.cfm

Grid-Generation

The use of the local coordinate transformation methods of references [1] and [11–13] makes it possible to incorporate any general grid-generation scheme with the algorithm for solving the potential equation in the transonic regime. Here a general grid-generation scheme similar to, but simpler than, that proposed by Thompson, et al. [14] will be described.

A conceptually simple way to generate body-oriented coordinate systems is through a sequence of conformal and shearing transformations. In practice, this analytical approach becomes complicated for complex geometries because of the large number of transformations in sequence, and thus is limited to those geometries for which the sequence can be carried out. A numerical approach, suggested by Thompson, et al. [14] is capable of treating essentially arbitrary geometries, but requires considerable machine resources to generate the mesh, and the mesh may contain undesirable features, such as a high degree of nonorthogonality. The method described here is nearly as general as Thompson's, but is simpler to implement and results in grids that are more nearly orthogonal.

The basic idea of the present method is to try to generate numerically a coordinate transformation that is nearly conformal. The transformation is obtained by solving, either uncoupled or coupled, Laplace's equations for the physical coordinates subject to a choice of boundary values that is nearly consistent with the requirements of conformality. Let ξ and η be the real and imaginary parts of an analytic function $Z = \xi + i\eta$ of the complex variable $z = x + iy$, where x and y are coordinates in the physical domain. The Cauchy-Riemann conditions thus require

$$\frac{\partial \xi}{\partial x} = \frac{\partial \eta}{\partial y} \tag{1}$$

and

$$\frac{\partial \xi}{\partial y} = \frac{\partial \eta}{\partial x}. \tag{2}$$

Equivalently,

$$\frac{\partial x}{\partial \xi} = \frac{\partial y}{\partial \eta} \tag{3}$$

and

$$\frac{\partial x}{\partial \eta} = -\frac{\partial y}{\partial \xi}. \tag{4}$$

Equations (1) and (2) can be differentiated and combined to yield

$$\frac{\partial^2 \xi}{\partial x^2} + \frac{\partial^2 \xi}{\partial y^2} = 0 \tag{5}$$

$$\frac{\partial^2 \eta}{\partial x^2} + \frac{\partial^2 \eta}{\partial y^2} = 0. \tag{6}$$

Thompson, et al. [14] modified equations (5) and (6) by the addition of a source term on the right side to control mesh stretching or clustering, then re-cast them in the computational coordinates ξ and η to give

$$(x_\eta^2 + y_\eta^2)x_{\xi\xi} - 2(x_\xi x_\eta + y_\xi y_\eta)x_{\xi\eta} + (x_\xi^2 + y_\xi^2)x_{\eta\eta} = P_1(\xi,\eta) \tag{7}$$

$$(x_\eta^2 + y_\eta^2)y_{\xi\xi} - 2(x_\xi x_\eta + y_\xi y_\eta)y_{\xi\eta} + (x_\xi^2 + y_\xi^2)y_{\eta\eta} = P_2(\xi,\eta), \tag{8}$$

where subscripts ξ and η denote differentiation with respect to ξ and η, respectively. Solving these two equations has almost the same degree of difficulty as solving the transonic flow problem; Holst [15] used these equations to generate a mesh for two-dimensional transonic flow problems and indicated that despite his use of an efficient approximate factorization method, the mesh-generation step required approximately the same amount of CPU time as the transonic flow calculation.

By directly applying equations (3) and (4), instead of equations (1) and (2), simpler equations can be formulated and solved with much less effort. Assume that the flowfield about a nacelle with a centerbody is mapped to a rectangular computational domain as shown in Fig. 1; the upper edge of the computational domain represents the cowl surface, the lower edge the axis of symmetry and the hub surface, the right edge the cross-section at the compressor face, and the left edge the outer farfield boundary, which is nearly a semicircle centered approximately at the cowl leading edge. The computational domain shown here is topologically different from that presented in reference [1]. There, the right edge of the computational domain represented the hub surface and the lower edge the axis of symmetry. The mesh thus generated becomes distorted far inside the nacelle, and can pose difficulties in computing flowfields with significant potential gradients there.

Differentiating and combining equations (3) and (4) yield the following two uncoupled Laplace equations

$$x_{\xi\xi} + x_{\eta\eta} = 0 \tag{9}$$

$$y_{\xi\xi} + y_{\eta\eta} = 0 \tag{10}$$

which can be solved for the mesh coordinates by a conventional successive line overrelaxation method. Care must be taken in specifying the boundary conditions for equations (9) and (10) to ensure that the resultant mesh is well-behaved. An orthogonal (indeed conformal) mesh is assured if $x + iy$ is an

Nomenclature

a = local speed of sound
a_0 = stagnation speed of sound
c_1 = constant defined in equation (16)
$c^{(n)}$ = correction of potential function at nth iteration
$e^{(n)}$ = error of potential function after n iterations
f = stretching function
h = constant defined in equation (13)
M_∞ = freestream Mach number
M_1 = average Mach number at cowl throat
$M_{+\infty}$ = Mach number at downstream infinity inside nacelle
P_1, P_2 = functions defined in equations (7) and (8)
q = total velocity
s = curvilinear coordinate in the streamwise direction
u = velocity in the x direction
v = velocity in the y direction
x = Cartesian coordinate in axial direction
y = Cartesian coordinate in radial direction
z = complex variable ($\equiv x + iy$)
Z = complex variable ($\equiv X + iY$)
X, Y = orthogonal coordinates in the computational plane
γ = ratio of specific heats
λ_1 = dominant eigenvalue of relaxation matrix
ξ, η = orthogonal coordinates in the computational plane
ϕ = potential function

A, **B** and **C** matrices defined in Appendix

Downloaded 02 Jun 2010 to 171.66.16.103. Redistribution subject to ASME license or copyright; see http://www.asme.org/terms/Terms_Use.cfm

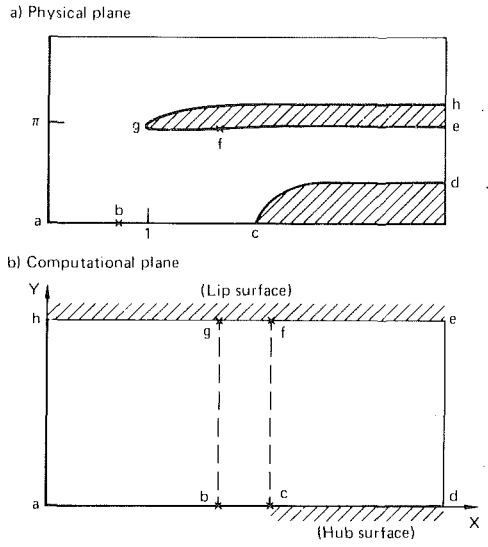

Fig. 1 Transformation of coordinate system

analytical function of $\xi + i\eta$. Thus one straightforward way to choose the boundary conditions is through the application of simple mapping functions.

For nacelle geometries with or without the centerbodies, the physical coordinates of the boundary points are defined with the help of mapping function

$$z = Z - e^{-Z}, \tag{11}$$

after the nacelle coordinates are scaled such that point $(1, \pi)$ lies just inside the leading edge of the cowl lip. Equation (11) was used in Ref. 8 to generate grids for nacelles without centerbodies. In the computational domain shown in Fig. 1(*b*), $\xi = \xi_a$ along the edge *h-a*, $\xi = \xi_d$ along the edge *d-e*, $\eta = 0$ along the edge *a-b-c*, $\eta \doteq 0$ along the edge *c-d*, and $n \doteq \pi$ along the *e-f-g-h*.

It is frequently desirable to introduce stretching functions so that mesh lines can be concentrated in regions of expected high gradients. This can be done implicitly by a suitable choice of the boundary values used to specify the grid, but the effect of the stretching must be accounted for in equations (9) and (10). For the geometries treated here, it is necessary to stretch the grid only in the ξ-direction. This is accomplished as follows.

Let X and Y be the coordinates in the computational plane, related to ξ and η as

$$X = f(\xi) \tag{12}$$

$$Y = h\eta \tag{13}$$

where $f(\xi)$ is an implicit stretching function which will be determined by applying the Cauchy-Riemann condition during the iteration, and h is a constant. Applying this transformation to equations (9) and (10) and neglecting the second derivatives of the stretching function gives

$$c_1 x_{XX} + x_{YY} = 0 \tag{14}$$

$$c_1 y_{XX} + y_{YY} = 0, \tag{15}$$

where

$$c_1 = \left[\frac{f'(\xi)}{h}\right]^2 \tag{16}$$

From equations (3) and (4), it is clear that

$$c_1 = \frac{y_Y^2}{x_X^2} = \frac{x_Y^2}{y_X^2} = \frac{y_Y^2 + x_Y^2}{x_X^2 + y_X^2} \tag{17}$$

Equations (14) and (15) can be considered to describe a stretched grid under an approximated conformal mapping, if the boundary values are chosen to be at least approximately consistent with equation (11).

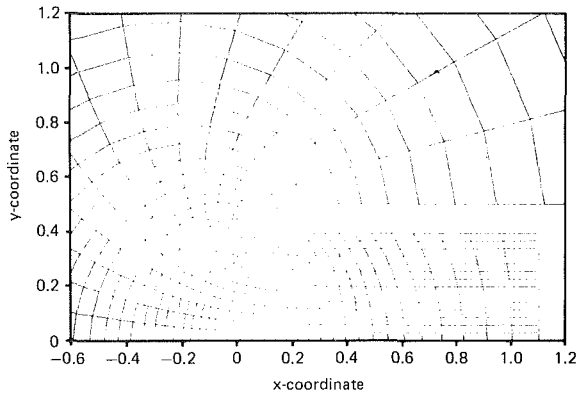

Fig. 2 Douglas research cowl contour and coordinate grid (intermediate mesh)

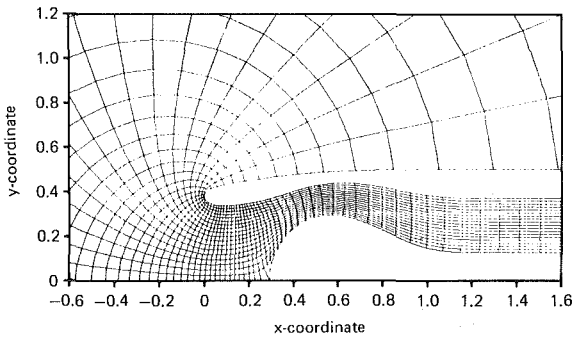

Fig. 3 A modified DC-8 engine inlet contour and coordinate grid (intermediate mesh)

These equations for the grid coordinates are solved by successive line overrelaxation. In each relaxation step, the last expression in equation (17) is used to compute the coefficient c_1 based on the solution from the previous iteration. Since c_1 should be a function only of ξ, either the local values or the average of values calculated on each ξ-line can be used in practice. Although equations (14) and (15) are nonlinear and coupled, the convergence rate of their solution is almost as good as that of the uncoupled Laplace equations, equations (9) and (10).

Grids generated using this approach are shown in Figs. 2 and 3 for two typical geometries. The stretching in ξ as described in equation (12) is used in both cases to move grid points further downstream inside the nacelles. The number of relaxation steps required to generate mesh coordinates with maximum residual less than 10^{-5} is about 40 for the coarse meshes (32 × 9), 80 for the intermediate meshes (64 × 18) and 150 for the final meshes (128 × 36). The total CPU time required for generating three meshes is about one minute on a Cyber 175.

Potential Flowfield Calculation

The equation governing the velocity potential ϕ for axisymmetric irrotational flow is

$$(a^2 - u^2)\phi_{xx} + (a^2 - v^2)\phi_{yy} - 2uv\ \phi_{xy} + a^2 \frac{v}{y} = 0, \tag{18}$$

where the local speed of sound a is determined from the energy equation

$$a^2 = a_0{}^2 - (\gamma - 1)(u^2 + v^2)/2. \tag{19}$$

On the axis, $y = 0$, and equation (18) becomes

Downloaded 02 Jun 2010 to 171.66.16.103. Redistribution subject to ASME license or copyright; see http://www.asme.org/terms/Terms_Use.cfm

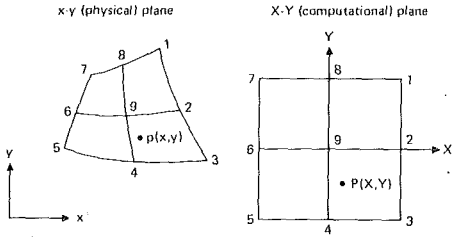

Fig. 4 Transformation of nine-point element

$$(a^2 - u^2)\phi_{xx} + 2a^2\phi_{yy} = 0. \tag{20}$$

A finite difference approximation to equation (18) can be constructed using the rotated difference scheme [1, 5, 12]. In order to apply the finite difference method on a uniform mesh, a coordinate transformation is generally required. Derivatives of the velocity potential in two arbitrary coordinate systems are related to each other as (1):

$$\begin{Bmatrix} \phi_x \\ \phi_y \end{Bmatrix} = \mathbf{A} \begin{Bmatrix} \phi_X \\ \phi_Y \end{Bmatrix} \tag{21}$$

$$\begin{Bmatrix} \phi_{xx} \\ \phi_{yy} \\ \phi_{xy} \end{Bmatrix} = -\mathbf{BCA} \begin{Bmatrix} \phi_X \\ \phi_Y \end{Bmatrix} + \mathbf{B} \begin{Bmatrix} \phi_{XX} \\ \phi_{YY} \\ \phi_{XY} \end{Bmatrix}, \tag{22}$$

where matrices **A**, **B** and **C** are 2×2, 3×3 and 3×2 whose elements are functions of x_X, y_X, x_{XX}, y_{XX}, x_Y, y_Y, x_{YY}, y_{YY}, and y_{XY}; they are defined in the Appendix.

A local coordinate transformation based on the nine-point element suggested in reference [1] is adopted here. Figure 4 shows the transformation of a nonuniform nine-point element in the physical plane to a uniform nine-point element in the computational plane with X and Y varying from -1 to 1. At the control point 9, where $X=Y=0$, the following expressions hold (consistent with central differencing)

$$x_X = (x_2 - x_6)/2 \tag{23a}$$

$$y_X = (y_2 - y_6)/2 \tag{23b}$$

$$\phi_X = (\phi_2 - \phi_6)/2 \tag{23c}$$

$$x_Y = (x_8 - x_4)/2 \tag{23d}$$

$$x_{XX} = x_2 - 2x_9 + x_6 \tag{23e}$$

$$x_{YY} = x_8 - 2x_9 + x_4 \tag{23f}$$

$$x_{XY} = (x_1 - x_3 + x_5 - x_7)/4$$

. . .etc.

Substitution of equations (23) into equations (21) and (22) results in a second-order accurate, central difference approximation to the full potential equation. Such a scheme is appropriate for purely subsonic flows. If the flow is locally supersonic, an artificial viscosity term is explicitly added to provide an upwind bias to the difference equations. The terms added are chosen to model those introduced by the rotated difference scheme of Jameson [5]. Further details of the difference equations and the relaxation process to solve them are obtained in reference [1].

Extrapolated Relaxation

The convergence rate of any relaxation scheme suffers as the mesh spacing approaches zero, because the spectral radius of the relaxation matrix approaches unity for most elliptic problems. This difficulty can be partially overcome by using a sequence of meshes, generally a coarse mesh, an intermediate mesh, and a fine mesh. The converged solution obtained on each mesh is used as the initial estimate for the next finer mesh. For flowfields inside engine inlet nacelles, the convergence rate suffers even more as mass flow ratio increases. An extrapolated relaxation scheme suggested by Caughey and Jameson [8] is adopted here to improve the convergence rate of the solutions. The extrapolated relaxation scheme has an advantage over other accelerated schemes in that it is extremely simple to apply to an existing relaxation code [8, 16, 17].

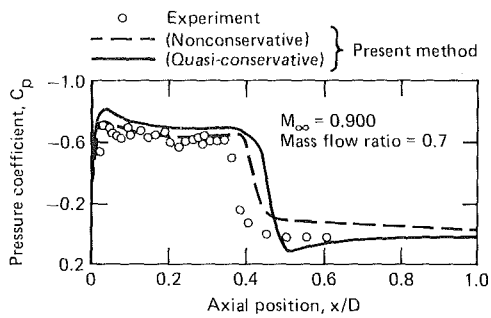

Fig. 5 Pressure distribution on the outer surface of a Douglas research cowl lip

Suppose that the relaxation matrix has distinct eigenvalues, ordered such that $1 > |\lambda_1| > \ldots\ldots > |\lambda_M|$. Then, after many, say n, iterations, the error vector. $\mathbf{e}(n) = \phi$, must approach the eigenvector corresponding to the dominant eigenvalue, so that

$$\mathbf{e}^{(n+1)} \sim \lambda_1 \mathbf{e}^{(n)}. \tag{24}$$

Similarly, the correction $c^{(n+1)} = \phi^{(n+1)} - \phi^{(n)}$ follows

$$\mathbf{c}^{(n+1)} \sim \lambda_1 \mathbf{c}^{(n)}, \tag{25}$$

and can be related to the error vector by

$$\mathbf{c}^{(n)} = \mathbf{e}^{(n+1)} - \mathbf{e}^{(n)}. \tag{26}$$

Using equations (24) and (26) gives

$$\mathbf{e}^{(n)} = \mathbf{c}^{(n)}/(1-\lambda_1)'. \tag{27}$$

Since $(1-\lambda_1)$ is very small for the grids typically used in practice, the error can be many times larger than the correction calculated by the relaxation procedure. To remove that error, equation (27) suggests that in situations where equations (24) and (25) hold, $\mathbf{e}^{(n)}/(1-\lambda_1)$ instead of $c^{(n)}$ should be added as the correction of the potential at the $(n+1)$st iteration.

A simple way to determine if a dominant eigenvalue exists is to follow the history of averaged λ, estimated using equation (25). At the end of each sweep of the entire field, the average λ and the standard deviation of the three recent values of average λ, are calculated. There are two thresholds built in the computer program for triggering the acceleration. The first is to require that the standard deviation of the three recent values of average λ be less than 0.0001. The second is to require that the value of λ be less than a critical value $(\lambda_1)_{cr}$ which is properly determined to reflect the mesh size. The values of $(\lambda_1)_{cr}$ chosen are 0.98 for the total number of grid points, N, <500, 0.99 for $500 \le N \le 2000$, 0.999 for $2000 \le N \le 4000$, and 0.9995 for $N > 4000$. A last precaution is to make sure that the multiplication factor, $1/(1-\lambda_1)$, is always less than a certain number. In our cases, 200 is chosen as the maximum multiplication factor. The accelerated relaxation scheme thus generated has worked well for all cases.

Numerical Results

Results will now be presented for flowfields about typical engine inlet nacells for both the high freestream Mach number and low mass-flow ratios associated with transonic cruise and

Downloaded 02 Jun 2010 to 171.66.16.103. Redistribution subject to ASME license or copyright; see http://www.asme.org/terms/Terms_Use.cfm

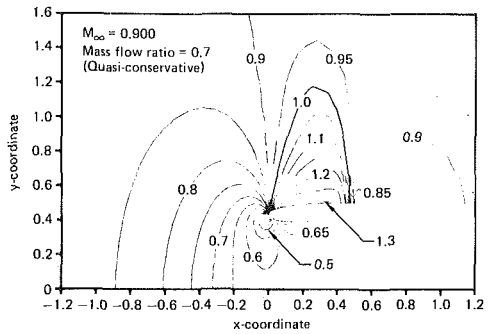

Fig. 6 Mach number contours for the flowfield about a Douglas research cowl

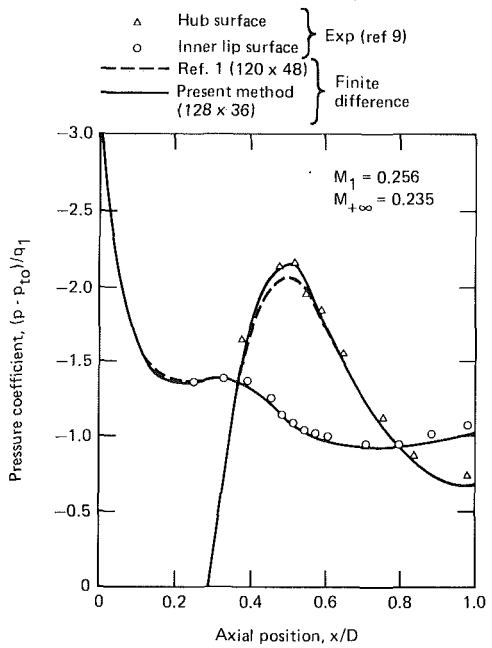

Fig. 7 Pressure distribution on a modified DC-8 engine inlet with an enlarged hub

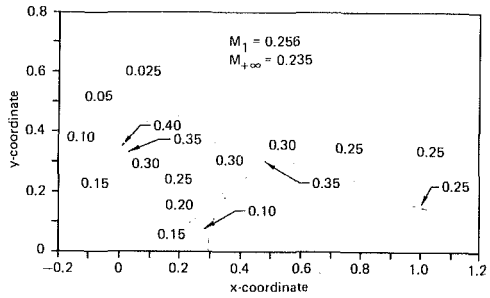

Fig. 8 Mach number contour for flowfield about a modified DC-8 engine inlet

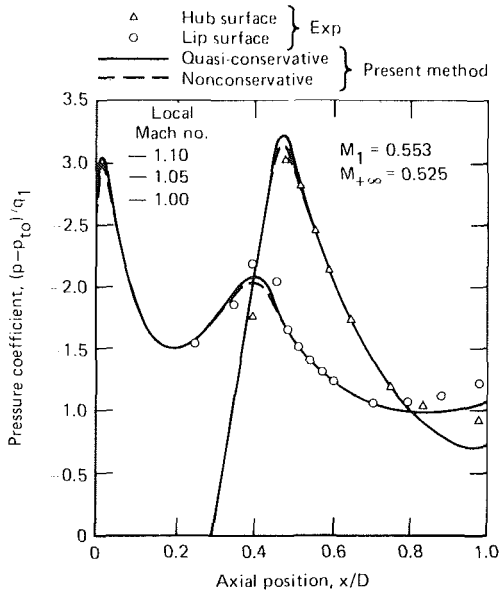

Fig. 9 Pressure distribution on a modified DC-8 engine inlet

the nearly zero freestream Mach number and high mass-flow ratios associated with take-off acceleration. The embedded supersonic regions occur near the cowl outer surface for the former cases, and near the centerbody surface inside the nacelle for the latter cases. The results to be presented have been calculated on a sequence of three grids, each grid being obtained from the preceeding one by halving the grid spacing in each direction. The program occupies 130 k (octal) storage on the Cyber 175. In general, convergent solutions are obtained after the maximum corrections have been reduced by four orders of magnitude.

Figure 5 presents the measured and calculated pressure distributions on the outside surface of a research cowl designed and tested by the Douglas Aircraft Company [18]. The cowl geometry and the intermediate mesh used for the computation are shown in Fig. 2. The freestream Mach number is 0.900, and the mass-flow ratio (capture area) is 0.700. Both quasi-conservative and nonconservative solutions are presented. Discussions of the differences between quasi-conservative and nonconservative solutions can be found in reference [1]. In general, the nonconservative solutions predict the shock location better, and the quasi-conservative solutions predict the shock strength better. The final grid contains 128 × 32 mesh cells in the x and y directions, respectively. A typical run requires about three to four minutes on the Cyber 175. 250 relaxation steps in the finest mesh were used. Results for various freestream Mach numbers for the same cowl can also be found in references [1 and 8]. The Mach number contours for the quasi-conservative result shown in Fig. 5 are presented in Fig. 6.

The inlet contour shown in Fig. 3 represents a modified DC-8 engine inlet with an enlarged centerbody. Experimental data at nearly zero freestream speed was obtained for this inlet by Marsh et al. [19] in a noise-suppression study. In the calculations, the freestream speed was set identically zero, and the March number at the compressor face, $M_{+\infty}$, was determined from the experimental data and specified as a boundary condition there. The final solutions were obtained on a 128 × 32 mesh. Figures 7 and 9 present the measured and calculated pressure distributions on the inner surface of the cowl and on the surface of the centerbody. The pressure coefficient in the figures is defined as the static pressure minus the stagnation pressure normalized by the average dynamic pressure at the cowl throat. The Mach number M_1 is the average Mach number at the cowl throat used to normalize the pressure coefficient. The pressure distribution calculated by the present method is compared with the experimental data for $M_1 = 0.256$ and $M_{+\infty} = 0.235$ in Fig. 7. The Mach number contours for the same result are shown in Fig. 8. The pressure distribution and the Mach number contours for the case with $M_1 = 0.553$ and $M_{+\infty} = 0.525$ are presented in Figs. 9 and 10, respectively. Because of a sharp change in the cross-sectional area of the flow passage, the flow accelerates and then decelerates when passing over the hub surface. In Fig. 10 a significant supersonic region is apparent near the crest of the centerbody. For the case in Fig. 7, the extrapolated relaxation has been successfully applied to obtain

Downloaded 02 Jun 2010 to 171.66.16.103. Redistribution subject to ASME license or copyright; see http://www.asme.org/terms/Terms_Use.cfm

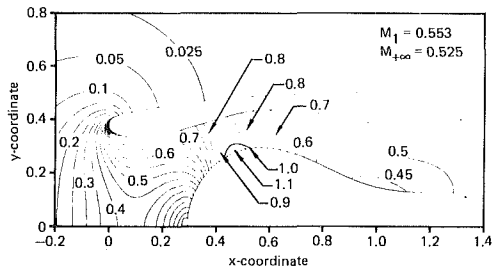

Fig. 10 Mach number contours for the flowfield about a modified DC-8 engine inlet

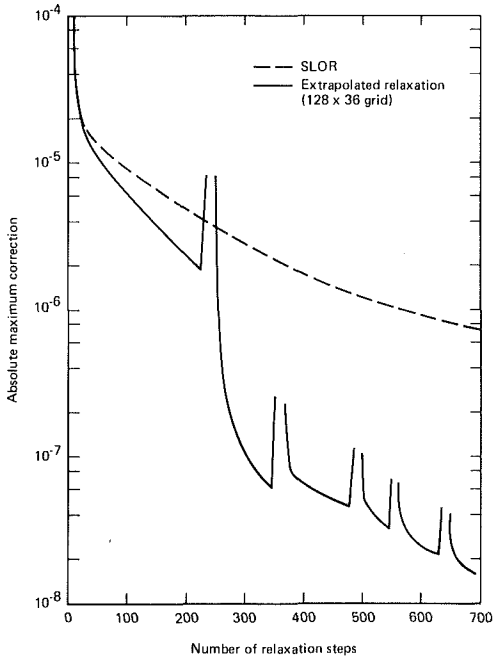

Fig. 11 Convergence histories of extrapolated and SLOR schemes

convergent solutions. The total CPU time for the run is about three minutes. About 120 relaxation steps are needed in the finest mesh. For the case in Fig. 9, the improvement of the convergent rate using the extrapolated relaxation is not as dramatic as the case in Fig. 7, mainly because of the appearance of supersonic region near the hub. About 300 relaxation steps were used in the finest mesh, and the total CPU time for the run is about six minutes. Both the quasi-conservative and nonconservative solutions are shown. The peak pressure value of the nonconservative solution is slightly lower than that of the quasi-conservative solution. In spite of the severe adverse pressure gradient inside the nacelle in this case, the calculated results agree reasonably well with those of the experiment. In the transonic flowfield calculations, the convergence behavior of the solution is sensitive to any numerical inaccuracy. The distortion of the mesh inside the nacelle used in reference [1] eventually leads to divergent solutions for high mass-flow ratio cases.

An example of the effect of extrapolation upon the iterative process is presented in Fig. 11. The extrapolated relaxation is particularly useful for cases where large potential gradients exist inside the nacelle. In solving the relaxation equation, the sweep direction is always downstream in order to stabilize the solution; however, the correction information resulting from the large gradients inside nacelle must propagate upstream. This fact leads to slow convergence rates of the solutions. Figure 11 illustrates the improved convergence rate of the extrapolated relaxation scheme over the conventional successive-line-over-relaxation scheme for the engine inlet shown in Fig. 3 with $M_1 = 0.256$ and $M_{+\infty} = 0.235$. The maximum correction is plotted versus the relaxation step. As the convergence rate decreases, the dominant eigenvalue becomes pronounced and approaches unity. Immediately after the extrapolation, larger corrections are produced, but these decrease sharply after a few relaxation steps. The extrapolated scheme improves the convergence rate on all three meshes.

Conclusions

A general grid-generation scheme, similar to but simpler than Thompson's method, has been presented. Modified Laplace equations which nearly satisfy the requirement of conformality are solved for the mesh coordinates by a successive line over-relaxation method. The scheme converges quickly, and has potential application for the generation of nearly orthogonal and body-conforming coordinate systems for flowfields about rather general geometries.

By combining the general grid-generation scheme with the general solver for transonic potential flowfield developed in reference [1], difficulties encountered in Reference [1] in treating embedded supersonic regions inside nacelleas are ovecome. Results obtained for high subsonic freestream and for high mass-flow ratio cases agree well with experimental results.

References

1 Chen, L. T., and Caughey, D. A., "Calculation of Transonic Inlet Flowfields Using Generalized Coordinates," *J. of Aircraft,* Vol. 17, Mar. 1980, pp. 167–174.

2 Murman, E. M., and Cole, J. D., "Calculation of Plane Steady Transonic Flows," *AIAA Journal,* Vol. 9, Jan. 1971, pp. 114–121.

3 Garabedian, P. R., and Korn, D. G., "Analysis of Transonic Airfoils," *Communications on Pure and Applied Mathematics,* Vol. 24, 1972, pp. 841.

4 Jameson, A., "Transonic Flow Calculations for Airfoils and Bodies of Revolution," Grumman Aerodynamics Report 370-71-1, Dec. 1971.

5 Jameson, A., "Iterative Solution of Transonic Flows Over Airfoils and Wings, Including Flows at Mach 1," *Communications on Pure and Applied Mathematics,* Vol. 27, 1974, pp. 283–309.

6 Colehour, J. L., "Transonic Flow Analysis Using a Stream-Line Coordinate Transformation Procedure," *AIAA* Paper No. 73-658, 1973.

7 Arlinger, B. G., "Calculation of Transonic Flow Around Axisymmetric Inlets," *AIAA Journal,* Vol. 13, Dec. 1975, pp. 1614–1621.

8 Caughey, D. A., and Jameson, A., "Accelerated Iterative Calculation of Transonic Nacelle Flowfields," *AIAA Journal,* Vol. 15, Oct. 1977, pp. 1474–1480.

9 Reyhner, T. A., "Cartesian Mesh Solution for Axisymmetric Transonic Potential Flow Around Inlets," *AIAA Journal,* Vol. 15, May 1977, pp. 624–631.

10 Reyhner, T. A., "Transonic Potential Flow Around Axisymmetric Inlets and Bodies at Angle-of-Attack," *AIAA Journal,* Vol. 15, Sept. 1977, pp. 1299–1306.

11 Chen, L. T., and Caughey, D. A., "A Higher-Order Finite Difference Scheme for Transonic Flowfields Around Complex 3-D Geometries," *Proceedings of AIAA 4th Computational Fluid Dynamics Conference,* Williamsburg, Va., July 1979.

12 Caughey, D. A., and Jameson, A., "Numerical Calculation of Transonic Potential Flow About Wing-Body Combinations," *AIAA Journal,* Vol. 17, Feb. 1979, pp. 175–181.

13 Caughey, D. A., and Jameson, A., "Progress in the Application of Finite-Volume Methods to Wing-Fuselage Calculations," *AIAA* Paper No. 79-1513, July 1979.

14 Thompson, J. F., Thames, F. C., and Mastin, C. M., "Automatic Numerical Generation of Body-Fitted Curvilinear Coordinate System," *Journal of Computational Physics,* Vol. 15, July 1974, pp. 299–319.

15 Holst, T. L., "An Implicit Algorithm for the Conservative Transonic Full Potential Equation Using an Arbitrary Mesh," *AIAA* Paper No. 78-1113, July 1978.

16 Caughey, D. A., "Numerical Calculation of Transonic Potential Flows," Lecture notes presented at Short Course on Advances in Computational Fluid Dynamics, at the University of Tennessee Space Institute, Tullahoma, Tenn., Dec. 1978.

17 Cheng, H. K., and Hafez, M. M., "Convergence Acceleration and Shock Fitting for Transonic Flow Computations," *AIAA* Paper No. 78-113, 1978.

18 Unpublished data, Douglas Aircraft Company, Long Beach Ca.

19 Marsh, A. H., Elias, I., Hoehne, J. C., and Frasca, R. L., "A Study of Turbofan-Engine Compressor-Noise-Suppression Techniques," NASA CR-1056, June 1968.

Downloaded 02 Jun 2010 to 171.66.16.103. Redistribution subject to ASME license or copyright; see http://www.asme.org/terms/Terms_Use.cfm

APPENDIX

Useful Matrices

The matrices **A, B** and **C** used in equations (20) and (21) are

$$\mathbf{A} = (\mathbf{J}^T)^{-1} = \begin{bmatrix} x_X & y_X \\ x_Y & y_Y \end{bmatrix}^{-1} \tag{A1}$$

$$\mathbf{B} = \begin{bmatrix} x_X^2 & y_X^2 & 2x_X y_X \\ x_Y^2 & y_Y^2 & 2x_Y y_Y \\ x_X x_Y & y_X y_Y & (x_X y_Y + x_Y y_X) \end{bmatrix}^{-1}$$

$$= \frac{1}{D^2} \begin{bmatrix} y_Y^2 & y_X^2 & -2y_Y y_X \\ x_Y^2 & x_X^2 & -2x_Y x_X \\ -y_Y x_Y & -y_X x_X & (x_X y_Y + x_Y y_X) \end{bmatrix} \tag{A2}$$

$$\mathbf{C} = \begin{bmatrix} x_{XX} & y_{XX} \\ x_{YY} & y_{YY} \\ x_{XY} & y_{XY} \end{bmatrix} \tag{A3}$$

where

$$D = x_X y_Y - x_Y y_X. \tag{A4}$$

Downloaded 02 Jun 2010 to 171.66.16.103. Redistribution subject to ASME license or copyright; see http://www.asme.org/terms/Terms_Use.cfm

The Flow Properties of Rooms With Small Ventilation Openings

A. D. Gosman
P. V. Nielsen
A. Restivo
J. H. Whitelaw

Imperial College of Science and Technology,
Department of Mechanical Engineering,
Fluids Section,
London SW7 2BX, England

Measured and calculated properties relevant to the flow in ventilated rooms are reported. The measurements were obtained by laser-Doppler anemometry in a small-scale model room with a single square inlet. The calculations made use of a numerical procedure which solves, in finite-difference form, the elliptic partial-differential equations for three components of velocity, the pressure, the turbulence energy and its dissipation rate. Calculated results are shown to be in close agreement with the present measurements and with other available experimental data. With this justification, the procedure is used to quantify the dependence of the velocity characteristics of different geometric arrangements. The results provide guide lines for the design of ventilation systems.

1 Introduction

In previous papers, Nielsen, Restivo, and Whitelaw [1, 2] reported calculations of flow properties of relevance to ventilation and obtained with a two-dimensional calculation procedure. The results were restricted to flows which were two-dimensional or near two-dimensional. The purpose of the present paper is to report calculations for three-dimensional arrangements and, as before, to demonstrate their quantitative value by comparison with corresponding measurements.

The practical relevance of the investigation relates to the ventilation of rooms which is often achieved by supplying fresh, temperature-controlled air through a small, rectangular opening close to a ceiling. The return opening is normally located close to the floor but has considerably less influence on the velocity distributions within the room. There is a need for a procedure which will allow the velocity, and ultimately the temperature distributions, to be determined as a function of room geometry, mass flow and geometrical arrangement of a ventilation supply and return. The results presented here demonstrate the extent to which this can be achieved by the numerical solution of appropriate differential equations.

The calculation procedure is an extension of that described by Nielsen, Restivo and Whitelaw to include the third velocity component. This extension is relatively straight forward but results in a need for many more grid nodes and, as a result of this and comparatively slow convergence, long computing times. As a consequence, efforts have been made to increase the rate of convergence of the iterative procedure and the methodology and results of this effort are described. In addition, an economy of grid nodes is achieved by incorporating wall-jet development assumptions where these can be supported by reliable data; this precludes the need for a large number of grid nodes to describe the flow in the immediate vicinity of the inlet opening.

Contributed by the Fluids Engineering Division for publication in the JOURNAL OF FLUIDS ENGINEERING. Manuscript received by the Fluids Engineering Division, July 12, 1979.

The discretized nature of the solution method together with the assumptions inherent in a two-equation turbulence model imply that the calculated results can only be approximate. As a consequence, it is necessary to test the procedure by comparison with experimental data. Previous experimental studies of three-dimensional flow have been reported, for example, by Blum [3], Hestad [4] , and Jackman [5, 6] and some of these data are referred to in the results section. Unfortunately, they do not provide sufficient details to allow accurate comparisons and, to meet this requirement, new measurements are reported here and were obtained with the same laser-Doppler arrangement described by Nielsen, Restivo, and Whitelaw.

The flow configuration, anemometer and measured results are described in the following section. Section 3 introduces the calculation procedure and presents details of its application to the present flows. Predicted and measured flows are compared and discussed in section 4 and summary conclusions are presented in a final section.

2 Flow, Configuration, Anemometer and Experimental Results

Values of the longitudinal component of mean velocity and the corresponding normal stress were measured with a laser-Doppler anemometer. The anemometer, air-seeding arrangement and signal-processing instrumentation are identical to those described by Nielsen, Restivo, and Whitelaw.

The flow was arranged in a model fabricated from perspex and schematically represented in Fig. 1. The height of the model room, H, was 89.3 mm and the other dimensions correspond to the nondimensional quantities

$$L/H = 3.0, \quad W/H = 1.0, \quad h/H = 0.1,$$
$$w/H = 0.1 \text{ and } t/H = 0.16.$$

The inlet plane was preceded by a straight channel of square section, 270 mm long, and resulted in the initial profiles displayed in Fig. 2. It is clear that the mean velocity profiles have thick boundary layers of size comparable to $h/2$

Copyright © 1980 by ASME

Downloaded 02 Jun 2010 to 171.66.16.103. Redistribution subject to ASME license or copyright; see http://www.asme.org/terms/Terms_Use.cfm

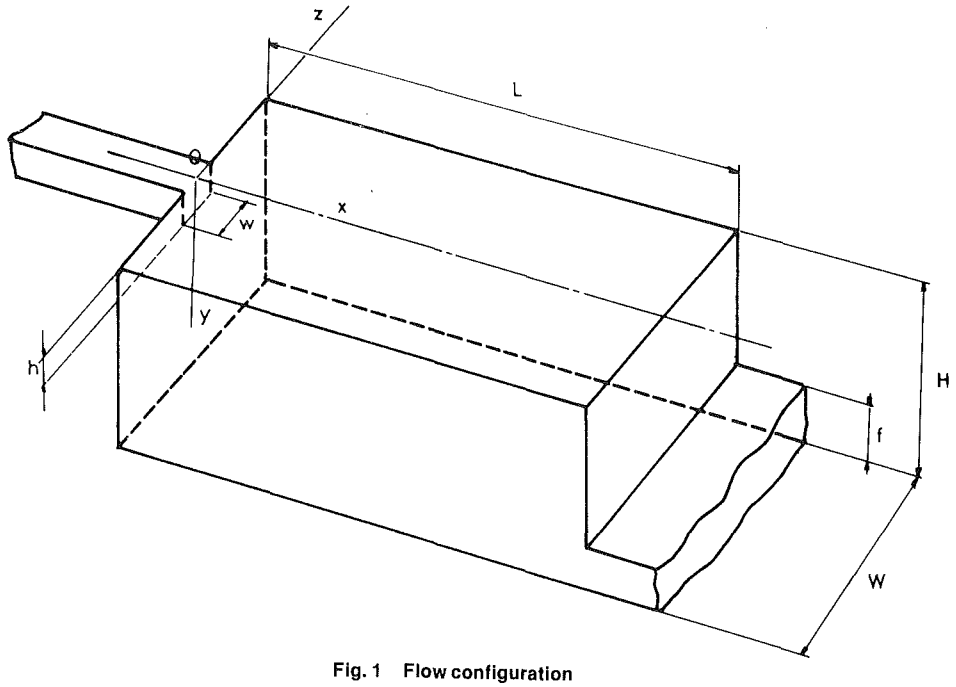

Fig. 1 Flow configuration

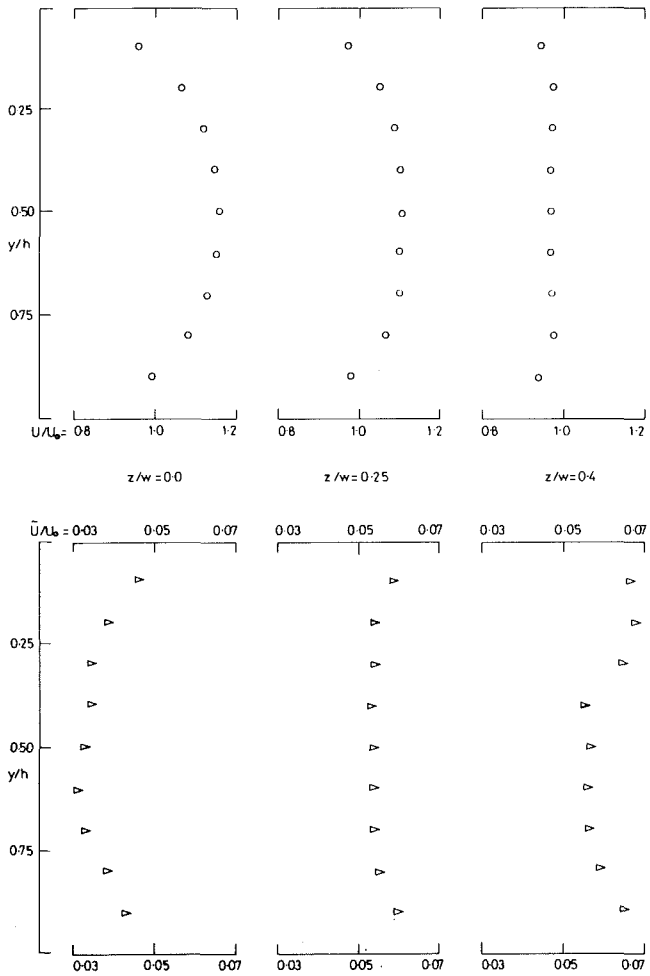

Fig. 2 Measured values of mean longitudinal velocity and the rms of the corresponding fluctuations in the inlet plane: $L/H=3$, $W/H=1$, $h/H=0.1$, $w/W=0.1$

although the centre line turbulence intensity does not exceed 3 percent. At the Reynolds number used for most of the experiments i.e. Re = 9000 based on h and the velocity at $h/2$, U_0, energy spectra were obtained in all regions of the flow and were typical of a turbulent flow; no influence of Reynolds number was detected in the present range of measurements.

Figure 3(*a*) presents profiles of longitudinal velocity at two different z-planes, corresponding to z/W values of 0.0 and 0.4, and Fig. 3(*b*) the maximum velocity decay in the symmetry plane of the jet. The calculations shown on these figures will be discussed in section 4. The measurements of Fig. 3(*a*) demonstrate that the square jet spreads in the y and z directions and, at x/H of 1.0, the maximum velocity in the symmetry plane is 20 times that at z/W of 0.4. Further downstream, at x/H of 2.0, the jet has spread to a more even velocity distribution but could not usefully be approximated by two-dimensional equations. As might be expected, the reverse flow velocities are less strongly influenced by the geometry of the inlet but are still significantly three-dimensional.

The upstream region of the inlet flow is represented, in greater detail, in Fig. 4. These measurements were obtained to allow comparisons with those of alternative inlet geometries and give further information on the development of a three dimensional wall jet issuing from a small orifice. The measurements are presented in non-dimensional form, with the maximum velocity U_m and the thickness at $U_m/2$ as normalising factors, and the results nearly reduce to a single curve, although some scatter is apparent. Rajaratnam and Pani [7] suggested that the velocity profiles are well described by a single nondimensional curve for x/h above 10, but the relative importance of h/H in this particular geometry is likely to have affected the jet development. The velocity decay in the jet under the ceiling is also compared with the square wall-jet results of Sforza and Herbst [8] and Rajaratnam and Pani [7] in Fig. 3(*b*), and the agreement is satisfactory up to x/H of about 2.5, until the jet decelerates towards the end wall.

Measured values of normal stress are not presented here because they are similar to those of the previous near two-dimensional results and carry little additional information.

Downloaded 02 Jun 2010 to 171.66.16.103. Redistribution subject to ASME license or copyright; see http://www.asme.org/terms/Terms_Use.cfm

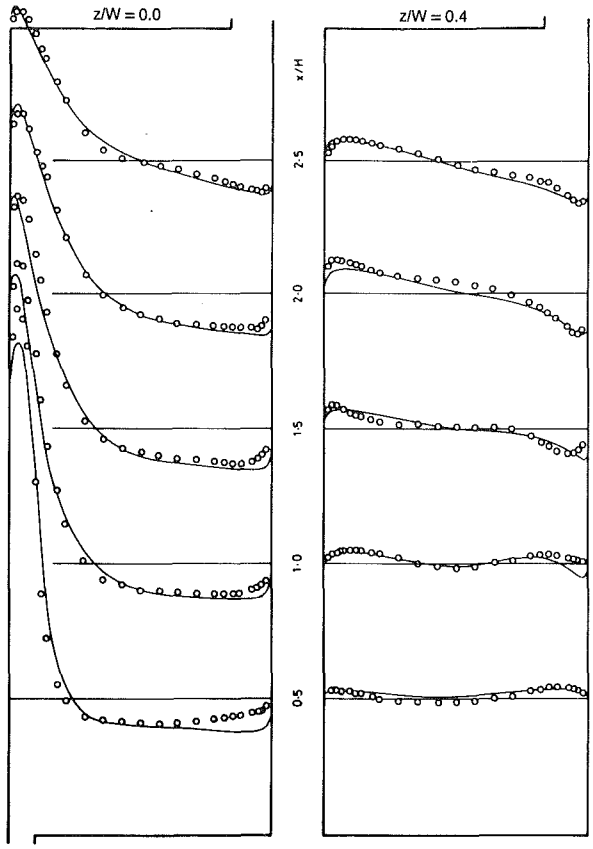

Fig. 3(a) Measured and calculated profiles of longitudinal velocity at z/W of 0.0 and 0.4

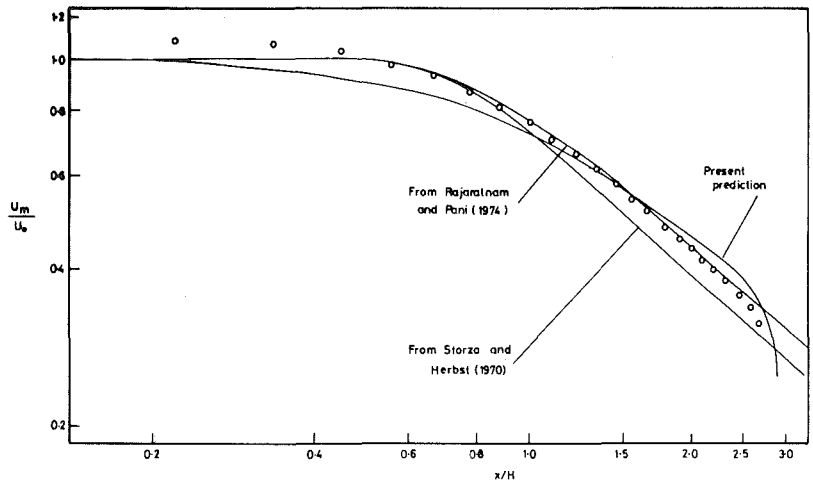

Fig. 3(b) Measured and calculated profiles of maximum velocity decay at z/W of 0.0
$L/H = 3$, $W/H = 1$, $h/H = 0.1$, $w/H = 0.1$.

The corresponding signals as examined on an oscilloscope and on power spectra did not exhibit predominant frequencies and the rms values varied from 0.25 U_0 in the exterior shear layer of the jet, at $z = 0$, $x = 0.5$H to $0.03U_0$ in the regions of lower mean velocity near the bottom corners below the inlet opening. The experimental uncertainty, previously discussed in reference [1], was better than ± 0.5 percent in mean velocity and ± 1 percent in rms values, for velocities above 0.5 m/s.

3 Calculation Procedure

The predictions were obtained by numerical solution of the time-averaged Navier-Stokes equations, supplemented by the two-equation '$k-\epsilon$' turbulence model from which the turbulent Reynolds stresses are extracted. The equations solved are of the general form

$$\frac{\partial}{\partial x_j}(\rho U_j \phi) = \frac{\partial}{\partial x_j}\left(\Gamma_\phi \frac{\partial \phi}{\partial x_j}\right) + S_\phi \tag{1}$$

where the dependent variable ϕ may be any of the following: the three components of velocity U_1, U_2, U_3 (hereafter referred to for convenience as U, V, and W respectively), turbulence energy k, and its dissipation rate ϵ. Definitions of the coefficients Γ_ϕ and S_ϕ corresponding to each of these are

Downloaded 02 Jun 2010 to 171.66.16.103. Redistribution subject to ASME license or copyright; see http://www.asme.org/terms/Terms_Use.cfm

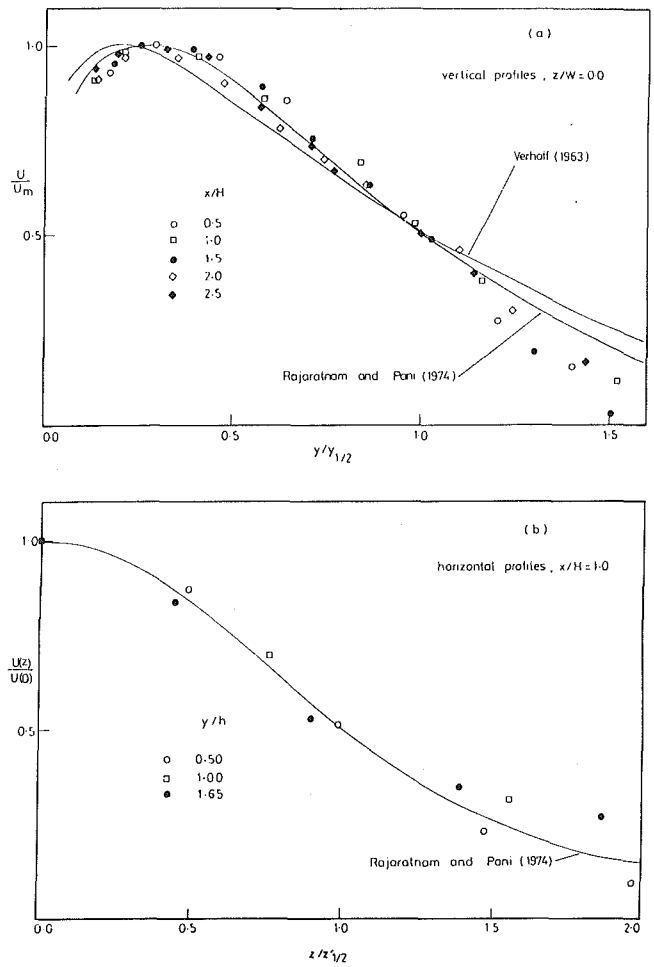

Fig. 4 Measured values of mean longitudinal velocity in the upstream region

listed in Table 1, as are the values of the empirical coefficients appearing in the turbulence model.

Table 1 Definition of Γ_ϕ and S_ϕ for conservation equations solved

Equation	ϕ	Γ_ϕ	S_ϕ
Continuity	1	0	0
Direction-i momentum	U_i	μ_{eff}	$-\frac{\partial P}{\partial x_i}+\frac{\partial}{\partial x_j}\left[\mu_{\text{eff}}\left(\frac{\partial U_i}{\partial x_j}+\frac{\partial U_j}{\partial x_i}\right)\right]$
Turbulence energy	k	$\mu_{\text{eff}}/\sigma_k$	$G-\rho\epsilon$
Turbulence dissipation	ϵ	$\mu_{\text{eff}}/\sigma_\epsilon$	$\frac{\epsilon}{k}(C_1 G - C_2\rho\epsilon)$

Notes:

1. $G \equiv \mu_{\text{eff}}\frac{\partial U_i}{\partial x_j}\left(\frac{\partial U_i}{\partial x_j}+\frac{\partial U_j}{\partial x_i}\right)$; $\mu_{\text{eff}} \equiv \mu + \mu_t = \mu + C_\mu \rho k^{2/}\epsilon$
2. Turbulence model parameters assigned following values: $C_\mu = 0.09$, $C = 1.44$, $C_2 = 1.92$, $\sigma_k = 1$, $\sigma_\epsilon = 1.22$, $\kappa = 0.42$, $E = 9.79$.

Following now conventional practice, the boundary conditions at solid surfaces are applied indirectly via "wall functions" of the form:

$$V_R^+ = \frac{1}{\kappa}\ln(En^+) \tag{2}$$

$$\partial k/\partial n = 0 \tag{3}$$

$$\epsilon = C_\mu^{\frac{3}{4}} k^{\frac{3}{2}}/\kappa n \tag{4}$$

where $V_R^+ \equiv C_\mu^{\frac{1}{4}}\rho k^{\frac{1}{2}} V_R/\tau_w$, $n^+ \equiv C_\mu^{\frac{1}{4}}\rho k^{\frac{1}{2}} n/\mu$,

and n, V_R and τ_w are, respectively, the normal distance from, resultant velocity in planes parallel to, and resultant shear stress at, the wall. Values of the constants E and κ are given in Table 1.

For some of the calculations, the inlet conditions were also applied in an indirect manner as will be described below, while at the outlet the only prescription required was on the normal velocity, which was taken as uniform.

The differential equations were cast in finite-difference form and solved by a procedure akin to that employed by Nielsen, et al. [1, 2] in their calculations of two-dimensional flow, which in turn was based on the methodology described by Caretto, et al. [9] viz., use of staggered grids for the velocities, formulation of the difference equations in implicit, conservative form using hybrid central/upwind differencing (which insures realistic behavior in regions of both small and large mesh Reynolds number), recovery of pressure via a continuity-based equation and solution of the difference equations by an ADI-like iterative procedure.

The present procedure also shares with the earlier studies, and the three-dimensional furnace calculations of Abou Ellail et al. [10], the important feature of excluding the volume immediately surrounding the inlet from the normal calculations and instead imposing boundary conditions at its surface. This allows the more economical resolution of the jet-like flow emanating from the inlet, which is small in relation to the size of the room. The volume is prescribed large enough for the emerging jet to be adequately resolved by the numerical grid used elsewhere; the result is a significant reduction in the required computer storage and run time.

The downstream surface of the prescribed jet volume is important (the calculations proved to be relatively insensitive to the conditions imposed at entrainment boundaries) and, in principle, the conditions there may be determined by theoretical means (using, for example, an economical forward-marching procedure to determine, in a separate calculation, the jet development from entrance) or from experiment. For example, as demonstrated by the measurements of Rajaratnam and Pani [7], the velocity distributions in jets resulting from circular, square or other nearly axisymmetrical openings of the same area, issuing along a plane surface are all well described by the same nondimensional mean profiles at locations downstream of around 10 diameters. The decay of the maximum velocity and the growth rates were also shown to be similar. In view of these findings, available wall jet data has been used as a basis for the prescription of the new boundary conditions required in cases where measured data is not available and the relative dimension h/H is small enough for the jet to develop before the influence of the walls of the room becomes important. Where this data does not include turbulence measurements, the required parameters are estimated by solving the turbulence equations with the measured velocities inserted. The particular treatments employed in the present calculations will be described as each case is presented.

The rate of convergence of the iterative method is crucial to three-dimensional procedures of the present kind and special steps were taken to accelerate it, while keeping storage requirements within reasonable bounds. Thus, with one exception, the ADI solution technique was confined to a single set of cross-sectional planes in order to limit the coefficient storage requirements, while improved account was taken of plane-to-plane interactions using block velocity and

Downloaded 02 Jun 2010 to 171.66.16.103. Redistribution subject to ASME license or copyright; see http://www.asme.org/terms/Terms_Use.cfm

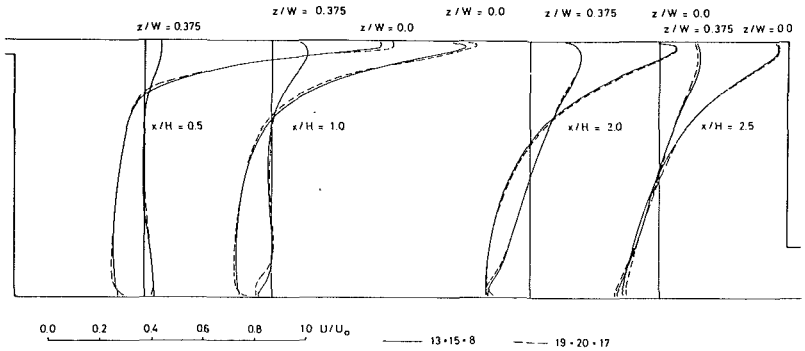

Fig. 5 Influence of number of grid nodes on calculated values of mean longitudinal velocity: $L/H=3$, $W/H=1$, $h/H=0.056$, $w/W=0.5$

pressure adjustments based on global continuity and momentum conservation. The sole exception was the pressure equations, whose strongly elliptic character favoured the use of a full three-dimensional ADI procedure, and whose particular coefficient structure allowed this to be done using little additional storage. These techniques reduced computing times by some 50% of those for the unmodified procedure.

4 Calculated Results

The influence of the number of grid nodes on the solutions obtained was investigated and typical results are shown in Fig. 5 for conditions corresponding to the second entry of Table 2. These results, which were obtained without the special inlet treatment described earlier, show discrepancies of the order of 5 percent of the maximum velocity between a numerical grid with $13\times15\times8$ and $19\times20\times17$ nodes. Tests with smaller numbers of nodes indicated a monotonic convergence of the results towards those with the maximum number of nodes. It is clear that discrepancies as indicated by Fig. 5 will be associated with all practical numbers of grid nodes but, as the comparison of the following paragraphs will show, this order of precision is adequate for ventilation design purposes, and the associated computing time, on a CDC 6600, of about 17 min for a $13\times15\times8$ grids (corresponding to 210 iterations and residual mass sources less than 1 percent of the through flow) may also be regarded as acceptable.

To establish confidence in the overall procedure and to attempt to quantify precision by comparing calculations with measurements, three geometrical configurations were considered and are indicated in Table 2.

Table 2 Configurations used for comparisons of Figs. 3, 6, and 7

Source of experimental data	L/H	W/H	h/H	w/H	Re
Present measurements	3.0	1.0	0.1	0.1	9,000
Nielson, Restivo, and Whitelaw [1]	3.0	1.0	0.056	0.5	5,000
Blum [3]	3.0	1.0	circular diffuser $d/H=0.04$		93,000

The general features of these flows are indicated by the predicted vector plots[1] of Fig. 6(*a*), which relate to the geometry of reference [1]. The circulation patterns are clearly different in the elevations at $z=0$ and $z=0.47$ W, with the centre of the circulation vortex located further upstream close to the side wall and opposite flow directions in the bottom area below the opening. Inspection of the plan view at $y=0.97H$ indicates two vortices in this area rotating about near-vertical axes. These calculations were performed with a $13\times15\times8$ grid and measured downstream boundary conditions as described below.

The velocity profiles of Figs. 6(*b*) and 6(*c*) to relate to the same geometry and indicate differences between measurements and calculations of up to 10 percent of the maximum velocity, which occur mainly in the vicinity of the side walls near the ceiling and in the regions of lower velocity in the reverse flow. The maximum reverse flow velocity, measured close to the side walls, is predicted within 2 percent of the maximum velocity. Figure 6(*c*) indicates that the predicted and measured decay of the maximum velocity in the jet downstream of the starting plane corresponds to the first stage of development of a slender three-dimensional wall jet, designated as the "characteristic decay region" by Sforza [11].

For these calculations, measured profiles of longitudinal velocity were prescribed at the grid nodes located in the plane of $x/H=1.0$ and y/H up to 0.12. The longitudinal velocity at the remaining nodes, and the other variables at all nodes, were calculated over the entire flow domain. The results showed smooth variation of calculated properties at the nodes adjacent to $x/H=1.0$ and $y/H<0.12$ as may be seen from Fig. 6(*a*).

The present measurements are also adequately represented by the calculation procedure, as indicated by Fig. 3(*a*) and (*b*), and the maximum discrepancy between calculation and measurement is of the order of 5 percent of the inlet velocity. The results were obtained without the special inlet treatment which was unnecessary due to the comparatively large value of h/H. The grid had $14\times14\times9$ nodes and a constant velocity profile was prescribed at the inlet.

In the measurements of Blum [3], obtained with a Pitot-tube, the jet issued from a circular opening of diameter small compared to other room dimensions. The results, which were obtained with a $13\times15\times8$ grid, are shown on Fig. 7 and indicate a discrepancy of around 10 percent in the horizontal spreading rate of the jet adjacent to the ceiling and near to the side walls at $x/H=2.14$. The decay of maximum velocity is also slightly underpredicted, with an associated difference of 5 percent in the centre-line at the $x/H=2.54$. The general agreement is, however, satisfactory and in the reverse flow, for example, the discrepancies are below 1 percent of the maximum flow velocity. Due to the small inlet dimensions, calculations with boundary conditions prescribed at the inlet opening lead to poor agreement with the measured data, with the present number of grid nodes, as shown in Fig. 7(*b*) and better results were obtained again with the special inlet treatment described in section 3. The longitudinal velocity was prescribed at the nodes in the volume limited by the planes of $x=1.14H$, $y=0.1H$ and $z=0.31H$, and in these nodes the velocity was assumed to conform with non-dimensional profiles typical of a developed wall jet, in line with Rajaratnam and Pani [7] and the turbulence parameters were

[1] These do not show the vectors in the outlet plane; however the flow there is prescribed as horizontal and uniform, as explained earlier.

Downloaded 02 Jun 2010 to 171.66.16.103. Redistribution subject to ASME license or copyright; see http://www.asme.org/terms/Terms_Use.cfm

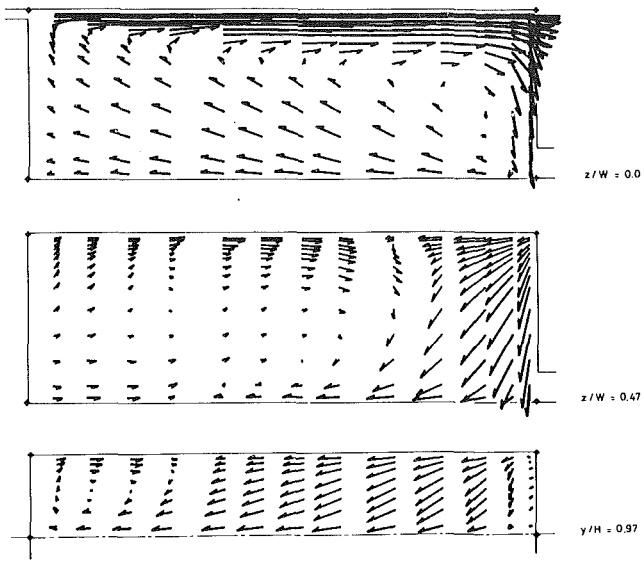

Fig. 6(*a*) Calculated velocity vectors at $z/W=0$ and 0.47 and at $y/H=0.97$

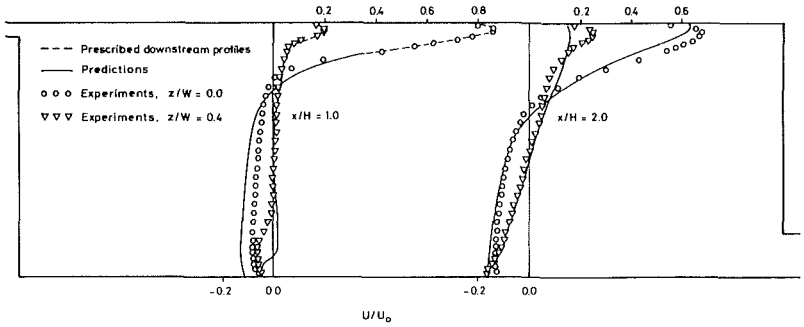

Fig. 6(*b*) Measured and calculated profiles of mean longitudinal velocity at $x/H=1$ and 2

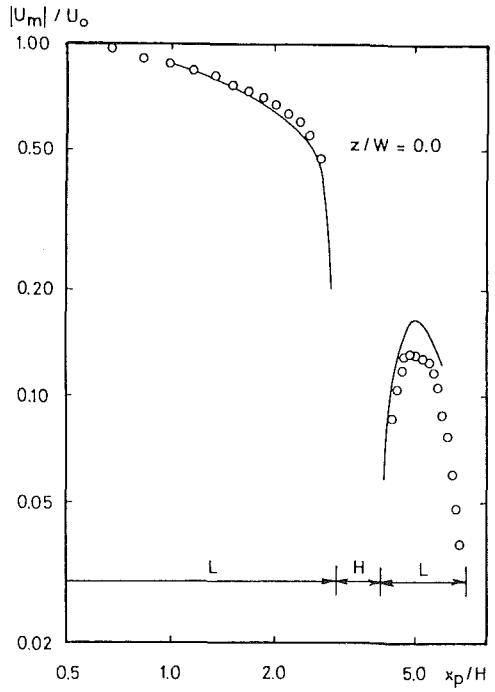

Fig. 6(*c*) Measured and calculated profiles of maximum velocity around the perimeter, x_p.
$L/H=3$, $W/H=1$, $h/H=0.056$, $w/W=0.5$.

Downloaded 02 Jun 2010 to 171.66.16.103. Redistribution subject to ASME license or copyright; see http://www.asme.org/terms/Terms_Use.cfm

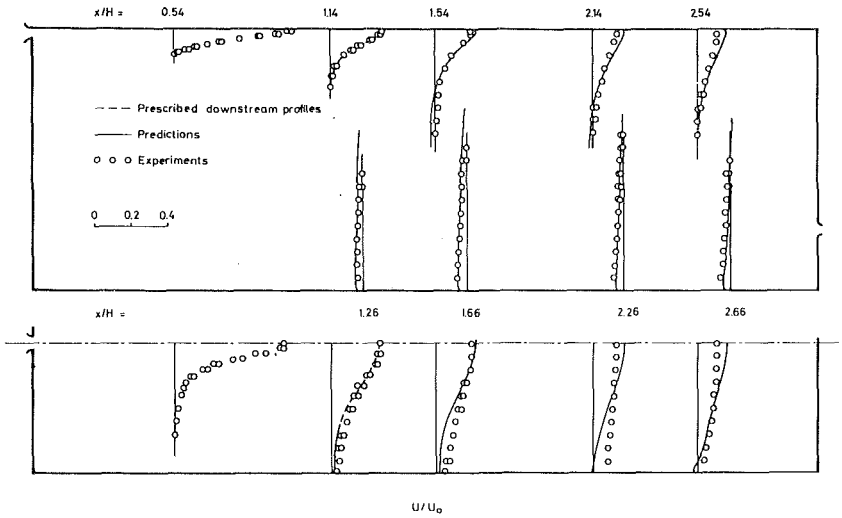

Fig. 7(*a*) Comparison of calculated mean longitudinal velocity with the measurements of Blum [3]

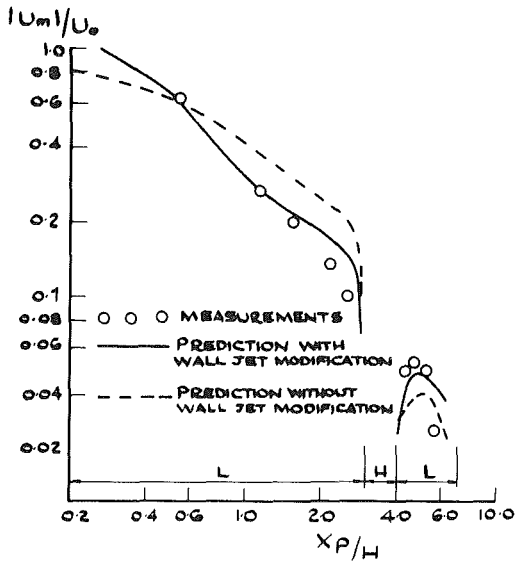

Fig. 7(*b*) Comparison of calculated maximum velocity around the perimeter with the measurements of Blum [3].
$L/H=3$, $W/H=1$, $d/H=0.04$.

estimated as described earlier. The longitudinal velocity at the remaining nodes and the node values of all other properties were calculated by the numerical procedure: it should be noted that the remaining volume and number of nodes were both large in relation to the prescribed region, so in no sense is this practice equivalent to prescribing the entire flow field.

5 Discussion

In general, the results described in the previous section confirm that the calculation procedure is capable of representing the experimentally determined flow patterns with a typical precision of 5% of the maximum velocity. To achieve this order of precision requires more than 1500 nodes to represent a symmetrical half of the flow and the use of an inlet jet-flow correlation for small inlet area. Discrepancies increase as the number of nodes is decreased and as one or both dimensions of the air supply arrangement is decreased. Attempts to perform calculations with a similar number of nodes and without the initial-jet-flow correlations resulted in significantly greater discrepancies as indicated in Fig. 7(*b*). This clearly demonstrates the difficulty associated with the numerical calculations of all flows where small changes in dimensions can lead to large effects.

Since the present calculations involve a significant use of computer time, with associated cost, it is appropriate to consider the possibility that a simpler turbulence model might adequately represent the present flow. Figure 8 presents calculated contours of turbulent kinetic energy and dissipation length scale ($l=k^{3/2}/\epsilon$) associated with the geometry of Blum, and shows the variations of both properties. The variations in length scale, in particular, are fairly regular and an algebraic formulation may be possible. In view of the range of geometric arrangements associated with ventilation, the greater generality associated with the transport model renders it more appropriate.

The capabilities of the present procedure and its precision have been established in the previous paragraphs and, on this basis, the results of Fig. 9 were obtained to provide new information of relevance to designers. They relate to a square inlet, a room of square cross section ($W/H=1$) and a length to height ratio of 3.0, and were obtained with prescribed inlet conditions similar to those used to predict Blum's measured

Downloaded 02 Jun 2010 to 171.66.16.103. Redistribution subject to ASME license or copyright; see http://www.asme.org/terms/Terms_Use.cfm

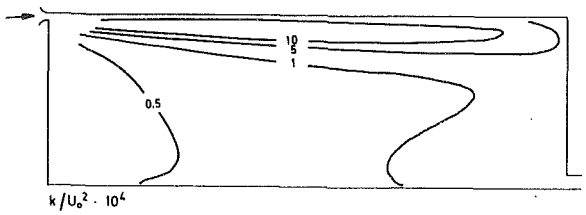

Fig. 8(a) Contours of turbulence kinetic energy

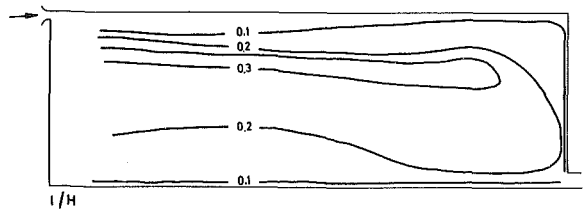

Fig. 8(b) Contours of the length scale $l=k^{3/2}/\epsilon$ $L/H=3$, $W/H=1$, $d/H=0.04$

data. The maximum velocity in the reverse flow, U_{rm}, is plotted against the relative area of the inlet, a/A $(=hw/(HW))$: it is clear that increasing the size of the supply opening also increases the maximum reverse velocity, if the inlet velocity U_0 is kept constant. Closer examination of Fig. 9 indicates that, for small openings, U_{rm}/U_0 tends to vary as $(a/A)^{0.5}$, i.e. the maximum reverse velocity is approximately proportional to the square root of the momentum flow rate at the inlet opening $\sqrt{aU_0}$. This is in accord with the findings of reference 5 for rooms with side wall mounted diffusers.

In practice, the flow rate is commonly determined by air refreshment requirements, i.e. aU_0 must be assumed constant; then U_{rm} increases with decreasing a, and tends to vary as $a^{-0.5}$ for small a/A ratios. In Fig. 9 the results from the earlier two-dimensional calculations have been included and it is clear that although U_{rm} tends to vary as $a^{-0.5}$ in both cases for constant mass flow rate, the two-dimensional values are higher (10 percent at $a/A=0.003$ and 30 percent at $a/A=0.01$).

5 Conclusions

The following more important conclusions may be extracted from the previous text:

1. The measurements provide further evidence of the flow patterns associated with small inlet openings and in particular of the extent of three-dimensionality in the inlet region and in the occupied area of rooms. For identical inlet velocity, the velocity levels associated with the square opening were lower than those for the half width slot of reference [1], as was expected in view of the different inlet areas, but the overall flow patterns in both geometries are closely related.

2. The present numerical solutions of the three-dimensional flow equations allow the representation of available measurements with a precision of around 5 percent of the maximum velocity. The inclusion of differential equations for the conservation of turbulent kinetic energy and dissipation rate is desirable but may not be necessary. The numerical precision is limited by the number of nodes which can be afforded; the precision quoted relates to approximately 1500 nodes in a symmetrical half plane and with a special inlet treatment to obviate the need for a concentration of nodes in this region.

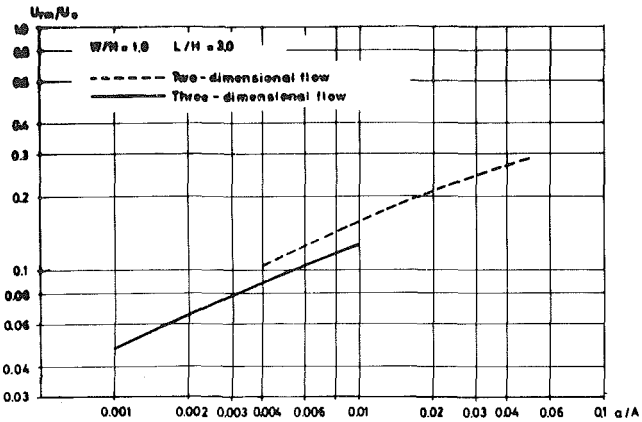

Fig. 9 Calculated nondimensional, maximum reverse velocity as a function of relative inlet area

3. The results indicate that the maximum velocity in the reverse flow is essentially determined by the area of the supply opening and not by its shape, provided the overall dimensions of the opening are small and they also show that U_{rm}/U_0 tends to vary as $(a/A)^{0.5}$ which is consistent with the earlier two-dimensional conclusions although the present values are some 10 to 30 percent lower.

Acknowledgments

The authors wish to acknowledge personal financial support from the Danish Government Fund for Scientific and Industrial Research (PVN) and from Comissão Permanente INVOTAN and Instituto Nacional de Investigacao Cientifica (AR). Danfoss A/S (PVN) and the University of Oporto (AR) kindly released their staff to allow this work to be carried out. The experimental and computational work was supported by the Science Research Council and part of the calculations by Danfoss A/S, to whom all authors record their thanks.

References

1 Nielsen, P. V., Restivo, A., and Whitelaw, J. H., "The Velocity Characteristics of Ventilated Rooms, ASME JOURNAL FLUIDS ENGINEERING, Vol. 100, 1968, p. 308.

2 Nielsen, P. V., Restivo, A. and Whitelaw, J. H., "Buoyancy Affected Flows in Ventilated Rooms," To be published in *Numerical Heat Transfer Journal.*

3 Blum, W., 1956, Diplomarbeit, T. H. Aachen.

4 Hestad, T., "En dimensjoneringsmetode for tilluftsorganer basert på teori, fullskalaforsøk og praktisk erfaring," Tekniska meddelanden nr. 83, Inst. för Uppvärmnings-och Ventilationsteknik, KTH, Stockholm, 1975.

5 Jackman, P. J., "Air Movement in Rooms With Side-Wall Mounted Grilles - a Design Procedure," HVRA, Report No. 65, 1970.

6 Jackman, P. J., "Air Movement in Rooms With Sill-Mounted Grilles - a Design Procedure," HVRA, Report No. 71, 1971.

7 Rajaratnam, N., and Pani, B. S., "Three-Dimensional Turbulent Wall Jets," *Proc. A.S.C.E.*, J. Hydraul. Div., Vol. 100, 1974, p. 69.

8 Sforza, P. M. and Herbst, G., 1970. A study of three-dimensional incompressible turbulent wall jets, J. AIAA, 8, 276.

9 Caretto, L. S., Gosman, A. D., Patankar, S. V., and Spalding, D. B., "Two Calculation Procedures for Steady, Three-Dimensional Flows With Recirculation," *Proc. 3rd Int. Conference on Num. Methods in Fluid Dynamics,* Springer Verlag, 1972.

10 Abou Ellail, M. M. M., Gosman, A. D., Lockwood, F. C. and Megahed, I. E. A., "The Prediction of Reaction and Heat Transfer in Three-Dimensional Combustion Chambers," Presented at AIAA/ASME Thermophysics and Heat Transfer Conference, Palo Alto, May 1978.

11 Sforza, P. M., "Three-Dimensional Free Jets and Wall Jets: Applications to Heating and Ventilation," Polytechnic Institute of New York, 1977.

Downloaded 02 Jun 2010 to 171.66.16.103. Redistribution subject to ASME license or copyright; see http://www.asme.org/terms/Terms_Use.cfm

Aspects of Outflow From Large Vessels

J. Kubie[1]

H. S. Oates

Central Electricity
Research Laboratories,
Leatherhead, Surrey, England

An investigation has been made of flow phenomena associated with outflow from large horizontal cylindrical vessels with a vortex-free outlet on their bottom surface. This paper concentrates on the flow regimes and the variation of the level in the vessels with the flowrate. It is shown, both theoretically and experimentally, that there are two distinct regimes of outflow from the vessel, which are separated by a critical flowrate which is a strong function of the diameter of the outflow orifice. For the flowrates below the critical the level variation does not depend on the diameter of the outflow orifice, but the level variation depends strongly on it for the flowrates above the critical value. A model of transition between the flow regimes is also developed.

1 Introduction

This paper presents an investigation of some aspects of outflow from large horizontal cylindrical vessels with a vortex-free outlet on their bottom surface. This work was undertaken in order to describe the hydraulic behavior, and in particular the variation of the water level in the vessel with the flowrate. Such horizontal vessels are used in many process plants and the importance of the water level in the vessel is that it is one of the parameters which are used to control the operation of the whole plant.

The variation of the water level with the water flowrate is poorly understood, though Simpson [1] gives some attention to the problem of outflow from cylindrical vertical vessels. He shows that at low water flowrates, when the level in the vessel is low, the flow forms a circular weir as it discharges through the outlet. Furthermore, the cross-sectional area of the outlet is not completely occupied by water and the orifice is self-venting. At higher water flowrates the outlet chokes, starts to behave as a conventional orifice and the flowrate depends on the pressure difference over it. Simpson [1] also gives empirical formulae for the transition between the two flow regimes.

Here the problem of a horizontal cylinder is considered and it is shown that the fundamental processes governing the outflow are similar. At low water flowrates the flow can be described by a modified weir equation and the water level then does not depend on the design of the outlet. At higher water flowrates the outflow is governed by a standard orifice-type equation. A method for predicting the transition between the two flow regimes is developed and is shown to be applicable also to the case of a vertical cylindrical vessel.

Only a large vessel, that is a vessel in which the influence of the viscous and the surface tension forces is negligible, is investigated in this work.

2 Experimental Investigations

2.1 Experimental Apparatus. A diagram of the experimental apparatus is shown in Fig. 1. Water, which was used as the working fluid in this work, was introduced through two parallel horizontal manifolds each containing eight downward pointing nozzles. Two kinds of nozzles were used, with diameters of 10 and 20 mm. The water from the smaller nozzles had a substantial downward momentum and created foam in the water. The momentum was reduced by incorporating a 3mm thick horizontal layer of 10 mm by 5.5 mm diamond mesh (approximately 75 percent free area) set 240 mm above the bottom of the vessel, well above the water level.

Various outlet designs were investigated and they are sketched in Fig. 2. It should be noted that Option Ia is a profiled Option I used to investigate the effect of a contoured outlet on the outflow characteristic.

Some vessels have an off-center outlet and this was modelled by placing a baffle in the vessel (as shown in Fig. 1) and by plugging the nozzles to the right of the baffle.

Two basic experimental arrangements were used during the present work: one with a long downcomer (shown in Fig. 1) and the other with a short downcomer. The length of the downcomer in the former case was about 1600 mm and the end of the downcomer was sometimes freely discharging above the water level in the tank and sometimes submerged below the water level (sealed downcomer). In the latter case the downcomer was 80 mm long and it was freely discharging into the tank via a large funnel. The water from the tank was returned by a centrifugal pump to the spray manifolds.

The water flow into the vessel was measured with an orifice plate and the water level near the end of the vessel was measured with a side glass. The static pressure near the top of the long downcomer was measured with an air-water manometer 127 mm below the base of the vessel. The water flowrate was determined to within 3 percent, the water level to within 3 mm and the static pressure near the top of the downcomer to within 10 percent.

[1] Present Address: Engineering Department, CEGB SER, Laud House, London EC1, England.

Contributed by the Fluids Engineering Division for publication in the JOURNAL OF FLUIDS ENGINEERING. Manuscript received by the Fluids Engineering Division, June 13, 1978.

Copyright © 1980 by ASME

Downloaded 02 Jun 2010 to 171.66.16.103. Redistribution subject to ASME license or copyright; see http://www.asme.org/terms/Terms_Use.cfm

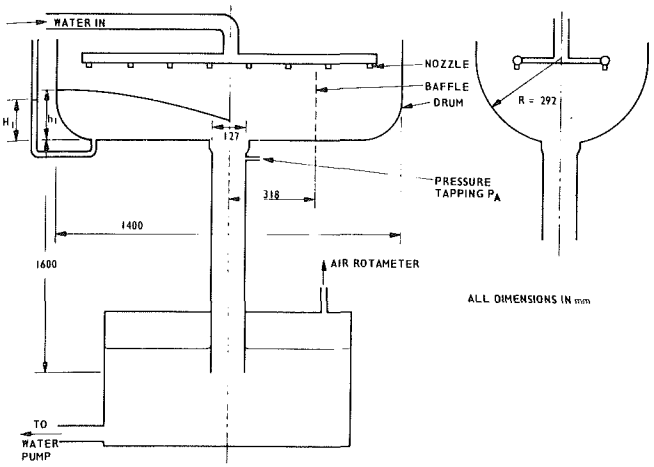

Fig. 1 Experimental arrangements with the long downcomer

2.2 Experimental Results. Experimental results of the perceived water level H_1 (measured as indicated in Fig. 1) versus the total water flowrate for the case of the long downcomer with the sealed outlet are plotted in Figs. 3 and 4 for the case of the off-center outlet (with the baffle) and the center outlet (without the baffle), respectively. Both figures contain results obtained with the three outlet designs and with the two nozzle sizes. It can be seen that the water level depends only on the nozzles used and not on the design of the outlet, and that the level is greater for the smaller nozzles, especially at high water flowrates. (The reason for terminating the experiments with the smaller nozzles at the water flowrate of about 11.5 *l/s* is that, because of the large pressure drop across the smaller nozzles, higher water flowrates could not be achieved.) It is noted that the water level plotted for the off-center outlet is that at the vessel end away from the baffle. The water level at the other end was lower than H_1.

The flow regime within the downcomer was (i) freely-falling water at low water flowrates and (ii) homogeneous full pipe flow of water and entrained air at higher water flowrates. For the case of the low downcomer with the sealed outlet the pressure, p_A, just below the outlet, was about atmospheric during freely-falling water flow regime, indicating a self-venting system between the downcomer and the atmosphere in the vessel. There was an increasingly negative pressure as the water flowrate increased during the full pipe flow regime. This is demonstrated in Fig. 5 from which it can be observed that the transition to full pipe flow takes place at lower water flowrates for smaller outlet orifice diameters.

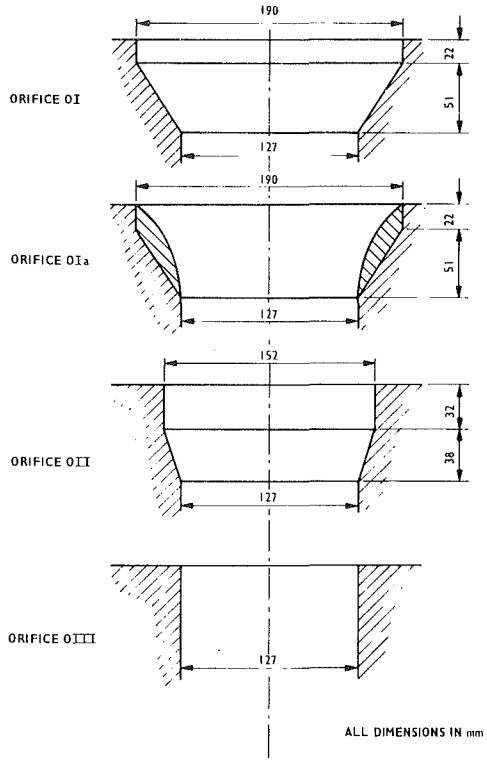

Fig. 2 Outlet orifices used during the present investigation

Experimental results of the perceived water level, H_1, versus the total water flowrate for the case of the short, freely discharging downcomer and the center outflow are plotted in Fig. 6. The figure contains results obtained with the three outlet designs and with the two sizes of nozzles.

The level variations within the vessel for the case of the freely discharging long downcomer were the same as for the case of the sealed long downcomer, provided the transition to full pipe flow had taken place. If, for some reason, full pipe flow could not be achieved, the water level rose. Similarly, the pressure near the top of the downcomer at higher water flowrates was negative when transition to full pipe flow occurred, otherwise it stayed atmospheric.

3 Theoretical Analysis and Discussion

3.1 Weir-Type Outflow. Referring to Fig. 7, assume that the actual level of the fluid at the end of the vessel is, for given flow conditions, equal to h_1. This level depends on (i) the

Nomenclature

A = cross-sectional area of the fluid on the bottom of the vessel, m^2
c_d = discharge coefficient
c_{dc} = generalized liquid discharge coefficient
g = gravitational acceleration, m s^{-2}
h = maximum depth of the fluid on the bottom of the vessel, m
H = equivalent water level, m
H_T = total head, m
ΔH = suction head below the outflow orifice, m
P_A = pressure, N m^{-2}
Q_W = volumetric flowrate to one side of the downcomer, m^3 s^{-1}
Q_T = total volumetric flowrate through the downcomer, m^3 s^{-1}
r = radius of the outflow orifice at the top of the downcomer, m
R = radius of the cylindrical vessel, m
V_{2W} = water velocity at station 2, m s^{-1}
x = distance of the center of pressure below the surface, m
Z = function given by equation (A5)
α = halfangle subtended by the fluid on the bottom of the drum
ϵ = voidage
ϕ = function defined by equation (12)
ρ = density, kg m^{-3}
ψ = function defined by equation (A3)

Subscripts and Superscripts

C = critical value
W = water
0 = obtained with zero voidage
1,2,3 = stations 1, 2, 3

Downloaded 02 Jun 2010 to 171.66.16.103. Redistribution subject to ASME license or copyright; see http://www.asme.org/terms/Terms_Use.cfm

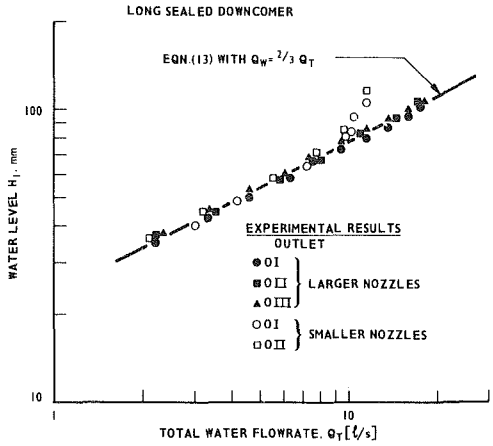

Fig. 3 Variation of the water level with the water flowrate for the off-center outlet with the long sealed downcomer

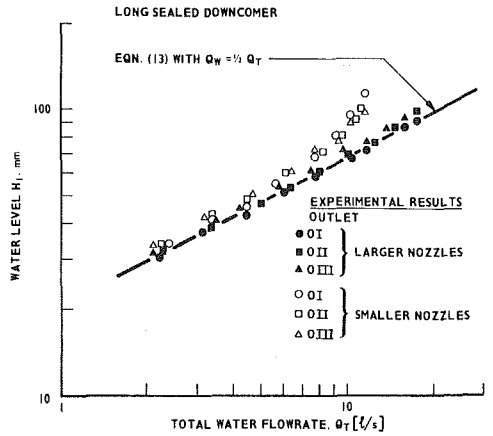

Fig. 4 Variation of the water level with the water flowrate for the center outlet with the long sealed downcomer

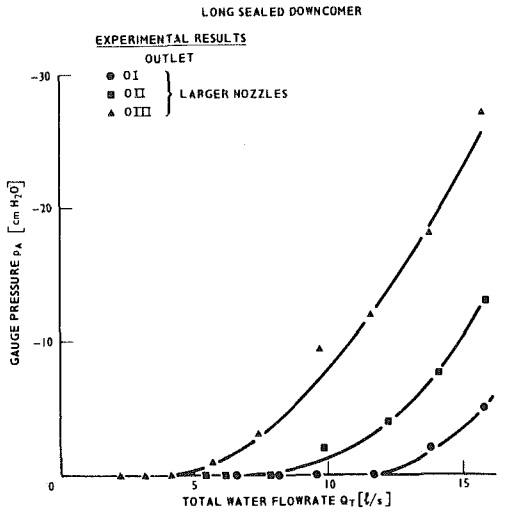

Fig. 5 Plot of pressure p_A versus the water flowrate for the center outlet with the long sealed downcomer

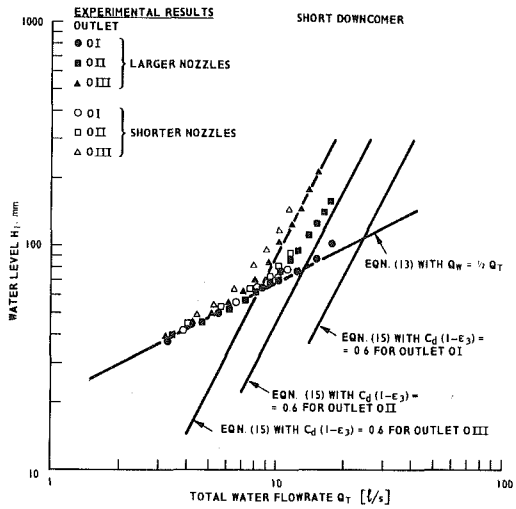

Fig. 6 Variation of the water level with the water flowrate for the center outlet with the short downcomer

design of the vessel and its internals, (ii) the design of the outlet and (iii) the effect of downstream controls and obstructions, the influence of which can propagate upstream to influence the level within the vessel. Obviously, if the level in the vessel is to be controlled by a downstream device, the level must depend predominantly on the resistance provided by this device and should not depend on the design of the vessel and the outlet.

Consider a vessel with a center outlet for which the effect of the downstream obstructions is negligible. The level in the vessel will not depend on the design of the outlet if the outlet can discharge all the fluid supplied to it. Instead the level will be only required to provide a mechanism for supplying the fluid towards the outlet. This problem was investigated by Gardner and Crow [2] for a special case when there is only liquid on the bottom of the vessel. Their method will now be generalized to take into account the influence of entrained air, since because of the method of introducing the water into the vessel, the fluid on the bottom of the vessel consists, in general, of a mixture of water and air.

First, it is assumed that the flow in the vessel may be approximated by a one-dimensional flow along a channel to a plane sink at station 2; the positions of the stations 1 and 2 being shown in Fig. 7. Secondly, the amount of entrained air is quantified in the usual manner by defining an area voidage, ϵ, which is the ratio of the cross sectional area occupied by air mixed with the water on the bottom of the vessel and the total cross sectional area of the air-water mixture there. Consistent with the above assumption it is further assumed that the voidage varies only along the length of the channel and is equal to ϵ_1 and ϵ_2 at stations 1 and 2, respectively.

Neglecting the contribution of air, the momentum balance between stations 1 and 2 is

$$g\rho_1 x_1 A_1 - g\rho_2 x_2 A_2 = \rho_W V_{2W}^2 (1-\epsilon_2) A_2 \tag{1}$$

where ρ is the density, A is the cross-sectional area of the mixture, x is the distance of the center of pressure below the surface, g is the gravitational acceleration, V_{2W} is the water velocity at station 2 and subscripts 1, 2, and W refer to the stations 1 and 2 and the water, respectively.

Since, furthermore

$$V_{2W} = \frac{Q_W}{(1-\epsilon_2)A_2} \tag{2}$$

$$\rho_1 = (1-\epsilon_1)\rho_W \tag{3}$$

$$\rho_2 = (1-\epsilon_2)\rho_W, \tag{4}$$

where Q_W is the volumetric flowrate to one side of the downcomer, equation (1) can be rewritten as

$$(1-\epsilon_1)x_1 A_1 - (1-\epsilon_2)x_2 A_2 = \frac{Q_W^2}{(1-\epsilon_2)g\ A_2} \tag{5}$$

Downloaded 02 Jun 2010 to 171.66.16.103. Redistribution subject to ASME license or copyright; see http://www.asme.org/terms/Terms_Use.cfm

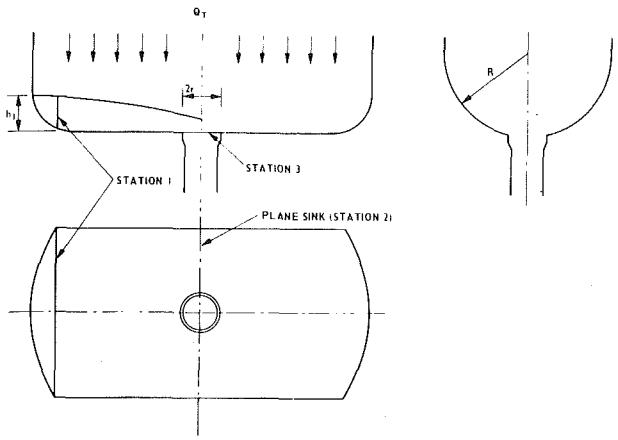

Fig. 7 System considered in the analysis

Assuming that the critical conditions are reached at station 2 (i.e. that the flowrate is maximum), equation (5) can be solved numerically as described in the Appendix and the numerical results can be approximated, with the maximum error of 7 percent, by

$$\frac{h_2}{R} = \frac{2}{3}\left[\frac{1-\epsilon_1}{1-\epsilon_2}\right]^{0.4}\frac{h_1}{R} \tag{6}$$

$$\frac{Q_W}{[gR^5]^{1/2}} = 0.647[1-\epsilon_1]^{0.8}[1-\epsilon_2]^{0.2}\left(\frac{h_1}{R}\right)^{1.98} \tag{7}$$

provided that

$$0.01 \le \frac{h_1}{R} \le 1 \tag{8}$$

$$\left.\begin{aligned}\epsilon_1 &\le 0.9\\ \epsilon_2 &\le 0.9\end{aligned}\right\} \tag{9}$$

where h_1 and h_2 are the maximum depths of the fluid on the bottom of the vessel at stations 1 and 2, respectively, and R is the radius of the horizontal vessel.

However, h_1 is the level of the homogeneous mixture of air and water at the end of the vessel. This level was measured with a water filled side glass and thus an equivalent (or perceived) water level H_1 was determined, which is related to h_1 by

$$H_1 = (1-\epsilon_1)h_1 \tag{10}$$

Thus

$$\frac{Q_W}{[gR^5]^{1/2}} = 0.647\phi(\epsilon)\left(\frac{H_1}{R}\right)^{1.98} \tag{11}$$

where

$$\phi(\epsilon) \simeq \frac{[1-\epsilon_2]^{0.2}}{[1-\epsilon_1]^{1.2}}. \tag{12}$$

When there is only water on the bottom of the vessel, $\epsilon_1 = \epsilon_2 = 0$ and $\phi(\epsilon) = 1$, and the perceived water level H_1^0 is obtained from equation (11) as

$$\frac{Q_W}{[gR^5]^{1/2}} = 0.647\left(\frac{H_1^0}{R}\right)^{1.98} \tag{13}$$

This result is similar to that obtained by Gardner and Crow [2], though it is more accurate over the range $0.01 \le H_1^0/R \le 1.0$. However in the practical range of the ratio H_1^0/R, they are virtually identical.

The perceived levels H_1 and H_1^0 are, from equations (11) and (13), related by

$$\frac{H_1}{H_1^0} \simeq \frac{1}{[\phi(\epsilon)]^{0.5}} \tag{14}$$

Hence the effect of entrained air mixed with water is to alter the measured (or perceived) level, which may rise or fall, depending on the values of ϵ_1 and ϵ_2. It should be noted that, provided the voidage is small it has negligible influence on the level variation.

The theoretical results given by equation (13) are included in Figs. 3, 4, and 6. In Fig. 3 the theoretical result was obtained with $Q_W = 2/3\ Q_T$, since two thirds of the flow was supplied to the side where the level was measured and in Figs. 4 and 6 with $Q_W = \frac{1}{2}\ Q_T$, since the outlet was at the center of the vessel. (It should be noted that equations (11) or (13) should be used only for $Q_W \ge \frac{1}{2}\ Q_T$, since for $Q_W < \frac{1}{2}\ Q_T$ the level is in between that given by equations (11) or (13) and the level on the other side of the vessel.)

For the case of the long sealed downcomer Figs. 3 and 4 show that the theoretical results of equation (13) are in excellent agreement with the experimental data obtained with the larger nozzles but that there is some divergence when smaller nozzles were used. The probable reason for this divergence is that the smaller nozzles discharge the water with greater velocity thus increasing the aeration of the water pool on the bottom of the vessel and hence its voidage. It was observed visually during the experimental work that the voidage ϵ was small at station 1 but considerable at station 2. Equation (14) then shows that the perceived water level could increase by up to $(1-\epsilon_2)^{-0.1}$. The perceived water level obtained with the smaller nozzles, H_1, is, for the water flowrate of 11.5 *l/s*, about 30 percent greater than the level H_1^0 predicted by equation (13). This implies a voidage of about 90 percent which, in view of the high water velocity from the smaller nozzles, is not impossible.

3.2 Orifice-Type Outflow and Transition. For the case of the short downcomer Fig. 6 shows that equation (13) describes the level variation well, provided that the water flowrate is smaller than a certain critical value. For water flowrates greater than the critical the level rises well above those given by equation (13) or equation (11). This is because for high water flowrates the outlet cannot discharge all the fluid supplied to it and it chokes (Souders, et al. [3]). The outlet thus provides the controlling resistance to the flow and the level variation can then be described by the usual orifice-type equation

$$Q_T = c_d[1-\epsilon_3]\pi r^2\sqrt{2gH_T} \tag{15}$$

where

$$H_T = H_1 + \Delta H \tag{16}$$

and where r is the radius of the outlet at the top of the downcomer, ϵ_3 is the voidage there (see Fig. 7), c_d is the coefficient of discharge, which for the single phase flow and large H_1 is about 0.6, and ΔH is the head given by the difference between the static pressure above the water level in the vessel and the static pressure just below the outlet and is, of course, zero for the present arrangement with the short downcomer. The form of equation (15) indicates that in this case the level H_1 depends strongly on the value of the voidage ϵ_3.

It was noted during the experimental work that as H_1 increased during the orifice-type flow, the amount of entrained air, and thus the voidage ϵ_3, decreased. Equations (15) and (16) with $c_d = 0.6$, $\Delta H = 0.0$ and $\epsilon_3 = 0.0$ are included in Fig. 6 which demonstrates that the experimental results tend asymptotically to this line.

It is observed from Figs. 3 and 4 that in the case of the long

Downloaded 02 Jun 2010 to 171.66.16.103. Redistribution subject to ASME license or copyright; see http://www.asme.org/terms/Terms_Use.cfm

sealed downcomer the water levels follow the theoretical line given by equation (13) (or equation (11)) and that no transition to the orifice-type flow is indicated. This is because of the development of the suction pressure below the outlet (see Fig. 5) which increases the total head over the outlet (see equation (16)) thus improving its apparent discharge characteristic so that all fluid supplied to the outlet can be discharged. The level is then controlled by the process of supplying the water towards the outlet – i.e. equation (13) or (11). In the case of the short downcomer the suction pressure below the outlet cannot develop and thus the level H_1 has to increase in accordance with equations (15) and (16) with $\Delta H = 0.0$.

Hence the onset of the development of the suction pressure below the outlet with a long sealed downcomer is thus another indication of the transition to the orifice-type flow and can be used as the criterion for the critical condition.

The critical water flowrate is achieved when the levels given by equations (11), and (15) and (16) with $\Delta H = 0.0$ are the same. Hence

$$\frac{Q_W^C}{[gr^5]^{1/2}} = \left[6.15 c_{dc}{}^2 \frac{(1-\epsilon_1)^{0.6}(1-\epsilon_3)^2}{(1-\epsilon_2)^{0.1}}\right]^{2/3} \left(\frac{r}{R}\right)^{0.175} \quad (17)$$

where c_{dc} is the critical value of the discharge coefficient and Q_W^C is, for the center outlet, half of the total critical water flowrate. It can be observed from equation (17) that the influence of ϵ_1 and ϵ_2 on the critical water flowrate is small compared with ϵ_3 and thus ϵ_1 and ϵ_2 are assumed to be zero. Using the suction pressure curves of Fig. 5 and other experimental data, it is found that at transition to the orifice-type flow

$$c_{dc}(1-\epsilon_3) \simeq 0.4, \quad (18)$$

where the product $c_{dc}(1-\epsilon_3)$ may be regarded as the generalized liquid discharge coefficient for two-phase gas-liquid flow. Substituting equation (18) in equation (17), the critical total water flowrate, Q_T^C, is finally obtained as

$$\frac{Q_T^C}{[gr^5]^{1/2}} \simeq 2\left(\frac{r}{R}\right)^{0.175} \quad (19)$$

which predicts the critical water flowrate to within 15 percent.

Thus for the case of center outlet, the outlet starts choking for the condition of equation (19) when the generalized discharge coefficient is about 0.4. As the flowrate increases, the discharge coefficient rises to about 0.6, as shown in Fig. 6. The change is understandable in that the level at the end of the vessel only approximates to the head over the outlet when the outlet is well submerged.

3.3 Axisymmetric Outflow. The concept of the critical flow for transition between the two regimes of vortex-free outflow from cylindrical horizontal vessels is applied to vertical cylindrical vessels as follows:

For the case of axisymmetric flow from a vertical cylindrical vessel with a flat bottom, the self-venting flow is governed by a weir-type equation, which for the case of zero voidage was derived by Souders, et al. [3] as

$$\frac{Q_T}{[gr^5]^{1/2}} = 3.71\left(\frac{H_1}{r}\right)^{1.5} \quad (20)$$

where H_1 is the depth of the liquid at the edge of the vessel. For high flowrates, when the orifice is choked, the flow is described by the usual orifice-type equation, which for an open vessel with a short downcomer is given by equations (15) and (16) with $\Delta H = 0.0$ and $\epsilon_3 = 0.0$. The critical condition is reached, as in Section 3.2, when the levels given by both equations are the same. Hence the critical level and the critical flowrate for the transition to choking are given as

$$\frac{H_1^C}{r} = 1.2 c_{dc} \quad (21)$$

$$\frac{Q_T^C}{[gr^5]^{1/2}} = 4.86 c_{dc}{}^{1.5} \quad (22)$$

Simpson [1] states that the transition to choking flow takes place at $H_1^C/r = 0.5$. Taking the value of the critical generalized liquid discharge coefficient $c_{dc} = 0.4$, obtained during the present work in horizontal cylindrical vessels, it is found that $H_1^C/r = 0.48$. Simpson further states that $Q_T^C/(gr^5)^{1/2}$ is usually about 1.33, but is sometimes as high as 2.44. The value of the discharge coefficient at transition is about 0.4; however the highest value of the discharge coefficient is about 0.6. Using these two values of the discharge coefficient it is found from equation (22) that $Q_T^C/(gr^5)^{1/2}$ should usually be about 1.23 but that it could be as high as 2.26. Since all the critical values obtained by the present method are close to those quoted by Simpson [1], this adds further confidence in the theories developed in this work.

3.4 Applications. In the case of subcooled liquids the transition to orifice-type flow is not necessarily manifested by a rapid increase in the level in the vessel. This is because, depending on the arrangements of the downcomer, suction pressure can sometimes develop below the outlet and this, as pointed out in Section 3.2, improves the apparent discharge capacity of the outlet.

However, in the case of a saturated liquid, which is in contact only with its vapor, the situation is unambiguous. This is because the pressure in the vessel and the pressure below the outlet both tend to the saturation pressure. This implies that the pressure difference ΔH is zero and thus that the transition to orifice-type flow is always discernible by a rapid rise in the liquid level in the vessel.

4 Conclusions

It has been shown that, as in the case of axisymmetric outflow from vertical vessels, there also are two regimes of vortex-free outflow from large horizontal cylindrical vessels. At low water flowrates the flow is described by a weir-type equation and at higher water flowrates by an orifice-type equation.

An expression has been developed for transition between the two flow regimes. It has been found experimentally that at transition the generalized liquid discharge coefficient is 0.4 which is considerably below 0.6, which is the value for fully developed orifice flow. Hence for flowrates just above the critical the flow is transitional and true orifice flow is delayed to higher flowrates. The model for transition is applicable also to vertical cylindrical vessels.

Acknowledgments

This work was carried out at the Central Electricity Research Laboratories and is published by permission of the Central Electricity Generating Board.

References

1 Simpson, L. L., *Chem. Eng.*, Vol. 75, No. 13, 1968, p. 192.
2 Gardner, G. C., and Crow, I. G., *Chem. Eng. Sci.*, Vol. 26, 1971, p. 211.
3 Souders, M. Jr., Huntington, R. L., Corneil, H. G., and Emert, F. L., *Ind. Eng. Chem.*, Vol. 30, 1938, p. 86.

Downloaded 02 Jun 2010 to 171.66.16.103. Redistribution subject to ASME license or copyright; see http://www.asme.org/terms/Terms_Use.cfm

APPENDIX

The Method of Solution of Equation (5)

The cross-sectional area of the liquid on the bottom of the drum, A, and its moment of inertia, xA, are calculated as

$$A = R^2(\alpha - \sin\alpha \cos\alpha) \tag{A1}$$

$$xA = R^3\psi(\alpha) \tag{A2}$$

where

$$\psi(\alpha) = \frac{2}{3}\sin^3\alpha - \alpha\ \cos\alpha + \frac{1}{2}\sin 2\alpha\ \cos\alpha \tag{A3}$$

and where 2α is the angle subtended by the interface of the liquid on the bottom of the drum. Equation (5) can then be rewritten as

$$\frac{{Q_W}^2}{gR^5}\frac{1}{(1-\epsilon_2)^2} = Z \tag{A4}$$

where

$$Z = (\alpha_2 - \sin\alpha_2\ \cos\alpha_2)\left\{\frac{1-\epsilon_1}{1-\epsilon_2}\psi(\alpha_1) - \psi(\alpha_2)\right\}. \tag{A5}$$

Equations (A4) and (A5) show that the flowrate Q_W depends on two variables, α_1 and α_2, so that an additional constraint must be imposed. Since it can be shown that for each α_1 the flowrate goes through a maximum as α_2 increases, the additional constraint specifies that the flowrate must be at its maximum. This is equivalent to a statement that critical conditions are reached at station 2.

The maximum flowrate is obtained from

$$\frac{\partial Z}{\partial \alpha_2} = 0 \tag{A6}$$

and thus from equation (A5) the relationship between α_1 and α_2 is

$$\frac{\alpha_2^2}{\sin\alpha_2} - 4\alpha_2\ \cos\alpha_2 + 3\ \sin\alpha_2\ \cos^2\alpha_2 + \frac{4}{3}\sin^3\alpha_2 = 2\frac{1-\epsilon_1}{1-\epsilon_2}\psi(\alpha_1). \tag{A7}$$

Equation (A7) must be solved numerically, but the results may be approximated by equation (6). Finally, the numerical solution of equations (A5) and (A7) yields the relationship between the level h_1 and the flowrate Q_W. The numerical solution may be approximated by equation (7).

Downloaded 02 Jun 2010 to 171.66.16.103. Redistribution subject to ASME license or copyright; see http://www.asme.org/terms/Terms_Use.cfm

J. H. Horlock

Vice-Chancellor.
Mem. ASME

C. F. Grainger

Research Fellow,

University of Salford,
Salford, England

Linearized Solutions for the Supersonic Flow Through Turbomachinery Blade Rows (Using Actuator Disk Theory)

An actuator disk method is developed for calculating the flow through the blade rows of a turbomachine in which the velocity relative to the blading may be supersonic. The method is compared with calculations of the fully supersonic flow through a twisted blade row using a three-dimensional method of characteristics.

Introduction

A variety of sophisticated methods for calculating flows in turbomachinery have been developed in recent years (see the reviews by Japikse [1], Horlock and Perkins [2]. Two approaches which have been most widely used are the matrix-through-flow (MTF) and streamline curvature (SLC) methods.

However, there are major limitations which arise in their application. Each method can be used to solve the swirling flow in a duct, or the clearance space between blade rows, when the meridional component of Mach number (M_m) is less than unity, although the absolute flow may be supersonic. They may also be used within the blade rows (with the same limitations on M_m) when the tangential velocity distribution is specified along the streamlines (the "design" problem). However, the methods fail to solve the flow within blade rows of specified geometry (the "analysis" problem), when the Mach number relative to the blade rows (M_{rel}) exceeds unity. The physical interpretation of these limitations is simple. In supersonic swirling duct flow, pressure perturbations can just move upstream from a point when the Mach cone emanating from that point has a forward edge which lies just ahead of the tangential direction (i.e., when the meridional Mach number is just subsonic). In "bladed flows" the cone is restricted by neighboring blade surfaces and pressure perturbations can only move upstream along the streamlines.

These limitations have prevented the use of the MTF and SLC methods in the accurate analysis of high speed flows in turbomachinery where relative Mach numbers exceed unity. This paper describes another approach to the solution of the flow in such machines – an actuator disc method, in which the meridional component of Mach number in the duct flow regions must be less than unity, but relative flow (including that in the blade regions, of small spacing and chord) may be supersonic. (Oates, Knight and Carey [3] have shown that actuator disk theory may be used under such conditions.) Solutions to a fully supersonic flow (through a twisted blade row) obtained by this method are compared with a recently developed characteristics method (for which the relative flow must be supersonic throughout the flow field).

It should be emphasised that the solution given applies only to the case where the blade row is operating at the so-called "choking incidence" condition, when the flow angle at the leading edge is set by the inlet blade shape and inlet Mach number and when the "covered" part of the blading is supersonic. Supersonic rows often operate at or near design point with a slightly detached shock at the leading edge, when such a control on inlet angle is not imposed by the leading edge conditions alone. The analyis given here does not cover that case, but only the less common "incidence choked" condition.

Methods of Calculations Presently Used, and Their Limitations

In the MTF method (Wu [4] and Marsh [5]) the equations of motion are first written in terms of partial derivatives taken along stream surfaces within the flow field. The continuity equation and one momentum equation (usually the radial equation) are then combined into a single second-order partial differential equation for a stream-function (ψ). This equation is converted into a finite difference equation, and solved either by matrix inversion (Marsh) or by relaxation methods (Perkins [6]), together with an equation relating density (ρ) and stream-function (ψ).

The conditions for the stream-function equation to remain elliptic are that $M_m < 1$ (for duct flow or for the design problem with tangential velocity distributions specified) and $M_{rel} < 1$ (for the analysis problem of flow through blading of specified geometry). Further the equation used for calculating the density has two solutions, one for $M_m < 1$, the other for $M_m > 1$ (in the duct flow or design case); and one solution for $M_{rel} < 1$, another for $M_{rel} > 1$ (in the analysis case).

Marsh restricted his solutions to $M_m < 1$ (for duct and "design" flows) and to $M_{rel} < 1$ (for the bladed "analysis" flow) to ensure the basic equation remained elliptic and to

Contributed by the Fluids Engineering Division of The American Society of Mechanical Engineers and presented at the Fluids Engineering Conference, New Orleans, La., March 10–13, 1980. Manuscript received by the Fluids Engineering Division May 29, 1979. Paper No. 80-FE-7.

Copyright © 1980 by ASME

Downloaded 02 Jun 2010 to 171.66.16.103. Redistribution subject to ASME license or copyright; see http://www.asme.org/terms/Terms_Use.cfm

avoid ambiguity in calculation of the density. However, some convergent solutions have been obtained for slightly supersonic flows by various devices (see the review by Horlock and Perkins [2]). Gelder [17] used the density obtained from a previous iteration instead of that obtained from the current iteration. Perkins [6] used a technique similar to that developed by Emmons [8], obtaining convergent solutions for mildly supersonic flow by first solving the density equation, using the stream-function from the previous iteration, and then using the new density values to correct the stream-function solution.

In the SLC method the radial equation of motion is usually written in the form of a differential equation for the meridional velocity c_m viz.

$$\frac{\partial c_m}{\partial r} = c_m K(r) - \frac{L(r)}{c_m} \tag{1}$$

where $K(r)$ and $L(r)$ are functions of the radial coordinate r. Using K and L from a previous iteration, this equation is integrated with respect to r, usually from one annulus wall (where the velocity is guessed as c_{ma}) to the other, to give a new estimate of the meridional velocity $c_m(r)$. The continuity equation is then checked to see if it is satisfied by the estimated distribution of c_m, values of ρ usually obtained from the current iteration, and ϕ, the angle between the meridional streamline and the axial direction. If continuity is not satisfied, the starting value of c_{ma} is changed until it *is* satisfied. The streamlines may now be located in the meridional plane, and their slope (ϕ) and radius of curvature (r_c) are determined. New values of $K(r)$ and $L(r)$ are obtained, and the cycle of calculations is repeated.

Marsh [9] has shown that unique solutions can only be obtained in this way if $M_m < 1$ (for duct flows and the "design" case) and $M_{rel} < 1$ (for solutions within blade rows in the "analysis" case); that is, for the same limiting conditions which apply to the MTF method. However, he shows that if Gelder's technique is used (employing density from the previous rather than the current iteration) the solution is always unique.

To summarize the present position, the MTF method has been used to great effect with calculation grid points within the blade rows, but it is subject to the Mach number limitations which Wu originally specified: the most critical is that the relative flow within the blade rows should be subsonic in the "analysis" case. The SLC method has also been widely used; it has similar limitations although, as Marsh [9] points out, these have not perhaps been appreciated. It has been employed to obtain answers (but essentially incorrect ones) when the relative flow is supersonic within blade rows of specified geometry but when the calculation stations are located outside the rows. At such a station $M_m < 1$ and the outlet angle from the upsteam row is known, so a unique solution for $c_m(r)$ is obtained. However, information from this solution is then allowed to pass through the upstream blade rows via the next calculation of streamline curvature (r_c). For the "analysis" case such information should not be transmitted if the local relative Mach number within the blade row is supersonic; further the supersonic flow may impose restrictions on flow angles at blade leading edge stations which are not taken account of in most calculations.

We should note, however, that the SLC method has been successfully used by Bindon and Carmichael [10] for supersonic relative flow in the "blade-to-blade" plane; these are essentially two-dimensional duct flows, similar to the nozzle flows studied by Emmons [8]. Bindon and Carmichael integrate the equation of motion normal to the streamlines, and use only "upwind" distributions of velocity to determine streamline curvature when the local flow becomes supersonic. They appear to obtain convergent solutions for the same type of mildly supersonic flows that Gelder studied.

There is a further complication in determining unique solutions in supersonic swirling flow, by both MTF and SLC methods. It may be illustrated by reference to transonic flow through a turbine row.

Usually, in calculating the flow at a trailing edge station the outlet angle is specified from the blade geometry and two-dimensional information (empirical or calculated). In supersonic flow the outlet angle is a function not only of the blade geometry but also the pressure ratio between the blade throat and the trailing edge (see Horlock [11]). Since the contraction or expansion of the streamlines between these stations in the meridional plane is unknown, that pressure ratio is also unknown and the outlet angle to be used in the MTF or SLC methods is initially indeterminate. Similarly, at the leading edge of a compressor row, two-dimensional information suggests that in supersonic flow the inlet angle is a unique function of blade geometry and the local (leading edge) Mach number. The spanwise distribution of flow angle at that axial location cannot therefore be specified until the local Mach number is known. That comes only from solution of the MTF or SLC equations, which are in turn dependent on specification of the radial distribution of the flow angles, including that at the leading edge.

The limitations of the two methods, in the analysis of the flow in transonic and supersonic turbomachines, have been recognized and alternative methods have been developed for

Nomenclature

$\bar{c}, c$ = vector, scalar velocity
c_p, c_v = specific heats
f = impulse function
h = enthalpy
l = blade length
p = pressure
g = general property
r = radius
s = entropy
u, v, w = velocty components
x, y, z = coordinate system
A_n = Fourier coefficients (for velocity perturbation)
F, G, H = constants defined in Appendix
K, L = functions of radius
M = Mach number
T = temperature
Q_n, T_n, U_n, V_n = Fourier coefficients
α = flow angle (angle between blade-to-blade streamline and axial directions)
β = blade angle
γ = ratio of specific heats
ϵ = blade spacing
ϕ = streamline slope (angle between meridional streamline and axial direction)
ψ = streamfunction
ρ = density
ξ = stagger of blades
λ = $(1 - \bar{M}_x^2)^{1/2}$

Subscripts

c = relating to curvature in meridional plane
d = just downstream of disc
m = meridional
0 = stagnation conditions
rel = relative
u = just upstream of disc
x = in x direction
1 = far downstream
2 = far upstream or far downstream

Superscripts

$-$ = mean (average in spanwise direction)
= perturbation

Downloaded 02 Jun 2010 to 171.66.16.103. Redistribution subject to ASME license or copyright; see http://www.asme.org/terms/Terms_Use.cfm

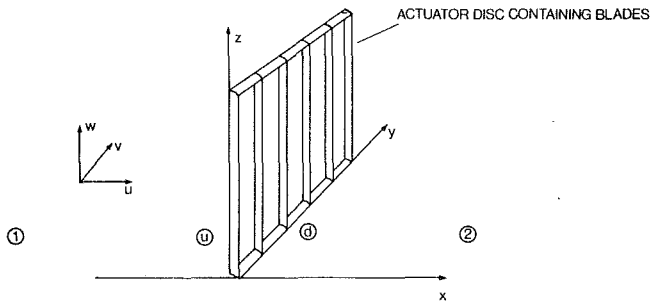

Fig. 1 Coordinate system

use in such cases. One such alternative is the time-marching method devised by MacDonald [12] and developed by Denton [13], which has no similar Mach number limitations but is expensive in computer time, particularly in three dimensions. Another method now available for flows which are everywhere relatively supersonic is the three-dimensional characteristic solution developed by Walkden [14] and applied to turbomachinery flows by Grainger [15], [16]; but again this method is expensive in computer time.

In this paper we introduce a simpler method of dealing with flows where $M_{rel} > 1$ but the meridional Mach number (M_m) is less than unity. We use actuator disk theory, which has been used by Hawthorne and Ringrose [17] to give linearised solutions for free vortex flows (or flows with small shear) under such conditions. Oates, Knight, and Carey, [3] have presented a variational formulation of the compressible through flow problem which enables the calculation of flow through highly loaded disks to be made. Here we develop the linearized solution of Hawthrone and Ringrose, for supersonic entry flow.

The actuator disk method tackles the flow within a blade row by artifically reducing the blade chord to zero and then matching two duct flows (one upstream, one downstream) across a disk or discontinuity. Because the chord is assumed to be very small, it is valid to assume the local "blade-to-blade" flow is essentially two-dimensional. So, in subsonic flows, two-dimensional information (e.g., blade outlet angle, blade losses) has been introduced in the matching process. In this paper we allow the absolute or relative flow to be supersonic; we use the (valid) acutator disk solutions for axially subsonic duct flow on either side of the disk and again introduce two-dimensional information about the blade sections in the matching process. However, this information now relates to supersonic flow.

Use of the SLC method to calculate meridional plane solutions with relative supersonic flows within the blade rows was criticised above because supersonic effects are usually ignored. The actuator disk method developed here cannot be subjected to criticism on this score, although it does involve the basic approximation of reducing the blade chord to zero. But it should be reasonably accurate in the prediction of the complicated three-dimensional supersonic flow through blade rows of high aspect ratio, such as large ducted fans and the final rows of L.P. steam turbines.

However, it should be emphasized again that the solution is only valid for the case of "fully started" supersonic flows, when the flow rate is controlled by the geometry of the leading part of the blading (and the entry Mach number, for curved blades). If the back pressure is too high or the downstream throat too small, an "unstarted" flow is obtained with detached bow wave shocks, and the back pressure sets the flow rate (see Starken [18] for a discussion of these flow regimes, and Dunker, Strinning and Weyner [19] for an experimental study of the flows in a transonic axial compressor rotor).

Actuation Disk Analysis for Supersonic Flow

General Discussion. Subsonic compressible flow through cascade actuator disks has been studied by Horlock [20], for shear flows (in Cartesian and coordinates) and by Hawthorne and Ringrose [17], for perturbations of three-dimensional free vortex flows (in cylindrical coordinate). Here we develop the former analysis for flow where the absolute velocity is supersonic but the axial component of Mach number is less than unity; the extension to cylindrical coordinates is straightforward. We assume flow of a perfect gas.

Figure 1 shows the (x, y, z) coordinate system that we use, with the disk (u/d) located at $x = 0$. The entry and exit flows, at stations 1 and 2 respectively, have no "radial" component of velocity ($w = 0$), there being no pressure gradient there

$$\frac{dp_1}{dz} = \frac{dp_2}{dz} = 0$$

However, nonuniform velocity distributions ($u(z) = \bar{u} + u_\infty'(z)$, $v(z) = \bar{v} + v_\infty'(z)$) may exist at these two locations; the bar superscript indicates a mean velocity (averaged in the spanwise direction), and the subscript infinity refers to station 1 or station 2. u_∞', v_∞' are rotational velocity distributions there.

It is shown in reference (20) that additional irrotational perturbation velocities u', v' may arise upstream and downstream of the actuator disc, of the form:

$$u' = -\sum_{n=1}^{\infty} \frac{A_{nu}}{\lambda_1} e^{n\pi x/\lambda_1 l} \cos\frac{n\pi z}{l} \tag{2a}$$

$$w' = \sum_{n=1}^{\infty} A_{n_u} e^{n\pi x/\lambda_1 l} \sin\frac{n\pi z}{l} \quad (-\infty < x < 0) \tag{2b}$$

$$u' = \sum_{n=1}^{\infty} \frac{A_{n_d}}{\lambda_2} e^{-n\pi x/\lambda_2 l} \cos\frac{n\pi z}{l} \tag{3a}$$

$$w' = \sum_{n=1}^{\infty} A_{n_d} e^{-n\pi x/\lambda_2 l} \sin\frac{n\pi z}{l} \quad (0 < x < \infty) \tag{3b}$$

where

$$\lambda_1 = (1 - \bar{M}_{x_1}^2)^{1/2}, \quad \lambda_2 = (1 - \bar{M}_{x_2}^2)^{1/2}$$

and $\bar{M}_{x_1}$, $\bar{M}_{x_2}$ are axial components of the mean Mach number upstream and downstream.

Further it is shown that density perturbations associated with these irrotational velocity fields are given by

$$\frac{\rho'}{\bar{\rho}} = -\bar{M}_x^2 \left(\frac{u'}{\bar{u}}\right) \tag{4}$$

The tangential velocity components cannot change between the infinity station (∞) and the disc.

$$\left.\begin{aligned} v_1(z) &= v_u(z) \\ v_2(z) &= v_d(z) \end{aligned}\right\} \tag{5}$$

since no tangential force is exerted on the fluid outside the disc.

All these relations hold for supersonic flow as long as $\bar{M}_x < 1$; however, other critical differences from subsonic flow arise.

Under subsonic conditions the overall mass flow (from a reservoir of given stagnation conditions) is set by back pressure p_2. Across the disc (say a stator row) a stagnation pressure loss (or entropy increase $\Delta s = s_d - s_u$) is usually specified, together with the outlet gas angle ($\alpha_d = \tan^{-1}(v_d/u_d)$), both usually as functions of the inlet flow angle ($\alpha_u = \tan^{-1}(v_u/u_u)$). The entropy drifts unchanged along the

Downloaded 02 Jun 2010 to 171.66.16.103. Redistribution subject to ASME license or copyright; see http://www.asme.org/terms/Terms_Use.cfm

streamlines, and for small perturbations of the mean flow $s_1(z) = s_u(z)$, $s_2(z) = s_d(z)$. The velocity components $u_2(z)$, $v_2(z)$ are derived from the analysis, so the kinetic head may be subtracted from the known stagnation condition ($h_{02} = h_{0d} = h_{0u} = h_{01}$) to give static enthalpy h_2 (or temperature T_2). With s_2 and h_2 (or T_2) thus known, the thermodynamic state is specified and the static pressure p_2 determined. It is this static pressure which must be applied as a back pressure to the cascade to pass the required flow.

For the actuator disk in subsonic flow, given the inlet conditions ($h_{01}(z)$, $u_1(z)$, $v_1(z)$) and the performance of the cascade ($\alpha_d(z)$, $\Delta s(z)$), there are essentially five unknowns to be determined: $u_2(z)$, $v_2(z)$, A_{n_u}, A_{n_d} and one thermodynamic property (say s_2).

These five unknowns are obtained by applying the following conditions across the disc:

continuity $\rho_u u_u = \rho_d u_d$ (6)

radial momentum $\rho_u u_u w_u = \rho_d u_d w_d$ (7)

stagnation enthalpy $h_{0_d} = h_{0_u}$ (8)

Kutta condition at d $v_d = u_d \tan \alpha_d$ (9)

entropy change $s_d = s_u + \Delta s$ (10)

The equations for stagnation enthalpy and entropy are usually combined using the Crocco equation,

$$\nabla h_0 - T \nabla s = \tilde{c} \times \tilde{\omega} \tag{11}$$

where $\tilde{\omega}$ is the vorticity.

In supersonic flow we have a more difficult problem of matching the flow at the disk, although the five unknowns remain unchanged. We again assume that, because the blade chord (disk thickness) is small compared with blade length, the local flow within the disc is two-dimensional (as is assumed for subsonic flow in the specification of α_d and Δs).

In two-dimensional supersonic blade-to-blade flows, "fully started," which we study here, the flow relative to the blading is supersonic, the flow angle at the leading edge (α_u) is set by the blade inlet angle β_u and inlet Mach number; in particular if the blades are flat plates then $\alpha_u = \beta_u$, independent of Mach number. Further the outlet angle and the entropy change are functions of the blade geometry and the pressure ratio (p_u/p_d). Several analyses for determining the outlet angle have been given (see Horlock [11]). Perhaps the best of these analyses is that given by Traupel (21); in order to obtain α_d and Δs for a turbine row he applies the momentum equation parallel to the blading downstream of the throat, together with continuity and energy equations.

For the actuator disk in supersonic flow we again use

continuity $\rho_u u_u = \rho_d u_d$ (6*a*)

radial momentum $\rho_u u_u w_u = \rho_d u_d w_d$ (7*a*)

stagnation enthalpy $h_{0_u} = h_{0_d}$ (8*a*)

as in subsonic flow. However, we replace the *trailing edge* flow angle condition by one at the *leading edge*, the unique incidence condition,

$$\alpha_u = \tan^{-1}(v_u/v_d) \tag{12}$$

where α_u is specified.

One further equation is then required. Our initial attempts at solution involved specifying both α_d and $\Delta s = s_d - s_u$ as in subsonic flow, obtaining these from the two-dimensional "Traupel-type" analysis, both α_d and Δs being determined as functions of p_u/p_d (or ρ_u/ρ_d).

However, this approach gave a total of six equations for the five unknowns, and overspecified the problem; the "Traupel-type" analysis involves use of two of the equations ($\rho_u u_u = \rho_d u_d$ and $h_{0u} = h_{0d}$) which are already used in the three-dimensional matching relation anyway.

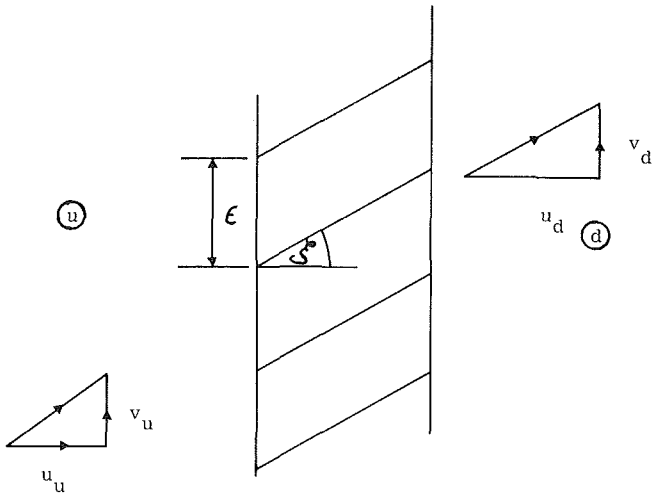

Fig. 2 Flow across actuator disk of flat plates

We have therefore simply used one additional equation – the momentum equation parallel to the blades – at all radial stations. For flat plates, the supersonic entry flow is parallel to the blades of stagger (ξ) but the leaving flow will, in general, be at a different angle ($\alpha_d = \tan^{-1}(v_d/u_d)$). Figure 2 illustrates the flow within and just outside of the disc. We write the momentum equation in the direction of the stagger line (neglecting shear stresses) as

$$f_u = p_u \epsilon \cos\xi + \rho_u u_u \epsilon \, (u_u \sec \xi)$$
$$= f_d = p_d \epsilon \cos\xi + \rho_d u_d \epsilon \, (u_d \cos \xi + v_d \sin\xi)$$

i.e. $$p_u + \rho_u u_u^2 \sec^2 \xi = p_d + \rho_d u_d (u_d + v_d \tan\xi) \tag{13}$$

We develop this approach for a cascade of flat plates in the Appendix.

In summary, the general approach to supersonic flow through an actuator disk is as follows. To find the five unknowns ($u_2, v_2, s_2, A_{n_u}, A_{n_d}$) we match specific mass flow (ρu), radial velocity (w) and stagnation enthalpy (h_0) across the disc; we replace the control of angle (α_d) at the trailing edge (in subsonic flow) by control of angle (α_u) at the leading edge (in supersonic flow); and we replace the specified entropy change (Δs in subsonic flow) by use of the momentum equation parallel to the blades (matching $f_u = f_d$). In doing so we note that matching of ρu, h_0, f can be combined, as in Traupel's two-dimensional analysis, to give α_d and ($s_d - s_u$) as functions of (p_u/p_d), although we do not develop the analysis in that way.

It must be emphasized that *in supersonic flow* it is the inlet angle (α_u) that controls the flow rate – not, as in subsonic flow, the back pressure p_2, assuming however that p_2 is low enough to create supersonic flow inside the blade passage.[1] p_2 can be varied to alter the outlet angle α_d but not the flow rate (the downstream state is determined from p_2 and $h_2 = h_{0_2} - (u_2^2 + v_2^2)/2$ and the entropy s_2 is thus obtained). *In subsonic flow* $\Delta s = s_d - s_u$ is specified and gives the fifth unknown directly – a second thermodynamic property (s_2) far downstream, from which p_2 can be obtained.

Detailed Analysis. As an example of this general approach to supersonic flow through a cascade actuator disk, we

[1] The phase "inside the blade passage" is necessary here in order to exclude the case in which the upsteam flow is supersonic, but the back pressure is high enough, or the throat is small enough, to cause the blades to operate with detached bow wave shocks, as discussed in the introduction. This is sometimes referred to as "stable subscritical" or "unstarted" operation.

Downloaded 02 Jun 2010 to 171.66.16.103. Redistribution subject to ASME license or copyright; see http://www.asme.org/terms/Terms_Use.cfm

describe the three-dimensional flow through a twisted, "flat-plate" cascade (of stagger $\xi(z)$) as a perturbation of a two-dimensional flow through an untwisted cascade with the same mean stagger ($\bar{\xi}$). In that basic flow (described by a bar superscript) the flow is at zero incidence, and the inlet flow conditions ($u_1 = \bar{u}$, $v_1 = \bar{v}$, $M_1 = \bar{M}$, $\alpha_1 = \bar{\xi}$) are unchanged in passage through the cascade (u/d) to station 2.

Perturbations of this basic flow may be caused by:

(i) a small change in back pressure

$$p_2' = p_2 - \bar{p}$$

(*ii*) a small change in stagger,

$$\xi' = \xi(z) - \bar{\xi}$$

(iii) a small rotational change in entry velocity, either

$$v_1' = v_1(z) - \bar{v}$$

or

$$u_1' = u_1(z) = \bar{u}$$

The first change causes a two-dimensioal perturbation, but the second and third cause three-dimensional perturbations.

We indicate small perturbations from the basic flow by a dash subscript ($'$); they may be expressed as the sum of a Fourier series. Thus, for example, a perturbation $q' = q - \bar{q}$ may be expressed in the form

$$q' = Q_0 + \sum_{n=1}^{\infty} Q_n \cos\frac{n\pi z}{l} \tag{14}$$

The irrotational perturbations u' and w' described by equations (2) and (3), do not involve constant terms (such as Q_0) since they are both zero at $x = \pm\infty$. The rotational perturbations of velocity at entry (u_1', v_1'), and of stagger (ξ'), similarly do not involve constant terms; a change of stagger, constant along the blade length, would cause an associated (constant) change in $\bar{u}$ and $\bar{v}$ and is best dealt with by assuming a different basic two-dimensional flow. However, the perturbation p_2' can involve *only* a constant term (P_0), since there can be no variation of pressure with z far downstream. Finally, we shall assume that the rotational perturbations at entry may be imposed without change of the thermodynamic state at 1 – i.e., $p_1' = \rho_1' = T_1' = s_1' = 0$. This implies that the shear at entry is caused not by introduction of irreversibility (e.g., gauzes, or losses in previous blade rows) but by variations in stagnation enthalpy and flow angle (e.g., by work variation in an upstream blade row). The analysis given below can easily be modified to deal with the alternative of shear production by irreversibility (i.e., of h_{01} and p_1 constant, T_1 and ρ_1 variable).

The local value of a flow property is written as the sum of the basic value, the "infinity" (rotational) perturbation and the irrotational perturbation:

$$q = \bar{q} + q_1'(z) + q'(x, z) \quad \text{upstream}$$

or

$$q = \bar{q} + q_2'(z) + q'(x, z) \quad \text{downstream}$$

We consider first the radial momentum equation (7) which, with the continuity equation (6), yields

$$w_u = w_d \tag{15}$$

From equations (2*b*) and (3*b*) for the radial velocity, it follows that

$$A_{n_u} = A_{n_d} = A_n \tag{16}$$

We next apply the leading edge condition

$$\tan\alpha_u = \tan\xi = v_u/u_u$$

i.e. $$\tan(\bar{\xi} + \xi') = \tan\bar{\xi} + \Delta(\tan\xi) = \frac{(\bar{v}+v_1')}{(\bar{u}+u_1'+u_u')}$$

so that

$$\left(\frac{u_u'}{\bar{u}}\right) = \left(\frac{v_1'}{\bar{u}}\right)\cot\xi - \frac{\Delta(\tan\xi)}{\tan\bar{\xi}} - \left(\frac{u_1'}{\bar{u}}\right) \tag{17}$$

With

$$\Delta(\tan\xi) = \sum_{n=1}^{\infty} T_n \cos\frac{n\pi z}{l} \tag{18}$$

$$u_1' = \sum_{n=1}^{\infty} U_n \cos\frac{n\pi z}{l} \tag{19}$$

$$v_1' = \sum_{n=1}^{\infty} V_n \cos\frac{n\pi z}{l} \tag{20}$$

and from (2*a*)

$$u_u' = -\sum_{n=1}^{\infty} \frac{A_n}{\bar{\lambda}} \cos\frac{n\pi z}{l} \tag{21}$$

it follows that

$$\bar{u}T_n + \tan\bar{\xi}(U_n - (A_n/\lambda)) = V_n$$

and

$$A_n = \bar{\lambda}\{(\bar{u}T_n - V_n)\cos\bar{\xi} + U_n\} \tag{22}$$

The perturbation velocity field (u', w') is thus completely defined on *both* sides of the disc by application of two conditions – the twist given to the blading and the upstream shear distribution.

The remainder of the solution involves determination of the rotational velocity distributions far downstream ($u_2'(z)$, $v_2'(z)$) and the outlet thermodynamic state. $p_2 = \bar{p} + p_2'$ is specified, and we choose the second property to be determined as $\rho_2 = \bar{\rho} + \rho_2'(z)$. In the general case we would now match (ρ_u), h_0 and f across the disc. However, for the case of a small perturbation from the basic (—) flow, it may be shown that conservation of these three quanities leads to the result that the entropy change is of second order (see Appendix). We can, therefore, obtain a solution by using the isentropic relation between density change and pressure change immediately,

$$\frac{\rho_2'}{\bar{\rho}} = \frac{1}{\gamma}\left(\frac{p_2'}{\bar{p}}\right) \tag{23}$$

and two of the three conservation equations (say continuity and stagnation enthalpy).

The continuity equation yields

$$(\bar{\rho} + \rho_u')(\bar{u} + u_1' + u_u') = (\bar{\rho} + \rho_2' + \rho_d')(\bar{u} + u_2' + u_d')$$

or

$$\frac{u_2'}{\bar{u}} + \frac{\rho_2'}{\bar{\rho}} = 2\lambda^2\frac{u_u'}{\bar{u}} + \frac{u_1'}{\bar{u}}$$

$$= 2\lambda^2\left(\frac{v_1'}{\bar{v}}\cot\bar{\xi} - \frac{\Delta(\tan\xi)}{\tan\bar{\xi}}\right) + \frac{u_1'}{\bar{u}}(1 - 2\lambda^2) \tag{24}$$

The stagnation enthalpy equation gives

$$\left(\frac{\gamma}{\gamma-1}\right)\frac{p_u}{\rho_u} + \frac{(u_u^2 + v_u^2)}{2} = \left(\frac{\gamma}{\gamma-1}\right)\frac{p_d}{\rho_d} + \frac{(u_d^2 + v_d^2)}{2}$$

and with

$$p_u = \bar{p} + p_u' = \bar{p} - \bar{\rho}\bar{u}^2\left(\frac{u_u'}{\bar{u}}\right)$$

$$p_d = \bar{p} + p_d' + p_2'$$

$$= \bar{p} - \bar{\rho}\bar{u}^2\left(\frac{u_d'}{\bar{u}}\right) + p_2'$$

Downloaded 02 Jun 2010 to 171.66.16.103. Redistribution subject to ASME license or copyright; see http://www.asme.org/terms/Terms_Use.cfm

$$\rho_u = \bar{\rho}\left(1 - \bar{M}_x^2 \frac{u_u'}{\bar{u}}\right)$$

$$\rho_d = \bar{\rho}\left(1 - \bar{M}_x{}^2 \frac{u_d'}{\bar{u}}\right) + \rho_2'$$

it follows that

$$\frac{u_2'}{\bar{u}} + \tan\bar{\xi}\frac{v_2'}{\bar{u}} - \frac{1}{(\gamma-1)}\bar{M}_x{}^2\left(\frac{\rho_2'}{\bar{\rho}}\right) = \frac{u_1'}{\bar{u}} + \tan\bar{\xi}\left(\frac{v_1'}{\bar{u}}\right) - \left(\frac{\gamma}{\gamma-1}\right)\frac{p_2'}{\bar{\rho}\bar{u}^2} \quad (25)$$

Equations (23), (24) and (25) are three equations for $(u_2'/\bar{u})$, $(v_2'/\bar{u})$, $(\rho_2'/\bar{\rho})$ in terms of $(p_2'/\bar{\rho}\bar{u}^2)$, $(u_1'/\bar{u})$, $(v_1'/\bar{u})$. Their solution gives

$$\frac{u_2'}{\bar{u}} = (1 - 2\lambda^2)\frac{u_1'}{\bar{u}} + 2\lambda^2 \cot\bar{\xi}\frac{v_1'}{\bar{u}} - 2\gamma^2\frac{\Delta(\tan\xi)}{\tan\bar{\xi}} - \frac{p_2'}{\gamma\bar{p}} \quad (26)$$

$$\frac{v_2'}{\bar{u}} = 2\lambda^2\frac{u_1'}{\bar{u}}\cot\bar{\xi} - \lambda^2\cot\bar{\xi}\left(\frac{p_2'}{\bar{\rho}\bar{u}^2}\right) + (1 - 2\lambda^2\cot\bar{\xi})\frac{v_1'}{\bar{u}} + 2\lambda^2\cot\bar{\xi}\frac{\Delta(\tan\xi)}{\tan\bar{\xi}} \quad (27)$$

$$\frac{\rho_2'}{\bar{\rho}} = \frac{1}{\gamma}\frac{p_2'}{\bar{p}} \quad (23)$$

and the various Fourier coefficients related, if required.

The problem is now completely solved. Equations (6) and (22) give the three-dimensional flow in terms of the upstream shear $(u_1'/\bar{u},\ v_1' - \bar{v})$ and the blade twist $(\Delta(\tan\xi)/\tan\xi)$. Equations (23), (26) and (27) give the downstream infinity flow conditions at station 2 in terms of the same variables, plus the variation in the back pressure.

The Characteristics Method

A method of calculating three-dimensional fully supersonic flows through turbomachinery blade rows has been developed by Grainger using numerical analysis devised by Walkden [14]. The flow field is initially transformed into a set of coordinates based on the body geometry, and a method of characteristics is then used, it being assumed that the flow is isentropic.

Grainger's initial studies [15] related to two-dimensional flow through cascades, but subsequently he developed the method for three-dimensional flow through blade rows [16]. In particular, he has calculated the supersonic flow through three-dimensional stationary and rotating blade rows, including the flow through a twisted flat plate cascade.

Comparison of the Two Methods

The actuator disk method has been compared with Grainger's calculation of the supersonic flow through a cascade of twisted flat plates. The mean cascade stagger $(\bar{\xi})$ was taken as 60 deg and the inlet Mach number M_{rel} as 1.6. The axial Mach number was thus 0.8 $(\bar{M}_x = 1.6\cos 60°)$ with $\lambda_1 = \lambda_2 = 0.6$. A linear variation of $(\Delta\tan\xi)/\tan\xi$ was introduced to determine its effect alone (p_2', u_1' and v_1' were set at zero). The maximum variation of $\Delta(\tan\xi)/\tan\bar{\xi}$ was 0.144 at the ends of the plates. An aspect ratio (blade length to chord) of 5 was specified for the calculation using the method of characteristics.

Comparisons between the two methods of calculation are plotted in Fig. 3. The velocity perturbations are normalized with respect to the upstream velocity. The results of the characteristics calculation were averaged from blade to blade.

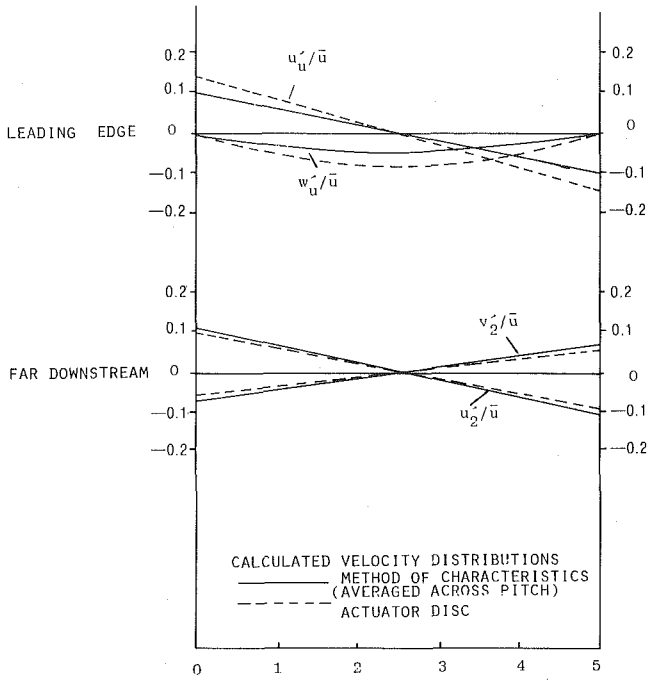

Fig. 3 Flow through twisted cascade (blade axial chord unity for characteristics solution)

Agreement between the results is good, but the actuator disk method over-estimates the magnitude of the three-dimensional flow. Agreement would be expected to be better still for higher aspect ratio (i.e., with the blade geometry approaching more closely the concept of an actuator disk of vanishing chord).

Discussion

Clearly the actuator disc approach gives a correct physical interpretation of what happens in three-dimensional supersonic flows through blade rows. As in other applications of actuator disk theory, its value is probably in providing such a physical description rather than a method of calculation that is of immediate use in practical cases.

The extension of the analysis to supersonic free-vortex flow in cylindrical coordinates is not difficult and leads to similar expressions for the three-dimensional perturbations. But designers are more likely to wish to know how their existing numerical methods can be modified in the light of the current work.

A major conclusion is that the assumption of "two-dimensional unique incidence" used in the actuator disc analysis is quite good for aspect ratios of 5:1 and greater. For lower aspect ratios there appears to be little alternative to using either the method of characteristics or a time marching method.

For high aspect ratios blading, it should be possible to use either the MTF or SLC methods outside the blade rows, but with the *entry* angles controlled by two-dimensional unique incidence in supersonic regions. It should also be possible to use developments of the "Traupel-type" of two-dimensional analysis to give local *outlet* angle and entropy increase.

The actuator disc analysis shows that radial shifts of meridional streamlines take place downstream of a single disc to correct the radial movement upstream that is necessary to meet the "unique incidence" condition. But pressure changes downstream cannot be transmitted through the supersonic flow within the blade row to modify this three-dimensional

Downloaded 02 Jun 2010 to 171.66.16.103. Redistribution subject to ASME license or copyright; see http://www.asme.org/terms/Terms_Use.cfm

movement of the flow upstream. The calculation of streamline curvature at an axial location from information on streamline shapes downstream is clearly of doubtful validity when the flow past the blading is relatively supersonic.

Conclusions

An actuator disk method of analysis has been developed for the estimation of three-dimensional flow through cascades of twisted blades in which the relative flow is supersonic, but the axial component of Mach number is less than unity. The dominant feature in such three-dimensional flows is that of the "unique incidence" effect which occurs at the leading edge of the blading and which produces sufficient radial flow between far upstream and the leading edge to ensure that the entry flow is locally of correct incidence.

References

1 Japikse, D., "Review-Progress in Numerical Turbomachinery Analysis," ASME JOURNAL OF FLUIDS ENGINEERING, Vol. 98, 1976, pp. 592-606.

2 Perkins, H. J., and Horlock, J. H., "Computation of Flows in Turbomachinery," *Finite Elements in Fluids,* Chapter 8, J. Wiley, 1975.

3 Oates, G. C., Knight, C. J., Carey, G. F., "A Variational Formulation of the Compressible Through-Flow Problem," *Journal of Engineering for Power,* Vol. 98, 1976, pp. 1-8.

4 Chung, Hua Wu, "A General Theory of Three-Dimensional Flow in Subsonic and Supersonic Turbo-Machines of Axial, Radial and Mixed Flow Types," NACA, T.N. 2604, 1952.

5 Marsh, H., "A Digital Computer Program for the Through-Flow Fluid Mechanics in an Arbitrary Turbo-Machine Using a Matrix Method," Aero Research Council, R & M No. 3509, 1968.

6 Perkins, J. H., "The Analysis of Steady Flow Through Turbomachines," GEC Power Engineering Internal Report W/M (3C), p. 1641, 1970.

7 Gelder, D., Unpublished GEC report, 1969.

8 Emmons, H. W., "The Theoretical Flow of an Ideal Frictionless Adiabatic Perfect Gas Inside of a Two-Dimensional Hyperbolic Nozzle," NACA Tech Note 1003, 1946.

9 Marsh, H., "The Uniqueness of Turbomachinery Flow Calculations Using the Streamline Curvature and Matrix-Through-Flow Methods," *Journal of Mech. Eng. Science,* Vol. 13, No. 6, 1971, p. 376.

10 Bindon, J. P., and Carmichael, A. D., "Streamline Curvature Analysis of Compressible and High Mach Number Cascade Flows," *Journal of Mech. Eng. Science,* Vol. 13, No. 5, 1971, pp. 344-357.

11 Horlock, J. H., *Axial Flow Turbines,* Butterworth, 1966.

12 McDonald, P. W., "The Computation of Transonic Flow Through Two-Dimensional Gas Turbine Cascades," ASME Paper 71-GT189, 1971.

13 Denton, J. D., "A Time-Marching Method for Two and Three-Dimensional Blade to Blade Flows," ARC Report 35, 367, 1974.

14 Walkden, F., Caine, P., and Laws, G. T., "A Locally Two-Dimensional Numerical Method for Calculating Three-Dimensional Supersonic Flows," *Journal of Computational Physics,* Vol. 27, No. 1, 1978, pp. 103-122.

15 Grainger, C. F., "Supersonic Flow Calculations for Turbomachinery Cascades," ARC Report No. 37495, (1978).

16 Grainger, C. F., "Three-Dimensional Supersonic Flow Through a Cascade of Twisted Flat Plates," ASME Paper No. 80 FE-3, 1980.

17 Hawthorne, W. R., and Ringrose, J., "Actuator Disk Theory of the Compressible Flow in Free-Vortex Turbomachinery," *Proc. Institution of Mech. Engrs.,* Vol. 178, Part 3 I(ii), 1963-1964, p. 1.

18 Starken, H., "Transonic and Supersonic Flows in Cascades," Lecture notes ASME course Iowa State University, 1975.

19 Dunker, R. J., Strinning, P. E., and Weyer, H. B., "Experimental Study of the Flow Field Within a Transonic Axial Compressor Rotor," Trans. ASME Paper 77-GT-28, 1977.

20 Horlock, J. H., "The Compressible Flow Through Cascade Actuator Discs," *Aeronautical Quarterly,* Vol. 9, (1958) 110.

21 Traupel, W., *Thermische Turbomaschinen,* Springer-Verlag, Berlin, 1960.

APPENDIX

Two-Dimensional Supersonic Flow Across an Actuator Disk

We require detailed information about the flow across the actuator disk, which we can then use to match the flow fields upstream and downstream of the disk. We follow the approach developed by Traupel [21] in which, to determine the flow downstream of a choked turbine nozzle, he simply applied the continuity, steady flow energy and momentum equations (the last in the direction parallel to the blades, assumed to be straight and perpendicular to the throat) between the throat and far downstream.

Here we consider the fully supersonic two-dimensional flow across a cascade of flat plates. In the basic unperturbed condition (indicated by a bar superscript) the flow is everywhere parallel to the blades which are set at stagger $\bar{\xi}$. As explained in the main text, conditions up to the leading edge are unchanged if the back pressure is altered, the flow remaining one of zero incidence. However, the flow some way downstream of the trailing edge (assumed to be uniform, wave patterns having died away) will not now be parallel to the blades (Fig. 2). We write the continuity, steady flow energy and momentum equations between the station upstream of the blades (station 1 or station u, where $p_1 = p_u = \bar{p}$, $u_1 = u_u = \bar{u}$ etc.) and station d which we assume to be several chords downstream of the disk – but still close to $x = 0$, as the blade chord is infinitesimally small.

The continuity equation is

$$G = \bar{\rho}\bar{u} = \rho_d u_d \tag{A1}$$

The stagnation enthalpy is conserved so that

$$H = \bar{h}_0 = h_{0_d}$$

i.e.

$$H = \left(\frac{\gamma}{\gamma-1}\right)\frac{p_d}{\rho_d} + \frac{u_d^2 + v_d^2}{2} \tag{A2}$$

The momentum equation parallel to the blades is

$$\begin{aligned} F &= \bar{p} + \bar{\rho}\bar{u}^2 \sec^2 \bar{\xi} \\ &= p_d + \rho_d u_d (u_d + v_d \tan \bar{\xi}) \end{aligned} \tag{A3}$$

Since the upstream conditions are known, F, G and H are constants, and the equations (A1), (A2), and (A3) form three equations for three unknowns, ρ_d, u_d and v_d, if the back pressure p_d is specified.

The entropy increase can then be determined,

$$s_d - s_u = c_v \log_e\left(\frac{p_d}{\bar{p}}\right) + c_p \log_e\left(\frac{\bar{\rho}}{\rho_d}\right) \tag{A4}$$

Solution of these equations for the downstream flow conditions is straightforward but algebraically complex: details are not given here.

However, the case of a small perturbation of the basic flow is of particular interest, and is used in the main text. We may then write

$$\begin{aligned} p_d &= \bar{p} + p' \\ \rho_d &= \bar{\rho} + \rho' \\ u_d &= \bar{u} + u' \\ v_d &= \bar{v} + v' \end{aligned}$$

and the three equations become

$$\frac{u'}{\bar{u}} + \frac{\rho'}{\bar{\rho}} = 0 \tag{A5}$$

$$\frac{p'}{\bar{p}} - \frac{\rho'}{\bar{\rho}} + (\gamma-1)\bar{M}_x^2\left[\frac{u'}{\bar{u}} + \tan^2\bar{\xi}\frac{v'}{\bar{v}}\right] = 0 \tag{A6}$$

$$\frac{p'}{\bar{p}} + \gamma\bar{M}_x^2\left[\frac{u'}{\bar{u}} + \tan^2\bar{\xi}\frac{v'}{\bar{v}}\right] = 0 \tag{A7}$$

Solutions of these equations are

$$\frac{u'}{\bar{u}} = -\frac{1}{\gamma}\frac{p'}{\bar{p}} \tag{A8}$$

Downloaded 02 Jun 2010 to 171.66.16.103. Redistribution subject to ASME license or copyright; see http://www.asme.org/terms/Terms_Use.cfm

$$\frac{v'}{\bar{v}} = \frac{1}{\gamma}\frac{p'}{\bar{p}}\frac{[\bar{M}_x^2 - 1]}{\bar{M}_x^2 \tan^2 \bar{\xi}} \tag{A9}$$

$$\frac{\rho'}{\bar{\rho}} = \frac{1}{\gamma}\frac{p'}{\bar{p}} \tag{A10}$$

Small changes in back pressure thus lead to small changes in axial and tangential velocity (with a small angle change) and a small change in density. However, the solution for the density perturbation, equation (A10), clearly shows the flow is isentropic, for

$$s' = c_v \frac{p'}{\bar{p}} - c_p \frac{\rho'}{\bar{\rho}} = 0 \tag{A11}$$

In the main text, we use the isentropic relation (equation (A10)) directly rather than applying the momentum equation along the stagger line of the blades.

Downloaded 02 Jun 2010 to 171.66.16.103. Redistribution subject to ASME license or copyright; see http://www.asme.org/terms/Terms_Use.cfm

Three Dimensional Supersonic Flow Through a Cascade of Twisted Flat Plates

C. F. Grainger
Research Fellow,
University of Salford,
Salford, England

The three-dimensional flow through a cascade of twisted flat-plate blades is calculated using a computer program based on a finite-difference approximation to the method of characteristics. The relative flow is supersonic but the axial flow is subsonic. For two-dimensional flow under similar conditions, the inlet flow field is one of "unique-incidence," the effect discussed by Starken (5) and others. The main purpose of the present work is to extend the understanding of this effect to three-dimensional flow. Important differences between the two and three-dimensional flow fields are explained in terms of the interaction between neighboring sections of the flow.

Introduction

The problem of calculating the inviscid flow through a turbomachine in which the relative flows are subsonic has largely been solved, particularly by the use of the streamline curvature and matrix through flow techniques. However, these methods break down when the relative flow becomes supersonic, and other approaches have to be used. The one adopted in this paper involves a finite difference approximation to the method of characteristics and can be used when the flow is fully supersonic. The method (which is fully described in Walkden [1] is developed from differential equations of continuity and momentum in each of the three directions together with an isentropic flow equation. These equations are transformed into a coordinate system in which the body surfaces are constant coordinate planes to ensure that boundary conditions are treated accurately, then characteristic relationships are extracted and solved by finite difference methods. Shocks are smoothed over a small number of mesh points and are not treated as discontinuities because of the immense complication of following multiple shock surfaces which reflect from walls and criss-cross in three-dimensions. For weak shocks, the isentropic assumption is adequate, but obviously gives increasing errors with increasing shock strength. In order to cope easily with multiple body problems (such as a cascade of blades), the flow is divided into a number of regions (separated usually by the solid bodies) and the computer program calculates the flow in each region in turn. This treatment of the multiple body problem represents an improvement over the mathematically similar characteristics methods of Martinon [2] and Frühauf [3].

But the main task of the work reported here, was to improve the understanding of three-dimensional flow effects and to derive simple explanations for them.

Contributed by the Fluids Engineering Division of the American Society of Mechanical Engineers and presented at the Fluids Engineering Conference, New Orleans, La., March 10-13, 1980. Manuscript received by the Fluids Engineering Division, February 25, 1980. Paper No. 80-FE-3.

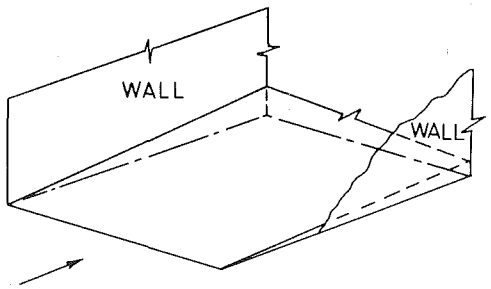

Fig. 1 Twisted wedge between walls

Thus, as an introduction to the complete calculation of the supersonic flow through a three-dimensional cascade of twisted blades, the flow over a twisted wedge, placed between two walls (Fig. 1) was first studied. The aim of this calculation was to reveal the basic effects associated with the development of a shock of variable strength when it is constrained between walls. Understanding this is an essential element of a full understanding of the flow into a rotating blade row where the shock at the leading edge is of variable strength and is constrained by the hub and casing. However, the effects due to rotation and converging casing or hub would obscure this effect if the whole flow through the blade row was modelled, so this simple case was calculated first. Indeed, it is hoped that this approach is more valuable to a designer and for general understanding than to simply calculate one case for the flow through an actual blade row.

Subsequently the flow field past the first thirty blades of a semi-infinite cascade of twisted flat-plate blades (Fig. 2) was calculated. The aim of this calculation was to find the flow field about a blade in an infinite cascade of twisted blades. It was expected that such a "repeating" flow would be set up about a blade situated a few blades along the semi-infinite cascade. (This assumption has been justified for two-dimensional cascades by Ferry [4], Starken [5] and others.) For the cascade of twisted blades studied, this assumption was

Copyright © 1980 by ASME
Downloaded 02 Jun 2010 to 171.66.16.103. Redistribution subject to ASME license or copyright; see http://www.asme.org/terms/Terms_Use.cfm

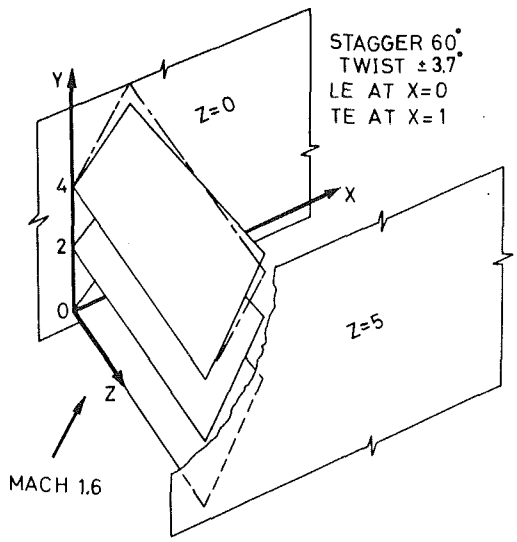

Fig. 2 Twisted flat-plate cascade

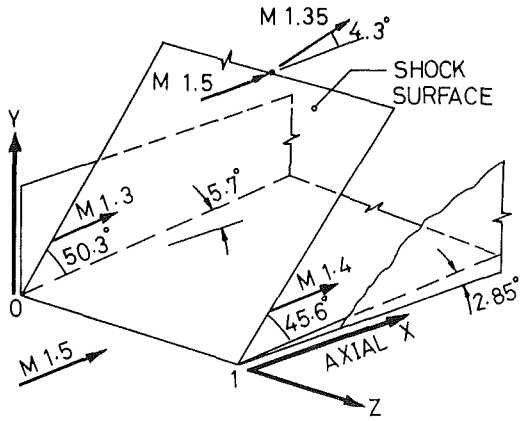

Fig. 3 Geometry of twisted wedge and shock surface

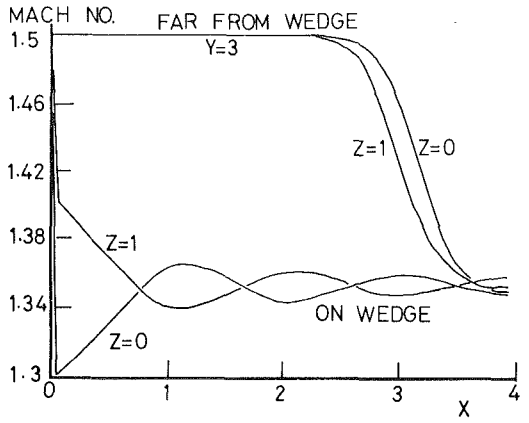

Fig. 4 Flow over twisted wedge - Mach number distribution on wedge and far from wedge ($y = 3$)

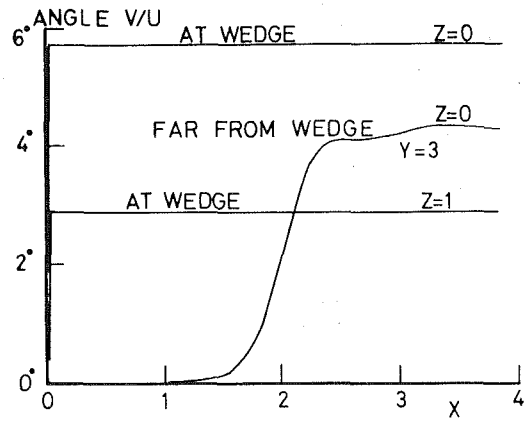

Fig. 5 Flow over twisted wedge - flow angle distribution

valid because the flow field over an individual blade stabilised to a repeating pattern after a few blades. However, it was necessary to calculate the flow past thirty blades in order to establish the flow conditions further upstream.

Supersonic Flow Over a Twisted Wedge

The detailed geometry of the twisted wedge is shown in Fig. 3. A uniform flow at Mach number 1.5 strikes the wedge which turns the flow from an angle of 2.85 degrees at one wall to an angle of 5.7 degrees at the other, the wedge angle varying linearly between the two side walls containing the flow. A rectilinear coordinate system (x,y,z) is used, with y approximately zero on the wedge because the wedge angle is everywhere small. We refer to the z direction as the "radial" direction, since in a turbomachine the blades are generally radial. The length of the wedge is taken as unity. A shock surface of variable strength and angle originates at the leading edge of the wedge.

The Flow Near the Wedge

The Mach number distribution along the wedge, at each end of the wedge (i.e., at x,0,0; x,0,1) is plotted in Fig. 4. Immediately behind the shock ($x = 0$), there is a gradient in Mach number along the leading edge (radial or z direction) and a substantial difference in the flow conditions at (0,0,0) and (0,0,1). This radial gradient is a result of the variation of the imposed flow deflection (and hence shock strength) along the wedge (see Fig. 5). The radial pressure gradient then produces a radial flow downstream of the shock, and this is illustrated in Fig. 6, where the radial velocity w is plotted against x along a line drawn on the wedge near mid-span ($y = 0$, $z = 0.4$). Figures 4 and 6 show that both the Mach number and radial velocity oscillate further downstream, with a half-wavelength of approximately unity.

This effect can be interpreted by considering the propagation along each of the characteristics emanating from the two sidewall corners on the wedge just downstream of the shock (near coordinates 0 and 1 on Fig. 3). The radial pressure gradient produced by the shock of varying strength produces a radial velocity in the middle of the channel but cannot produce a radial velocity at the sidewall. Thus, each of those characteristics transmits an opposing effect which is sufficient to balance the radial pressure gradient and keep the flow parallel to the sidewall. At an average Mach number of 1.35 the Mach angle is 48 degrees, so that the characteristics cross the channel of unit width in an axial distance of 1.06, and first meet in the middle at approximately $x = 0.5$. At that point, their cumulative effect is twice as strong as the initial radial

Nomenclature

(x,y,z) x = axial
z = "radial"
ξ = stagger Angle
α = downstream Flow Angle

Downloaded 02 Jun 2010 to 171.66.16.103. Redistribution subject to ASME license or copyright; see http://www.asme.org/terms/Terms_Use.cfm

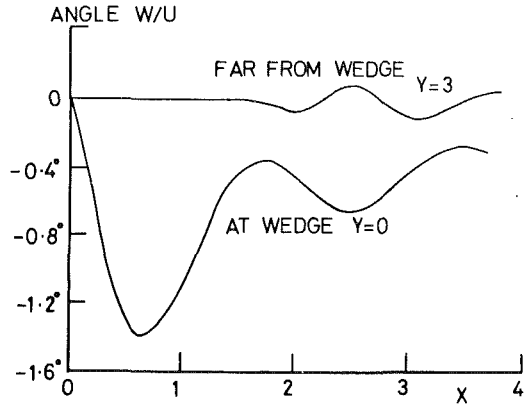

Fig. 6 Flow over twisted wedge - "radial" velocity distribution near mid-span (Z = 0.4)

pressure gradient and opposed to it, so that the resultant pressure gradient is equal and opposite to the initial pressure gradient and begins to reduce the radial velocity. Upon reaching the opposite sidewall, each characteristic is reflected with a change in effect and proceeds to re-cross the channel. When they cross in the centre (at about $x = 1.5$) they again cause a reversal in radial pressure gradient, and the radial velocity begins to reverse direction again. This process continues, with the characteristics zig-zagging across the channel and producing the oscillating radial velocity shown in Fig. 6. The effect of the characteristics as they reach the sidewalls is shown in Fig. 4; they reverse the axial gradient of Mach number each time they cross the channel (in an axial distance of about 1 unit).

The Flow Far From the Wedge

Figures 4, 5 and 6 also show the variations in flow properties away from the wedge (at $y = 3$). The radial flow near mid-span ($(y,z) = (3,0.4)$) has a much smaller amplitude of variation with x than at the wedge (see Fig. 6), and its mean value remains close to zero. The flow deflection through the shock at the "inside" wall ($y,z = (3,0)$ in Fig. 5) is 4.2 degrees, which is close to the spanwise mean value of the wedge angle.

Behind the shock, far from the wedge the flow angle is determined by the combined effect of the characteristics coming from all along the wedge leading edge - some having been reflected from the sidewalls too. The combined effect of these characteristics is a "mean" characteristic which produces a flow at Mach 1.35 at an angle of 4.3 degrees to the incident flow. The radial flow is almost zero. The distance from the wedge at which the flow becomes two-dimensional depends on the wedge span and the Mach angle. The Mach angle is greater at the low Mach number (high wedge angle) side of the wedge, and the influence of that side reaches into the stream further upstream than the influence of the high Mach number (low wedge angle) side. However, in this example the far field conditions are not signficiantly biased towards the low Mach number side of the wedge because the spanwise variations are small.

Far away from the wedge (at $y = 6$), the radial velocity remains zero as the shock is crossed. The shock is radially uniform and the flow deflection across it is calculated as 4.3 degrees (approximately the spanwise mean of the wedge angle). Thus the effect of the twisted wedge upon the far field is approximately the same as the two-dimensional effect of a wedge of constant angle (4.3 degrees).

Supersonic Flow Past a Twisted Plate Cascade

The semi-infinite cascade of twisted plate blades is shown in Fig. 2. The axial chord of the blades was taken as unity and the aspect ratio as 5. The blade twist was linear in tan (§) about a mean stagger of 60 degrees; the stagger varying from 56 to 63.23 degrees. The inlet Mach number was taken as 1.6.

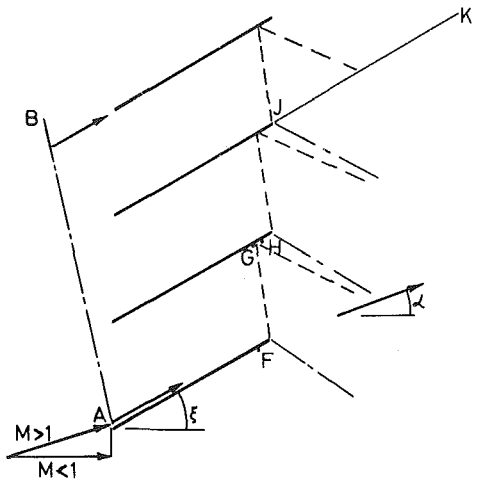

Fig. 7 Section view of flat plate cascade

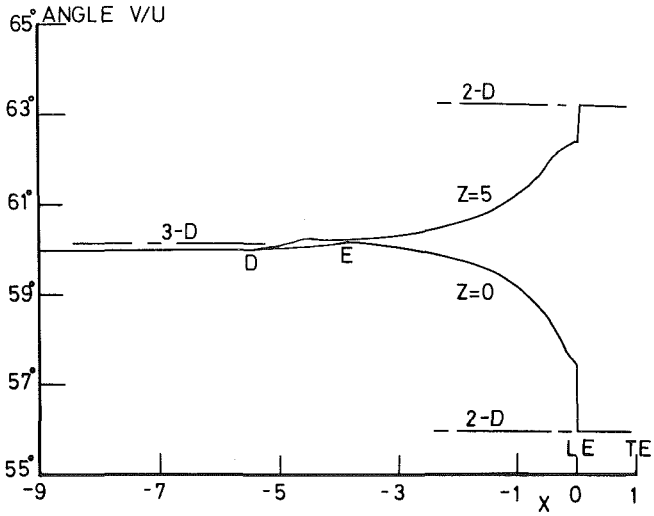

Fig. 8 Flow through twisted cascade - flow angle distribution upstream of cascade

The Upstream Flow

The "Unique-incidence" effect for a two-dimensional cascade is reviewed by Starken [5] and is now briefly outlined for the very simple case of a cascade of flat plates. Consider the flow on to the semi-infinite cascade shown in Fig. 7, where the relative flow is supersonic, but the axial flow is subsonic. The flow adjusts itself until it is parallel to the blades by means of a wave AB (a compression wave in the diagram). Regardless of the initial flow angle, the wave AB turns the flow to stagger angle (ξ) so that it is tangent to the blades. The "unique incidence" is thus zero for this flat plate cascade; the flow is thus tangent to all the blades after the first, and there are no shocks or expansion waves at the leading edges. For curved blades, the argument is slightly different (see Ferri [4] or Starken [5]), the "unique incidence" being a function of the Mach number and the blade geometry. In order to highlight the three-dimensional effects, only flat (but twisted) plates were considered in the three-dimensional flow.

For the supersonic flow through the cascade of twisted blades (Fig. 2), it was expected that a wave front (similar to AB in the two-dimensional flow to Fig. 7) would arise, turn-

Downloaded 02 Jun 2010 to 171.66.16.103. Redistribution subject to ASME license or copyright; see http://www.asme.org/terms/Terms_Use.cfm

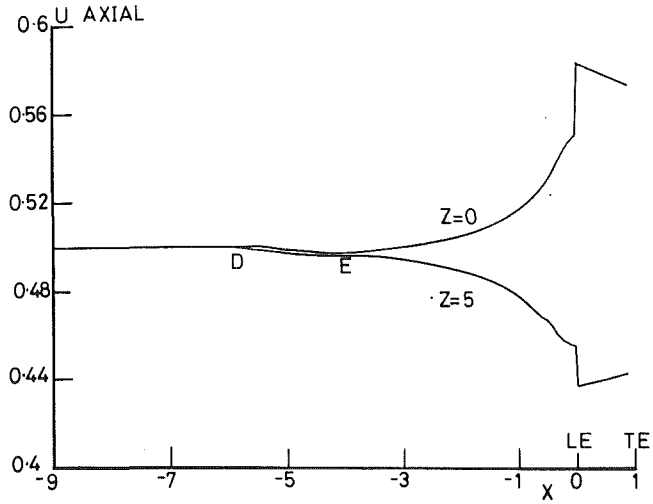

Fig. 9 Flow through twisted cascade - axial velocity distribution upstream of cascade

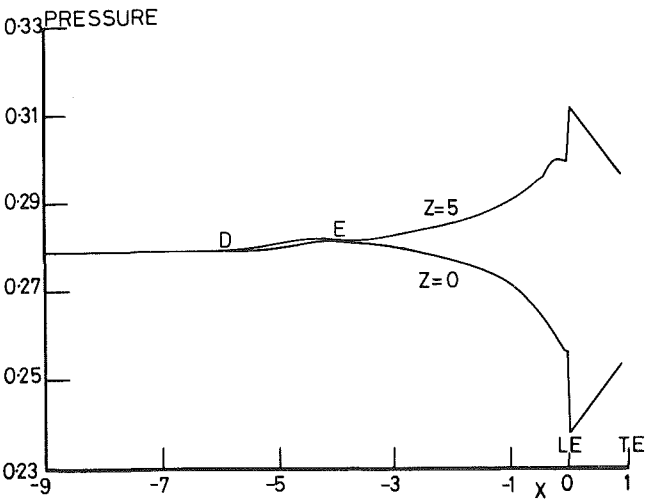

Fig. 10 Flow through twisted cascade - pressure distribution upstream of cascade

ing the upstream flow to some "unique incidence" condition. The calculation showed the flow stabilising quickly near the leading edges of succesive blades up the cascade. However, the wave front moved so slowly away from the cascade that the calculations had to be continued for some thirty blades before it became clearly distinguishable from the flow pattern near the leading edge.

The Upstream Flow Field

The flow field near the 25th blade is illustrated in Figures 8, 9, 10, and 11. The variations of flow properties are shown along straight lines drawn at 60 degrees to the x axis (parallel to the mean stagger line); these lines pass through the leading edges and over the upper surfaces of the blades. Downstream they again follow lines at 60 degrees to the x axis. (Note that the graphs do not show the conditions averaged from blade to blade.)

In each of these four graphs the segment DE contains the wave front analogous to the wave AB of Fig. 7. This wave front changes the upstream flow initially assumed, to the upstream flow at point E, i.e., the conditions at point E are the "unique incidence" conditions for this cascade of twisted blades at the given Mach number. The segment from E to the leading edge of the blades includes the flow perturbations

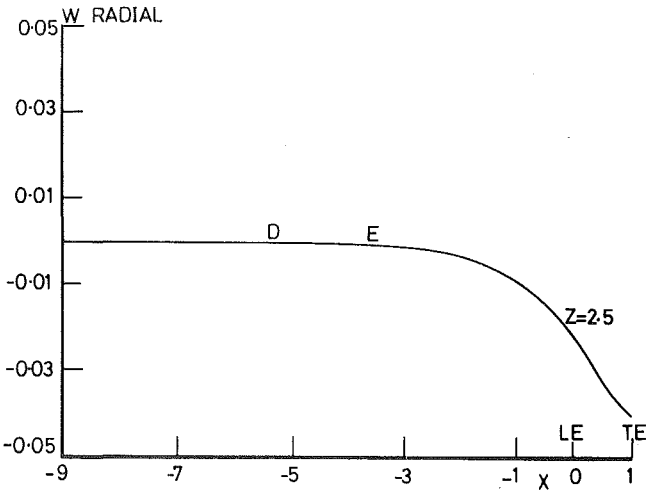

Fig. 11 Flow through twisted cascade - "radial" velocity distribution of mid-span

near the leading edge of a blade in an infinite cascade. The unique flow conditions at the leading edges were established by about the fifth blade of the thirty, but the point E was then so close to the cascade that the pattern was distorted near the leading edges of the blades.

The segment DE includes a "settling" wave front which moves upstream away from the cascade; and the segment from E to the leading edge includes the steady state, three-dimensional flow upstream perturbation.

Figures 8 to 11 show that there are four distinct differences between the two and three-dimensional flows.

(*a*) Fig. 8 shows that there is a single "unique incidence" for the whole of this cascade (0.2 degrees at point E). The two-dimensional value of "unique incidence" at each section of the blade (zero for the flat plate blades) is not valid in three-dimensional flow. The calculations were repeated with various numbers of mesh points to confirm that this value is meaningful.

(*b*) The "unique incidence" conditions at point E are not the average of the two-dimensional value for the blade (zero), but are biased toward the lowest Mach number side ($z = 5$). In fact, the average blade angle is less than 60 degrees (56 degrees at $z = 0$ to 63.2 at $z = 5$), which makes this point even more significant.

(*c*) There are discontinuities at the leading edges, varying from a shock at $z = 5$ to a strong expansion at $z = 0$ (with virtually no shocks at the center). These effects are illustrated in Figs. 8 (which shows flow angle variation), 9 (which shows axial velocity variation) and 10 (which shows pressure variation) all along the walls.

(*d*) Substantial radial velocities arise upstream of the leading edge (see Fig. 11) on the blade mid-span.

Discussion

We first consider the development of the "settling" wave DE. It originates at the leading edge of the first blade of the cascade, as a three-dimensional wave front deflecting the flow by differing angles at each radius. Therefore it is similar to the wave located at the leading edge of the twisted wedge (see Fig. 3). In like manner, far away from the first blade, the wave front DE becomes two-dimensional; and this is evident from Fig. 8 which shows how the wave front deflects the flow at each "radius" (Z) by the same amount, to the "unique" conditions at point E.

We next consider the flow from point E to the leading edge of the blades as representing the flow field near a blade in an infinite cascade. Waves exist which change the flow con-

Downloaded 02 Jun 2010 to 171.66.16.103. Redistribution subject to ASME license or copyright; see http://www.asme.org/terms/Terms_Use.cfm

ditions between point E and the leading edges by varying amounts at each radius. These waves are generated at the leading edges where they turn the flow tangent to the blades. However, as any one wave moves away from the leading edge, waves from the walls and from the neighbouring blade sections diminish its effect (in a similar manner to the changes produced near the twisted wedge of Fig. 3). As a result, the local wave will not change the flow on to the next blade by enough to make the flow tangent to the blade at each radius. Therefore the leading edge discontinuities shown in Figures 8 to 11 are repeated at the next leading edge, and an identical wave is thus generated. The reduction in strength of the local waves leads eventually to a two-dimensional wave front far away from the blade generating the wave, the same as it did for the wedge flow.

The development of the three-dimensional shock ahead of the wedge thus provides the key to understanding the cascade upstream flow.

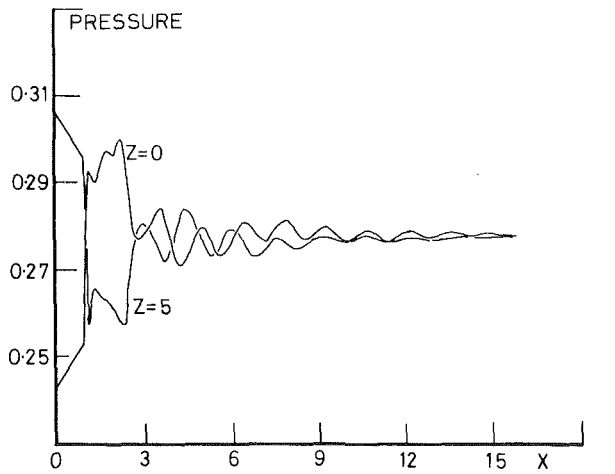

Fig. 12 Flow through twisted cascade - pressure distribution downstream

The Flow Through the Blade Passage and Downstream

For a two-dimensional flat plate cascade operating at zero incidence in supersonic flow, there is a uniform flow through the blade passage until the trailing edge is reached. As shown in Fig. 7 shock and expansion wave systems are set up at the trailing edges corresponding to the downstream pressure and flow angle (α). This wave system may be obtained by specifying a flow angle at the trailing edge of the first blade and calculating the resultant flow pattern and ultimately the downstream pressure. This was done for two-dimensional flow and the flow downstream of the first few blades of a semi-infinite cascade obtained. After a few blades the flow pattern repeated from blade to blade. (One condition is required for calcualtions where the downstream axial Mach number is subsonic. It is that no changes are propagated along characteristics originating far downstream and moving upstream to strike the cascade. This provides the lower boundary condition for the calculation of the flow field for the first blade of the semi-infinite cascade.)

A similar procedure was used for these three-dimensional cascade calculations. First the upstream flow field was calculated, together with the flow through the blade passage up to the trailing edge. Then a guess was made of the radial distribution of flow properties along a line just before the trailing edge of the first blade of the cascade (points F in Fig. 7). Finally, the flow field was calcualted downstream of the first few blades of the cascade using the lower boundary condition specified above. A check was then made that the calculation produced the required zero radial pressure gradient far downstream.

The guessed distribution of properties along the radial line at F was made as follows. (The flow within the blade passage had already been calculated so that conditions at points G (Fig. 7) were known; point H is the image of point F.)

(i) The flow was assumed to be tangent to the blade at each radius.

(ii) The stagnation enthalpy was assumed to be equal to the stagnation enthalpy at G (known), at each radius.

(iii) The entropy at F was assumed to be equal to the entropy at G (i.e., the shock was weak).

(iv) The radial velocity distribution at F was assumed to be equal to the radial velocity distribution at G. Under these restrictions, only the radial distribution of pressure at F was required to be guessed. It was chosen to be constant on the first blade; this then led to nonzero gradients of pressure at H on the second and subsequent blades, but to a constant radial pressure far downstream of the fifth blade along the cascade (see Fig. 12). (About five blades up the semi-infinite cascades

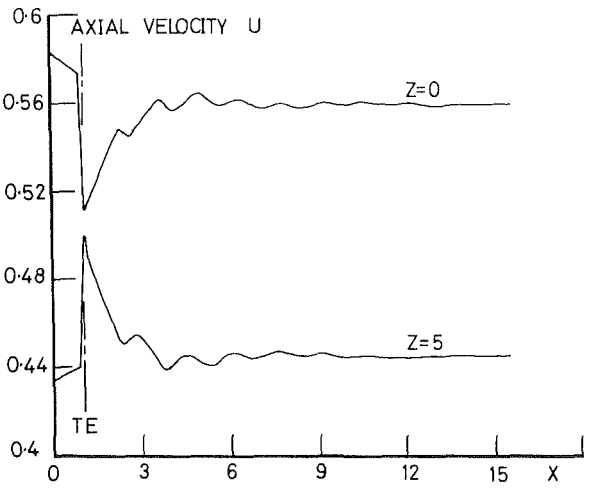

Fig. 13 Flow through twisted cascade - axial velocity distribution downstream

were calculated before the downstream flow converged to the results shown in Figs. 12 to 15.)

A restriction of the finite difference technique became apparent in modelling the flow at the trailing edge and just downstream. At this point two flows of different velocity converge to produce a slip plane across which there is a step change in both the radial and streamwise components of velocity. This can only be modelled by this finite difference technique for small discontinuities, which, in this case, were spread over a few mesh points (a more satisfactory procedure would involve calculating the slip plane as a discontinuity and following its development and intersection with shocks etc., but that involves immense programming problems).

Important features of these calculated distributions are:

(*a*) Within the passage there are strong axial and radial gradients of all the flow properties.

(*b*) There are strong waves generated at the trailing edges, varying from a shock at $z = 0$ to a sharp expansion at $z = 5$ (see Fig. 12).

(*c*) The flow properties have damped oscillations of long wavelength, with the wavelength determined by the blade height and Mach angle (caused by characteristics crossing the blade passages from wall to wall as with the wedge flow). At a Mach number of about 1.6, the Mach angle is 38 degrees, so that one crossing of the blade from one end wall to the other is achieved in a streamwise distance of 6.4, corresponding to an

Downloaded 02 Jun 2010 to 171.66.16.103. Redistribution subject to ASME license or copyright; see http://www.asme.org/terms/Terms_Use.cfm

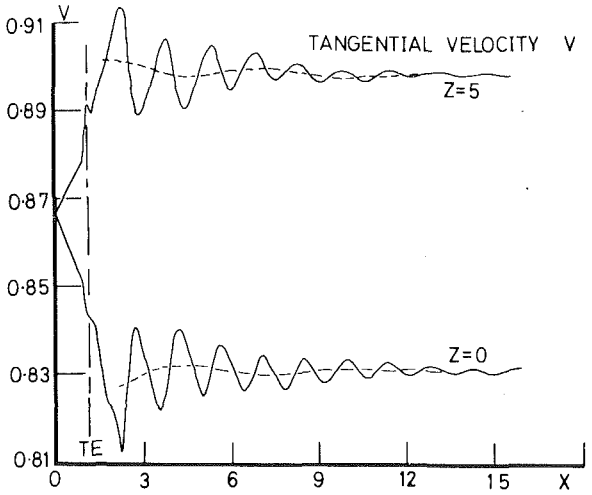

Fig. 14 Flow through twisted cascade · tangential velocity distribution downstream

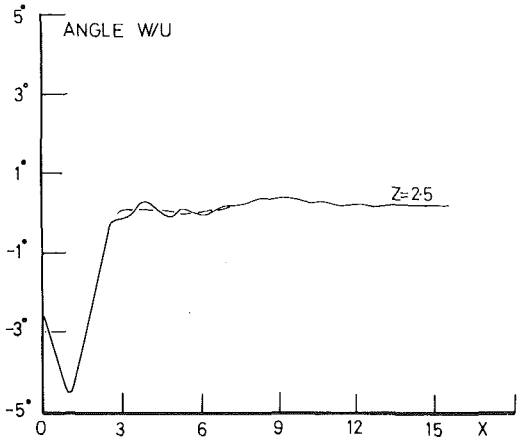

Fig. 15 Flow through twisted cascade · "radial" flow angle downstream at mid-span

axial distance of 3.2 (see Figs. 14 and 15 for this flow through a 60 degrees staggered cascade, where these oscillations are shown by dashed lines).

(*d*) There are oscillations of shorter wavelength, determined by the blade spacing and Mach angle. These oscillations correspond to the waves generated at the trailing edges of the blades and shown by dashed lines in Fig. 7. At a Mach angle of 38 degrees, with a blade spacing of 1 (normal to the blade), the passage is crossed in a distance of 13., and the resulting wavelength is 1.5 in the axial direction. This compares closely with the wavelength of the variations shown in Figs. 12 to 15.

Conclusions

The inviscid flow past a blade in a cascade of twisted blades of finite length has been calculated, for the case where the relative flow is supersonic but the axial flow is subsonic (both upstream and downstream). Comparisons with two-dimensional flows show considerable differences; in particular, two-dimensional concepts of "unique incidence" must be modified for three-dimensional flows. The three-dimensional effects may be interpreted by reference to the development of a three-dimensional shock over a twisted wedge located between end walls.

References

1 Walkden, F., Caine, P., and Laws, G.T., "A Locally Two-Dimensional Numerical Method for Calculating Three-Dimensional Supersonic Flows," *Journal of Computational Physics*, Vol. 27, No. 1, 1978, pp. 103–122.

2 Martinon, J., "Use of the Characteristic Method for the Prediction of the Three-Dimensional Flow Field in High Transonic Compressors," ASME Paper No. 79-GT-34, 1979.

3 Frühauf, H. H., "A Method of Characteristics for Three-Dimensional, Steady Supersonic Flow in Rotating and Stationary Cascades," ESRO TT-44, July 1975.

4 Ferri, A., "The Supersonic Compressor," *Aerodynamics of Turbines and Compressors*, (W. R. Hawthrone, Ed.), *High Speed Aerodynamics and Jet Propulsion*, Oxford University Press, London, Vol. X, 1964, jpp. 384–397.

5 Starken, H., "Transonic and Supersonic Flows in Cascades," ASME Course, Fluid Dynamics of Turbomachinery, Iowa State University, 1975.

Downloaded 02 Jun 2010 to 171.66.16.103. Redistribution subject to ASME license or copyright; see http://www.asme.org/terms/Terms_Use.cfm

M. A. Hoffman
Professor.

R. K. Takahashi
Research Assistant.

R. D. Monson
Research Assistant.

University of California,
Davis, Calif. 95616

Annular Liquid Jet Experiments

Experiments have been performed to determine the length for convergence or closure of a vertical, hollow annular water jet due to the action of surface tension forces. The data agree well with theoretical predictions up to the maximum velocity where reliable data could be obtained (4.4 m/s). These experiments extend the range of confirmation of the theories in terms of the dimensionless parameter, $N_c \equiv \hat{We}/Fr^2$, from about 0.01 to over 100. The stability of the annular jet subjected to natural and external disturbances is also discussed briefly. Finally the results of a series of experiments on the flow spreading or splitting due to the presence of wedge-shaped obstacles in the path of the annular jet flow are presented.

1 Introduction

The quantitative study of annular liquid jets goes back at least to the 1869 paper of Boussinesq [1]. Interest in this subject has been revived recently by Maniscalco, et al. in connection with certain pulsed fusion reactor system concepts [2]. In these fusion reactors, a small pellet containing deuterium and tritium is caused to undergo nuclear fusion through intense compression and heating by lasers, electron beams or ion beams. During the fusion process, the products of the pulsed fusion reaction, high energy neutrons, alpha particles, X-rays, and the unreacted ions flow toward the reactor vessel, and can do severe erosion damage to the inner wall. In addition, the neutrons can penetrate far into the structure (on the order of a meter or more) and do additional damage [e.g., see reference 3]. In an attempt to create a self-healing or renewable wall, the idea of placing a vertical annular jet or "waterfall" of liquid lithium about 50 to 70 cm thick and about 10 meters in diameter in the reactor vessel between the fusion pellet and the vessel walls was proposed [2]; the nominal inlet flow velocity proposed for the annular lithium jet was about 5 m/s. This was the motivation for the present series of experiments.

The shape of a typical vertical annular jet flow is shown in Fig. 1. The gravity force accelerates the flow in the vertical direction while surface tension forces cause the flow to accelerate inward, tending to close up the hollow space and create a nearly-cylindrical, solid jet. The convergence length, L^*, is defined as the length to closure of the hollow region (see Fig. 1). Hovingh [4] developed scaling laws for the large lithium annular jets which predict convergence lengths of kilometers.

As will be shown in the derivation of the equations, a key parameter in determining the convergence length of annular jets is the dimensionless convergence number, $N_c \equiv \hat{We}/Fr^2$, where $\hat{We}$ is the Weber number and Fr is the Froude number. For the laser fusion reactor, N_c has values on the order of 10^4 for the proposed annular lithium jet. One of our key objectives was to conduct water jet experiments at the highest possible values of N_c while still using as large an annular jet as possible in order to extend the range of experimental verification of the theory for the convergence length. As will be seen, we succeeded in extending the previous experimental results from N_c values of about 0.01 to over 10^2.

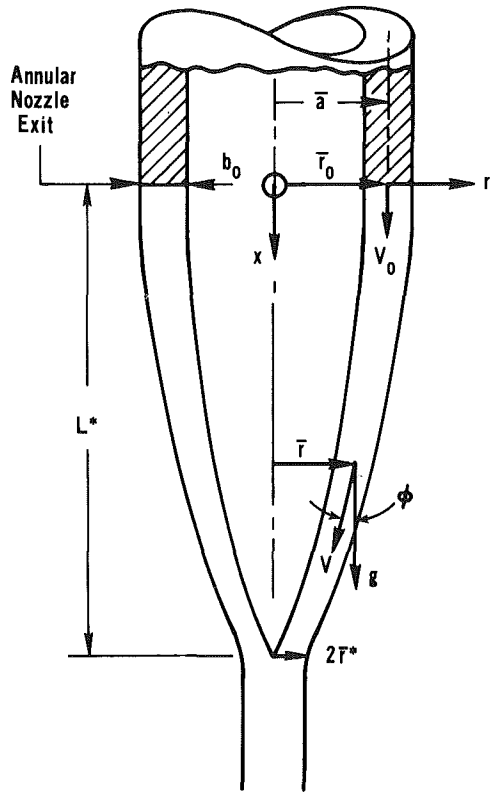

Fig. 1 Cross-section of a near-vertical, hollow annular jet showing the key parameters involved in the solution for the closure or convergence length, L^*

One of the earliest experimental studies of the convergence length of annular jets is that of Binnie and Squire [5]. They conducted experiments on a small vertical water jet produced

Contributed by the Fluids Engineering Division for publication in the JOURNAL OF FLUIDS ENGINEERING. Manuscript received by the Fluids Engineering Division, December 22, 1978.

Copyright © 1980 by ASME
Downloaded 02 Jun 2010 to 171.66.16.103. Redistribution subject to ASME license or copyright; see http://www.asme.org/terms/Terms_Use.cfm

by an orifice with a mean diameter of about 0.8 cm and a gap of about 0.32 cm; the maximum velocity was about 2.8 m/s. In 1962, Baird and Davidson [6] studied the various flow regimes possible with vertical annular jets produced by an annular orifice with a mean diameter of 1.24 cm and a gap of 0.029 cm. Here the maximum velocity was about 2.6 m/s. They also studied the effect of small pressure differences across the annulus on the convergence length.

An area of research closely related to annular jets is that on water bells. Water bells were often used in the past to determine the surface tension of liquids, and some of the more recent studies relevant to our present research include the works of Hopwood [7], Lance and Perry [8], Taylor [9] and Dumbleton [10]. Water bells are generally produced by the impingement of a round jet on a disk shaped obstruction or on another water jet. The subsequent bell-like shape is influenced by both surface tension and gravity forces. It can be seen that the hollow annular vertical jet is a special case of a water bell with an initial vertical velocity.

2 Theory for Convergence Length

2.1 Review of the General Equations for a Nearly Vertical Jet. The general differential equations for a water bell presented by Lance and Perry [8] are based on those of Boussinesq [1]. They are nonlinear and require numerical solution to find the water bell shape for the specified initial conditions. One such numerical method has been provided by Dumbleton [10]. Because we have a near-vertical annular jet it is convenient to have equations in cylindrical coordinates. Transforming the equations of reference [8] from their tangential-normal coordinate system to our cylindrical coordinate system, we obtain the following vertical and radial momentum equations valid for a thin jet:

$$\ddot{x}=g-\frac{2\sigma}{\rho b\bar{r}}\sin\ \phi\ \cos\ \phi-\frac{2\sigma}{\rho b\bar{r}_v}\sin\ \phi \tag{1}$$

$$\ddot{\bar{r}}=-\frac{2\sigma}{\rho b\bar{r}}\cos^2\phi-\frac{2\sigma}{\rho b\bar{r}_v}\cos\ \phi \tag{2}$$

where ϕ is the angle in the vertical plane between the tangent to the jet surface and the vertical (Fig. 1), $\bar{r}_v$ is the mean radius of curvature in the vertical plane at a particular axial location, $\bar{r}$ is the local mean radius of curvature in the horizontal plane, b is the local jet thickness, ρ is the liquid density and σ is the surface tension coefficient. The continuity equation is given by:

$$\bar{r}b\rho V\ \cos\ \phi=\bar{r}_0 b_0\rho V_0\ \cos\ \phi_0 \tag{3}$$

where V is the local total velocity and subscript "0" refers to conditions at the annular nozzle exit (see Fig. 1). It should be noted that in these equations the two mean radii of curvature, $\bar{r}$ and $\bar{r}_v$, are assumed to be positive, and the signs of the surface tension force terms are correctly given for these forces acting inward toward the x axis.

For our special case of an initially vertical annular jet of sufficiently high velocity such that the angle ϕ is always small (except perhaps very near the closure point), the nondimensionalized radial momentum equation becomes:

$$\frac{d^2R}{d\tau^2}=-\frac{(1+\tau)}{N_c}\left[1+\frac{\bar{r}_0}{\bar{r}_v}R\right] \tag{4}$$

where the dimensionless time $\tau\equiv gt/V_0$ and the dimensionless mean radius $R\equiv\bar{r}/\bar{r}_0$. We have defined a convergence parameter which is a function of the jet Weber and Froude numbers:

$$N_c=\frac{g^2\bar{r}_0^2 b_0\rho}{2V_0^2\sigma}=\frac{(\rho V_0^2 b_0/2\sigma)}{(V_0^2/g\bar{r}_0)^2}=\frac{\hat{\mathrm{We}}}{\mathrm{Fr}^2} \tag{5}$$

The nondimensionalized curvature in the vertical plane for nearly vertical flow is given approximately by:

$$\frac{\bar{r}_0}{\bar{r}_v}\simeq\bar{r}_0\left|\frac{d^2\bar{r}}{dx^2}\right|=-\frac{1}{\mathrm{Fr}^2(1+\tau)^2}\left[\frac{d^2R}{d\tau^2}-\frac{1}{(1+\tau)}\frac{dR}{d\tau}\right] \tag{6}$$

Substituting equation (6) in equation (4) yields the final nonlinear differential equation for the near-vertical annular jet:

$$\frac{d^2R}{d\tau^2}\left[1-\frac{R}{\hat{\mathrm{We}}(1+\tau)}\right]+\left[\frac{R}{\hat{\mathrm{We}}(1+\tau)^2}\right]\frac{dR}{d\tau}=-\frac{(1+\tau)}{N_c} \tag{7}$$

2.2 Special Case of High Weber Number Flow. If the Weber number is high enough such that the radius of curvature in the vertical plane is very large, the second and third terms on the left hand side of equation (7) become negligible. In this limit, the resulting equation is linear and can be integrated twice to yield the nondimensional time to convergence or closure, τ^*:

$$\tau^{*3}+3\tau^{*2}-6N_c\left(\frac{dR}{d\tau}\right)_0\tau^*-6N_c(1-R^*)=0 \tag{8}$$

where $\tau^*\equiv gt^*/V_0$ and t^* is the flow time from the nozzle exit to the closure point. $(dR/d\tau)_0$ accounts for any small initial radial velocity component of the jet and R^* is the nondimensional mean jet radius at convergence:

Nomenclature

$\bar{a}$ = mean annular nozzle radius
b = annular jet thickness
b^* = annular jet thickness at convergence or closure
Fr = $V_0^2/g\bar{r}_0$ = Froude number
g = acceleration of gravity
L^* = convergence or closure length
N_c = $\rho g^2\bar{r}_0^2 b_0/2V_0^2\sigma=\hat{\mathrm{We}}/\mathrm{Fr}^2$ = convergence number
r = radial coordinate
$\bar{r}$ = mean radius of the annular jet
$\bar{r}_0$ = initial mean radius of annular jet at the nozzle exit (assumed equal to $\bar{a}$)
r_v = radius of curvature of the annular jet in the vertical plane
$\bar{r}^*$ = mean jet radius at convergence or closure
R = $\bar{r}/\bar{r}_0$ = dimensionless mean radius
R^* = $\bar{r}^*/\bar{r}_0$ = dimensionless mean jet radius at convergence
t = time
t^* = flow time from the nozzle exit to the closure point
V = velocity in the tangential direction
V_0 = initial velocity at the nozzle exit
w = half-width of a wedge
$\hat{\mathrm{We}}$ = $\rho V_0^2 b_0/2\sigma$ = Weber number (the ^ is to distinguish it from Weber numbers based on other lengths)
x = vertical coordinate
γ = half-angle of a wedge
δ = half-angle of the flow spreading
ϕ = angle of the annular jet velocity vector from the vertical (positive for a converging jet)
σ = surface tension coefficient
τ = gt/V_0 = dimensionless time
τ^* = gt^*/V_0 = dimensionless time to convergence or closure

Subscripts

0 = initial flow conditions at the nozzle exit

Superscripts

* = conditions at the point where the hollow jet closes (or converges)

Downloaded 02 Jun 2010 to 171.66.16.103. Redistribution subject to ASME license or copyright; see http://www.asme.org/terms/Terms_Use.cfm

$$R^* \equiv \frac{\bar{r}^*}{\bar{r}_0} = \frac{b^*}{2\bar{r}_0} = \sqrt{\frac{b_0}{2\bar{r}_0(1+\tau^*)}} \tag{9}$$

which has been evaluated using the continuity equation (3).

Combining equations (8) and (9) we obtain a seventh-order linear algebraic equation in τ^* which must be solved numerically. One especially tractable limiting case is where $(dR/d\tau)_0 = R^* = 0$; this yields the following cubic algebraic equation:

$$\tau^{*3} + 3\tau^{*2} - 6N_c = 0 \tag{10}$$

It should be noted that the convergence length is related to the nondimensional time to convergence by integrating equation (1):

$$\frac{L^* g}{V_0^2} = \tau^* \left(1 + \frac{\tau^*}{2}\right) \tag{11}$$

Once τ^* is obtained from the solution of equation (10), L^* can be calculated using equation (11). A slightly different form of equation (10) was obtained and solved by Hovingh [4]. In our derivation of equations (8) and (10), we have improved upon Hovingh's original derivation by including the surface tension forces from *both* the inner and outer surfaces. This modified Hovingh theory will be compared to the exact theory of Lance and Perry [8] and to the experimental data in Section 4.

3 Experimental Apparatus

The vertical annular jet was produced by using two concentric plexiglas tubes, 85 cm long in an attempt to get a purely vertical initial flow with a known velocity profile. The two tubes were adjusted to be concentric at the exit to within about ± 0.6 percent in mean radius (or about ± 4 percent for the initial jet thickness). The laboratory industrial water flowed first through a long horizontal pipe which included a standard ASME orifice and then through a vertical 2 in. (5.08 cm) diameter PVC pipe about one meter long. The plexiglas tubes were attached to this vertical pipe as shown in Fig. 2. A conical transition piece and straightening vanes were installed at the top of the annulus and two pressure equalizer passages were installed using standard 1/8 in. (0.32 cm) diameter tubes.

The annular jet had an initial mean diameter of 4.45 cm and an initial thickness of 0.635 cm with initial jet velocities from about 0.15 to 10 m/s. The diameter to thickness ratio was chosen at about 7.0 to simulate the nominal value for the full-scale lithium jet. The velocity range also covers that proposed for the fusion reactor application. This resulted in convergence numbers, N_c from about 0.02 to about 100 for our experiments.

The orifice plate was calibrated using the standard technique of measuring the time required to fill a large drum, and the calculated velocities were only about 2 to 3 percent below the ASME calibration curves [11] with an uncertainty of ± 3 percent. The water temperature was measured to ± 2°C with a mercury/glass thermometer, which resulted in uncertainties much less than ± 1 percent in the water density and the surface tension coefficient. The resultant uncertainty in the dimensionless convergence parameter, N_c, due to the uncertainties in all the variables in N_c is estimated to be ± 8 percent. (All uncertainties quoted in this paper are for 20:1 odds [12].)

For the high flow velocities, above about 3 m/s the jet surface was highly turbulent and the hollow region could not be seen through the water. The jet convergence length was then measured by placing a meter stick next to the jet and measuring to the point of inflection where the jet diameter appeared to become essentially constant. This was checked for a few cases using flash photographs and also using redundant runs, and the agreement was always better than about ± 2 cm in the measured convergence lengths. For lower

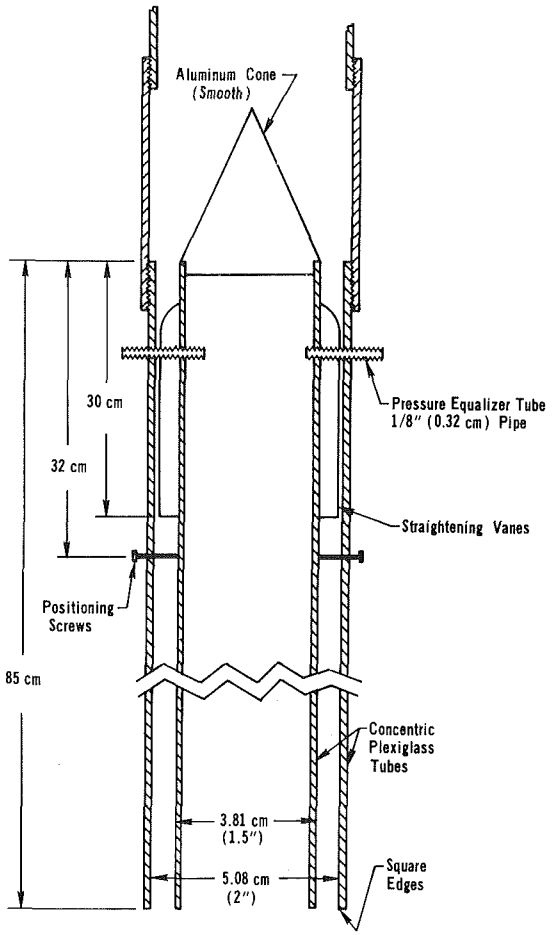

Fig. 2 Cross-section of the concentric plexiglas tube apparatus used to produce the annular jet

velocities below about 3 m/s, the jet surface was transparent enough to see the hollow region, and for these cases the inflection point method was found to agree with the visual observation of the closure point to within about ± 0.5 cm.

4 Results and Discussion

The experimental results for the three most extensive experimental run series are shown in Fig. 3. For Run Series I, with one pressure-equalizer vent tube, the convergence length increased approximately as expected with increasing jet velocity up to about 1.6 m/s and then behaved as shown in the figure. We hypothesized that the jet was acting as an ejector pump and was reducing the pressure inside the annular region to slightly below atmospheric pressure at the higher velocities in spite of the single pressure equalizer tube installed in the original apparatus. It is estimated that a pressure difference of only about 3 Pa ($\sim 4 \times 10^{-4}$ psi) is sufficient to create a pressure force equal to the initial surface tension force for our particular jet geometry. To test our hypothesis, we installed a second pressure-equalizer vent tube (as shown on Fig. 2) and reran the high velocity runs. The results were gratifying in that the data (Run Series II) seemed to follow the correct trend up to almost 3 m/s.

The apparatus was then modified extensively by removing the aluminum cone shown in Fig. 2 and replacing it with a large-diameter vent tube which was entirely open to the atmosphere [13]. From Fig. 3, the data of Run Series III can be seen to follow the trend of the modified Hovingh theory for $R^* = 0$ (equation (10)) very well up to the maximum useful velocity possible with this modified apparatus of about 4.4 m/s. (Above this velocity the convergence length was so long

Downloaded 02 Jun 2010 to 171.66.16.103. Redistribution subject to ASME license or copyright; see http://www.asme.org/terms/Terms_Use.cfm

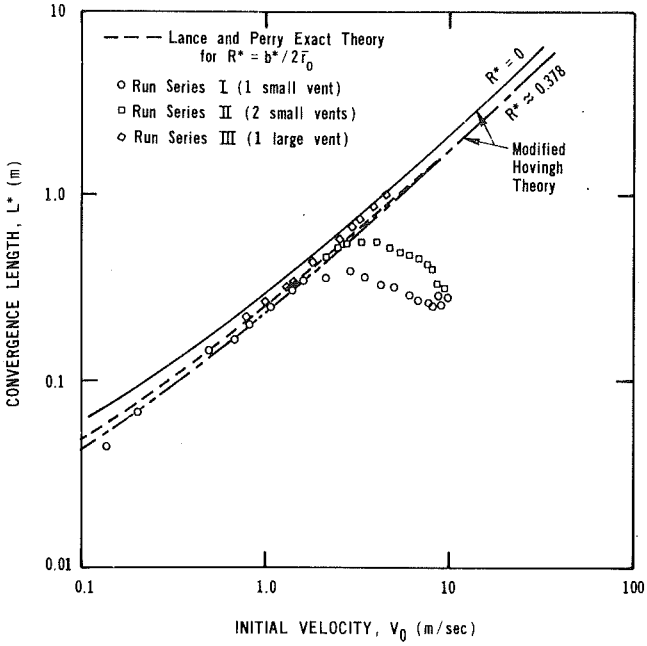

Fig. 3 Comparison of the experimental results for the closure or convergence length with three theoretical models

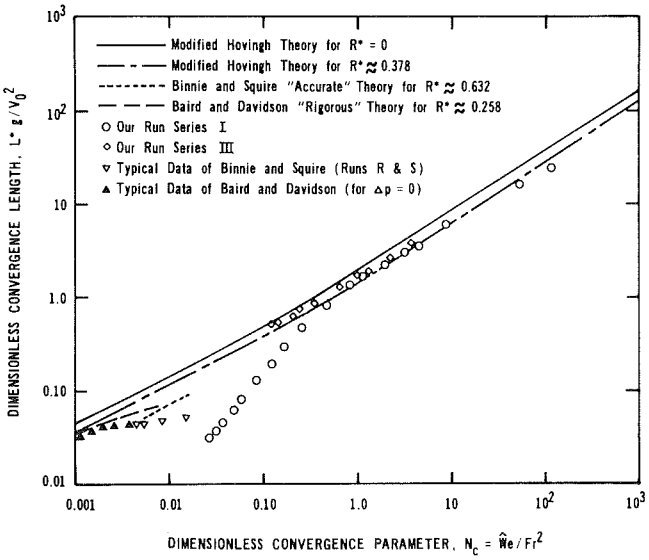

Fig. 4 Nondimensional presentation of the experimental convergence length data from three different experiments and comparison with theory

that the convergence point was almost at the surface of the water in the collection tank.) However, the data can be seen to lie about 5 to 15 percent below this simplified version of the theory with $R^* = 0$.

Hovingh's theory can be corrected approximately for the effect of finite $\bar{r}^*$ very simply by assuming that the jet velocity is high enough to stay almost constant to the convergence point. Then equation (9) becomes simply

$$R^* \simeq \sqrt{\frac{b_0}{2\bar{r}_0}} = 0.378$$

for our jet geometry. This overestimates R^* slightly, and its inclusion in the solution of equation (8) can be seen from Fig. 3 to over-correct the theory somewhat compared to the data of Run Series III.

We have also solved the full equations of Lance and Perry numerically [14] and plotted them on Fig. 3 as the dashed

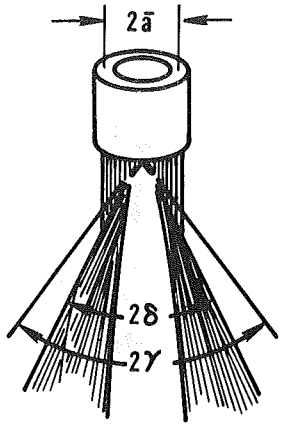

(a) Geometry for Annular Flow Experiments

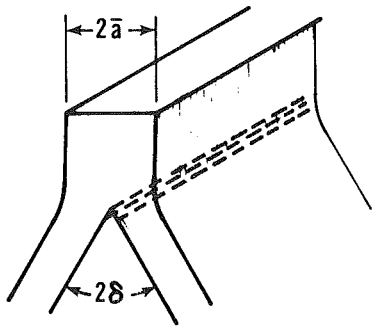

(b) Geometry for 2-D Sheet Jet Theory

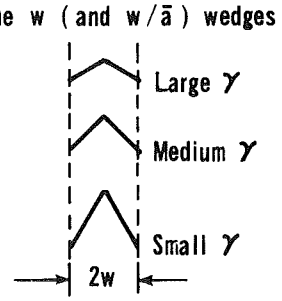

(c) Method for Variation of Wedge Angle

Fig. 5 Geometry of the wedge penetration experiments in the annular jet and comparison with an ideal 2-D sheet jet geometry

curve. The difference between the Hovingh theory for $R^* = 0.378$ and Lance and Perry's exact theory is due to the more accurate evaluation of R^* and to the effect of the jet radius of curvature in the vertical plane included in the latter. While these two effects can be seen from Fig. 3 to be quite small for our experimental conditions, the data of Run Series III does appear to agree better with the more exact theory of Lance and Perry (which is still a laminar flow theory and does not include the effects of turbulence).

In order to compare the earlier results of Binnie and Squire [5] and Baird and Davidson [6] with our data, the non-dimensional plot of L^*g/V_0^2 versus N_c shown in Fig. 4 has

Downloaded 02 Jun 2010 to 171.66.16.103. Redistribution subject to ASME license or copyright; see http://www.asme.org/terms/Terms_Use.cfm

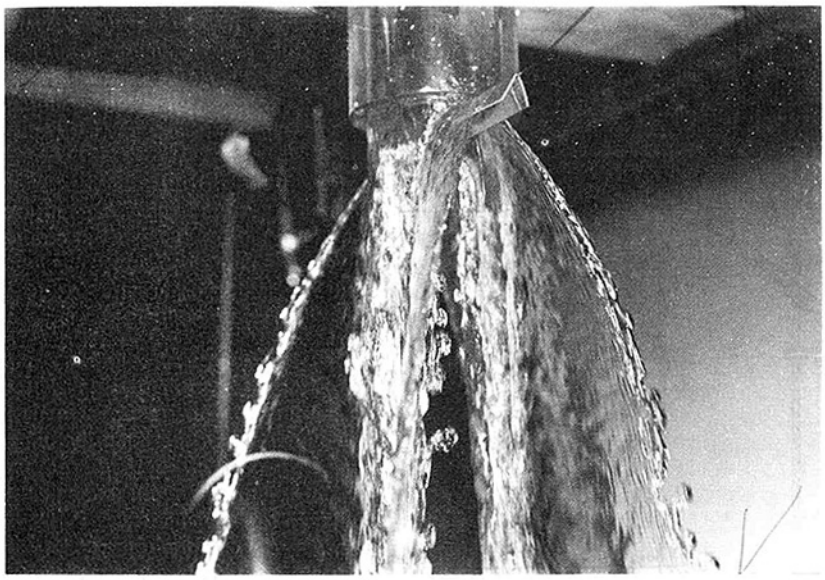

Fig. 6 Typical experimental flow pattern around a wedge-shaped obstacle penetrating through both sides of the annular jet showing the 3-D nature of the flow

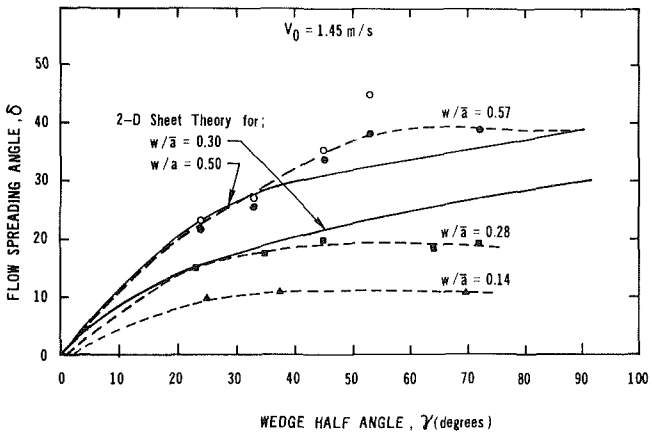

Fig. 7 Experimental flow splitting or spreading angle for three families of wedges at a relatively low flow velocity of 1.45 m/s and comparison with the ideal 2-D sheet jet theory

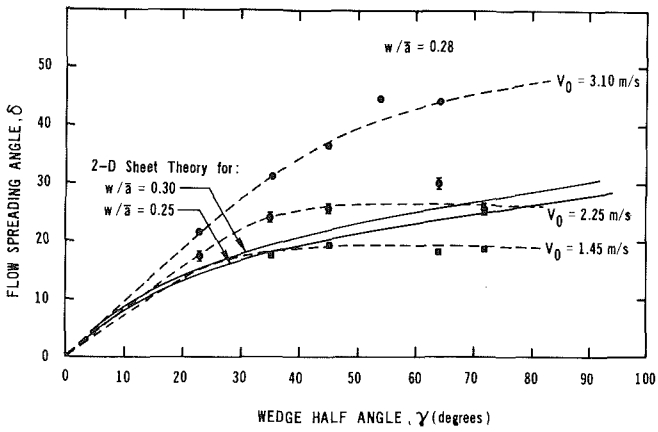

Fig. 8 Effect of flow velocity on the flow spreading angle for a single family of wedges with $w/\bar{a}$ = 0.28

been prepared. It can be seen that all these data tend to follow the same basic trend. It should be noted that low velocity data are to the right and higher velocity data are toward the left on this nondimensional plot.

Baird and Davidson present their own integrated theoretical results for Boussinesq's theory for their particular nozzle geometry and a finite $\bar{r}^* = 0.16$ cm ($R^* = 0.258$). A nondimensionalized version of their theoretical results (termed "accurate" in reference [6]) is shown by the dashed curve on Fig. 4. The theory can be seen to agree reasonably well with their experimental results.

Binnie and Squire developed their own approximations to the basic Boussinesq equations which they also solved numerically for their nozzle and plotted in their paper. We have nondimensionalized their results (termed "rigorous" in reference [5]) and presented them as the dotted curve on Fig. 4. Their theoretical results include a finite $\bar{r}^* = 0.251$ cm ($R^* = 0.632$), but the agreement with their data is only fair, particularly at the lower velocities (data points on the right) where they had some difficulty suppressing an initial divergence of their annular jet flow.

We have not put the exact theoretical results from the integration of Lance and Perry's equations on this figure for the sake of clarity, but it can be seen from Fig. 3 that this curve would fall in between the two Hovingh theory curves. It should be noted that there is not a single universal curve for any of the theories with finite R^* or finite r_v effects included; that is, each different nozzle geometry will have a different theoretical curve.

From Fig. 4, it can be seen that our experiments have extended the confirmed range of the convergence theories by about four orders of magnitude in N_c. However, the region of interest for the large radius and large thickness lithium annular jet is still far to the right near values of N_c typically on the order of 10^4. The corresponding convergence lengths predicted by both Hovingh's and Lance and Perry's theoretical results are many kilometers.

A brief look was taken at the problem of jet breakup. In the presence of the "natural" disturbances due to jet turbulence and the laboratory environment (building vibrations, etc.), we saw no evidence of breakup for flow lengths of almost seventy mean nozzle diameters. We have also run some initial qualitative experiments with forced excitation using pulsed air jets around the outer circumference of the annular jet as it exits from the plexiglas tubes. Near-axisymmetric waves which travelled down the jet were observed, but no signs of

Downloaded 02 Jun 2010 to 171.66.16.103. Redistribution subject to ASME license or copyright; see http://www.asme.org/terms/Terms_Use.cfm

breakup were seen. However, further experiments in this area are clearly necessary.

5 Penetration Studies

In the pulsed-fusion application, the annular jet must be penetrated with tubes in order to get laser, electron or ion beams into the central region where the fusion pellet is to be irradiated. We assumed that the tube would be streamlined on top and we simulated this streamlining by simple wedges of half angle γ, as shown in Fig. 5. The wedges penetrated all the way through both sides of the annular jet, which simulates two beam tubes facing one another.

We were interested in investigating the effects of rather large penetrations at velocities above 1 m/s. Typical ratios of the wedge half-width to the mean radius of the annular nozzle, $w/\bar{a}$, of 0.14, 0.28, and 0.57 were studied over a range of wedge half angles, γ, from about 23 deg to about 72 deg. A flash photograph of a typical flow over such a wedge is shown in Fig. 6. It can be seen that the flow has a complex three-dimensional form with momentum effects appearing to dominate the flow spreading or splitting below the wedge.

From flash photographs of the head-on view of the flow, such as sketched in Fig. 5(*a*), the total flow spreading angle, 2δ, was measured 2.5 cm below the wedge with an estimated accuracy of $\pm$ 2 deg. Results for three families of wedges with three different values of $w/\bar{a}$ are shown in Fig. 7 for the lowest velocity investigated systematically, 1.45 m/s. (A typical family of wedges with constant $w/\bar{a}$ is made as shown in Fig. 5(*c*).) Dashed lines have been added to Fig. 7 only to aid the eye in following the trends in the data points.

It appears impractical to try to develop a theory for the actual three-dimensional flow. However, the theory for a two-dimensional sheet jet flow of finite thickness impinging on a wedge (Fig. 5(*b*)) has been solved in the potential flow approximation by Siao and Hubbard and their results are reported in references [15] and [16]. These theoretical results, taken from the figures in the above two references, have been replotted on Fig. 7 for two cases, $w/\bar{a} = 0.30$ and 0.50.

It can be seen from Fig. 7 that the flow spreading angle for our complex 3-D flow tends to agree with the ideal 2-D jet theory at the smaller wedge angles for this flow velocity of 1.45 m/s. These results confirm that momentum effects dominate the flow pattern. At the larger wedge angles the 3-D effects tend to increase and evidently cause the flow spreading angle to tend to level out, probably because the 3-D effects allow the flow to spread along the wedge as well as split sideways (see Fig. 6).

The effect of jet velocity is shown in Fig. 8 for one family of wedges with a constant $w/\bar{a} = 0.28$. As the velocity is increased, the departure from the ideal 2-D sheet jet theory can be seen to occur at lower and lower wedge angles. This again can be attributed to the 3-D effects, since these effects tend to become more important as the velocity is increased.

6 Conclusions

This experimental study has provided additional data for modelling the fluid dynamic behavior of vertical annular jet flows, and the conclusions can be summarized as follows:

(*a*) The experiments with small diameter annular water jets confirm that the simple scaling law developed by Hovingh can be used to predict the convergence length up to values of the convergence number, N_c, of about 10^2 with good accuracy. As far as the fusion reactor application is concerned, an extrapolation of the theory by two orders of magnitude in the convergence number indicates that the lithium annular jet will probably not converge appreciably for the proposed reactor flow conditions unless a radially-inward component of velocity is produced by the nozzle [17].

(*b*) No breakup of the small-scale annular jet due to the naturally occurring disturbances in our experiments has been observed for vertical flow distances of almost seventy mean nozzle diameters.

(*c*) When a wedge-shaped obstacle is placed in the path of the annular jet, a complex, three-dimensional flow pattern results. However, at low jet velocities up to about 1.5 m/s and for small wedge half angles up to about 30 deg, the flow spreading or splitting angle agrees reasonably well with the potential flow solution for a two-dimensional sheet jet; from this we can infer that momentum effects dominate the flow spreading. At higher flow velocities and/or wedge angles, 3-D effects become very important and the flow splitting angle tends to saturate or level out.

Acknowledgments

We wish to express our special thanks to several students including Akbar Mokhtarani, Philip Chang, Dirk Dinsmore and Michael Calora for their diligent efforts in obtaining a large part of these data, and to James Maniscalco, Mike Monsler, Jack Hovingh, and Wayne Meier of LLL for their support, encouragement and their many helpful suggestions. This work was supported by the Laser Fusion Systems Studies Group of the Lawrence Livermore Laboratory (LLL) on Intramural Purchase Order No. 6774105.

References

1 Boussinesq, J., *Comptes Rendus de l'Academie des Sciences,* Paris, Vol. 69, 1869, p. 128.

2 Maniscalco, J. A., Meier, W. R., and Monsler, M. J., "Conceptual Design of a Laser Fusion Powerplant," UCRL-79652, Lawrence Livermore Laboratory, July 14, 1977.

3 Hovingh, J., "First Wall Response to Energy Deposition in Conceptual Laser Fusion Reactors," UCRL-77588, Rev. I, Lawrence Livermore Laboratory, Feb. 1976.

4 Hovingh, J., "Stability of a Flowing Circular Annular Liquid Curtain," Internal Memo SS&A-77-108, Lawrence Livermore Lab., Aug. 8, 1977.

5 Binnie, A. M., and Squire, H. B., "Liquid Jets of Annular Cross-Section," *The Engineer,* Vol. 171, London, Apr. 11, 1941, pp. 236-238.

6 Baird, M. H. I., and Davidson, J. F., "Annular Jets, Part I," *Chemical Engineering Science,* Vol. 17, 1962, pp. 467-472.

7 Hopwood, F. L., "Water Bells," *Proceedings of the Physical Society,* Vol. B65, No. 385B, London, Jan. 1952, pp. 2-5.

8 Lance, G. N., and Perry, R. L., "Water Bells," *Proceedings of the Physical Society,* Vol. B66, No. 397B, London, Dec. 1953, pp. 1067-1072.

9 Taylor, Sir Geoffrey, "The Dynamics of Thin Sheets of Fluid, Part I - Water Bells," *Proceedings of the Royal Society,* Vol. 253, London, Dec. 1959, pp. 289-295.

10 Dumbleton, J. H., "Effect of Gravity on the Shape of Water Bells," *Journal of Applied Physics,* Vol. 40, No. 10, Sept. 1969, pp. 3950-3954.

11 ASME, *Flow Measurement,* Power Test Codes Supplement, Chapter 4, Part 5, 1959.

12 Kline, S. J., and McClintock, F. A., "Describing Uncertainties in Single-Sample Experiments," *Mechanical Engineering,* Vol. 75, No. 1, Jan. 1953, pp. 3-8.

13 Monson, R. M., "Experimental Studies of Round Water Jets with Forced Nozzle Vibrations," M.S. thesis, Department of Mechanical Engineering, University of California, Davis (in preparation).

14 Takahashi, R. K., "Experimental Investigation of the Stability of Liquid Sheet Jets," M.S. thesis, Department of Mechanical Engineering, University of California, Davis, Dec. 1978.

15 Robertson, J. M., *Hydrodynamics in Theory and Application,* Prentice-Hall, Englewood Cliffs, N.J., 1965, pp. 456-460.

16 Yih, C. S., *Fluid Mechanics,* McGraw-Hill, N.Y., 1969, pp. 146-152.

17 Paul, D. D., "Dynamics of Newtonian Annular Jets," RPT UWFDM-287, Nuclear Engineering Department, Univ. of Wisconsin, Dec. 1978.

Downloaded 02 Jun 2010 to 171.66.16.103. Redistribution subject to ASME license or copyright; see http://www.asme.org/terms/Terms_Use.cfm

Calculation of Turbulent Wall Jets With an Algebraic Reynolds Stress Model

M. Ljuboja[1]

W. Rodi

Sonderforschungsbereich 80,
University of Karlsruhe,
Karlsruhe, W. Germany

A modified version of the k-ϵ turbulence model is developed which predicts well the main features of turbulent wall jets. The model relates the turbulent shear stress to the mean velocity gradient, the turbulent kinetic energy k, and the dissipation rate ϵ by way of the Kolmogorov-Prandtl eddy viscosity relation and determines k and ϵ from transport equations. The empirical constant in the Kolmogorov-Prandtl relation is replaced by a function which is derived by reducing a model form of the Reynolds stress transport equations to algebraic expressions, retaining the wall damping correction to the pressure-strain model used in these equations. The modified k-ϵ model is applied to a wall jet in stagnant surroundings as well as to a wall jet in a moving stream, and the predictions are compared with experimental data. The agreement is good with respect to most features of these flows.

Introduction

Turbulent wall jets are an important test case for "general" turbulence models because they contain a nearwall as well as a free layer, both interacting with each other. The two layers are identified in Fig. 1, where the flow configuration considered in this paper is sketched. Wall jets were found to spread significantly less than free jets; this reduction in spreading rate appears to be due not so much to the action of the wall shear stress on the flow but mainly to the damping of lateral velocity fluctuations by the wall. This damping effect penetrates into the outer layer and, since the lateral momentum transfer is closely linked to the lateral fluctuations, the shear stress and thus the spreading of the jet is reduced. Inversely, the relatively high turbulence in the outer layer has a sort of free-stream-turbulence effect on the near-wall layer.

Commonly used eddy viscosity models do not account for the damping of lateral fluctuations by the presence of a wall (unless this is put in empirically) and thus tend to overpredict the spreading of the wall jet when empirical constants are used that give the correct spreading for the free jet. For example, the widely adopted k-ϵ model [1] produces a spreading rate more than 30 percent too high when the standard constants are used which are suitable for many other flows. Second order closure models employing transport equations for the Reynolds stresses [2] can predict the wall jet correctly with the standard constants, but only when the wall influence on the pressure-strain correlation appearing in the Reynolds-stress equations is accounted for [3,4]. Predictions with a Reynolds-stress equation model not accounting for this influence yielded a rate of spread which was still 20 percent too high [5]. The pressure-strain models suggested in [2] and [6] produce the observed damping of the lateral fluctuations, and the latter will be adopted in the present work.

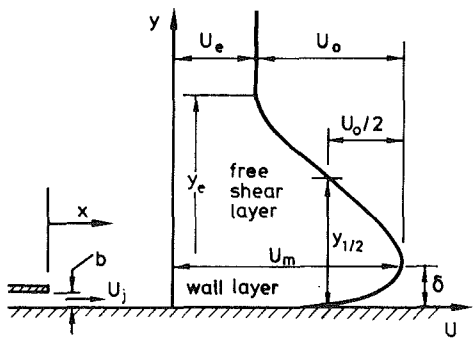

Fig. 1 Flow configuration

Reynolds stress equation models are complex and expensive in application. The purpose of this paper is to show that the wall damping effect in wall jets can also be obtained with a simpler model in which the stress equations are reduced to algebraic expressions. This reduction leads to an eddy viscosity model which predicts well the main features of wall jets. It does of course not predict the experimental observation that the points of zero shear stress and zero velocity gradient do not conicide; the difference between these locations is however relatively small and of little practical importance. In the following section the Reynolds stress equations as modelled in [6] are reduced to algebraic expressions by introducing simplifying assumptions about the convection and diffusion terms. The resulting shear stress expression is of the form of the Kolmogorov-Prandtl eddy

[1] On leave from Unis, Sarajewo, Yugoslavia.

Contributed by the Fluids Engineering Division of THE AMERICAN SOCIETY OF MECHANICAL ENGINEERS and presented at the ASME-CSME Applied Mechanics, Fluids Engineering, and Bioengineering Conference, Niagara Falls, N.Y. June 1979. Manuscript received by the Fluids Engineering Division, July 25, 1979.

Copyright © 1980 by ASME

Downloaded 02 Jun 2010 to 171.66.16.103. Redistribution subject to ASME license or copyright; see http://www.asme.org/terms/Terms_Use.cfm

viscosity relation, but with the empirical constant c_μ now replaced by a function which is an outcome of the derivation. The kinetic energy k of the turbulent motion and the rate of its dissipation appearing in this shear-stress expression are determined from differential transport equations. The model is applied to wall jets in stagnant and moving surroundings and the predictions are shown to compare favorably with experiments.

Mathematical Model

Mean Flow Equations. The mean velocity field of two-dimensional wall jets is governed by the thin-shear layer form of the streamwise momentum equation

$$U\frac{\partial U}{\partial x}+V\frac{\partial u}{\partial y}=-\frac{\partial \overline{uv}}{\partial y} \tag{1}$$

and by the continuity equation

$$\frac{\partial U}{\partial x}+\frac{\partial V}{\partial y}=0, \tag{2}$$

where U and V are the mean flow velocity and u and v the fluctuating velocity components in the x and y direction, as shown in Fig. 1. As is usual for thin shear layers, the normal stress term has been neglected in the momentum equation (1). The viscous stress term $\nu\partial U/\partial y$ has also been omitted from (1) so that this equation is not valid very near the wall; as will be discussed below in the section on boundary conditions, the approach followed in this paper is to integrate the equations only to a point outside the viscous sublayer and to connect the velocity at this point to the wall shear stress via the logarithmic law of the wall.

Turbulence Model. A turbulence model is required to determine the turbulent shear stress $\overline{uv}$ (strictly speaking $-\rho\overline{uv}$ is the shear stress) appearing in the momentum equation. Here we propose to modify the so-called $k-\epsilon$ turbulence model so that it accounts for the damping effect of the wall on the lateral fluctuations and consequently for the lower shear stress caused by this damping. The standard version of the $k-\epsilon$ model, which works well for the free jet and many other flows [1,7,8] will first be described briefly (for a detailed description see [1]). This model connects the shear stress to the mean velocity gradient via the eddy viscosity concept.

$$-\overline{uv}=\nu_t\frac{\partial U}{\partial y} \tag{3}$$

and relates the (kinematic) eddy viscosity ν_t to the kinetic energy of the turbulent motion, k, and to the rate of its dissipation, ϵ, via the Kolmogorov-Prandtl expression

$$\nu_t=c_\mu\frac{k^2}{\epsilon}, \tag{4}$$

where c_μ is an empirical constant. The distribution of the turbulence parameters k and ϵ over the flow field is obtained by solving the following, semi-empirical transport equations for these quantities:

$$U\frac{\partial k}{\partial x}+V\frac{\partial k}{\partial y}=\frac{\partial}{\partial y}\left(\frac{\nu_t}{\sigma_k}\frac{\partial k}{\partial y}\right)+\underbrace{\nu_t\left(\frac{\partial U}{\partial y}\right)^2}_{\text{P = production}}-\epsilon \tag{5}$$

$$U\frac{\partial \epsilon}{\partial x}+V\frac{\partial \epsilon}{\partial y}=\frac{\partial}{\partial y}\left(\frac{\nu_t}{\sigma_\epsilon}\frac{\partial \epsilon}{\partial y}\right)+c_{\epsilon 1}\frac{\epsilon}{k}\nu_t\left(\frac{\partial U}{\partial y}\right)^2-c_{\epsilon 2}\frac{\epsilon^2}{k} \tag{6}$$

These equations are also of a form valid only for thin shear layers outside the viscous sublayer and they contain further empirical constants. The values usually adopted for the empirical constants in the $k-\epsilon$ model are those quoted in [1]; they are listed in Table 1.
With these constants, the rate of spread of a plane free jet is predicted correctly but that of a wall jet is overpredicted by more than 30 percent (see Table 3).

In what follows, the k - ϵ model is modified by allowing the parameter c_μ to vary. The law describing this variation is found by simplifying a modelled form of the transport equation for the shear stress $\overline{uv}$. Turbulence models employing this equation (together with equations for other stress components) were found to describe well the influence of walls in both wall boundary layers [2] and wall jets [3,4]; it is the retention of the wall effect upon simplification of the stress equations which is the essential feature of the present model development.

Nomenclature

b = slot width of jet nozzle
c's = constants in turbulence model
E = friction parameter in logarithmic velocity law (22)
f = wall damping function (13)
G's = wall correction function defined in (19) and (20)
k = kinetic energy of turbulence $=\frac{1}{2}(\overline{u^2}+\overline{v^2}+\overline{w^2})$
L = length scale of turbulence
P = production of k
P_{ij} = production of $\overline{u_iu_j}$
p = fluctuating pressure
Re = jet exit Reynolds number $= U_jb/\nu$
U,V,W = mean velocity components in x,y,z direction
u,v,w = fluctuating components in x,y,z direction
U_i = mean velocity component in x_i direction
u_i = fluctuating velocity component in x_i direction
U_e = free stream velocity
U_m = maximum velocity
U_j = jet exit velocity
U_τ = friction velocity $=\sqrt{\tau_w/\rho}$
x,y,z = coordinates
x_i = coordinates in tensor notation
$y_{1/2}$ = jet half width (see Fig. 1)
y^+ = dimensionless wall distance $={}_\tau y/\nu$
δ = wall distance of point of maximum velocity
δ_{ij} = Kronecker delta (= 1 for $i=j$ and 0 for $i\neq j$)
ϵ = dissipation rate of k
ϵ_{ij} = dissipation rate of $\overline{u_iu_j}$
κ = von Kármán constant
ν = kinematic molecular viscosity
ν_t = eddy (or turbulent) viscosity
π_{ij} = pressure-strain correlation
ρ = fluid density
$\sigma_{k,\epsilon}$ = diffusion constants in k, ϵ-equations
τ = shear stress
τ_w = wall shear stress

Subscripts

c = values at point y_c
e = external stream
j = jet exit
m = maximum velocity
w = wall

Overbars

= time averaging

Downloaded 02 Jun 2010 to 171.66.16.103. Redistribution subject to ASME license or copyright; see http://www.asme.org/terms/Terms_Use.cfm

Table 1 Values of empirical constants in the standard k - ϵ model

c_μ	σ_k	σ_ϵ	$c_{\epsilon 1}$	$c_{\epsilon 2}$
0.09	1.	1.3	1.44	1.92

We start this development from the exact transport equation for the Reynolds stresses $\overline{u_i u_j}$ which, for high Reynolds numbers, may be written in the following form:

$$U_l \frac{\partial \overline{u_i u_j}}{\partial x_l} = -\frac{\partial}{\partial x_l}(\overline{u_l u_i u_j}) - \frac{1}{\rho}\left(\overline{\frac{\partial u_j p}{\partial x_i}} + \overline{\frac{\partial u_i p}{\partial x_j}}\right) - 2\nu \overline{\frac{\partial u_i}{\partial x_l}\frac{\partial u_j}{\partial x_l}}$$

convective transport; diffusive transport; ϵ_{ij} = viscous destruction

$$-\overline{u_i u_l}\frac{\partial U_j}{\partial x_l} - \overline{u_j u_l}\frac{\partial U_i}{\partial x_l} + \overline{\frac{p}{\rho}\left(\frac{\partial u_i}{\partial x_j} + \frac{\partial u_j}{\partial x_i}\right)} \qquad (7)$$

P_{ij} = production; π_{ij} = pressure-strain

The contraction of this equation (summation over the 3 equations for the normal stresses u_i^2) yields the equation for the turbulent kineric energy k, the thin-shear layer form of which is equation (5). At the so-called second-order closure level, the turbulence correlations appearing in the diffusion, pressure-strain, and dissipation terms are approximated by models relating them to the Reynolds stresses, the mean velocity field, and some turbulence length scale (or, what is equivalent, to the dissipation rate ϵ). The diffusion model is not of interest here because both convective and diffusive transport will be the subject of further simplification. The viscous dissipation is modelled as usual by assuming that the small-scale turbulent motion responsible for the dissipation is isotropic at high Reynolds numbers:

$$\epsilon_{ij} = \frac{2}{3}\epsilon\,\delta_{ij}. \qquad (8)$$

The pressure strain correlation π_{ij} receives contributions from two processes, one being due to the interaction of fluctuating velocities only ($\pi_{ij,1}$) and the other arising from the interaction of mean strain and fluctuating velocities ($\pi_{ij,2}$). Rotta's [9] proposal for the first part to be proportional to the anisotropy of the turbulence is adopted here:

$$\pi_{ij,1} = -c_1 \frac{\epsilon}{k}\left(\overline{u_i u_j} - \frac{2}{3}\delta_{ij}k\right). \qquad (9)$$

For the second part, Launder, Reece and Rodi [2] introduced a rather refined model which was shown to predict quite well the individual stress components in a number of flows. The following truncated form of the model was however found to perform nearly equally well and will be adopted here:

$$\pi_{ij,2} = -c_2\left(P_{ij} - \frac{2}{3}\delta_{ij}P\right) \qquad (10)$$

In this relation P_{ij} and P are the production of $\overline{u_i u_j}$ and k, respectively, as defined in equations (5)[1] and (7).

In local equilibrium shear layers, where convection and diffusion terms in equation (7) are absent, the ratios of the individual stresses $u_i u_j$ to each other (and thus to $k = 1/2\,\overline{u_i u_i}$) are determined solely by the pressure-strain model. Experiments have shown that these ratios are significantly different in shear layers near to and remote from walls: in near-wall turbulence the level of fluctuating velocity normal to the surface is much damped as discussed already, while that parallel to the main flow is enhanced relative to free shear flow. The pressure-strain model introduced thus far does not produce these differences because it does not account for any wall effect. This effect can be included by a wall correction to the pressure-strain model, and various proposals have been made in the literature. As additive correction to the first part $\pi_{ij,1}$ we adopt a proposal made by Daly and Harlow [10] and independently by Shir [11] which is now also used by other authors (e.g. [6]).

$$\pi'_{ij,1} = c'_1 \frac{\epsilon}{k}\left(\overline{u_n^2}\delta_{ij} - \frac{2}{3}\overline{u_n u_i}\delta_{nj} - \frac{3}{2}\overline{u_n u_j}\delta_{ni}\right) f\left(\frac{L}{y}\right) \qquad (11)$$

Gibson and Launder [6] extended this proposal by introducing an analogous additive correction for $\pi_{ij,2}$:

$$\pi'_{ij,2} = c'_2\left(\pi_{nn,2}\delta_{ij} - \frac{3}{2}\pi_{ni,2}\delta_{nj} - \frac{3}{2}\pi_{nj,2}\delta_{ni}\right) f\left(\frac{L}{y}\right) \qquad (12)$$

In these expressions n denotes the direction normal to the wall and y is the distance from the wall. The function $f(L/y)$ is to reduce the effect of the wall correction with increasing distance from the wall; L is a length scale characterizing the energy containing eddies. A linear relationship was found to be adequate [2,3,4] which, with $L \propto k^{3/2}/\epsilon$, can be written as

$$f = \frac{k^{3/2}}{c_w y \epsilon} \qquad (13)$$

In contrast to the flat-plate boundary layers and channels investigated in [2], in wall jets the kinetic energy k and thus the function f may rise first with distance from the wall (see Fig. 4) before it approaches zero further away. As the wall-damping effect should be strongest near the wall, such a behavior appears unreasonable; therefore whenever f exceeded its near-wall value it was replaced by this value in the calculations presented below. This admittedly rather crude measure was also adopted by Irwin [4] in his stress-equation model. The coefficient c_w in (13) was chosen such that the function f has a value of unity clost to the wall where turbulence is in local equilibrium. This choice yielded $c_w = \kappa/c_\mu^{3/4}$, as will be shown below in the section on boundary conditions; it also fixes the coefficients c_1' and c_2' in the near-wall corrections, whose determination will also be discussed below. The constants c_1 and c_2 were taken from [6],[2] and all the constants in the pressure-strain model are compiled in Table 2.

For the wall jets considered here, the Reynolds stresses $\overline{uv}$ and $\overline{v^2}$ are of prime importance, and the modelled transport equations for these stresses are as follows:

$$\frac{D\overline{uv}}{Dt} = \mathrm{Diff}_{\overline{uv}} - \overline{v^2}\frac{\partial U}{\partial y} - c_1\frac{\epsilon}{k}\overline{uv}\left(1 + \frac{3}{2}\frac{c_1'}{c_1}f\right) + c_2\overline{v^2}\frac{\partial U}{\partial y}\left(1 - \frac{3}{2}c_2'f\right) \qquad (14)$$

$$\frac{D\overline{v^2}}{Dt} = \mathrm{Diff}_{\overline{v^2}} - c_1\frac{\epsilon}{k}\left[\left(1 + 2\frac{c_1'}{c_1}f\right)\overline{v^2} - \frac{2}{3}k\right] - \frac{2}{3}c_2\overline{uv}\frac{\partial U}{\partial y}(1 - 2c'_2 f) - \frac{2}{3}\epsilon \qquad (15)$$

convection; diff.; prod.; pressure-strain; diss.

[1] Equation (5) contains already the eddy viscosity assumption. In the exact equation the production of k is $-\overline{u_i u_j}\,\partial U_i/\partial x_j$.

[2] In an earlier version of the paper presented at the ASME Symposium on Turbulent Boundary Layers, Niagara Falls, June 1979, somewhat different constants suggested in earlier works [12,13] were used.

Downloaded 02 Jun 2010 to 171.66.16.103. Redistribution subject to ASME license or copyright; see http://www.asme.org/terms/Terms_Use.cfm

Table 2 Constants in the pressure-strain model

c_1	c_2	c_1'	c_2'	c_w
1.8	0.6	.6	.3	3.72

These equations were obtained by incorporating the model assumptions (8) to (12) into (7) and by neglecting certain terms according to the usual thin shear layer approximation.

A Reynolds-stress-equation turbulence closure for the wall jet may be obtained by adding the equations for k and ϵ to the stress equations (14) and (15), of course with an explicit model also for the diffusion terms (see e.g. [2]). Based on the successful predictions of Reece [3] and Irwin [4] with similar schemes (mainly the wall corrections to the pressure-strain model where somewhat different) one can expect this closure scheme to yield satisfactory predictions for free jets and wall jets, both with respect to the spreading rate and, in the latter case, the experimental observation that points of zero shear stress and zero mean velocity gradient do not coincide. Essential for obtaining the correct spreading rate of the wall jet is the inclusion of the wall correction to the pressure-strain-model; for Hanjalic and Launder [5] did predict the shear stress and velocity gradient to vanish at different points but overpredicted the spreading by 20 percent with their shear-stress equation model which did not include a wall correction and used a constant value of $\overline{v^2}/k$ obtained from free-shear layer experiments.

The stress equations (14) and (15) are differential equations because of the appearance of differential expressions in the convective and diffusive transport terms (not explicitly shown in case of the latter). The aim here is to reduce these equations to algebraic expressions, thereby obtaining a simpler model, yet retaining the main features of the original model, in particular the wall damping effect. One way to obtain algebraic stress relations is to simply neglect the transport terms in equations (14) and (15). This leads to a certain inconsistency in the simulation of $\overline{v^2}$ since, when the other normal stress components $\overline{u^2}$ and $\overline{w^2}$ are determined from the corresponding algebraic relations, the sum of the 3 resulting normal stresses is equal to $2k$ only in the special case of local equilibrium, i.e., when production $P(=-\overline{uv}\partial U/\partial y)$ and dissipation ϵ of k are equal. As k is determined from the transport equation (5) in the model discussed here, production and dissipation in (5) are not assumed to be in balance and thus will generally not be equal. The inconsistency resulting for $\overline{v^2}$ can be removed if, according to the suggestion of Rodi [14], the transport of $\overline{v^2}$ is not neglected but assumed proportional to the transport of k, which is equal to $P-\epsilon$:

$$\left(\frac{D\overline{v^2}}{Dt}-\mathrm{Diff}_{\overline{v^2}}\right)=\frac{\overline{v^2}}{k}\left(\frac{Dk}{Dt}-\mathrm{Diff}_k\right)=\frac{\overline{v^2}}{k}(P-\epsilon). \quad (16)$$

A similar approximation could, of course, be introduced also for the transport of $\overline{uv}$, but preliminary calculations with this produced no beneficial effect. Therefore, and since in contrast to the normal stresses the neglect of transport of the shear stress does not introduce an inconsistency, the transport of $\overline{uv}$ was neglected in the present model. With this and relation (16) for the transport of $\overline{v^2}$, the stress equations (14) and (15) can be reduced to

$$-\overline{uv}=\underbrace{\frac{1-c_2+\frac{3}{2}c_2c_2'f}{c_1+\frac{3}{2}c'f}}_{c_\mu}\frac{\overline{v^2}}{k}\frac{k^2}{\epsilon}\frac{\partial U}{\partial y} \quad (17)$$

$$\frac{\overline{v^2}}{k}=\frac{2}{3}\frac{c_1-1+\frac{P}{\epsilon}(c_2-2c_2c_2'f)}{c_1+\frac{P}{\epsilon}-1+2c_1'f} \quad (18)$$

Equation (17) can be seen to be equivalent to a combination of the eddy-viscosity relation (3) and the Kolmogorov-Prandtl formula (4), with c_μ now depending on P/ϵ and the wall-correction function f when $\overline{v^2}/k$ is eliminated with the aid of (18). For free shear layers ($f=0$) with $P\approx\epsilon$ these results $c_\mu=0.115$ from (17) and (18) when c_1 and c_2 are given the values listed in Table 2. When this value of c_μ is used instead of the usual value of 0.09 (see Table 1) in the k-ϵ turbulence model, the rate of spread of the free jet is overpredicted. Therefore equations (17) and (18) are not used directly to determine the variation of c_μ but are rearranged as the product of two terms of which the first one does not depend on the wall-correction function f while the second one does:

$$c_\mu=\frac{\overline{v^2}}{k}\frac{1-c_2}{c_1}\underbrace{\frac{1+\frac{3}{2}\frac{c_2c_2'}{1-c_2}f}{1+\frac{3}{2}\frac{c_1'}{c_1}f}}_{G_1} \quad (19)$$

$$\frac{\overline{v^2}}{k}=\frac{2}{3}\frac{c_1-1+c_2\frac{P}{\epsilon}}{c_1+\frac{P}{\epsilon}-1}\underbrace{\frac{1-2\frac{c_2c_2'P/\epsilon}{c_1-1+c_2P/\epsilon}f}{1+2\frac{c_1'}{c_1+P/\epsilon-1}f}}_{G_2} \quad (20)$$

Elminiation of $\overline{v^2}/k$ in (19) with the aid of (20) then yields

$$c_\mu=F_\mu G_1G_2$$

with $$F_\mu=\frac{2}{3}\frac{1-c_2}{c_1}\frac{c_1-1+c_2P/\epsilon}{c_1+P/\epsilon-1}$$

In this expression G_1 and G_2 as defined in (19) and (20) depend on f while F_μ does not. We now replace F_μ by the constant value 0.09 so that the free jet (where $G_1=G_2=1$) is predicted correctly:

$$c_\mu=0.09\,G_1G_2. \quad (21)$$

This is the functional dependence proposed in this paper for the parameter c_μ in the k-ϵ model. Equation (21) implies that c_μ is equal to the usual value of 0.09 for free flows but is altered near walls through the correction functions G_1 and G_2 defined in (19) and (20). The rest of the k-ϵ model introduced earlier is retained unchanged.

Boundary Conditions. The turbulent model introduced above is valid only for fully turbulent flow at high Reynolds numbers so that it does not apply to the viscous sublayer very close to solid walls. Rather than extend the model to account for low Reynolds number phenomena as was done by Jones and Launder [15] the wall-function approach outlined in [1] is adopted here which allows the equations to be integrated outside the viscous sublayer only. We assume that just outside this sublayer there is a region where the velocity follows the logarithmic law of the wall, the turbulent shear stress $-\rho\overline{uv}$ is approximately equal to the wall shear stress τ_w, and production P and dissipation ϵ of the turbulent kinetic energy are approximately in balance. The first assumption implies that the velocity at a point in this region with wall distance y_c can be related to the wall shear stress by

$$\frac{U_c}{U_\tau}=\frac{1}{\kappa}\ln(y_c^+E), \quad (22)$$

Downloaded 02 Jun 2010 to 171.66.16.103. Redistribution subject to ASME license or copyright; see http://www.asme.org/terms/Terms_Use.cfm

where $U_\tau = (\tau_w/\rho)^{1/2}$ is the friction velocity, $y_c^+ = U_\tau y_c/\nu$ is a dimensionless wall distance, κ is the von Kármán constant and E a roughness parameter. κ was taken as 0.435 and E as 9.0 for smooth walls. These values were suggested by Patankar and Spalding [16] and were used in many previous k - ϵ model calculations.

The assumptions made above also imply that the value of k and ϵ at point y_c are [1]:

$$k_c = \frac{U_\tau^2}{\sqrt{c_\mu}}, \quad \epsilon_c = \frac{U_\tau^3}{\kappa y_c}. \tag{23}$$

These are the boundary conditions for k and ϵ applied at point y_c in the present calculations, the value of c_μ being determined by (21) at y_c. In order for the above assumptions to be approximately valid, point y_c should lie in the range $30 \leq y_c^+ \leq 50$, as experiments indicate (e.g.[17]) that the region in which the usual log-law holds is much smaller in wall jets than for example in boundary layers or channel flow.

It was mentioned already that the parameter c_w in (13) is chosen such that the wall correction function f has a value of unity near the wall, and more precisely we here fix this value at point y_c. With $f = 1$ and $P/\epsilon = 1$ at this point, (21) yields a relation for c_μ (and thus for $\overline{uv}/k$ according to (23)) and (18) a relation for $\overline{v^2}/k$ which both depend only on the parameters c_1' and c_2' once the constants c_1 and c_2 have been fixed. c_1' and c_2' in these relations were adjusted to yield values of $\overline{uv}/k$ and $\overline{v^2}/k$ close to 0.22 quoted in [3] as consensus of experimental values for both quantities in near-wall turbulence. With $c_1' = 0.6$ and $c_2' = 0.3$ as listed in Table 2, there follows from (18) $\overline{v^2}/k = 0.231$ and from (17) $c_\mu = 0.057$ (i.e. $\overline{uv}/k = 0.239$ according to (23)). The value of c_2' is the same as suggested by Gibson and Launder [6] but the value of c_1' is slightly higher (in [6] it was 0.5).

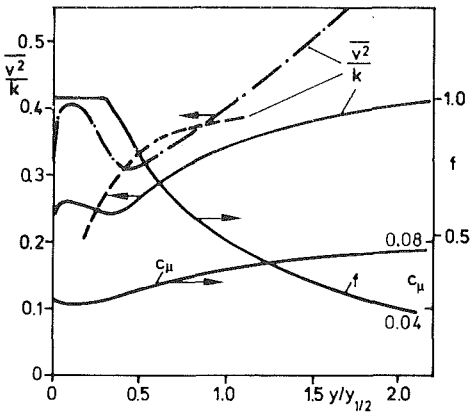

Fig. 2 Wall jet in stagnant surroundings, lateral distribution of $\overline{v^2}/k$, f and c_μ in the similarity region, — present calculations, – · – $\overline{v^2}/k$ calculations of Irwin [4], ···· $\overline{v^2}/k$ experiments [20]

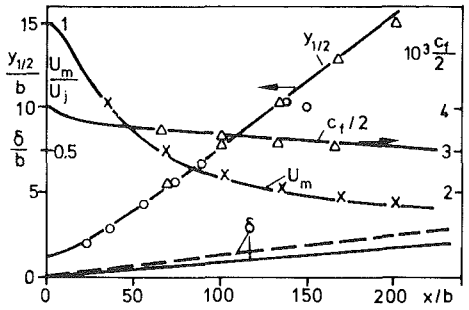

Fig. 3 Wall jet in stagnant surroundings, streamwise development of $y_{1/2}/b$, δ/b, U_m/U_j and c_f, — predictions, Δ x experiments of Tailland [17] for Re = 18000, o experiments of Guitton [20], ··· experimental correlation for δ/b of Kruka and Eskinazi [21]

Application of the Model

This section describes the application of the mathematical model introduced above to a wall jet in stagnant surrounding as well as to the wall jet in a moving stream studied experimentally by Kacker and Whitelaw [18]. The mean-flow equations (1) and (2) together with the k- and ϵ -equations (5) and (6) were solved numerically with the marching-forward procedure of Patankar and Spalding [16] for two-dimensional boundary layers. 40 grid nodes were used across the wall jet and the forward step was typically 0.015 times the jet width y_e.

Wall Jet in Stagnant Surroundings ($U_e = 0$). The calculations of this case were started at the nozzle exit ($x = 0$) with a uniform velocity profile and uniform distribution of k and ϵ corresponding to low turbulence. Various levels of k and ϵ were tried and found to have little influence on the development of the wall jet, except very near the exit. Downstream of an initial development region the profiles of the mean and turbulence quantities attain similarity, and the jet spreads linearly so that $dy_{1/2}/dx$ is constant. Table 3 compares predicted and measured values of $dy_{1/2}/dx$; predictions with the k - ϵ model using $c_\mu = 0.09$ are also included for both the wall jet and the plane free jet.

Table 3 Rates of spread $dy_{1/2}/dx$

	Predictions		
	c_μ from (21)	$c_\mu = 0.09$	Experiments
wall jet	0.076	0.106	0.073 - 0.076 [17]
free jet	--	.114	.11 [19]

The table shows that the model using the c_μ -function (21) predicts correctly the rate of spread of the wall jet while the model using $c_\mu = 0.09$ produces a value considerably too high.

In order to illustrate the wall-damping features of the present model, the lateral distributions of $\overline{v^2}/k$, f and c_μ are plotted in Fig. 2 for the similarity region of the wall jet; $\overline{v^2}/k$ was calculated from equation (18) and is compared with measurements of Guitton [20]. The figure shows that in this case the limitation imposed on the f-function (i.e. not to exceed a value of unity) is effective over the inner 1/6 of the jet width. Further, the wall-damping effect is felt across the whole jet as f has not fallen to zero at the jet edge ($y/y_{1/2} \approx 2.5$, see Fig. 4). $\overline{v^2}/k$ first rises with distance from the wall because P/ϵ decreases; a maximum is reached at the point of maximum velocity where P/ϵ is zero because the velocity gradient is zero. From here on, P/ϵ increases again, causing $\overline{v^2}/k$ to decrease somewhat as shown in Fig. 2. So far the behavior of $\overline{v^2}/k$ was determined entirely by P/ϵ because f was constant. When f starts to fall, $\overline{v^2}/k$ rises again and approaches a value pertaining to free shear layers. The up-down-up behavior of $\overline{v^2}/k$ is perhaps not realistic, but it is also present (and even more pronounced so) in the predictions of Irwin [4] obtained with a Reynolds stress equation model (see Fig. 2). This behavior appears to be due to the limitation imposed on the f-function, and a more refined relation for f seems necessary to obtain a more realistic distribution of $\overline{v^2}/k$ near the wall. More generally however the variation of $\overline{v^2}/k$, and in particular its reduction near the wall, is described correctly. The variation of c_μ is somewhat different from that of $\overline{v^2}/k$ and in this context it is important to remember that c_μ

Downloaded 02 Jun 2010 to 171.66.16.103. Redistribution subject to ASME license or copyright; see http://www.asme.org/terms/Terms_Use.cfm

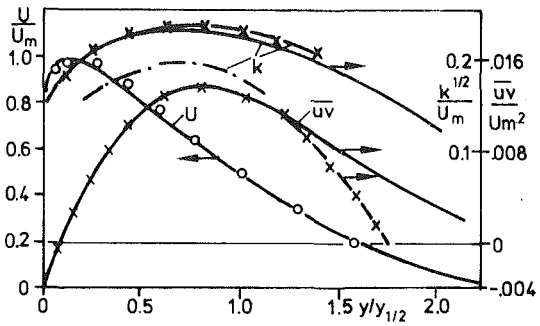

Fig. 4 Wall jet in stagnant surroundings, lateral profiles of velocity, shear stress and kinetic energy in the similarity region, _ predictions, o-x-experiments of Tailland [17], – • – experiments of Guitton [20]

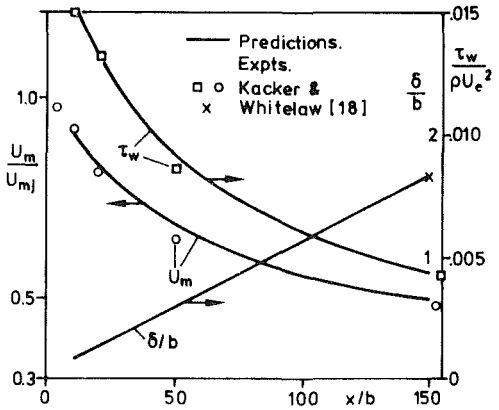

Fig. 5 Wall jet in a moving stream (U_e/U_j = 0.43), streamwise development of maximum velocity and its location, and of wall shear stress

is not calculated from (19) with $\overline{v^2}/k$ from (18) but from relation (21). On the average c_μ is significantly below 0.09 which explains the reduced rate of spread as compared with the spread obtained with the standard k- ϵ model using c_μ = 0.09.

Figure 3 shows the streamwise development of the jet half width $y_{1/2}$, the width of the wall layer δ, the maximum velocity U_m, and the wall friction coefficient $c_f = \tau_w/\frac{1}{2}\rho U_m^2$. The close agreement between predicted and measured half-width development is not surprising in view of the correctly predicted rate of spread discussed already. The predicted decay of U_m and c_f is also in good agreement with Tailland's [17] data. The increase of δ is under-predicted, which means that the velocity maximum is too close to the wall; this discrepancy will be considered further when the velocity profile is discussed.

Figure 4 compares predicted and measured lateral profiles of U, $\overline{uv}$, and k in the similarity region of the jet. The agreement for the velocity profile is very good except near the point of maximum velocity. According to the experiments the shear stress does not vanish at the point of maximum velocity so that there is a small region where the shear stress $-\rho\overline{uv}$ and the velocity gradient $\partial U/\partial y$ have opposite signs. Obviously, this region cannot be simulated correctly with an eddy viscosity model which forces the shear stress to vanish at the point of maximum velocity. Therefore, eddy viscosity models always predict the velocity maximum to lie too close to the wall, and a stress-equation model is necessary to reproduce correctly the observed behavior. The problematic region is however so small that its malprediction is not of practical significance. The profiles of $\overline{uv}$ and k also shown in Fig. 4 can be seen to be reasonably well predicted considering the uncertainties in the experimental results (note the difference in the k-measurements of Tailland [17] and Guitton [20]). Near the jet edge the predictions are perhaps somewhat too high,

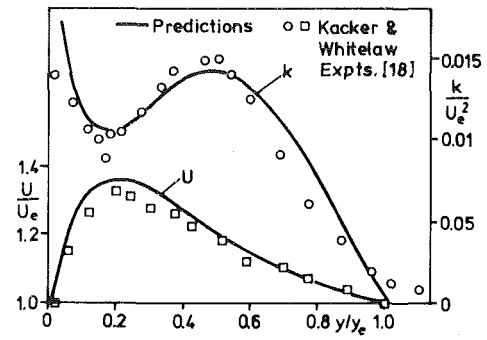

Fig. 6 Wall jet in a moving stream (U_e/U_j = 0.43), Lateral profiles of velocity and kinetic energy at x/b = 150

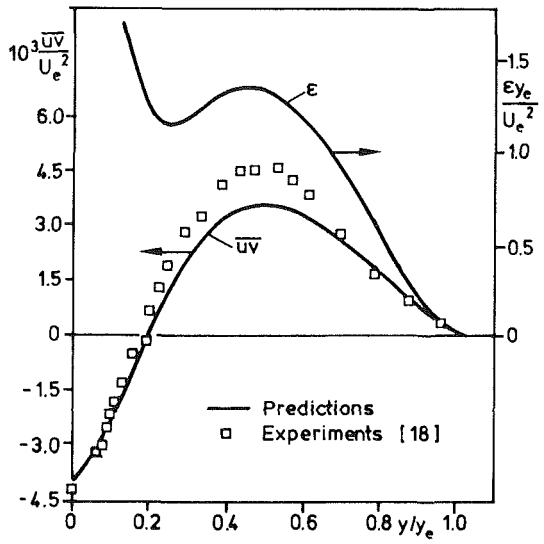

Fig.7 Wall jet in a moving stream (U_e/U_j = 0.43), lateral profiles of shear stress and dissipation rate at x/b = 150.

but there the turbulence measurements are also not very reliable.

Wall Jet in a Moving Stream (U_e/U_j = 0.43). The wall jet situation considered here was studied experimentally by Kacker and Whitelaw [18] (case with thin nozzle lip and U_e/U_j = 0.43). The calculation was started at x/b = 10 with the measured velocity and k- and uv-profiles as initial conditions (ϵ was obtained via equations (3) and (4)). The streamwise development of maximum velocity, dimensionless wall shear stress and wall-layer width δ is shown in Fig. 5. The agreement with the experimental data is satisfactory for all these quantities. It should be mentioned further that, in this case, the prediction for δ/b agrees well with the experimental correlation of Kruka and Eskinazi [21]. It therefore seems that the region where shear stress and velocity gradient have opposite signs is even less important in situations with a significant free stream velocity.

Figure 6 presents the lateral profiles of U and k at x/b = 150. The agreement between predictions and experiments is very good. The shape of the k-profile is now very much different from that in the case of stagnant surroundings. Because of the relatively weak shear in the free-layer region, less turbulence is produced there so that less turbulence energy can be transported towards the wall by diffusion. Therefore in the near-wall region the turbulence energy falls with distance from the wall as in a boundary layer; in contrast the turbulence energy rises in the wall jet in stagnant surroundings because of the high turbulence production in the free shear

Downloaded 02 Jun 2010 to 171.66.16.103. Redistribution subject to ASME license or copyright; see http://www.asme.org/terms/Terms_Use.cfm

layer. The lateral distribution of $\overline{uv}$ and ϵ at $x/b = 150$ is shown in Fig. 7. The shear stress distribution is again predicted fairly well, and the dissipation ϵ (for which no measurements are available) can be seen to vary in a similar way as the turbulence energy.

Conclusions

A modified version of the k- ϵ -turbulence model was derived which accounts for the wall damping of lateral fluctuations and the resulting reduction of shear stress experienced in wall jets. The wall-damping modification was obtained by simplifying Reynolds stress equations involving a wall correction in the modelled form of their pressure-strain term. The new model was shown to predict wall jets with an accuracy sufficient for practical purposes, and the conclusion may therefore be reached that wall-damping effects can be simulated realistically not only with a Reynolds-stress-equation model but also with the simpler modified k- ϵ -model.

Acknowledgments

The first author acknowledges financial support from the Deutsche Akademische Austauschdienst. The calculations were carried out on the BORROUGHS B7700 Computer of the University of Karlsruhe.

References

1 Launder, B.E., and Spalding, D.B., "The Numerical Computation of Turbulent Flow," *Computer Methods in Applied Mechanics and Engineering*, Vol. 3, 1974, pp. 269–289.

2 Launder, B.E., Reece, G.J., and Rodi, W., "Progress in the Development of a Reynolds Stress Turbulence Closure," *Journal of Fluid Mechanics*, Vol. 68, 1975, pp. 537–566.

3 Reece, G.J., "A Generalized Reynolds-Stress Model of Turbulence," Ph.D. thesis, University of London, 1977.

4 Irwin, H.P.A.H., "Measurements in Blown Boundary Layers and Their Prediction by Reynolds Stress Modelling," Ph.D. thesis, McGill University, 1974.

5 Hanjalić, K., and Launder, B.E., "A Reynolds Stress Model of Turbulence and its Application to Thin Shear Flows," *Journal of Fluid Mechanics*, Vol. 52, 1972, pp. 609–638.

6 Gibson, M.M., and Launder, B.E., "Ground Effect on Pressure Fluctuations in the Atmospheric Boundary Layer," *Journal of Fluid Mechanics*, Vol. 86, 1978, pp. 491–511.

7 Launder, B.E. et al., "The Prediction of Free-Shear Flows - A Comparison of the Performance of Six Turbulence Models," Proceedings Langley Free Shear Flows Conference, Vol. 1, NASA SP 320, 1973.

8 Rodi, W., *Turbulence Models and Their Application in Hydraulics*, International Association for Hydraulic Research, Delft, The Netherlands, 1980.

9 Rotta, J.C., *Turbulente Strömungen*, B.G. Teubner, Stuttgart, 1972.

10 Daly, B.J., and Harlow, F.H., "Transport Equations in Turbulence," *Physics of Fluids*, Vol. 13, 1970, pp. 2634–2649.

11 Shir, C.C., "A Preliminary Numerical Study of Atmospheric Turbulent Flow in the Idealized Planetary Boundary Layer," *Journal of the Atmospheric Sciences*, Vol. 30, 1973, pp. 1327–1339.

12 Gibson, M.M., and Launder, B.E., "On the Calculation of Horizontal Turbulent Free Shear Flow under Gravitational Influence," ASME *Journal of Heat Transfer*, Vol. 98, 1976, pp. 81–87.

13 Launder, B.E., "On the Effect of a Gravitational Field on the Turbulent Transport of Heat and Momentum," *Journal of Fluid Mechanics*, Vol. 67, 1975, pp. 569–581.

14 Rodi, W., "A New Algebraic Relation for Calculating the Reynolds Stresses," *Zeitschrift für Angewandte Mathematik and Mechanik*, Vol. 56, 1976, pp. 219–221.

15 Jones, W.P., and Lander, B.B., "The Prediction of Laminarization with a Two-Equation Model of Turbulence," *International Journal of Heat and Mass Transfer*, Vol. 15, 1972, pp. 301–314.

16 Patankar, S.V., and Spalding, D.B., *Heat and Mass Transfer in Boundary Layers*, 2nd ed., Intertext, London, 1970.

17 Tailland, A., "Contribution à l étude d ún jet plan dirigé tangentiellement a une paroi plane," Doctoral thesis, Univesite de Lyon, No. 618, 1970.

18 Kacker, S.C., and Whitelaw, J.H., "The Turbulence Characteristics of Two-Dimensional Wall-jet and Wall-Wake Flows," ASME *Journal of Applied Mechanics*, Vol. 38, 1971, pp. 239–252.

19 Rodi, W., "A Review of Experimental Data of Uniform Density Free Turbulent Boundary Layers," *Studies in Convection*, Vol. 1, ed. B.E. Launder, Academic Press, London, New York, San Francisco, 1975, pp. 79–165.

20 Guitton, D.E., "Some Contributions to the Study of Equilibrium and Non-Equilibrium Wall Jets over Curved Surfaces," Ph.D. thesis, McGill University, 1970.

21 Kruka, V. and Eskinazi, S., "The Wall-Jet in a Moving Stream," *Journal of Fluid Mechanics*, Vol. 20, 1964, pp. 555–579.

Downloaded 02 Jun 2010 to 171.66.16.103. Redistribution subject to ASME license or copyright; see http://www.asme.org/terms/Terms_Use.cfm

The Influence of Inlet Conditions on the Performance of Annular Diffusers

S. J. Stevens
Reader in Fluid Mechanics,
Department of Transport Technology,
University of Technology,
Loughborough, Leicestershire, LE113TU
England

G. J. Williams
Principal Research Technologist,
The General Electric Company Ltd.,
Whetstone, Leicestershire,
England

Low speed tests have been carried out to investigate the performance and mechanism of flow in two annular diffusers having center bodies of uniform diameter and conically diverging outer walls. In the first part of the investigation the diffusers were tested over a range of naturally developed inlet velocity profiles ranging from near-uniform to fully developed flow. Information is presented concerning the pressure recovery, total pressure loss, and characteristics of the outlet flow. Measurements have also been made of the mean velocity profile and turbulence structure at a number of stations along the length of the diffusers. The second part of the test program was devoted to studying the effects of increased inlet turbulence. The results show a marked improvement in the stability of the outlet flow and gains in pressure recovery, up to a maximum of 20 percent, with only small increases in total pressure loss.

Introduction

Although annular diffusers are used in gas turbines and turbomachinery installations it is only in the last decade that there have been any systematic investigations of their performance characteristics. The most notable contribution is that due to Sovran and Klomp [1] who tested over one hundred different geometries, nearly all of which had conically diverging center bodies with an inlet radius ratio $(R_i/R_o)_1$ of 0.55 or 0.70. The tests were carried out with a thin inlet boundary layer ($B_1 \simeq 0.02$) and the diffusers had a free discharge. The results are presented as contours of pressure recovery plotted against area ratio and nondimensional length $(\bar{L}/\Delta R_1)$. Although the influence of variations in the inlet velocity profile is discussed in terms of an area blockage concept, the outlet velocity profiles were not measured and therefore only approximate values of total pressures loss can be obtained. Howard, et al. [2] tested symmetrical annular diffusers and diffusers with center bodies of uniform diameter, using fully developed flow at inlet. The limits of the various flow regimes and the optimum performance lines were established. Thus, for naturally developed inlet conditions, there is a considerable amount of data which enables the prediction of pressure recovery to be made with confidence. However, information on the total pressure loss and the growth of the boundary layers along the walls of the diffuser is only available for a few geometries.

To date, most of the data have been derived from tests in which the inlet conditions were obtained by a carefully controlled growth of the boundary layers down an annular entry length and, under these conditions, the blockage concept successfully predicts the influence of inlet conditions. However, Livesey and Turner [3] showed that the inlet turbulence structure must also accompany the specification of the inlet blockage fraction and, in their review, Renau, Johnston and Kline [4] report that large-scale mixing at entry to a two-dimensional diffuser produced a significant increase in pressure recovery. Thus, where a high degree of turbulent mixing is present, as it is in many industrial flows, diffuser designs based on data from tests carried out with naturally developed inlet flows could be unduly conservative. This is particularly true of a diffuser situated downstream of an axial flow compressor where the flow at compressor outlet is that of a shear layer dominated by blade wakes and their interaction with the annulus wall boundary layers. It is important to note that in these circumstances Lockhart and Walker [5] observed a high level of turbulent mixing in both the radial and circumferential planes.

The present paper is a summary of a detailed study of the influence of inlet conditions on the overall and internal performance of two annular diffusers having center bodies of uniform diameter (Stevens [6] and Williams [7]). The first part of the paper considers naturally developed inlet conditions and the second part examines the influence of increased turbulent mixing.

Experimental Apparatus

The test facility is shown in Fig. 1. The entry length, diffuser, and settling length were mounted vertically, the advantage of this arrangement was that as all the inner tubes were spigotted together they could be positioned simply by three struts in the entry flare. In this way the influence of entry length supports was reduced to a minimum. Air was drawn from the laboratory through an integral flare and nose bullet into an annular approach pipe, the length of which could be varied to change the conditions at diffuser inlet from

Contributed by the Fluids Engineering Division and presented at the Fluids Engineering Conference, Niagara Falls, N.Y., June 1978. Manuscript received by the Fluids Engineering Division, October 3, 1978.

Copyright © 1980 by ASME
Downloaded 02 Jun 2010 to 171.66.16.103. Redistribution subject to ASME license or copyright; see http://www.asme.org/terms/Terms_Use.cfm

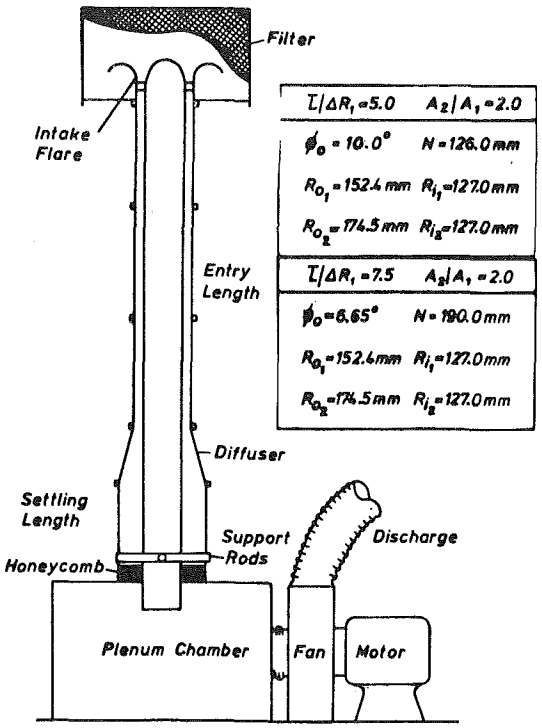

Fig. 1 Test facility

a uniform velocity profile ($L_e/D_{h_1} = 2$) to fully developed flow ($L_e/D_{h_1} = 50$). Stable transition to turbulent flow was ensured by mounting trip wires on the walls just downstream of the intake throat. The majority of the rig was constructed of plexiglass to a very high standard of accuracy (typically 0.254m ± 0.05mm diameter). The artificial methods used to generate increased levels of inlet turbulence, namely a wall mounted flow spoiler, and a coarse grid, are illustrated in Fig. 2.

In selecting the diffuser geometries to be investigated an inlet radius ratio $(R_i/R_o)_1$ of 0.83 was chosen as being typical of many turbomachinery applications. An area ratio of 2.0 was considered to be the limiting value for many designs and the non-dimensional lengths were based on the performance map of Sovran and Klomp, namely a Cp^* diffuser $\bar{L}/\Delta R_1 =$

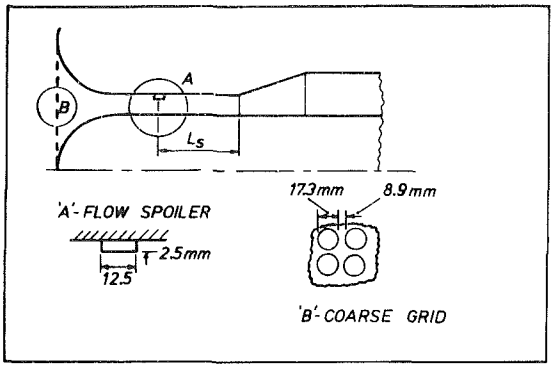

Fig. 2 Methods used to generate highly turbulent inlet profiles

5.0 and a Cp^{**} diffuser $\bar{L}/\Delta R_1 = 7.5$. The major geometric parameters are detailed in Fig. 1.

An almost constant dynamic pressure was maintained in the center of the annulus at a position 0.076m upstream of diffuser inlet. This corresponded to a velocity of 57m/s and a Reynolds number based on the inlet hydraulic diameter of 2×10^5.

Static pressure measurements were made at positions upstream of the diffuser inlet and along the diffuser and downstream settling length. At each position three tapings were made equally spaced around the surface of the inner and outer walls. Total pressure traverses were conducted along three equally spaced radii at each of twelve axial stations. The flattened total pressure tube had a wall thickness of 0.012mm, and an opening of 0.60mm by 1.2mm. The traverses were carried out normal to the walls of the tubes and all pressures were recorded on Betz projection manometers. The velocity profiles were calculated on the assumption that the static pressure along each radial traverse was the same as that measured at the wall.

Although an allowance was made for the displacement of the effective center of the pitot probe no correction was applied to take account of the effects of turbulence. Considerable uncertainty surrounds the estimation of errors in pitot tube measurements when the local turbulence level is high and the indicated velocities near the wall may be approximately 20 percent too high as the flow approaches near-separating conditions. In most cases velocity profiles taken along the three radial locations exhibited excellent symmetry of flow and the integrated mass flows at each station were within 2 percent of the inlet value.

Nomenclature

A = area of cross section
B = blocked area fraction
C_f = skin friction coefficient
C_p = pressure recovery coefficient
D = diameter of cross section
D_h = hydraulic diameter
H = boundary layer shape parameter δ^*/θ
l = mixing length $[-\overline{u'v'}/(du/dR)^2]^{1/2}$
$\bar{L}$ = mean wall length for annular diffusers
L_e = length of approach pipe upstream of diffuser
L_s = distance of spoiler from diffuser inlet
N = diffuser axial length
p = static pressure
P_t = total pressure
R = radius
Re = Reynolds number based on hydraulic diameter
ΔR = annulus height
u = local axial velocity
U = maximum velocity
v = local normal velocity
X = axial distance from diffuser inlet
y = distance normal to surface
α = velocity profile energy coefficient
δ = boundary layer thickness
δ^* = displacement thickness
θ = momentum thickness
λ = loss coefficient
$-\rho\overline{u'v'}$ = Reynolds shear stress
ρ = fluid density
τ = shear stress
ϕ = diffuser wall angle

Subscripts

1 = diffuser inlet
2 = diffuser outlet
i = inner wall
m = value at point of maximum velocity
o = outer wall

Superscripts

~ = mass-weighted mean value
− = mean value

Downloaded 02 Jun 2010 to 171.66.16.103. Redistribution subject to ASME license or copyright; see http://www.asme.org/terms/Terms_Use.cfm

Table 1 Inlet velocity profile parameters

Le/Dh_1	2.0	4.5	9.5	12.0	39.5	50.0
B_1	0.028	0.053	0.090	0.109	0.101	0.105
α_1	1.019	1.033	1.051	1.059	1.042	1.045

(Relative Uncertainty of $B_1 \pm 0.002$, $\alpha_1 \pm 0.02$)

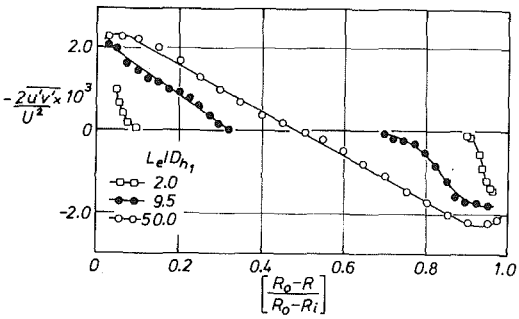

Fig. 3 Inlet turbulent shear stress distribution (Relative uncertainty of $2\overline{u'v'}/U^2 \pm 0.0002$)

Turbulence measurements were taken with a D.I.S.A. constant temperature hot wire anemometer. Measurements were made with straight and 45 deg slant probe elements using the same technique as that described by Goldberg [8]. The slant wire was presented at an angle of 45 deg to the direction of flow and rotated through 360 deg in 90 deg intervals. This facility, in combination with the straight wire readings, allowed the turbulence parameters u', v', w', $\overline{u'v'}$ and $\overline{u'w'}$ to be calculated.

Performance Evaluation

The definitions of total pressure loss and static pressure recovery coefficients are,

$$\tilde{\lambda}_{1-2} = (\tilde{P}_{t_1} - \tilde{P}_{t_2})/\alpha_1 \frac{1}{2} \rho \bar{u}_1^2 \text{ and}$$

$$\tilde{C}_{p_{1-2}} = (\tilde{P}_2 - \tilde{P}_1)/\alpha_1 \frac{1}{2} \rho \bar{u}_1^2$$

$$\bar{C}_{p1-2} = (\bar{p}_2 - \bar{p}_1/\alpha_1 \frac{1}{2} \bar{\rho} U_1^2$$

where $\tilde{P}_t = \tilde{P} + \alpha\rho/2\tilde{u}^2$. Writing the energy equation across the diffuser as

$$\tilde{P}_1 + \alpha_1 \frac{1}{2} \rho \bar{u}_1^2 = \tilde{P}_2 + \alpha_2 \frac{1}{2} \rho \bar{u}_2^2 + (\tilde{P}_{t_1} - \tilde{P}_{t_2}) \qquad (1)$$

and from continuity $A_1 \bar{u}_1 = A_2 \bar{u}_2$. Then equation (1) may be written as

$$\tilde{\lambda}_{1-2} = \left[1 - \frac{\alpha_2}{\alpha_1} \left(\frac{A_1}{A_2}\right)^2\right] - \tilde{C}_{p_{1-2}} \qquad (2)$$

Due to flow curvature there is a significant difference in static pressure across the annulus in the vicinity of diffuser inlet and, because of this, the inlet pressure was taken as the wall pressure measured $1.5D_{h_1}$ upstream of the inlet plane. Unfortunately, the calculation of $\tilde{\lambda}_{1-2}$ is very sensitive to change in the values of α_2 and $\tilde{C}_{p_{1-2}}$ and, because of this, the values of $\tilde{\lambda}_{1-2}$ may be in error by as much as ± 10 percent. However, no such uncertainty surrounds the value of $\tilde{C}_{p_{1-2}}$ which is considered to be within ± 3 percent.

Results and Discussion

Naturally Developed Inlet Conditions. The variation in velocity profile parameters with changes in the length of the approach pipe is summarized in Table 1. As noted by Lee [9], and many others, the parameters exhibit an oscillatory behaviour as fully developed flow is approached. Figure 3 illustrates the development of the inlet turbulent shear stress at selected entry lengths.

The state of the exit flow was observed using wool tufts. Adopting the definition of tuft behavior given by Carlson and Johnston [10] comments on the exit flow, together with the accompanying velocity profile integral parameters, are given in Table 2; where flow asymmetry was noted the worst case has been quoted. The transitory stall that occurred in the $\bar{L}/\Delta R_1 = 5$ diffuser was confined to patches on the outer wall over the region $X/N = 0.70$ to 1.0.

With the initial increase of inlet blockage fraction (B_1) there is a corresponding increase in B_2 and α_2, but as fully developed flow is approached the values decrease. This latter effect is attributed to the higher levels of inlet turbulent mixing in the near-wall regions for the flows with $Le/Dh_1 >$ 39.5 (see Fig. 3).

In addition, the overall performance measured in terms of pressure recovery and loss coefficient is presented in Table 2. Although the general levels of loss are quite low, the shorter length, Cp^*, diffuser does exhibit a slightly higher loss. The influence of inlet blockage predicted by Sovran and Klomp for the $\bar{L}/\Delta R_1 = 5$ diffuser, in which pressure forces are assumed to be dominant, is also included. Whereas the intitial decrease in pressure recovery is estimated correctly, the method fails to predict the subsequent rise in Cp as fully developed flow conditions are approached. This is because the method is essentially velocity profile based and makes no allowance for the effects of increased turbulent mixing. Nonetheless, the conclusion drawn by Sovran and Klomp that exit flow blockage and not energy loss is the major influence on pressure recovery is clearly illustrated.This is particularly true for the results achieved with fully-developed inflow where the reduction in presure recovery that occurs when the non-dimensional length is reduced from 7.5 to 5.0 is almost entirely attributable to increased exit blockage.

Because of the need to develop analytical techniques for the prediction of annular diffuser performance one of the aims of the investigation was the study of the internal performance in terms of the growth of the boundary layers. Their development along the walls of the diffusers, for fully developed flow ($B_1 = 0.105$) in terms of the shape parameter and momentum thickness is shown in Fig. 4. The most notable feature of these results is the difference in the growth of the shape parameters, dH/dx being much greater on the outer wall. In an adverse pressure gradient changes in profile shape (H) depend on the relative magnitude of the pressure gradient and Reynolds shear stress terms in the mean flow equations. An adverse pressure gradient causes H to increase, whereas the shear stress has the opposite effect. Since the static pressure is nearly constant across any section in the diffuser, the boundary layers on inner and outer walls must experience the same pressure gradient and therefore the asymmetric growth of the shape parameters must be due to: (i) initial distortion caused by the flow curvature at inlet and/or (ii) significantly different turbulence structures in the inner and outer wall layers. Although considerable care was taken to ensure a smooth change in outer wall angle, the measured pressure variation at the inlet [6 and 7] indicates that the initial pressure gradient on the outer wall is much higher. Furthermore, analysis of the turbulence structure [9] confirms that the influence of pressure forces predominate and therefore the asymmetric growth of the shape parameters is attributed to initial flow distortion near the outer wall caused by the curvature of flow at inlet which is then accentuated by the severe adverse pressure gradient. Similar conclusions have been drawn by Stevens and Fry [11] in work on an expanding center body diffuser.

A typical development of turbulent shear stress along the wall of a diffuser is presented in Fig. 5. The data, which is

Downloaded 02 Jun 2010 to 171.66.16.103. Redistribution subject to ASME license or copyright; see http://www.asme.org/terms/Terms_Use.cfm

Table 2 Overall performance and exit velocity profile parameters

$\bar{L}/\Delta R_1 = 7.5$ Diffuser

Le/Dh_1	$\bar{C}p_{1-2}$	$\bar{\lambda}_{1-2}$	B_2	α_2	Ho_2	Hi_2	Flow state outer wall	Flow state inner wall
2.0	0.595	0.080	0.261	1.381	2.45	1.92	U	S
4.5	0.557	0.090	0.323	1.494	2.65	1.91	TI	S
9.5	0.545	0.105	0.347	1.519	2.64	1.85	TI	S
12.0	0.545	0.085	0.364	1.543	2.71	1.81	TI	S
39.5	0.595	0.075	0.331	1.410	2.35	1.71	U	S
50.0	0.605	0.065	0.332	1.410	2.35	1.17	U	S

S - steady, U - unsteady, TI - incipient transitory stall, IT - intermittent transitory stall, T - transitory stall.

$\bar{L}/\Delta R_1 = 5.0$ Diffuser

Le/Dh_1	$\bar{C}p_{1-2}$	$\bar{C}p_{s-k}$	$\bar{\lambda}_{1-2}$	B_2	α_2	H_{o_2}	H_{i_2}	Flow state outer wall	Flow state inner wall
2.0	0.505	0.610	0.120	0.297	1.586	3.65	1.79	IT	U
4.5	0.440	0.530	0.125	0.378	1.808	3.89	1.73	IT	U
9.5	0.445	0.490	0.120	0.390	1.807	3.69	1.71	IT	U
12.0	0.445	0.495	0.120	0.406	1.833	3.71	1.72	IT	U
39.5	0.510	0.500	0.105	0.370	1.657	3.24	1.67	IT	U
50.0	0.520	0.500	0.075	0.380	1.740	3.52	1.69	IT	U

$\bar{C}p_{s-k}$ pressure recovery predicted by correlation due to Sovran and Klomp.

(Relative uncertainty of $\bar{C}p_{1-2} \pm 0.02$, $\bar{\lambda}_{1-2} \pm 0.03$, $B_2 \pm 0.02$, $\alpha_2 \pm 0.10$, $H_{o_2} \pm 0.25$, $H_{i_2} \pm 0.15$)

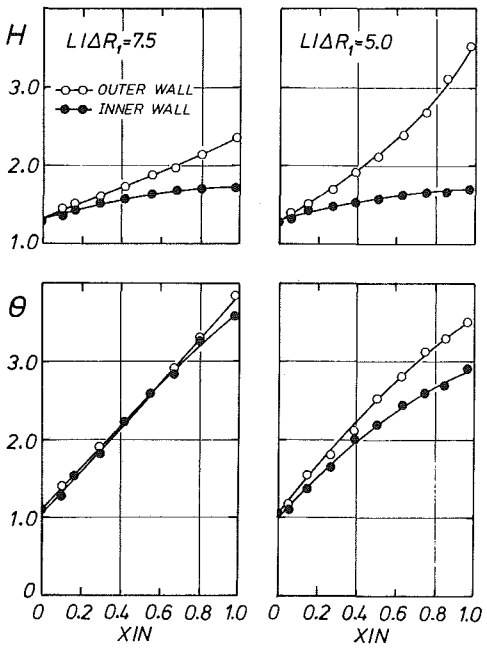

Fig. 4 Boundary layer development, $B_1 = 0.105$
(Relative uncertainties)

X/n	0 – 0.5	0.5 – 1.0
O	± 0.04	± 0.18
H	± 0.05	± 0.25

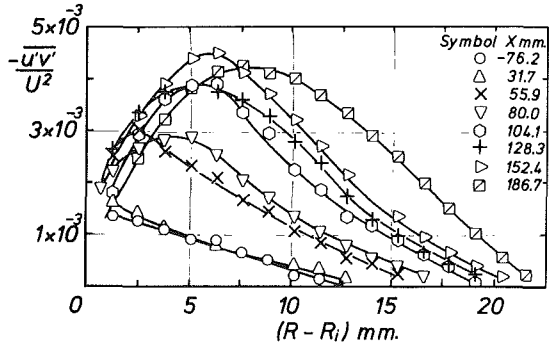

Fig. 5 Turbulent shear stress distribution along inner wall of $\bar{L}/\Delta R_1 = 7.5$ diffuser, $B_1 = 0.105$
(Relative uncertainties)

x	0 – 80mm	80 – 190mm
$-\overline{u'v'}/U^2$	± 0.0002	± 0.0012

similar to that due to Goldberg, show that in an adverse pressure gradient the value of $\overline{u'v'}/U^2$ near the wall rises rapidly to a maximum which increases and moves away from the wall as the flow proceeds downstream. The local skin friction coefficient was estimated from the measured velocity profiles using the Clauser method and a typical plot of the results is shown in Fig. 6. During the initial stages of diffusion there is an absence of any clear logarithmic portion in the profiles and therefore the values of C_f can only be considered as approximate. However, the logarithmic law of the wall is based on the assumption that the shear stress in the inner region of the layer remains constant at the wall value, and it has been shown that for some of the data this hypothesis is invalid. Thus, the failure of the velocity profiles to exhibit a logarithmic variation near the wall can be attributed to the severe adverse pressure gradient.

The axisymmetric form of the Momentum Integral Equation for the flow along the inner wall is:

$$\frac{d\theta i}{dx} = \frac{C_{fi}}{2} - (H_i + 2)\frac{\theta_i}{U}\frac{dU}{dx} + \frac{R_m^2 - R_i^2}{R_i}\frac{1}{2\rho U^2}\left(\frac{dP_t}{dx}\right)_m + \frac{1}{U^2}\int_{R_i}^{R_m}\frac{d}{dx}(\bar{u}'^2 + \bar{v}'^2_m - \bar{v}'^2)\frac{R}{R_i}\,dR \qquad (3)$$

At any station where a potential core is present $(dP_t/dx)_m$ and $d/dx(V'_m) = 0$.

A typical comparison of the measured value of $d\theta/dx$ with the experimentally determined right hand side of equation (3) is given in Fig. 7. Any marked divergence of the two sides of the equation is generally attributed to three-dimensional effects, and Coles [12] has found that a balance is rare for flows developing in a severe adverse pressure gradient. That the comparison for both diffusers is very good, together with the close agreement in integrated mass flow at all stations, is seen as sufficient evidence to confirm that the data is free from significant three-dimensional effects.

Tests With Increased Inlet Turbulence-Flow Spoiler. The object of these tests was to investigate the feasibility of

Downloaded 02 Jun 2010 to 171.66.16.103. Redistribution subject to ASME license or copyright; see http://www.asme.org/terms/Terms_Use.cfm

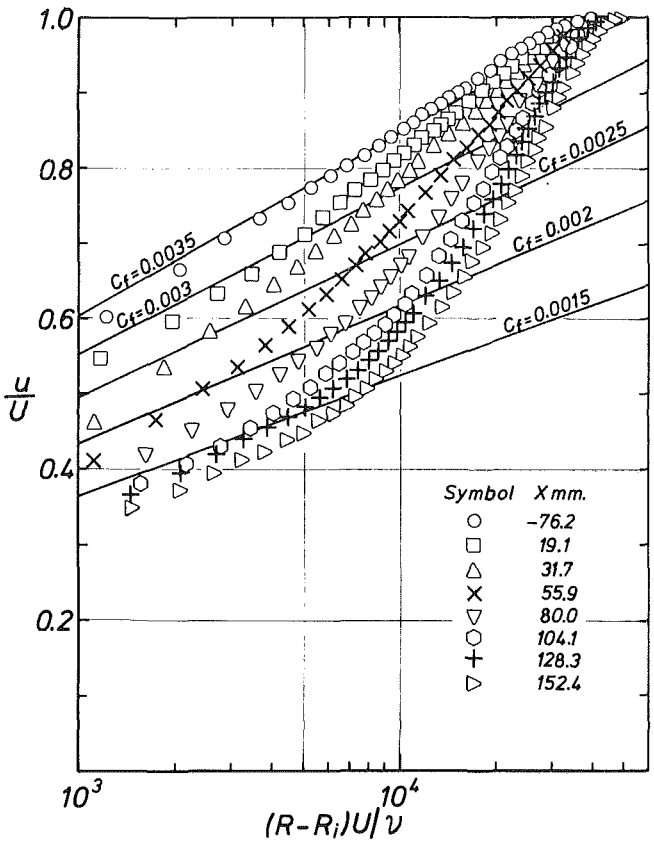

Fig. 6 Clauser plot of velocity profiles
$\bar{L}/\Delta R_1 = 7.5$, $B_1 = 0.105$
(Relative uncertainties)
x 0 – 80mm 80 – 190mm
u/U ± 0.01 ± 0.03

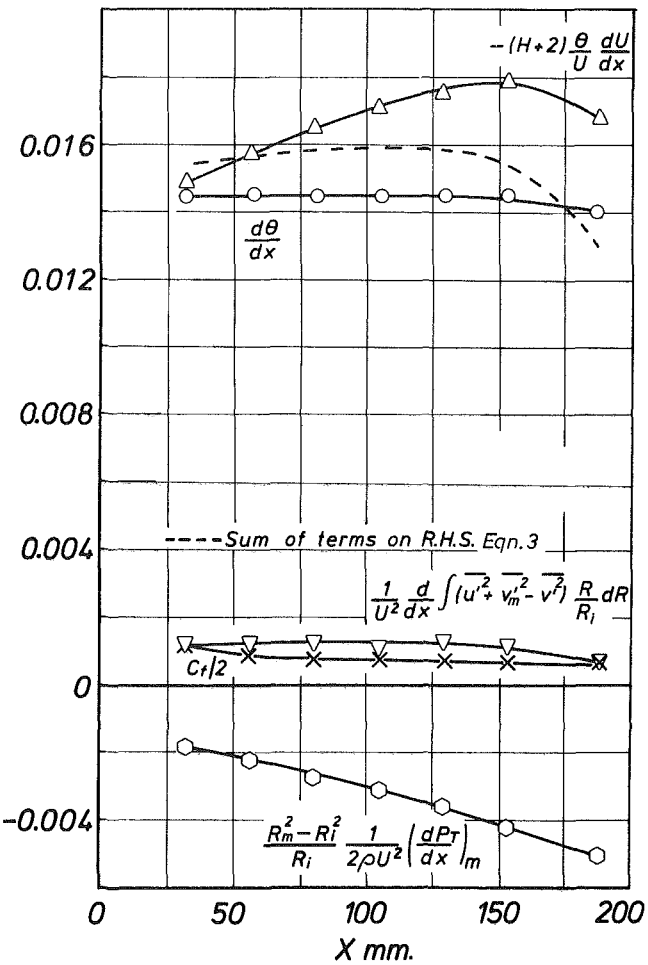

Fig. 7 Momentum balance along inner wall of $\bar{L}/\Delta R_1 = 7.5$ Diffuser, $B_1 = 0.105$

eliminating the stall in the $\bar{L}/\Delta R_1 = 5$ diffuser by increasing the level of turbulent mixing at inlet. Details of the spoiler used to generate the increased turbulence along the outer wall are given in Fig. 2. Prior to a detailed investigation of the internal flow mechanism, the position of the spoiler was optimized to give the maximum improvement in pressure recovery allied to stable exit flow conditions. Velocity and turbulent shear stress profiles, measured at a position 1.5 hydraulic diameters upstream of the diffuser entry plane, for various positions of the spoiler are presented in Fig. 8, the performance and outlet flow conditions are summarized in Table 3.

The variation of the integral parameters, B_1 and α_1, indicate that for $L_s/D_{h_1} > 4.0$ the "adjustment" of the inlet velocity profile is very slow, whereas the distribution of turbulent shear stress is still changing significantly. Comparing the integral parameters at the diffuser outlet with those achieved with naturally developed inlet conditions, it can be seen that increased turbulent mixing reduces the value of outer wall shape parameter H_{o_2}. This in turn lowers the outlet blockage, B_2, and energy coefficient α_2 and, since the losses are very similar, there is a consequent increase in pressure recovery. Maximum pressure recovery combined with stable outlet flow was achieved at $L_s/D_{h_1} = 7$ and therefore this configuration was chosen for further investigation.

Velocity profiles measured along the length of the diffuser exhibited excellent circumferential symmetry and the integrated mass flow at the various stations was in good agreement. The variation of the boundary layer parameters is presented in Fig. 9 also shown are the values measured with fully developed inflow for which the blockage fraction is similar. Whereas the development of flow along the inner wall is almost the same, with the spoiler fitted, the growth of the shape parameter on the outer wall is reduced substantially.

Although the maximum levels were about 30 percent higher, the development of the turbulent shear stress was found to be very similar to that observed with fully developed inflow. Analysis of the data very close to the wall revealed that $d\tau/dy \neq dp/dx$ and furthermore the difference could not be attributed to the influence of Reynolds normal stresses, implying that in this region advection terms are significant. Moreover, the values of mixing length l were, on average, 50 percent larger than those calculated for fully developed inflow. Figure 10 compares the experimental values of $d\theta/dx$ with the values calculated from the right-hand side of the momentum integral equation, equation (3). The level of agreement is again very good and, as with naturally developed inlet conditions, the pressure gradient term dominates the equation.

Test With Increased Inlet Turbulence — Coarse Grid. Whereas the preceding tests describe the influence of increased turbulent mixing superimposed on a thick inlet boundary layer, the tests with a coarse grid were intended to provide data on the effect of increased mixing applied to a thin inlet boundary layer. The inlet velocity profile and turbulent shear stress distribution are compared in Fig. 11 with the values for naturally developed flow $Le/D_{h_1} = 2$. Although there is a slight difference in the inlet velocity profiles, it is insufficient in itself to cause any significant variation in diffuser performance. However, the level of turbulent shear stress in the nearwall region is markedly greater than that associated with naturally developed flow. Hence the inlet conditions may be described as near uniform

Downloaded 02 Jun 2010 to 171.66.16.103. Redistribution subject to ASME license or copyright; see http://www.asme.org/terms/Terms_Use.cfm

Table 3 Overall Performance with flow spoiler at inlet

$\bar{L}/\Delta R_1 = 5.0$ Diffuser

Le/Dh_1	Ls/Dh_1	B_1	α_1	$\bar{C}p_{1-2}$	$\bar{\lambda}_{1-2}$	B_2	α_2	H_{o_2}	H_{i_2}	Flow state outer wall
9.5	3.0	0.134	1.085	0.535	0.106	0.380	1.564	2.64	1.72	T*
9.5	4.0	0.129	1.064	0.545	0.108	0.350	1.482	2.46	1.76	T*
9.5	5.0	0.123	1.051	0.560	0.075	0.370	1.551	2.63	1.84	IT
9.5	6.0	0.119	1.045	0.555	0.080	0.358	1.515	2.55	1.81	U
9.5	7.0	0.117	1.049	0.580	0.060	0.356	1.530	2.63	1.80	U
9.5	8.0	0.115	1.052	0.535	–	–	–	–	–	TI
9.5+	–	0.090	1.051	0.445	0.120	0.390	1.807	3.69	1.71	IT
50.0+	–	0.105	1.045	0.520	0.075	0.380	1.740	3.52	1.69	IT

+ naturally-developed inlet conditions * patches

(Relative uncertainty of $B_1 \pm 0.004$, $\alpha_1 \pm 0.04$, $\bar{C}p_{1-2} \pm 0.02$, $\bar{\lambda}_{1-2} \pm 0.03$, $B_2 \pm 0.02$, $\alpha_2 \pm 0.10$, $H_{o_2} \pm 0.25$, $H_{i_2} \pm 0.15$)

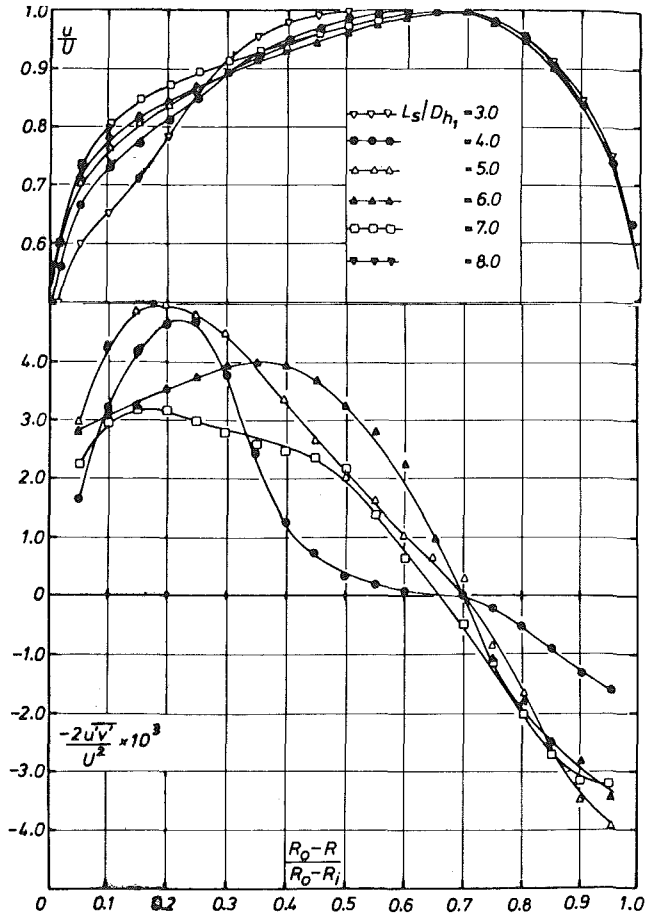

Fig. 8 Inlet conditions produced by flow spoiler
(Relative uncertainty of $u/U \pm 0.02$, $-2\overline{u'v'}/U^2 \pm 0.0004$)

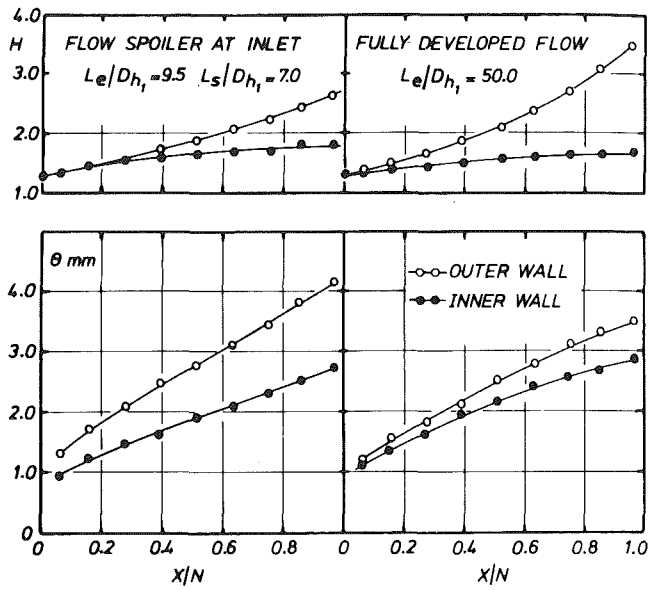

Fig. 9 Boundary layer development optimum spoiler position
(Relative uncertainties)

X/N	0 – 0.5	0.5 – 1.0
O	± 0.04	± 0.18
H	± 0.05	± 0.25

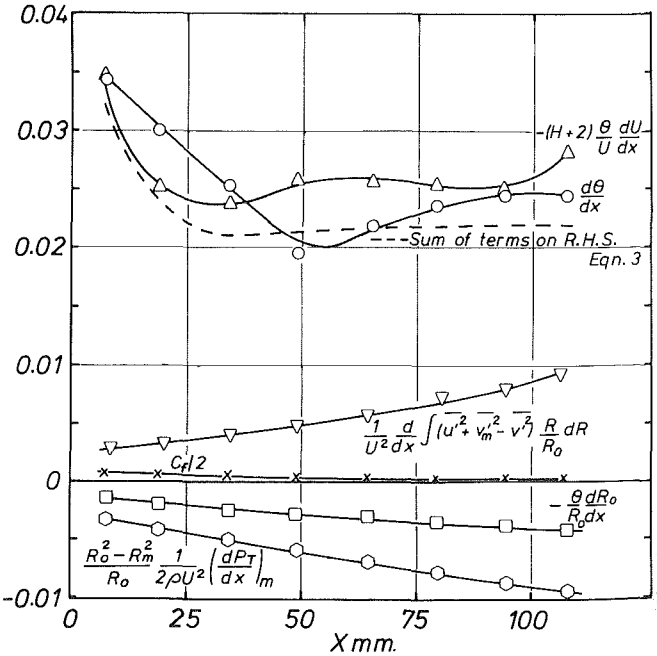

Fig. 10 Momentum balance along outer wall of $\bar{L}/\Delta R_1 = 5.0$ diffuser, optimum spoiler position

flow coupled with a high rate of mixing in the near wall regions.

The exit velocity profiles for both diffusers are compared in Fig. 12, and the values of profile shape parameter and energy coefficient, together with comments on the state of the flow, are listed in Table 4.

As a consequence of the increased mixing the shape parameter at exit on both inner and outer walls is reduced considerably, resulting in improved flow stability and a lower energy flux coefficient α_2. Comparison of the results for the $\bar{L}/\Delta R_1 = 5$ diffuser indicates that the influence of increased mixing is confined to the relevant wall boundary layer since, in the tests with a spoiler, only the outer wall shape parameter was affected. The overall performance is also summarized in Table 4. As in the tests with a spoiler, the total pressure loss is not affected significantly, and the lowering of the exit blockage is responsible for an appreciable increase in pressure recovery.

Downloaded 02 Jun 2010 to 171.66.16.103. Redistribution subject to ASME license or copyright; see http://www.asme.org/terms/Terms_Use.cfm

Table 4 Overall performance and exit velocity profile parameters

Grid-generated Inlet Conditions

$\bar{L}/\Delta R_1$	Le/Dh_1	B_1	$\bar{C}p_{1-2}$	$\bar{\lambda}_{1-2}$	α_2	H_{o_2}	H_{i_2}	Flow State outer wall
7.5	2.0+	0.028	0.595	0.080	1.381	2.45	1.92	U
7.5	2.0	0.044	0.635	0.090	1.160	1.72	1.47	S
5.0	2.0+	0.028	0.505	0.120	1.586	3.65	1.79	IT
5.0	2.0	0.044	0.595	0.125	1.170	1.90	1.50	U

+ naturally-developed inlet conditions

(Relative uncertainty of $B_1 = 0.004$, $\bar{C}p_{1-2} \pm 0.02$, $\bar{\lambda}_{1-2} \pm 0.03$, $\alpha_2 \pm 0.10$, $H_{o_2} \pm 0.25$, $H_{i_2} = \pm 0.15$)

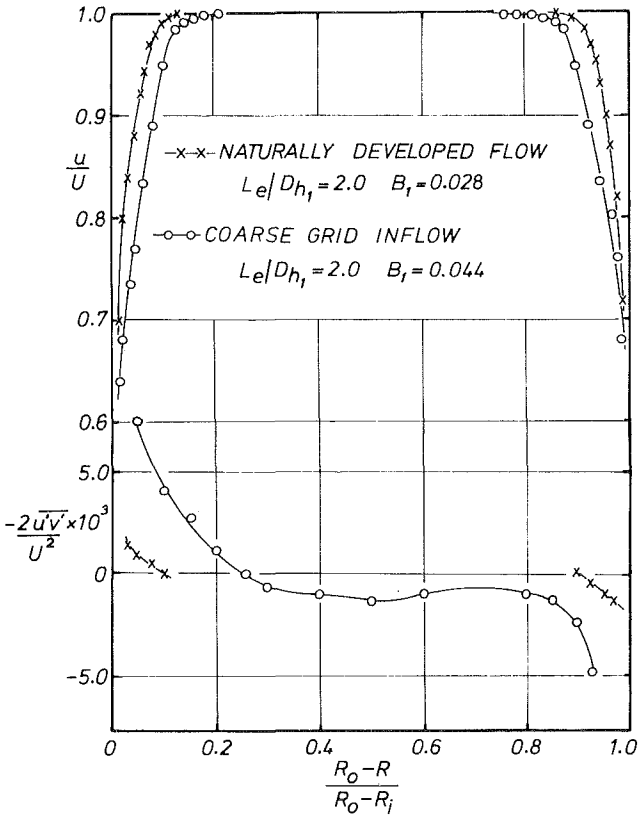

Fig. 11 Inlet conditions produced by Coarse Grid (Relative uncertainty of $u/U \pm 0.02$, $-2\overline{u'v'}/U^2 \pm 0.0004$)

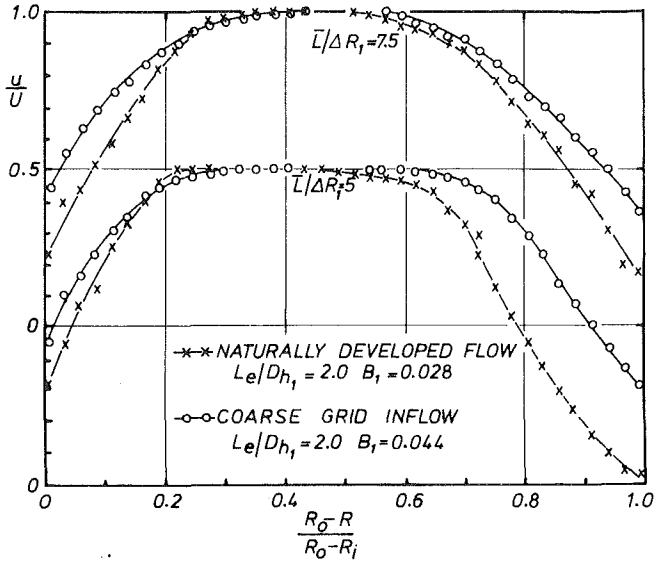

Fig. 12 Diffuser exit velocity profiles (Relative uncertainty of $u/U \pm 0.04$)

Conclusions

The influence of naturally developed inlet conditions on the performance of optimum annular diffusers has been investigated. Information on the pressure recovery, total pressure loss, and characteristics of the outlet flow, is presented. Measurements have been made of the mean velocity profile and turbulence structure at a number of stations along the length of the diffusers. The data which exhibits excellent symmetry of flow has been shown to be free from significant three-dimensional effects and may therefore be used as test cases for prediction methods.

An assessment of the effect of inlet turbulence has also been made. The results show a marked improvement in the stability of the outlet flow and gains in pressure recovery, up to a maximum of 20 percent, with only small increases in total pressure loss. For the optimum configuration, information is also presented on the growth of the boundary layers along the walls of the diffuser.

Acknowledgments

The authors are grateful to the Science Research Council and the Ministry of Defense (National Gas Turbine Establishment) for sponsoring the research program on which this paper is based.

References

1 Sovran, G., and Klomp, E.D., "Experimentally Determined Optimum Geometries for Rectilinear Diffussers with Rectangular, Conical or Annular Cross-section," *Fluid Mechanics of Internal Flow*, Elsevier, New York, 1967, p. 270-319.

2 Howard, J.H.G., Henseler, H.J., and Thronton-Trump, A.B., "Performance and Flow Regimes for Annular Diffusers," Paper 67-WA/FE-21, ASME, 1967.

3 Livesey, J.L., and Turner, J.T., "The Dependence of Diffuser Performance upon Inlet Flow Conditions," *Journal of Royal Aero. Soc.*, Vol. 69, 1965.

4 Renau, L.R., Johnston, J.P. and Kline, S.J., "Performance and Design of Straight, Two-dimensional Diffusers," Report PD-8, Mech.Eng.Dept., Stanford University, 1964.

5 Lockhart, R.C., and Walker, G.J., "The Influence of Viscous Interactions on the Flow Downstream of an Axial Compressor Stage," Presented at the 2nd International Symposium on Air Breathing Engines, University of Sheffield, March 1974.

6 Stevens, S.J., "Turbulent Incompressible Flow in Annular Diffusers," Ph.D. thesis, University of Loughborough, 1970.

7 Williams, G.J., "The Influence of Inlet Conditions on the Boundary Layer Growth and Overall Performance of Annular Diffusers," Ph.D. thesis, University of Loughborough, 1972.

8 Goldberg, P., "Upstream History and Apparent Stress in Turbulent Boundary Layers, "M.I.T. Gas Turbine Lab. Report No. 85, 1966.

9 Lee, B.E., "Some Effects of History on Turbulent Fluid Flow," Ph.D. thesis, University of Leicester, 1969.

10 Carlson, J., and Johnston, J.P., "Effects of Wall Shape on Flow Regimes and Performance in Straight, Two-Dimensional Diffusers," Report PD-11, Mech.Eng.Dept., Stanford University, 1965.

11 Stevens, S.J., and Fry, P., "Measurements of the Boundary Layer Growth in Annular Diffusers," *Journal of Aircraft*, Vol. 10, 1973.

12 Coles, D.E., "Proceedings Computation of Turbulent Boundary Layers - 1968 AFOSR-IFP-Stanford Conference," Vol. II, Stanford University, 1969.

Downloaded 02 Jun 2010 to 171.66.16.103. Redistribution subject to ASME license or copyright; see http://www.asme.org/terms/Terms_Use.cfm

Turbulent Boundary Layers With Unsteady Injection-Suction

D. T. Tsahalis

Westhollow Research Center,
Shell Development Company,
Houston, Texas 77001

The time dependent turbulent boundary-layer equations with a two-layer eddy viscosity model are integrated numerically over a porous flat plate for a steady outer flow and a sinusoidally distributed injection-suction that varies harmonically with time. The dependence of the unsteady wall shear on the frequency and strength of injection-suction is investigated. The present results indicate that the time-averaged skin friction is always larger than the skin friction observed over a non-porous flat plate. Comparison with previous theoretical results indicates that the time-averaged skin friction is always smaller than the skin friction observed over a porous flat plate with steady, simultaneous injection-suction of the same strength. The extension of eddy viscosity models, developed for steady flows, to unsteady flows is discussed.

Introduction

The problem of calculating the laminar/turbulent boundary layer over a porous surface with steady or unsteady injection and/or suction is of the greatest practical importance. Steady injection (blowing) and suction have been proved to be very effective in controlling the boundary layer for the purpose of increasing the lift and reducing the drag of aerodynamic surfaces. Specifically, higher lift is achieved by preventing the onset of separation by supplying additional energy to the separation-prone retarded fluid particles next to the wall (injection) or removing them before they separate (suction). The drag reduction is achieved with suction which shifts the point of transition of the boundary layer from laminar (lower drag) to turbulent (higher drag) by reducing the thickness of the laminar boundary layer which then becomes less prone to turning turbulent. Futhermore, steady injection of gas, which is the same as or different from that in the free stream, is employed in the thermal protection (transpiration cooling) of the blades of gas turbines and the inner walls of combustion chambers from high temperature gases, aerodynamic surfaces at high supersonic speeds, etc.

In the present paper the isothermal turbulent boundary layer for a steady outer flow over a flat plate with a sinusoidally distributed injection-suction that varies harmonically with time is studied numerically. The turbulent boundary layer is treated as a composite layer consisting of an inner and outer layer and the injection-suction fluid is the same as the free-stream fluid (uniform composition boundary layer). An upwind difference scheme is employed to integrate through regions of reversed flow (negative wall shear) if necessary.

Governing Equations and Method of Solution

Let u, v be the velocity components and x, y be the coordinates along and perpendicular to the wall, respectively. Let u', v' be the fluctuating velocity components, U_e the outer flow velocity, t the time, ρ the density, and μ the viscosity coefficient. Assuming steady outer flow, the unsteady boundary-layer equations for two-dimensional, incompressible, turbulent flow then read

$$\frac{\partial u^*}{\partial x^*} + \frac{\partial v^*}{\partial y^*} = 0 \tag{1}$$

$$\frac{\partial u^*}{\partial t^*} + u^* \frac{\partial u^*}{\partial x^*} + v^* \frac{\partial u^*}{\partial y^*} - U_e^* \frac{\partial U_e^*}{\partial x^*} = \frac{1}{\rho^*} \frac{\partial}{\partial y^*} \left(\mu^* \frac{\partial u^*}{\partial y^*} - \rho^* \overline{u^{*\prime} v^{*\prime}} \right) \tag{2}$$

where the overbar denotes time averaging and the stars represent dimensional quantities. The term $-\rho^* \overline{u^{*\prime} v^{*\prime}}$ is well known in the literature as the Reynolds stress. It is assumed here, i.e., unsteady flow, that the Reynolds stress can be modeled as in steady flow via an eddy viscosity model

$$\epsilon^* = -\rho^* \frac{\overline{u^{*\prime} v^{*\prime}}}{\dfrac{\partial u^*}{\partial y^*}} \tag{3}$$

where ϵ^* is the eddy or apparent turbulent viscosity.

Let U_∞^* be the free stream velocity, L^* a representative length of the problem, and $\mathrm{Re} = U_\infty^* L^* / \nu^*$ the Reynolds number. U_∞^* and L^* are used to nondimensionalize distances, time and velocities, and the system of equations (1) and (2), taking into account equation (3), is replaced by the system:

$$\frac{\partial u}{\partial x} + \frac{\partial v}{\partial y} = 0 \tag{4}$$

$$\frac{\partial u}{\partial t} + u \frac{\partial u}{\partial x} + v \frac{\partial u}{\partial y} - U_e \frac{\partial U_e}{\partial x} = \frac{\partial}{\partial y} \left(\bar{\epsilon} \frac{\partial u}{\partial y} \right) \tag{5}$$

where the coordinate y and the velocity component v have been stretched with the factor $\sqrt{\mathrm{Re}}$ and $\bar{\epsilon}$ is a nondimensional

Contributed by the Fluids Engineering Division for publication in the JOURNAL OF FLUIDS ENGINEERING. Manuscript received by the Fluids Engineering Division, June 19, 1978.

Copyright © 1980 by ASME

Downloaded 02 Jun 2010 to 171.66.16.103. Redistribution subject to ASME license or copyright; see http://www.asme.org/terms/Terms_Use.cfm

"total viscosity," incorporating both the molecular and apparent turbulent viscosities, that is,

$$\bar{\epsilon} = 1 + \frac{\epsilon^*}{\mu^*} \tag{6}$$

Experience from numerical analysis of laminar flows has indicated that integration is more convenient in terms of Görtler coordinates since the thickness of the boundary layer increases very mildly in the Görtler plane. Therefore, a modification of Görtler's transformation is introduced with new independent variables

$$\xi = \int_0^x U_e(x)\,dx, \quad \eta = \frac{U_e(x)}{\sqrt{2\xi}}y, \quad \tau = t \tag{7}$$

and new dependent variables

$$F = \frac{u}{U_e}, \quad V = \frac{\sqrt{2\xi}}{U_e}v + \frac{2\xi}{U_e}\frac{\partial \eta}{\partial x}F \tag{8}$$

for the velocity components in the ξ and η directions, respectively.

In terms of the new dependent and independent variables, equations (4) and (5) become

$$2\xi\frac{\partial F}{\partial \xi} + F + \frac{\partial V}{\partial \eta} = 0 \tag{9}$$

$$\frac{\partial^2 F}{\partial \eta^2} + A_1'\frac{\partial F}{\partial \eta} + A_2'F + A_3'\frac{\partial F}{\partial \xi} + A_4'\frac{\partial F}{\partial \tau} = 0 \tag{10}$$

where

$$A_1' = \frac{1}{\bar{\epsilon}}\left(-V + \frac{\partial \bar{\epsilon}}{\partial \eta}\right), \quad A_2' = -\frac{\beta}{\bar{\epsilon}}F, \quad A_3' = \frac{\beta}{\bar{\epsilon}},$$

$$A_4' = -\frac{2\xi}{\bar{\epsilon}}F, \quad A_5' = -\frac{2\xi}{\bar{\epsilon}U_e^2} \tag{11}$$

and β is the pressure gradient function given by

$$\beta = \frac{2\xi}{U_e}\frac{\partial U_e}{\partial \xi} \tag{12}$$

Equation (10) is brought [1, 2] in the form of a steady-state equation by introducing a difference form of the time derivative $\partial F/\partial \tau = (F - F^\circ)/\Delta\tau$ where $F^\circ = F(\tau - \Delta\tau)$. Equation (10) then takes the form

$$\frac{\partial^2 F}{\partial \eta^2} + A_1\frac{\partial F}{\partial \eta} + A_2F + A_3 + A_4\frac{\partial F}{\partial \xi} = 0 \tag{13}$$

where

$$A_1 = A_1', \; A_2 = A_2' + \frac{A_5'}{\Delta\tau}, \quad A_3 = A_3' - \frac{A_5'}{\Delta\tau}F^\circ, \quad A_4 = A_4' \tag{14}$$

The system of the differential equations (9) and (13) is solved numerically using a subroutine for steady flow developed by Werle and Davis [3]. An upwind differencing scheme is employed for integration through regions of reverse flow (negative wall shear) if necessary [1, 2]. More details about the numerical integration of time dependent laminar and turbulent flows can be found in [1, 2] and [4–8].

Eddy Viscosity Models

The turbulent boundary layer is treated as a composite layer consisting of an inner and an outer layer. In the inner layer the well known mixing length closure, originally introduced by Prandtl [9], is adopted. That is

$$\epsilon_i^* = \rho^* l^{*2}\left|\frac{\partial u^*}{\partial y^*}\right| \tag{15}$$

where the mixing length is assumed to have the form

$$l^* = K_l y^*\left[1 - \exp\left(-\frac{y^+}{A^+}\right)\right] \tag{16}$$

In the above equation, K_l is a constant empirically calculated and traditionally given the value 0.41,

$$y^+ = \frac{y^*}{\nu^*}\left(\frac{|\tau_w^*|}{\rho^*}\right)^{1/2} \tag{17}$$

τ^*_w being the wall shear stress, and A^+ is the Van Driest [10] damping factor. This factor was later generalized by Cebeci [11] to include the effects of pressure gradient and injection-suction. Various authors [12–14] have questioned the effectiveness of Cebeci's generalization for the case of a non-porous wall with pressure gradient. Considering, however, that in the present problem the wall is porous, i.e., nonzero injection-suction, Cebeci's generalization is adopted which reads

$$A^+ = 26\left\{-\frac{p^+}{v_w^+}\left[\exp\left(11.8v_w^+\right) - 1\right] + \exp\left(11.8v_w^+\right)\right\}^{-1/2} \tag{18}$$

Nomenclature

A_w = strength of injection-suction
b = permeability parameter (equation (37))
C_f = averaged skin friction coefficient
C_f' = local skin friction coefficient
F = normalized velocity component in the ξ-direction
f = frequency
j = intensity of injection and/or suction (equation (34))
L = representative length
l = wave length
Re = Reynolds number ($U^*_\infty L^*/\nu^*$)
T = absolute temperature
U_e = outer flow velocity
u = mean velocity component in x-direction
u' = fluctuating velocity component in x-direction
V = normalized velocity component in η-direction
v = mean velocity component in y-direction
v' = fluctuating velocity component in y-direction
x,y = Cartesian coordinates along and perpendicular to the wall, respectively
β = pressure gradient function (equation (12))
δ = boundary-layer thickness
δ_d = displacement thickness
δ_m = momentum thickness
ϵ = eddy viscosity
$\bar{\epsilon}$ = total viscosity (equation (6))
η = transformed stretched normal coordinate (equation (7))
μ = viscosity coefficient
ν = kinematic viscosity
ξ = transformed surface coordinate (equation (7))
ρ = fluid density
τ = transformed time (equation (7))
τ_w = wall shear stress

Subscripts

cr = critical value
$i\text{-}s$ = simultaneous injection and suction
max = maximum
0 = zero injection-suction
s = steady
t = unsteady
w = evaluation on the wall
∞ = free-stream condition

Superscripts

$-$ = time averaging
$*$ = dimensional quantity

Downloaded 02 Jun 2010 to 171.66.16.103. Redistribution subject to ASME license or copyright; see http://www.asme.org/terms/Terms_Use.cfm

where

$$v_w^+ = v_w^* \Big/ \left(\frac{|\tau_w^*|}{\rho^*} \right)^{1/2} \tag{19}$$

$$p^+ = -U_e^* \frac{dU_e^*}{dx^*} \nu^* \Big/ \left(\frac{|\tau_w^*|}{\rho^*} \right)^{3/2} \tag{20}$$

In equation (19) v_w^* is the wall injection-suction velocity.

In the outer layer Clauser's velocity defect law [15] is assumed and the eddy viscosity reads

$$\epsilon_0^* = \rho^* K_2 U_e^* \delta_d^* \bar{\gamma} \tag{21}$$

where K_2 is another empirical constant equal to 0.0168, δ_d^* is the displacement thickness given by

$$\delta_d^*(x^*,t^*) = \int_0^{\delta^*} \left[1 - \frac{u^*(x^*,y^*,t^*)}{U_e^*(x^*,t^*)} \right] dy^* \tag{22}$$

and $\bar{\gamma}$ is an intermittency factor [16] given by

$$2\bar{\gamma} = 1 - \text{erf}\left[5\left(\frac{y^*}{\delta^*} - 0.78 \right) \right] \tag{23}$$

In equations (22) and (23) δ^* is the boundary-layer thickness.

Moore and Ostrach [17] have shown that the common definition of the displacement thickness, given by equation (22), cannot be carried over to unsteady flow. According to Moore and Ostrach the displacement thickness for two-dimensional, incompressible, unsteady flow satisfies the following equation:

$$\frac{\partial}{\partial x^*} [\delta_d^*(x^*,t^*)\, U_e^*(x^*,t^*)] - \frac{\partial}{\partial x^*} \int_0^{\delta^*} [U_e^*(x^*,t^*) - u^*(x^*,y^*,t^*)] dy^* + \frac{\partial \delta^*(x^*,t^*)}{\partial t^*} = 0 \tag{24}$$

In the present problem, however, U_e^* is steady. Furthermore, as will be discussed later, the unsteady injection-suction velocity is (*a*) very small compared to U_e^* *and* (*b*) sinusoidally distributed along the wall and varies harmonically with time, i.e., zero mass transfer. Therefore, the effect of the injection-suction on the time-averaged velocity profile u^* is very small and is confined in a very thin layer close to the wall. This implies that the correction to the displacement thickness, as calculated from equation (22), obtained from equation (24) is negligible in the present problem. Consequently, the displacement thickness is calculated from equation (22).

In terms of Görtler's dependent and independent variables, the "total" viscosities for the inner and outer layers, respectively, read

$$\bar{\epsilon}_i = 1 + K_1^2 (2\xi \text{Re})^{1/2} [1 - \exp(-y^+/A^+)]^2 \left| \frac{\partial F}{\partial \eta} \right| \eta^2 \tag{25}$$

where

$$y^+ = (2\xi \text{Re})^{1/4} \left(\frac{\partial F}{\partial \eta} \Big|_w \right)^{1/2} \eta \tag{26}$$

$$A^+ = 26 \left\{ -2\xi V_w (dU_e/dx) \left(U_e \frac{\partial F}{\partial \eta} \Big|_w \right)^{-1} \cdot \left[\exp\left(11.8 V_w (2\xi Re)^{-1/4} \left(\frac{\partial F}{\partial \eta} \Big|_w \right)^{-1/2} \right) - 1 \right] + \exp\left[11.8 V_w (2\xi \text{Re})^{-1/4} \left(\frac{\partial F}{\partial \eta} \Big|_w \right)^{-1/2} \right] \right\}^{-1/2} \tag{27}$$

and

$$\bar{\epsilon}_0 = 1 + 0.5 K_2 (2\xi \text{Re})^{1/2} \{ 1 - \text{erf}[5(\eta \eta_\delta^{-1} - 0.78)] \} \cdot \int_0^{\eta_\delta} (1 - F)\, d\eta \tag{28}$$

where η_δ is the boundary-layer thickness.

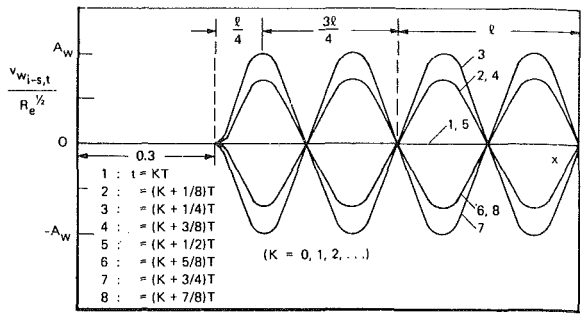

Fig. 1 The injection-suction velocity v_w versus the distance x at intervals within a period T

Turbulent Boundary Layers With Unsteady Injection-Suction

Calculations were performed for a steady outer flow over a porous flat plate with a sinusoidally distributed injection-suction that varies harmonically with time. To avoid any difficulties in the numerical integration in the neighborhood $x = 0$ for $v_w \neq 0$, the time-varying injection-suction distribution was assumed to be given by the following expressions (see Fig. 1);

$$v_{w_{i-s,t}} = 0 \text{ for } x < 0.3 \tag{29}$$

$$v_{w_{i-s,t}} = \frac{A_w}{2} \text{Re}^{1/2} \sin(\omega t) [1 + \cos[4\pi(x - 0.3)/l + \pi]] \text{ for } 0.3 \leq x \leq 0.3 + \frac{l}{4} \tag{30}$$

$$v_{w_{i-s,t}} = A_w \text{Re}^{1/2} \sin(\omega t) \cos\left[2\pi(x - 0.3)/l - \frac{\pi}{2} \right] \text{ for } x \geq 0.3 + \frac{l}{4} \tag{31}$$

where A_w, ω, and l are the strength, frequency, and wavelength of injection-suction. Notice that the time-varying injection-suction given by equations (29)–(31) (*a*) has a zero net flow, i.e., mass is not added or removed from the turbulent boundary layer and (*b*) is zero along the wall at $t = 0$ which allows the numerical integration to start by calculating the steady turbulent boundary layer over a nonporous wall.

The system of equations (9) and (13) subject to the boundary conditions of equations (29)–(31) and $u_w = 0$ was solved for the flow over a flat plate, $dU_e/dx = 0$.

All calculations were performed for a Reynolds number $\text{Re} = 5.834 \times 10^6$ corresponding to a free stream velocity $U_\infty^* = 15.24$ m/s, a representative length $L^* = 6.01$ m, and air kinematic viscosity $\nu^* = 1.57 \times 10^{-5}$ m^2/s. These values were selected so that the zero injection-suction turbulent boundary layer is the turbulent boundary layer achieved by Klebanoff [18] in his smooth hard plate experiments. Specifically, in Klebanoff's experiments $U_\infty^* = 15.24$ m/s, $\nu^* = 1.57 \times 10^{-5}$ m^2/s and the length Reynolds number, $\text{Re} = U_\infty^* x^*/\nu^*$, at the point $x^* = 4.328$ m measured from the virtual origin, i.e., apparent development length, was 4.2×10^6. At this point Klebanoff made all the measurements. In order to facilitate comparison with Klebanoff's experimental results, the results of the numerical calculations presented in this paper correspond to this point, i.e., $x = x^*/L^* = 4.328$ m/6.01 m = 0.72. Calculations were performed at the above

Downloaded 02 Jun 2010 to 171.66.16.103. Redistribution subject to ASME license or copyright; see http://www.asme.org/terms/Terms_Use.cfm

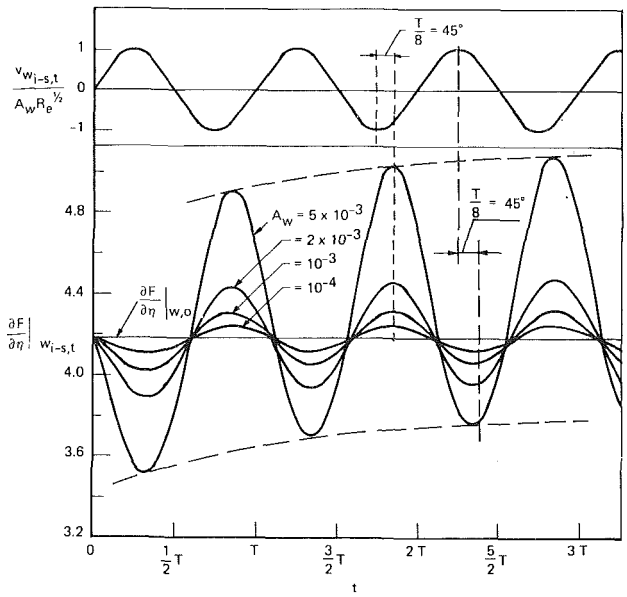

Fig. 2 The unsteady wall shear $\left.\frac{\partial F}{\partial \eta}\right|_{w_{i-s,t}}$ versus the time t $A_w = 10^{-4}, 10^{-3}, 2 \times 10^{-3}, 5 \times 10^{-3}$, at $x = 0.72; l = 0.08, f = 1000$

Reynolds number and a constant wavelength of injection-suction, $l = 0.08$.

For $A_w = 0$, i.e., flow over a non-porous flat plate, the present calculations predict that

$$\left.\frac{\partial F(x=0.72)}{\partial \eta}\right|_{w,0} = 4.1813 \tag{32}$$

where $(\partial F/\partial\eta)\,|_w$ is the wall shear and the subscript 0 indicates zero injection-suction. The corresponding local skin friction coefficient is

$$C_{f\,0}'\,|_{x=0.72} = \left.\frac{\tau_{w,0}^*}{\frac{1}{2}\rho^* U_\infty^{*2}}\right|_{x=0.72}$$

$$= \sqrt{\frac{2}{\xi \mathrm{Re}}}\left.\frac{\partial F(x=0.72)}{\partial \eta}\right|_{w,0} = 0.0028 \tag{33}$$

where $\xi = 0.72$ (see equation (7)). The above predicted value of the skin friction coefficient at $x = 0.72$ is in excellent agreement with the value of 0.0028 measured by Klebanoff at the same point. The excellent agreement between the calculated and the experimentally measured skin friction factor at $x = 0.72$, i.e., 4.328 m from the virtual origin, attests the accuracy of the present model for steady flows.

In Fig. 2 the unsteady wall shear $(\partial F/\partial\eta)\,|_{w_{i-s,t}}$ at $x = 0.72$ is plotted versus time for different strengths of injection-suction A_w and $f = 1000$. The amplitude of

$$\left.\frac{\partial F}{\partial \eta}\right|_{w_{i-s,t}}, \text{ i.e., } \left(\left.\frac{\partial F}{\partial \eta}\right|_{w_{i-s,t}}\right)_{\max} - \left.\frac{\partial F}{\partial \eta}\right|_{w,0},$$

increases with increasing strength of injection-suction A_w and tends to zero for zero injection-suction as was expected. Notice that the unsteady wall shear lags behind the quasi-steady wall shear which is maximum and minimum for maximum suction and injection, respectively. This lag appears to approach 45 deg in the limit for decreasing A_w. This behavior is opposite to the one found by Telionis and Tsahalis [7] in turbulent boundary layers over a flat plate with an oscillating outer flow with nonzero mean where the unsteady wall shear leads the quasi-steady wall shear by almost 45 deg (Stokes shear layer).

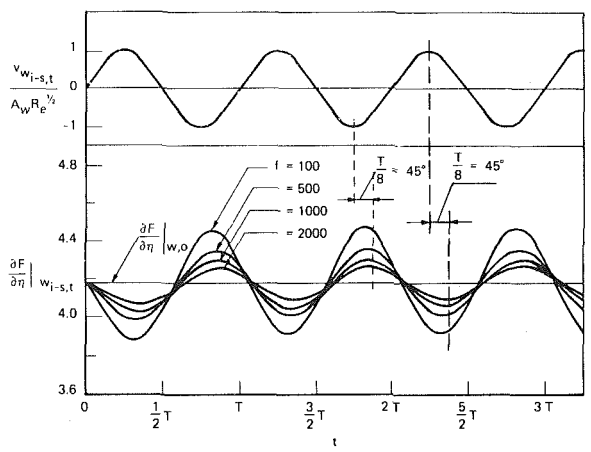

Fig. 3 The unsteady wall shear $\left.\frac{\partial F}{\partial \eta}\right|_{w_{i-s,t}}$ versus the time t $f = 100, 500, 1000, 2000$, at $x = 0.72; l = 0.08, A_w = 10^{-3}$

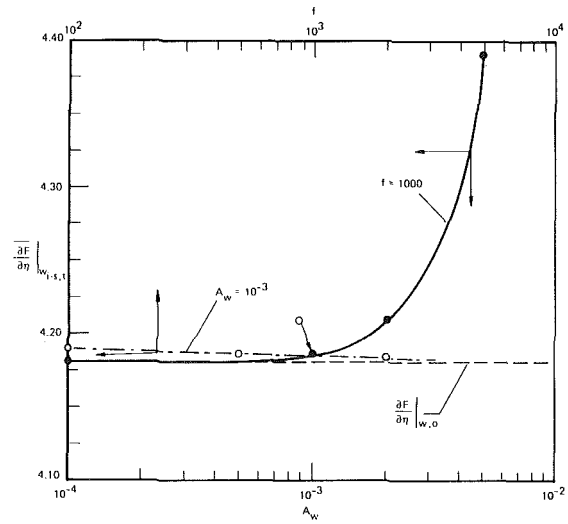

Fig. 4 The time averaged unsteady wall shear $\left.\frac{\overline{\partial F}}{\partial \eta}\right|_{w_{i-s,t}}$ versus the strength of injection-suction A_w and the frequency f for $f = 1000$ and $A_w = 10^{-3}$, respectively, at $x = 0.72; l = 0.08$

In Fig. 3 the unsteady wall shear $(\partial F/\partial\eta)\,|_{w_{i-s,t}}$ at $x = 0.72$ is plotted versus time for different frequencies of injection-suction f and $A_w = 10^{-3}$. The amplitude of $(\partial F/\partial\eta)\,|_{w_{i-s,t}}$ increases with decreasing frequency f and tends to zero for very high frequencies. That $(\partial F/\partial\eta)\,|_{w_{i-s,t}}$ tends to zero as f increases was expected because as $f \to \infty$, i.e., $T \to 0$, the mean turbulent flow does not have time to react to the unsteady injection-suction and eventually the porous wall degenerates into a nonporous one. Notice again that the unsteady wall shear lags behind the quasi-steady wall shear and that this lag appears to approach 45 deg in the limit for increasing f. Furthermore, the lag appears to approach 0 deg in the limit as $f \to 0$ as was expected, i.e., quasi-steady solution.

In Fig. 4 the time-averaged wall shear $(\overline{\partial F/\partial\eta})\,|_{w_{i-s,t}}$ over a period, T, where the overbar denotes time averaging, is plotted versus the injection-suction strength A_w and frequency f for $f = 1000$ and $A_w = 10^{-3}$, respectively. For all values of the strength of injection-suction, A_w, and frequency, f, considered in the present analysis, the time-averaged wall shear is larger than the corresponding wall

Downloaded 02 Jun 2010 to 171.66.16.103. Redistribution subject to ASME license or copyright; see http://www.asme.org/terms/Terms_Use.cfm

shear $(\partial F/\partial\eta)\,|_{w,0}$ over a nonporous wall. For $f = 1000$, the time-averaged wall shear $(\overline{\partial F/\partial\eta})\,|_{w_{i-s,t}}$ increases with increasing strength of injection-suction suction A_w and tends asymptotically to the wall shear $(\partial F/\partial\eta)\,|_{w,0}$ over a nonporous wall as $A_w \to 0$ as was expected. For $A_w = 10^{-3}$, the time-averaged wall shear $(\overline{\partial F/\partial\eta})\,|_{w_{i-s,t}}$ increases with decreasing frequency f and tends asymptotically to the wall shear $(\partial F/\partial\eta)\,|_{w,0}$ over a nonporous wall as $f \to \infty$. That

$$\lim_{f\to\infty} \overline{\frac{\partial F}{\partial\eta}}\bigg|_{w_{i-s,t}} = \frac{\partial F}{\partial\eta}\bigg|_{w,0}$$

was expected since for $f \to \infty$ the porous wall degenerates to a nonporous one. Furthermore, the fact that $(\overline{\partial F/\partial\eta})\,|_{w_{i-s,t}}$ increases with decreasing frequency f, where in the limit $f = 0$ a quasi-steady solution is recovered, indicates that the increase of $(\partial F/\partial\eta)\,|_{w,0}$ due to steady suction of given strength is larger than the decrease of $(\partial F/\partial\eta)\,|_{w,0}$ for a steady injection of the same strength.

Comparison With Previous Theoretical Results

Unfortunately, there is no experimental, theoretical or numerical information for turbulent boundary layers with unsteady, simultaneous injection and suction to compare the present predictions with. However, Leont'ev et al. [19] investigated experimentally, in a wind tunnel, steady turbulent boundary layers over a porous flat plate with steady, simultaneous injection and suction. Their porous surface consisted of a rectangular plate, 480mm long, 100mm wide, with 2880 openings arranged in 120 rows with 24 openings per row. The openings were arranged in straight-line order with a spacing of 4mm and their total area was 4.8 percent of the porous plate area. The air was simultaneously injected and sucked through alternating rows located one after the other. Consequently, the intensity of injection, j_i, and the intensity of suction, j_s, normalized to the entire area of the porous plate, were the same, that is,

$$j = j_i = j_s = \frac{|v^*_{w_{i\text{ or }s}}|}{U^*_\infty} \tag{34}$$

Furthermore, Leont'ev et al. developed a model for the calculation of the friction coefficient, averaged over the length of the porous plate, and the velocity profiles. According to their model

$$\frac{C_{f_{i-s,s}}}{C_{f_0}} = 1 + \left(\frac{b}{b_{cr}}\right)^2 \tag{35}$$

and

$$u_{i-s,s}(x,y) = \frac{1}{2}\left[\left(1-\frac{b}{b_{cr}}\right)u_{0,s}(x,y) + \frac{b}{b_{cr}}u^2_{0,s}(x,y)\right]$$

$$\cdot\left[2+\frac{b}{b_{cr}} - \frac{b}{b_{cr}}\left(1-\frac{b}{b_{cr}}\right)u_{0,s}(x,y) - \left(\frac{b}{b_{cr}}\right)^2 u^2_{0,s}(x,y)\right] \tag{36}$$

where b is the permeability parameter defined as

$$b = b_i = b_s = j\frac{2}{C_{f_0}} \tag{37}$$

and b_{cr} is a critical value of the parameter b, which for uniform composition boundary layers is given by [20]

$$b_{cr} \simeq \frac{4}{\frac{1}{3} + \frac{2}{3}\frac{T_w}{T_\infty}} \tag{38}$$

T_w and T_∞ being the absolute temperatures of the wall and the free stream, respectively. For $b > b_{cr}$ the skin friction coefficient and the velocity profiles given by equations (35) and (36) remain unchanged. In the Leont'ev et al. experiments

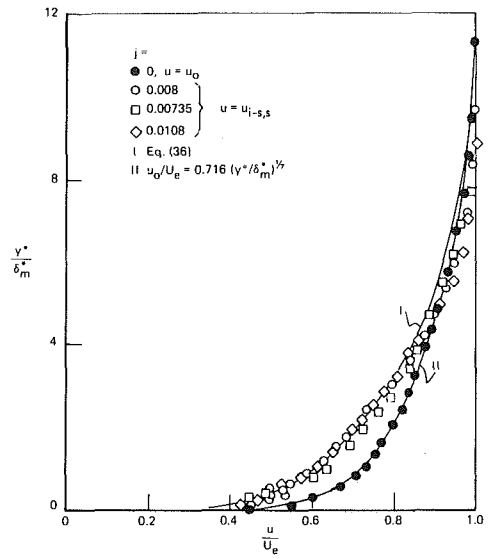

Fig. 5 Comparison of experimental data for steady, simultaneous injection-suction with the Leont'ev et al. model, reference [19]

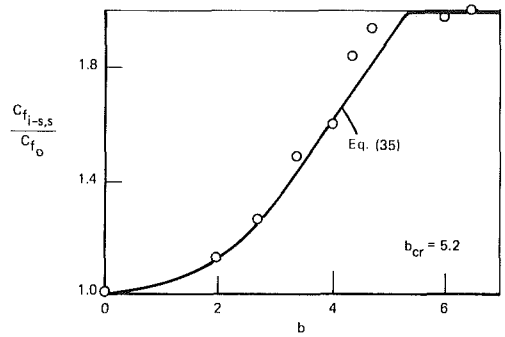

Fig. 6 Comparison of experimental data for steady, simultaneous injection-suction with the Leont'ev et al. model, reference [19]

$b_{cr} = 5.2$, i.e., $T_w < T_\infty$. In Figs. 5 and 6 the experimental data of Leont'ev et al. are shown together with the predictions of their model. The agreement between the experimental data and the model predictions is generally very good. However the model underpredicts the velocities at the outer portion of the boundary layer. Furthermore, the experimental injection-suction velocity profile is shown to be less full than the zero injection-suction velocity profile at the inner portion of the boundary layer but attains higher velocities at the outer portion of the boundary layer, i.e., the two velocity profiles cross each other.

In the present case $b_{cr} = 4.0$ because the boundary layer is isothermal, i.e., $T_w = T_\infty$, (see equation (38)). The intensity of injection and the intensity of suction, based on the maximum value of unsteady injection-suction, i.e.,

$$\left(v^*_{w_{i-s,t}}\right)_{\max} = v^*_{w_{i-s,t}}\bigg|_{\frac{\partial v^*_{w_{i-s,t}}}{\partial t^*}=0},$$

and normalized to the wavelength of injection-suction, l^*, are given by

$$j = j_i = j_s = \frac{\frac{1}{l^*}\int_{0.3L^*+Kl^*}^{0.3L^*+\left(K+\frac{1}{2}\right)l^*}\left(v^*_{w_{i-s,t}}\right)_{\max} dx^*}{U^*_\infty} = \frac{A_w}{\pi} \tag{39}$$

For comparison purposes, the length of the porous plate of the Leont'ev et al. experiments is represented by one

Downloaded 02 Jun 2010 to 171.66.16.103. Redistribution subject to ASME license or copyright; see http://www.asme.org/terms/Terms_Use.cfm

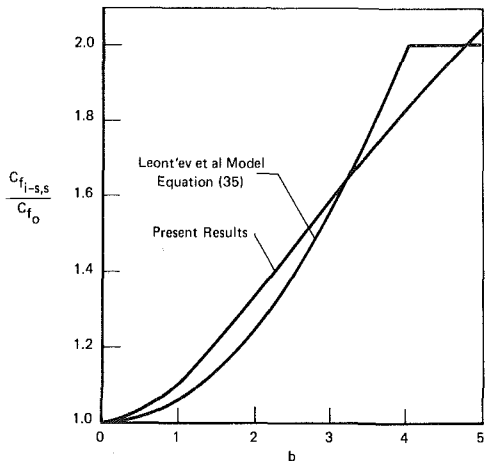

Fig. 7 Comparison of present results with the Leont'ev et al. model for steady injection-suction ($b_{cr} = 4.0$)

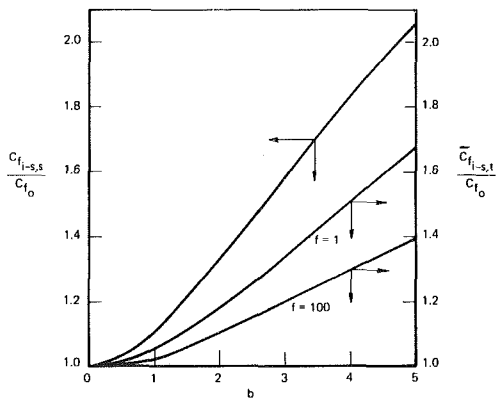

Fig. 8 Skin friction coefficient versus permeability parameter for steady or unsteady injection-suction

wavelength of injection-suction, $l = 0.08$, centered at $x = 0.72$, that is, $0.68 \le x \le 0.68 + l = 0.76$. For zero injection-suction, the skin friction coefficient, averaged over this segment, is $C_{f_0} = 0.00288$. For $C_{f_0} = 0.00288$ it is determined from equations (37) and (39) that the corresponding permeability parameter is given by

$$b = 221.05 A_w \tag{40}$$

Finally, it is pointed out that the above expression for the permeability parameter is also valid for the case of steady injection-suction of strength equal to the maximum value of unsteady injection-suction (see equation (39)).

At first it was decided to test the predictive capability of the present method for the case of steady injection-suction by comparing its predictions with those of the Leont'ev et al. model. This was achieved by performing the integration for $0 \le t \le T/4$ as in the case of unsteady injection-suction. Then at $t = T/4$ the boundary condition for the unsteady injection-suction, equations (29)–(31), was replaced by

$$v_{w_{i-s,s}} = v_{w_{i-s,t}} (t = T/4) \quad \text{for} \quad t \ge T/4 \tag{41}$$

and the unsteady program was left to continue the integration until a steady state solution was reached. In Fig. 7 the averaged skin friction coefficient, averaged over the length $0.68 \le x \le 0.76$, i.e.,

$$C_{f_{i-s,s}} = \frac{\int_{0.68L^*}^{0.68L^* + l^* = 0.76L^*} \tau^*_{w_{i-s,s}} dx^*}{\frac{1}{2}\rho^* U_\infty^{*2} l^*}$$

$$= \frac{1}{l}\sqrt{\frac{2}{\mathrm{Re}}} \int_{0.68}^{0.68 + l = 0.76} \sqrt{\frac{1}{x}} \left.\frac{\partial F}{\partial \eta}\right|_{w_{i-s,s}} dx \tag{42}$$

is plotted versus the permeability parameter. In the same figure the predictions of the Leont'ev et al. model are also plotted. The agreement is generally very good. The small discrepancies could be attributed to the rather large wavelength of injection-suction employed in the present calculations, i.e., $l^* = l \cdot L^* = 0.08 \cdot 6.01$ m $= 0.4808$ m. It should be pointed out, however, that the use of an alternative form of the Van Driest damping factor, as suggested by Kays (reference [21]), could further reduce the above small discrepancies.

Next, having established the predictive capability of the present method for steady injection-suction, the effect of unsteady injection-suction on the averaged skin friction coefficient observed over a porous flat plate with steady injection-suction was investigated. However, the accuracy of the predictions of the present method for unsteady injection-suction cannot be tested due to lack of related experimental, theoretical, or numerical information. Therefore, the following predictions for unsteady injection-suction should be treated only as qualitative ones.

In Fig. 8 the time-averaged skin friction coefficient, averaged over the length $0.68 \le x \le 0.76$, i.e.,

$$\bar{C}_{f_{i-s,t}} = \frac{\int_{0.68L^*}^{0.68L^* + l^* = 0.76L^*} \bar{\tau}^*_{w_{i-s,t}} dx^*}{\frac{1}{2}\rho^* U_\infty^{*2} l^*}$$

$$= \frac{1}{l}\sqrt{\frac{2}{\mathrm{Re}}} \int_{0.68}^{0.68 + l = 0.76} \sqrt{\frac{1}{x}} \left.\frac{\overline{\partial F}}{\partial \eta}\right|_{w_{i-s,t}} dx \tag{43}$$

is plotted versus the permeability parameter b for $f = 1$ and 100. In the same figure the predictions of the present method for steady injection-suction are also plotted. It is seen that $C_{f_{i-s,s}}$ and $\bar{C}_{f_{i-s,t}}$ exhibit the same type of dependence on b but $\bar{C}_{f_{i-s,t}} < C_{f_{i-s,s}}$. In Fig. 9 the skin friction coefficient $\bar{C}_{f_{i-s,t}}$ is plotted versus the injection-suction frequency for $b = 3$ ($A_w = 0.01357$). It is seen that $\bar{C}_{f_{i-s,t}}$ decreases with increasing frequency and tends asympotically to C_{f_0} for $f \to \infty$. That

$$\lim_{f \to \infty} \bar{C}_{f_{i-s,t}} \to C_{f_0}$$

was expected since for $f \to \infty$ the porous wall degenerates to a nonporous one. Furthermore, it is seen that

$$\lim_{f \to 0} \bar{C}_{f_{i-s,t}} < C_{f_{i-s,s}}.$$

which was also expected since

$$\lim_{f \to 0} \bar{C}_{f_{i-s,t}}$$

represents the time averaged skin friction coefficient of the quasi-steady solution, that is, the ensemble of solutions with steady injection-suction of strength corresponding to the strength of the unsteady injection-suction at different times of its harmonic variation, while $C_{f_{i-s,s}}$ is the averaged skin friction coefficient for steady injection-suction of strength equal to the maximum value of the unsteady injection-suction. This point is discussed in further detail in the Appendix.

Downloaded 02 Jun 2010 to 171.66.16.103. Redistribution subject to ASME license or copyright; see http://www.asme.org/terms/Terms_Use.cfm

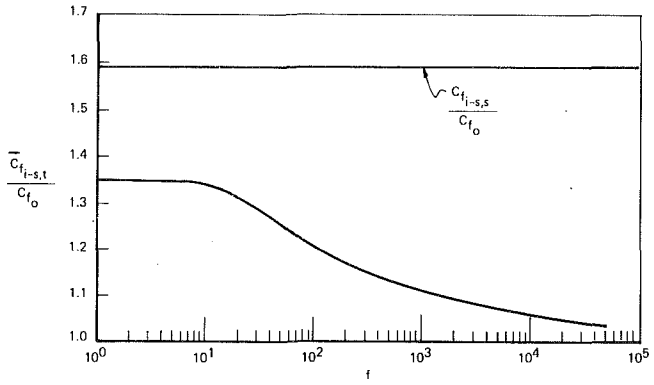

Fig. 9 Time-averaged skin friction coefficient $\bar{C}_{f_{i-s,t}}$ versus frequency of injection-suction f for $b = 3 (A_w = 0.01357)$

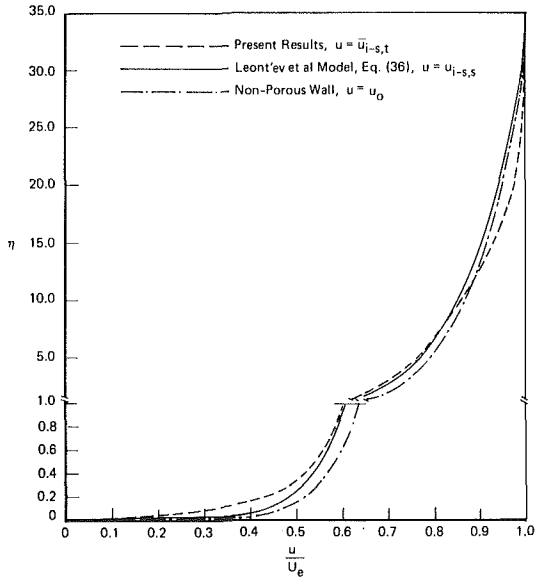

Fig. 10 Comparison of present results with the Leont'ev et al. model, $b = 1.110 (A_w = 5 \times 10^{-3})$ and $f = 10$

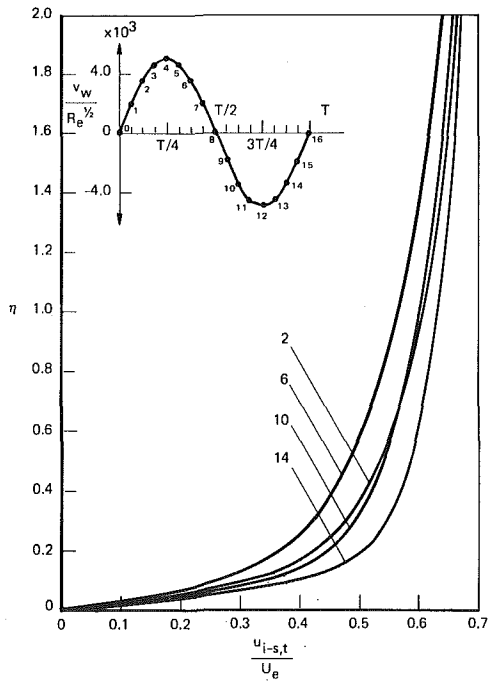

Fig. 11 Details of unsteady velocity profiles near the wall at $x = 0.72$, $b = 1.110 (A_w = 5 \times 10^{-3})$ and $f = 10$

In Fig. 10 the time-averaged profile $\bar{u}_{i-s,t}/U_e$ at $x = 0.72$ for $b = 1.110 (A_w = 5 \times 10^{-3})$ and $f = 10$ is plotted together with the velocity profiles $u_{i-s,s}/U_e$ predicted by the Leont'ev et al. model, and u_0/U_e for zero injection-suction. Please notice the change of scale at $\eta = 1$. It is seen that $\bar{u}_{i-s,t}/U_e$ is the least full velocity profile close to the wall but attains higher velocities at the outer portion of the boundary layer and crosses both the $u_{i-s,s}/U_e$ and the u_0/U_e velocity profiles. These features of the $u_{i-s,t}/U_e$ velocity profile are the same with the features of the experimentally measured velocity profile $u_{i-s,s}/U_e$ shown in Fig. 5. Finally, in Fig. 11 the details of some unsteady velocity profiles $u_{i-s,t}/U_e$ near the wall at $x = 0.72$ for $b = 1.110 (A_w = 5 \times 10^{-3})$ and $f = 10$ are shown.

Conclusions

The turbulent boundary layer over a porous flat plate for a steady outer flow and a sinusoidally distributed injection-suction that varies harmonically with time was investigated numerically.

The present results indicate that the unsteady wall shear lags behind the quasi-steady wall shear and that this lag approaches 45 deg in the limit for increasing frequency and decreasing strength of injection-suction. This behavior is opposite to the one found in turbulent boundary layers over a nonporous flat plate with an oscillating outer flow with non-vanishing mean where the unsteady wall shear leads the quasi-steady wall shear by almost 45 deg.

The most important result of the present study is that the time-averaged unsteady skin friction coefficient, averaged over a length equal to the wave length of injection-suction, is always (*a*) larger than the corresponding skin friction coefficient for a nonporous wall and (*b*) smaller than the corresponding skin friction coefficient for a porous flat plate with steady injection-suction of the same strength, for all values of the frequency and strength of injection-suction considered.

The classical eddy viscosity and mixing length models, developed for steady flows, were extended to unsteady flows. This approach certainly is only an attempt in estimating the possibility of calculating a certain class of unsteady turbulent flows with approximate models. It is argued, however, that since in the present problem the unsteadiness is confined in a thin layer very close to the wall where the Reynolds stress tends to zero and laminar friction dominates the use of eddy viscosity models developed for steady flows is not altogether unrealistic. The fact that the present calculations predict the expected behavior of the unsteady wall shear as the strength of the injection-suction goes to zero or the frequency goes to infinity lends credence to the above argument.

Acknowledgment

The author is indebted to one of the reviewers for bringing to his attention the work of Leont'ev et al., reference [19].

References

1 Tsahalis, D. T., "Unsteady Boundary Layers and Separation," Ph.D. thesis, Virginia Polytechnic and State University, Aug. 1974.

2 Telionis, D. P., Tsahalis, D. T., and Werle, M. J., "Numerical Investigation of Unsteady Boundary-Layer Separation," *Physics of Fluids,* Vol. 16, July 1973, pp. 968-973.

3 Werle, M. J., and Davis, R. T., "Incompressible Laminar Boundary Layers on a Parabola at an Angle of Attack: A Study of the Separation Point," *Journal of Applied Mechanics,* Vol. 39, 1972, pp. 7-12.

4 Telionis, D. P., and Tsahalis, D. T., "Response of Separation to Impulsive Changes of Outer Flow," *AIAA Journal,* Vol. 12, May 1974, pp. 614-619.

Downloaded 02 Jun 2010 to 171.66.16.103. Redistribution subject to ASME license or copyright; see http://www.asme.org/terms/Terms_Use.cfm

5 Telionis, D. P., and Tsahalis, D. T., "Unsteady Laminar Separation over Impulsively Moved Cylinders," *Acta Astronautica,* Vol. 1, Nov.-Dec. 1974, pp. 1487-1505.

6 Tsahalis, D. T., and Telionis, D. P., "Oscillating Laminar Boundary Layers and Unsteady Separation," *AIAA Journal,* Vol. 12, Nov. 1974, pp. 1469-1476.

7 Telionis, D. P., and Tsahalis, D. T., "Unsteady Turbulent Boundary Layers and Separation," *AIAA Journal,* Vol. 14, No. 4, Apr. 1976, pp. 468-474.

8 Telionis, D. P., "Calculations of Time Dependent Boundary Layers," *Unsteady Aerodynamics,* Vol. 1, edited by R. B. Kinney, University of Arizona Press, July 1975, pp. 155-190.

9 Schlichting, H., *Boundary Layer Theory,* 6th Edition, McGraw-Hill, 1968.

10 Van Driest, E. R., "On Turbulent Flow Near a Wall," *Journal of the Aeronautical Sciences,* Nov. 1956, pp. 1007-1011.

11 Cebeci, T., "The Behavior of Turbulent Flow Near a Porous Wall with Pressure Gradient," *AIAA Journal,* Vol. 8, No. 12, Dec. 1970, pp. 2152-2156.

12 Harris, E. J., "Numerical Solution of the Compressible Laminar, Transitional and Turbulent Boundary Layer Equations with Comparison to Experimental Data," Ph.D. thesis, Virginia Polytechnic Institute and State University, June 1970.

13 Pierce, F. J., and Klinksiek, W. F., "An Implicit Numerical Solution of the Turbulent Three-Dimensional Incompressible Boundary Layer Equations," Virginia Polytechnic Institute and State University Report No. VPI-E-71-14, July 1971.

14 Tsahalis, D. T., and Telionis, D. P., "On the Behavior of Turbulent Boundary Layers near the Point of Zero Wall Shear," Virginia Polytechnic Institute and State University Report No. VPI-E-74-20, Aug. 1974; also *AIAA Journal,* Vol. 13, No. 10, Oct. 1975, pp. 1261-1262.

15 Clauser, F. H., "The Turbulent Boundary Layer," *Advances in Applied Mechanics,* Vol. IV, Academic Press, 1956.

16 Cebeci, T., and Smith, A. M. O., *Analysis of Turbulent Boundary Layers,* Academic Press, New York, 1974.

17 Moore, F. K., and Ostrach, S., "Displacement Thickness of the Unsteady Boundary Layer," *Journal of the Aeronautical Sciences,* Jan. 1957, pp. 77-78.

18 Klebanoff, P. S., "Characteristics of Turbulence in a Boundary Layer with Zero Pressure Gradient," NACA Technical Note 3178, July 1954.

19 Leont'ev, A. I., Puzach, V. G., Komarov, V. P., Ermolaev, I. K., Dubina, N. V., and Fadeev, V. A., "Friction at the Surface of a Plate with Simultaneous Injection and Suction of Gas," *Journal of Engineering Physics,* Mar. 1978, pp. 872-876, Translation of Russian original *Inzhenerno-Fizicheskii Zhurnal,* Vol. 33, No. 2, Aug. 1977, pp. 204-209.

20 Kutateladze, S. S., and Leont'ev, A. I., *Turbulent Boundary Layers in Compressible Gases,* Academic Press Inc., New York, 1964 (Translated by D. B. Spalding).

21 Kays, W. M., "Heat Transfer to the Transpired Turbulent Boundary Layer," *International Journal of Heat and Mass Transfer,* Vol. 15, 1972, pp. 1023-1044.

APPENDIX

That

$$\lim_{f\to 0} \frac{\bar{C}_{fi-s,t}}{C_{f_0}} < \frac{C_{fi-s,s}}{C_{f_0}}$$

is easily proven as follows. Consider equations (42) and (43). Taking into account that the space integral and time integral (implicit in the term $(\overline{\partial F/\partial \eta})\,|_{w_{i-s,t}}$) in equation (43) are interchangeable it is obtained that

$$\frac{\bar{C}_{fi-s,t}}{C_{fi-s,s}} = \frac{\frac{1}{T}\int_0^T \left[\frac{1}{l}\sqrt{\frac{2}{\mathrm{Re}}}\int_{0.68}^{0.68+l=0.76} \sqrt{\frac{1}{x}}\,\frac{\partial F}{\partial \eta}\Big|_{w_{i-s,t}} dx\right] dt}{\frac{1}{l}\sqrt{\frac{2}{\mathrm{Re}}}\int_{0.68}^{0.68+l=0.76} \sqrt{\frac{1}{x}}\,\frac{\partial F}{\partial \eta}\Big|_{w_{i-s,s}} dx} \tag{A1}$$

where the term $(\partial F/\partial \eta)\,|_{w_{i-s,s}}$ in the denominator corresponds to steady injection-suction of strength equal to the maximum value of the unsteady injection-suction, i.e., $|v^*_w|_{\max}$ (see equation 41). In the limit $f\to 0$,

$$\frac{\partial F}{\partial \eta}\Big|_{w_{i-s,t}} = \frac{\partial F}{\partial \eta}\Big|_{w_{i-s,s}}$$

(see numerator) where the prime (′) indicates that $(\partial/\partial\eta)\,|'_{w_{i-s,s}}$ corresponds to steady injection-suction of strength $|v^*_w|_{\max}\cdot \sin\omega t$. This means that equation (A1) takes the following form in the limit

$$\lim_{f\to 0} \frac{\bar{C}_{fi-s,t}}{C_{fi-s,s}} = \frac{\frac{1}{T}\int_0^T C_{fi-s,s}(b)\,dt}{C_{fi-s,s}(b_{\max})} \tag{A2}$$

where b is the permeability parameter given by (see equations 34 and 37)

$$b = b_{\max}\sin\omega t \quad (\omega = 2\pi f) \tag{A3}$$

Since the present solution is a numerical one, i.e., no closed form solution exists, the analytical expression for $C_{fi-s,s}$ derived by Leont'ev et al., i.e., equation (35), will be utilized. From this equation

$$C_{fi-s,s}(b_{\max}) = \left[1+\left(\frac{b_{\max}}{b_{cr}}\right)^2\right]C_{f_0} \tag{A4}$$

$$C_{fi-s,s}(b) = \left[1+\left(\frac{b_{\max}\sin\omega t}{b_{cr}}\right)^2\right]C_{f_0} \tag{A5}$$

Substituting equations (A4) and (A5) into equation (A2) and performing the integration with respect to time, it follows that

$$\lim_{f\to 0} \frac{\bar{C}_{fi-s,t}}{C_{fi-s,s}} = \frac{1+0.5\left(\frac{b_{\max}}{b_{cr}}\right)^2}{1+\left(\frac{b_{\max}}{b_{cr}}\right)^2} < 1 \tag{A6}$$

From the above equation a rather interesting result is obtained, namely,

$$\lim_{f\to 0} \frac{\frac{\bar{C}_{fi-s,t}-C_{f_0}}{C_{f_0}}}{\frac{C_{fi-s,s}-C_{f_0}}{C_{f_0}}} = 0.5 \tag{A7}$$

From the numerical results shown in Fig. 9,

$$\frac{C_{fi-s,s}}{C_{f_0}} = 1.589$$

and

$$\frac{\bar{C}_{fi-s,t}}{C_{f_0}} = 1.344$$

in the limit as $f\to 0$, so that

$$\lim_{f\to 0} \frac{\frac{\bar{C}_{fi-s,t}-C_{f_0}}{C_{f_0}}}{\frac{C_{fi-s,s}-C_{f_0}}{C_{f_0}}} = 0.584 \tag{A8}$$

which is in good agreement with the prediction of the Leont'ev, et al. model (see equation (A7)).

Downloaded 02 Jun 2010 to 171.66.16.103. Redistribution subject to ASME license or copyright; see http://www.asme.org/terms/Terms_Use.cfm

Dimensionless Correlation of the Hanging Film Phenomenon

Roger Eichhorn
Dean of Engineering,
University of Kentucky,
Lexington, Ky.
Fellow ASME

The hanging film experiments of Wallis and Makkenchery and Pushkina and Sorokin are reviewed. The results indicate that the product of the Kutateladze number and the square root of the gas phase friction coefficient should be a constant for tubes for which the Bond number exceeds 20. A tentative dimensionless correlation of the data is advanced but more experiments are needed to resolve the mechanisms governing the phenomenon.

Introduction

A number of authors [1-6] have presented measurements of a situation in gas-liquid two phase flow which has been called the "hanging film phenomenon" by Wallis and Makkenchery [5]. In this situation a liquid film is held at rest on the inner surface of a tube by an upward flow of gas in the tube. A higher critical gas velocity exists above which the film attachment point (see Fig. 1) rises in the tube; and a lower critical gas velocity exists below which the film moves down the tube. Most of the authors report little or no difference between the two critical gas velocities. Wallis and Makkenchery, however, state that for small diameter tubes (≈ 6 mm) with air-water mixtures, the velocities differ by a factor of about two.

The early papers reported results for only one tube diameter, usually about 25 to 30 mm, and concentrated on air-water mixtures in polymethylmethacrylate (PMMA) tubes [1, 2]. Clift, et al. [3] used water-glycerol mixtures to study the effect of viscosity. They found little change in the lower critical gas velocity with a 40 fold change in viscosity.

Pushkina and Sorokin [4] used air-water mixtures in glass tubes of diameters ranging from 6.2 to 13.1 mm and a tube of "organic glass" of 309 mm. Their experimental results have been widely quoted because they can all be represented by the formula

$$\mathrm{Ku} = \frac{\rho_g^{1/2} \tilde{u}_g}{[\sigma g(\rho_f - \rho_g)]^{1/4}} \cong 3.2 \qquad (1)$$

where Ku is the Kutateladze number. Unfortunately, the Pushkina and Sorokin work is difficult to interpret. They do not define the term organic glass or give an adequate description of their experimental setup. And, neither they nor most of the early authors quoted the contact angle of the liquid on the tubes they used.

The Wallis and Makkenchery [5] experiments seem to be the most completely documented ones available. They reported values for the lower critical gas velocity for water in both PMMA and glass tubes; and moreover they stated carefully the conditions of the experiments and gave the static contact angles. Their results indicate that the lower critical air velocity increases with the tube diameter, and, for PMMA tubes where large diameters were available, reaches a constant value independent of the diameter. The limiting velocity for glass tubes was higher than that for PMMA tubes but in both cases the limit appeared to be given by equation (1). They attributed the difference in the critical gas velocity for glass and PMMA to differing contact angles for the two materials.

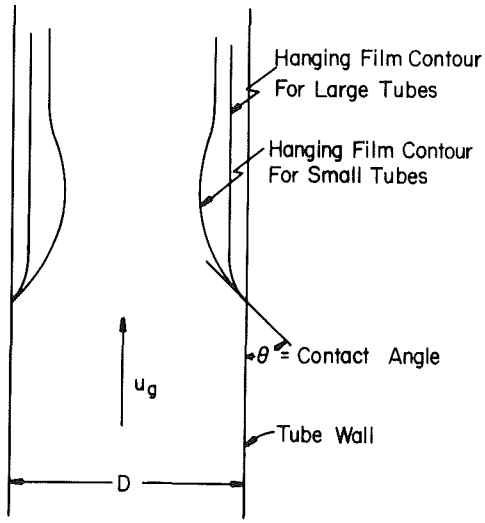

Fig. 1 Schematic representation of the hanging film phenomenon (as sketched in [5])

Wallis and Makkenchery use the Bond number as an independent variable:

$$\mathrm{Bo} \equiv D\left[\frac{g(\rho_f - \rho_g)}{\sigma}\right]^{1/2} \qquad (2)$$

where D is the tube diameter. For values of Bo > 40, for the PMMA tubes, their results indicated Ku $\cong 3.2$. Pushkina and Sorokin had found the same results for Bo > 6 in glass tubes, and a very modest reduction in Ku for lower values of Bo. The discrepancy between these two results has not been resolved.

Contributed by the Fluids Engineering Division of The American Society of Mechanical Engineers and presented at the Winter Annual Meeting, New York, N.Y., December 2-7, 1979. Manuscript received by the Fluids Engineering Division, November 9, 1978. Paper No. 79-WA/FE-16.

Copyright © 1980 by ASME
Downloaded 02 Jun 2010 to 171.66.16.103. Redistribution subject to ASME license or copyright; see http://www.asme.org/terms/Terms_Use.cfm

Wallis and Kuo [6] offered an approximate analysis[1] for the hanging film phenomenon and reported results for air-silicone oil in PMMA tubes. They state that the contact angle for silicone oil on PMMA is very small and quote results which indicate Ku $\cong$ 4.0 for large diameter tubes.

Critical flow events in counter-current flows are important in a variety of applications ranging from pipeline flows to nuclear reactor safety analysis. The limiting flow rates in the hanging film phenomenon should be one of the simplest of these events to analyze. In this note we use dimensional analysis to show the relationship between the important variables. We advance a tentative correlation formula and suggest further experimental measurements.

Identification of Dependent Variables in the Hanging Film Process

Consider a vertical tube of diameter D with a well rounded entrance on the lower end through which a gas of density ρ_g at superficial velocity $\bar{u}_g$ is supplied. A liquid of density ρ_f is supplied to an upper portion of the tube in some manner which will permit the formation of a liquid film on the inner tube wall.

At low values of $\bar{u}_g$, a counter-current flow of gas and liquid exists with a net upward flow of gas and a net downward flow of liquid. At high values of $\bar{u}_g$, a cocurrent flow of gas and liquid will exist provided there is a means available to introduce liquid into the system. Between these two extremes, several flow transitions occur. In this paper, we are exclusively concerned with the situation described in the introduction: the minimum gas velocity that is required to support a liquid film whose lower boundary is fixed above a portion of dry tube.

There exist two critical air velocities. If the air velocity is increased above the higher one, the film attachment point will rise in the tube. If it is decreased below the lower one, the film attachment point will descend in the tube. Between these two extremes the film thickness of liquid will vary but the attachment point will not move. Thus, if we reduce the gas velocity below the upper critical point, liquid will enter the tube and the film thickness will increase. Similarly, if we increase the gas velocity from a point above its lower critical value, the film thickness will decrease and the inventory of liquid contained within the tube will decrease.

Because there exists a range of gas velocities that will suspend the film in the tube without movement of the attachment point, there must also exist a range of film thicknesses and, therefore, levels of interfacial shear for a given position of the attachment point. Consequently, we expect there to be one critical velocity, one ciritical film thickness and one critical interfacial shear that will support the film at, say, the minimum hanging point. It also follows that specification of any one of the three will determine the other two and that any one of them can be regarded as a dependent variable in a dimensional analysis of the problem. The gas velocity is an obvious choice for a dependent variable because it can be controlled with ease and measured with certainty.

Presumably, as the gas velocity is decreased to approach the minimum hanging film point, the interfacial shear increases, and the film thickness increases until the film becomes unstable near the lower attachment point. It is as though we were to regard the inventory of liquid in the film as being contained in a reservoir with a valve controlled by the gas flow rate. As the gas flow decreases to some level, the valve can no longer be held closed and must open to allow liquid to drain. Bashforth, et al. [2] have succinctly described the phenomenon: "At the lowest air velocity at which measurements were taken (30.8 ft/s) there was slight loss of liquid from the bottom of the tube. Below this velocity, dumping suddenly became appreciable."

In the next section we shall examine the implications of dimensional analysis on the specification of the minimum hanging film point. The single independent variable will be related to the critical gas velocity. The dependent variables will be several physical properties of the gas and liquid and a single physical property to characterize the gas-liquid-tube interface system; the static contact angle. We shall not consider the film thickness or the interfacial shear since they should properly be regarded as alternate independent variables. In addition, few measurements of these variables are available.

Analysis

The critical gas velocity $\bar{u}_g$ should depend on the relative weight of the liquid $g(\rho_f - \rho_g)$, the gas and liquid densities and viscosities, ρ_g, ρ_f, μ_g, μ_f, the gas-liquid surface tension, σ, the tube diameter, D, and the contact angle, θ. A dimensional analysis with these variables will yield 9 - 3 = 6 dimensionless groups. They can conveniently be taken as the Kutateladze number, equation (1), the Bond number, equation (2), the density ratio, ρ_g/ρ_f, the viscosity ratio, μ_g/μ_f, a parameter involving properties only, and the contact angle, θ. Unfortunately, nothing new will be revealed by this selection because the process of choosing the variables uses only the minimum amount of physical information at our disposal.

As Bashforth, et al. have observed, the minimum hanging film point is associated with a "dumping" of liquid from the film. We therefore fix attention on the attachment region and assert that the critical velocity should be determined by the flow in the vicinity of the wall. A particular characteristic velocity in the gas phase, which we can use as a dependent variable, is the friction velocity, $u_g^* = \sqrt{\tau_w/\rho_g}$, appropriate to the dry tube upstream of the attachment point. This selection of a characteristic velocity should be especially appropriate for large tubes, where neither the mean gas velocity nor the tube diameter should appear separately as independent variables.

This reasoning leads us to assert that the force balance on

[1] The Wallis and Kuo analysis assumed an inviscid gas flow with slip along a motionless liquid film. Only a circumferentially uniform instability of the interface was permitted. The analysis provides some guidance to the physics involved.

Nomenclature

Bo = Bond number, equation (2)
C_f = skin friction coefficient, $2\tau_w/\rho_g \bar{u}_g^2$
D = tube diameter
g = gravitational acceleration
Ku, Ku* = Kutateladze number, equation (1), (4a)
Q = capillarity-buoyancy number, equation (4b)
Re_D = Reynolds number based on tube diameter
$\bar{u}_g$ = mean gas flow velocity
u_g^* = gas phase friction velocity, $\sqrt{\tau_w/\rho_g}$
ρ_f, ρ_g = liquid and gas densities
μ_f, μ_g = liquid and gas dynamic viscosities
θ = contact angle
τ_w = wall shear stress
σ = surface tension

Downloaded 02 Jun 2010 to 171.66.16.103. Redistribution subject to ASME license or copyright; see http://www.asme.org/terms/Terms_Use.cfm

the liquid film near its point of attachment to the wall is dependent on the relative liquid weight $g(\rho_f - \rho_g)$, the surface tension, σ, the tube diameter, D, the densities of the gas and liquid phases, ρ_g and ρ_f, respectively, their viscosities, μ_g and μ_f, the static contact angle measured in the liquid, θ, and as a dependent variable, the friction velocity in the gas phase, u_g^*. We presume the friction velocity to be characterized by its value in the bare tube immediately upstream of the attachment point. As the mean flow rate is reduced, the friction velocity decreases until a point is reached at which the film begins to move down the tube. Thus, we have:

$$u_g^* = f[g(\rho_f - \rho_g), \sigma, D, \rho_g, \rho_f, \mu_g, \mu_f, \theta] \tag{3}$$

There are nine variables in equation (3) and three dimensions. Since θ is already dimensionless we can choose the remaining five dimensionless groups as follows: a Kutateladze number based on the friction velocity;[2]

$$\mathrm{Ku}^* \equiv \frac{\rho_g^{1/2} u_g^*}{[\sigma g(\rho_f - \rho_g)]^{1/4}} \tag{4a}$$

the Bond number, equation (2);

a capillarity-buoyancy number;

$$Q \equiv \frac{\mu_g^4 g(\rho_f - \rho_g)_f}{\rho_g^2 \sigma^3} \tag{4b}$$

the density ratio;

$$\rho_r \equiv \rho_f / \rho_g \tag{4c}$$

and the viscosity ratio.

$$\mu_r = \mu_f / \mu_g \tag{4d}$$

The final functional formula for the critical value of Ku* thus becomes

$$\mathrm{Ku}^* = f(\mathrm{Bo}, Q, \theta, \rho_r, \mu_r) \tag{5}$$

An important feature of equation (5) is that the mean gas velocity, $\bar{u}_g$, does not appear explicitly. For large diameter tubes, Bo$\to\infty$ and the functional dependence on it should disappear. Once the fluid properties and the surface chemistry of the wall are specified, we should find Ku* = constant at the minimum hanging film point.

Equation (5) can be rewritten by using the wall friction coefficient, $C_f/2 = \tau_w/\rho_g \bar{u}_g^2 = (u_g^*/\bar{u}_g)^2$:

$$\mathrm{Ku}^* \equiv \mathrm{Ku}\sqrt{C_f/2} = f(\mathrm{Bo}, Q, \theta, \rho_r, \mu_r) \tag{6}$$

Since $C_f/2$ is a weak function of the gas phase Reynolds number, it is not surprising that Ku = const. has been quoted as the ultimate result for large tubes [4,5]. Actually, in addition to the gas phase Reynolds number, $C_f/2$ will depend on the entrance geometry for attachment points within the entrance length region and on the tube surface roughness. We will take it to be a function of the Reynolds number alone because most of the tubes that have been used are probably hydraulically smooth and because entrance lengths in turbulent flow are usually quite short. Also, adequate information does not exist to allow a more precise specification of the friction coefficient.

Most authors do not quote the Reynolds number explicitly, but it can be expressed in terms of Ku, Bo and Q as follows:

$$\mathrm{Re}_D \equiv Q^{-1/4}\mathrm{KuBo} \tag{7}$$

We are now able to check eqn. (6) against experimental data.

[2] Note that $\mathrm{Ku}^* \equiv \left[\frac{\tau_w^2}{\sigma g(\rho_f - \rho_g)}\right]^{1/4}$, so that the shear stress in the gas phase is being compared with a characteristic surface tension-buoyancy stress in the liquid phase. However, we are not implying that τ_w is the same as the interfacial shear stress between the gas and the liquid.

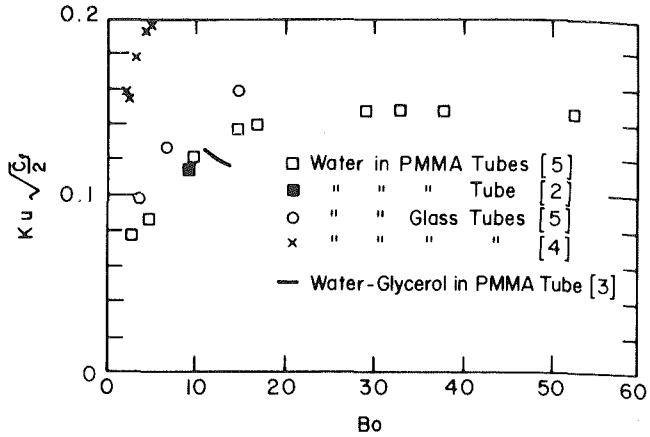

Fig. 2 Dimensionless representation of the lower limiting Kutateladze number

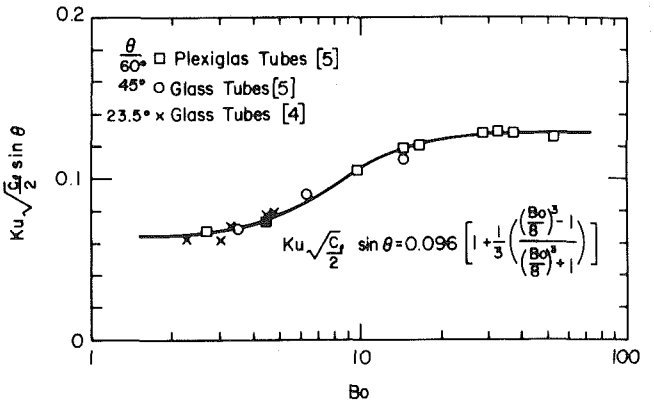

Fig. 3 Correlation of the lower limiting Kutateladze number

Results and Discussion

The properties for water and air at atmospheric conditions can be used to evaluate Q. The result is:

$$\mathrm{Re}_D \cong 850\ \mathrm{KuBo} \tag{7a}$$

The Reynolds number for the experiments reported by Wallis and Makkenchery ranged from 2340 to 142,000 with all but one data point above 4150. Thus we can evaluate the coefficient of friction from one of several turbulent flow relationships. Here we will use Prandtl's formula for smooth tubes reported by Schlichting [7]:

$$\sqrt{2/C_f} = 5.66 \log_{10}(\mathrm{Re}_D\sqrt{C_f/2}) + 0.292 \tag{8}$$

From Wallis and Makkenchery's Fig. 3, we read values of Ku and Bo, converted them to Re_D with equation (7*a*), and determined $C_f/2$ from eqn. (8). The ratio of the highest to the lowest value of $\sqrt{C_f/2}$ for the PMMA results is 1.7.

Figure 2 shows $\mathrm{Ku}\sqrt{C_f/2}$ plotted against Bo. It reveals that, in these coordinates, Ku* is constant for Bo > 20 for water in PMMA tubes. The final asymptote is

$$\mathrm{Ku}\sqrt{C_f/2} \cong 0.15 \tag{9}$$

Wallis and Makkenchery's data for glass tubes appear to be approaching a higher asymptote than 0.15. Pushkina and Sorokin's[3] results, also for glass tubes, are all much higher than the result for either of Wallis and Makkenchery's cases. Figure 2 also includes a single point from Bashforth, et al. [2] and several points from Clift, et al. [3] for air-water mixtures.

[3] Pushkina and Sorokin reduced the tube diameter by 0.4 mm in calculating their gas velocity for their three smallest tubes, to account for the film thickness. The bare tube values were used to determine the points in Fig. 2.

Downloaded 02 Jun 2010 to 171.66.16.103. Redistribution subject to ASME license or copyright; see http://www.asme.org/terms/Terms_Use.cfm

Both investigators used a PMMA tube. The effect of a 40 fold variation in viscosity is seen to be small [3].

A plot of Ku versus Bo (Fig. 3, reference [1]) also shows the diameter effect to disappear, but only for Bo $>$ 40. The asymptote for PMMA tubes is Ku $\cong$ 3.2 and the approach to it is gradual. For the data for glass tubes to approach the same asymptote as those for PMMA tubes would require an abrupt transition from the highest data point available to the line Ku = 3.2.

No ready explanation is apparent for the discrepancy between the glass tube results of Pushkina and Sorokin and Wallis and Makkenchery. For the former, the data points shown were scaled from Pushkina and Sorokin's plot of $\bar{u}_g$ versus D, and reduced in the manner described above. Other data points on their graph were not used since they were either for a different geometry or were for a tube of unspecified composition. The entrance conditions were not described by Pushkina and Sorokin but we can infer from their Fig. 1(*b*) that the gas entry geometry was a sharp edge. It is possible that a flow considerably different from Wallis and Makkenchery's would result in this case.

Pushkina and Sorokin evidently took the critical velocity to be the lowest velocity for which water was prevented from entering the funnel shaped upper entrance to the tube. This fact raises a question as to whether Pushkina and Sorokin's minimum hanging film point represents the same phenomenon as described by the other investigators.

Wallis and Makkenchery quote the contact angle for water on glass as 45 deg and for water on PMMA as 60 deg. None of the other authors report the contact angle for their experiments. The fact that Wallis and Makkenchery found a contact angle of 45 deg indicates that the surface of their glass tubes was contaminated. On clean glass, water has a very small contact angle and spreads readily over the surface [8]. Silicone liquids exhibit a creeping motion over most surfaces. The minimum hanging film phenomenon is likely to be quite different for silicone liquids than for water, so we have not included the Wallis and Kuo data in Fig. 2. Water on PMMA should exhibit a reproducible contact angle.

Figure 3 shows the data from Fig. 2 replotted on coordinates[4] $\mathrm{Ku}\sqrt{C_f/2}\sin\theta$ against $\log_{10}$ Bo. Values of θ = 60 deg for PMMA and 45 deg for glass (as reported in [5]) were used to reduce the Wallis and Makkenchery data. A contact angle of 23.5 deg was chosen for the Pushkina and Sorokin results merely to bring their data into the same range as the others.

An equation which correlates the data quite successfully is

$$\mathrm{Ku}\sqrt{C_f/2}\sin\theta = 0.096\left(1+\frac{1}{3}\left[\frac{(\mathrm{Bo}/8)^3-1}{(\mathrm{Bo}/8)^3+1}\right]\right) \qquad (10)$$

The root mean square difference between equation (10) and Wallis and Makkenchery's data is 2.6 percent; for Pushkina and Sorokin's data it is 7.5 percent. Some latitude is available in selecting the several numerical values in equation (10). No attempt was made to apply formal error minimization curve fitting schemes to the data.

The fact that $\mathrm{Ku}\sqrt{C_f/2}$ should become independent of Bo is not surprising. That the results in Fig. 3 indicate that it does so as well for small Bo, is not so easy to explain. Wallis and Makkenchery suggested that surface tension would close off the tube near Bo = 1.84. In addition, in their experiments (and, presumably, those of Pushkina and Sorokin as well) the Reynolds number for the lowest data point is perilously close to the laminar transitional value. If a laminar friction coefficient had been used to reduce the data, a much lower value would have been found for this lowest data point (Re_D = 2340).

We have found no obvious rationale for the form of the correlation equation (10). However, $\bar{u}_g \sin\theta$ is the component that the gas velocity would have normal to a film which meets the surface at an angle of θ.[5] If it is reasonable to suppose that momentum exchange in the normal direction is active in holding the film in position, this combination of terms will arise quite naturally.

To resolve the several questions raised by this analysis requires more experimental information. An apparatus to provide data to test against the ideas presented here should be one in which the flow entrance conditions can be carefully stated, the skin friction coefficient can be known with certainty and the contact angle prescribed. The measurement program should include a comprehensive visualization of the attachment point and the interface contour.

Since many of the applications involve metal surfaces and liquids containing surfactants, experiments only with glass and PMMA tubes and clean water are not likely to produce information of the generality needed. Experiments should also be done in annuli, rod bundles and other noncircular flow geometries.

Conclusions

1. Dimensional analysis of the hanging film phenomenon indicates that the lower limiting Kutateladze number based on the friction velocity should depend only on the fluid and wall properties for large diameter tubes.
2. The experiments of Wallis and Makkenchery indicate that the assertion in 1. is correct for Bo $>$ 20.
3. The existing data, where the static contact angle is known, can be successfully correlated by equation (10).
4. More experiments are needed to:
   - establish the generality of equation (10) or to develop an alternative
   - disclose the physical mechanisms governing the hanging film phenomenon and indicate the role of contact angle, wall properties, etc.

Acknowledgments

This work was begun in 1978 while I was employed as a summer staff member at EPRI. I am pleased to acknowledge their support and helpful discussions with Dr. K. H. Sun. J. H. Lienhard and A. H. P. Skelland contributed a number of useful ideas to this work.

References

1 Nicklin, D. J., and Davidson, J. F., "The Onset of Instability in Two-Phase Slug Flow," *Proc. Symp. on Two-Phase Fluid Flow,* Inst. Mech. Engrs., 1962, p. 29.

2 Bashforth, E. Q., Fraser, J. B. P., Hutchison, H. P., and Nedderman, R. M., "Two-Phase Flow in a Vertical Tube," *Chem. Eng. Sci.,* Vol. 18, 1963, p. 41.

3 Clift, R., Pritchard, C. L., and Nedderman, R. M., "The Effect of Viscosity on the Flooding Conditions in Wetted Wall Columns," *Chem. Eng. Sci.,* Vol. 21, 1966, p. 87.

4 Pushkina, O. L., and Sorokin, Yu. L., "Breakdown of Liquid Film Motion in Vertical Tubes," *Heat Transfer-Soviet Research,* Vol. 1, 1969, p. 56.

5 Wallis, G. B., and Makkenchery, S., "The Hanging Film Phenomenon in Vertical Annular Two-Phase Flow," ASME JOURNAL OF FLUIDS ENGINEERING, Vol. 96, 1974, p. 298.

6 Wallis, G. B., and Kuo, J. T., "The Behavior of Gas-Liquid Interfaces in Vertical Tubes," *Int. J. Multiphase Flow,* Vol. 2, 1976, p. 521.

7 Schlichting, H., *Boundary-Layer Theory,* 6th Edition, McGraw-Hill, New York, 1968.

8 Davies, J. T., and Rideal, E. K., *Interfacial Phenomena,* 2nd Edition, Academic Press, New York, 1963.

[4] The logarithmic coordinate is chosen only for convenience.

[5] Although a trigonometric function is evocative of a force or momentum balance, a power law variation, such as $\mathrm{Ku}\sqrt{C_f/2}\,\theta^n$, will do as well with $n \cong 2/3$.

Downloaded 02 Jun 2010 to 171.66.16.103. Redistribution subject to ASME license or copyright; see http://www.asme.org/terms/Terms_Use.cfm

M. Kiya
Associate Professor.

M. Arie
Professor.

Department of Mechanical Engineering,
Hokkaido University,
Sapporo, 060, Japan

S. Shoda
Engineer.
Nippon Kokan Co. Ltd.,
Tokyo, 100, Japan

An Increase in Base Pressure by Polymer Solutions Added to Separated Shear Layers

The change in the base pressure of a semicircular cylinder whose round side faced to the approaching stream was experimentally studied when the aqueous solutions of polyethyleneoxide (PEO) and polyacrylamide (PAM) were added to the boundary layer which eventually separated from the surface of the cylinder. The experiments were performed at a Reynolds number of 2.0×10^5, based on the base height of the cylinder. The base pressure was found to increase by 15 percent at its maximum by the injection of the polymer solutions as compared with the case of no injection. Saturation of the base-pressure increase was observed to exist with regard to the concentration of the polymer solutions and their velocity of injection.

1 Introduction

The reduction of resistance to turbulent shear flows of liquids through addition of small quantities of polymers of high molecular weight has received considerable attention. The research efforts and results available in this field have been reviewed and summarized from several points of view (e.g. Lumley [1], Hoyt [2], Landahl [3], Virk [4], Berman [5]). Although extensive theoretical and experimental works have been carried out with steady pipe flows, relatively few studies have been conducted on the effect of additives on the flow about bluff bodies. A rather detailed list of papers on experiments with different sizes and shapes of bodies (mostly spheres and circular cylinders) in various types and concentrations of polymers is included in Sarpkaya, et al. [6] with which the interested readers should consult. From these previous studies it was established that the drag force acting on bluff bodies submerged in the flow of polymer solutions is reduced as compared with the case of pure-water flow. It should be noted, however, that a complete understanding of the causes of the drag reduction in bluff-body flows has not obtained as yet, as remarked by Sarpkaya, et al. [6].

The injection of polymer solutions into the boundary layer along the surface of a body immersed in a flow of pure water can also reduce the drag force acting on the body. Vogel and Patterson [7] found that the drag-reduction effect can be produced on bodies of revolution by ejecting concentrated polymer solutions from a location near the nose. They ejected polyethyleneoxide solutions of various molecular weights and concentrations from a slot near the nose of the bodies to obtain a substantial reduction in measured drag in a water tunnel. For the most effective drag reduction with additives in external flows, the slot injection angle and the slot opening, together with the rate of injection of polymer solutions, must satisfy certain conditions, see e.g. Wu and Tulin [8]. Thurston and Jones [9] developed a non-Newtonian soluble coating to be applied to the surface of an underwater body. They obtained, for a test body of revolution, the reductions in total drag of 16–18 percent which, according to their estimation, corresponded to reductions in skin-friction drag of 27–30 percent, respectively. Wells [10] showed that the best friction-reduction performance would be obtained on a submerged vehicle in which polymers could be released either through a porous wall or from an ablating coating.

Unless such a body is properly streamlined, the boundary layers which reach the tail of the body will detach from its surface, thus producing a rather broad wake behind the body. Since the drag force acting on the body is the sum of pressure drag and skin-friction drag, it is important from practical point of view to examine the effect of types and concentrations of polymers included in the separated shear layers on the base pressure of the body. Within the authors' knowledge, such an investigation has not been performed as yet and therefore is the subject of the present paper.

2 Experimental Apparatus and Procedure

2.1 Water Channel. The experiments were performed in a recirculating water channel with an open perspex test section 0.4 m wide, 0.8 m high, and 4 m long. Tap water was recirculated in the channel. The capacity of the channel was approximately 9.52 m^3. In order to eliminate surface waves and to facilitate the visualization of flow around a test body, an upper cover plate 1.5 m long and 0.398 m wide, which consisted of 1 cm thick plexiglass, was installed in the open test section to form a closed flow passage between the cover plate and the floor of the test section, the height of the passage (H) being 14.5 cm as shown in Fig. 1. The cover plate was preceded by a contraction 0.3 m long which ensured a smooth entry of flow into the passage.

The cover plate had five short slits 1 cm wide and 3 cm long arranged normal to the main-flow direction with intervals 6

Contributed by the Fluids Engineering Division for publication in the JOURNAL OF FLUIDS ENGINEERING. Manuscript received by the Fluids Engineering Division, June 18, 1979.

Copyright © 1980 by ASME
Downloaded 02 Jun 2010 to 171.66.16.103. Redistribution subject to ASME license or copyright; see http://www.asme.org/terms/Terms_Use.cfm

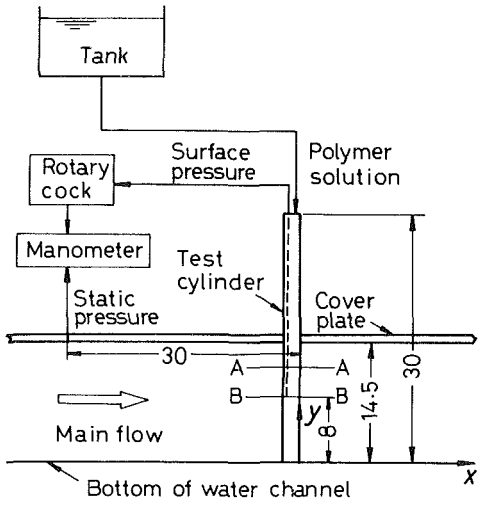

Fig. 1(*a*) Semicircular cylinder, flow passage, supply of polymer solutions and measurement of pressure. Unit in cm.

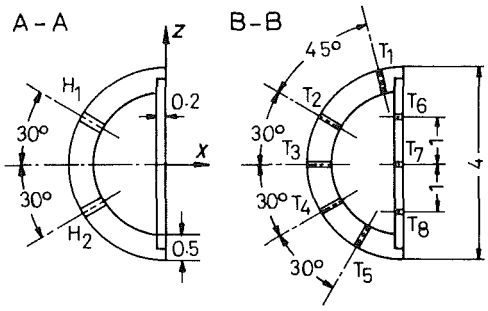

Fig. 1(*b*) Details of semicircular cylinder. Unit in cm. H_1 and H_2 are holes 0.18 cm in diameter for injection of polymer solutions. $T_1 \sim T_8$ are pressure taps 0.1 cm in diameter connected independently to rotary cock by small acrylicresin pipes.

cm and 9 cm at the position 35 cm downstream of the entrance of the flow passage. These slits were used to insert a Pitot-static tube which permitted the measurement of local velocity distribution in the passage. The Pitot-static tube was consisted of a total-head tube and a static-pressure tube, each being 0.13 cm in diameter, arranged in a plane which was made parallel to the floor of the channel during measurement. The difference between the total and static pressures was read on a Göttingen manometer. The slits were otherwise tightly sealed by blocks of the same dimension which were made flush with the inner surface of the cover plate. It may be noted that during experiment the passage was filled with water and a thin tranquil film of water existed on the outer surface of the cover plate.

2.2 Test Cylinder. The test cylinder is a semicircular cylinder shown in Fig. 1(*b*), the round side facing the approaching stream. The round part of the cylinder was made of carefully machined brass tube of 4 cm in diameter which was cut in half after machining. The rear side of the cylinder was consisted of a flat plexiglass 0.2 cm thick which was glued to the brass part in the manner shown in Fig. 1(*b*). One end of the cylinder was in contact with the floor of the test section and the other end passed through the cover plate, the part of the cylinder outside the cover plate being 15.5 cm long.

Several small-bore holes drilled normally to the front and rear surfaces at the plane 8 cm apart from the floor of the flow passage served as the pressure taps for the measurement of local pressure distribution along the periphery of the cylinder (see Fig. 1(*b*)). Three pressure taps were placed along the flat rear side of the cylinder in order to examine a possible change of the base pressure along the rear side. The pressure taps were independently connected to small acrylicresin pipes and led to a rotary valve which could choose a pressure tap to be fed to the Göttingen manometer outside the channel for the measurement of pressure. The Göttingen manometer measured the height of water column to the accuracy of 0.005 cm.

Two series of 0.18 cm diameter holes drilled radially from the round surface, whose angular position is shown in Fig. 1(*b*), allowed polymer solutions to be injected into the boundary layer along the surface of the cylinder. The spanwise distance between two consecutive holes in each row was 0.5 cm and thus the total number of the holes was 56 because the span of the cylinder in the flow passage was 14.5 cm.

Polymer solutions were supplied from a head tank outside the channel through three polyvinyl pipes to the inside of the cylinder whose volume was approximately 106 cm^3. The capacity of the head tank was 3800 cm^3 with the cross-sectional area of 190 cm^2. Since the upper end of the test cylinder was open to the atmosphere, the hydrostatic pressure of the polymer solutions inside the cylinder is approximately proportional to the depth of the polymer solutions. The polymer solutions supplied from the head tank occupied 60 - 80 percent of the inner volume of the cylinder, the height of

Nomenclature

c = concentration of polymer solutions
C_p = pressure coefficient = $(p - p_\infty)/[(1/2)\rho U_\infty^2]$
C_{pb} = base-pressure coefficient of semicircular cylinder without injection of polymer solutions
$\tilde{C}_{pb}$ = average base-pressure coefficient when flow patterns A and B alternately appear
C_{pbA} = base-pressure coefficient for pattern A
C_{pbB} = base-pressure coefficient for pattern B
C_{pbi} = base-pressure coefficient of semicircular cylinder with injection of polymer solutions
C_{pbl} = base-pressure coefficient of semicircular cylinder with shoulder plates
h = base height of semicircular cylinder
H = height of flow passage
l = length of shoulder plates (see Fig. 6)
p = pressure
p_∞ = pressure of approaching stream
Re = Reynolds number = $U_\infty h/\nu$
u = longitudinal velocity component
U_∞ = velocity of approaching stream
v_i = velocity of injection of polymer solutions
x,y,z = Cartesian coordinate system (see Fig. 1)
β_S = angle of separation measured from forward stagnation point
θ = angle measured from forward stagnation point of semicircular cylinder
λ = duration of time of pattern A
ν = kinematic viscosity of fluid
ρ = density of fluid

Downloaded 02 Jun 2010 to 171.66.16.103. Redistribution subject to ASME license or copyright; see http://www.asme.org/terms/Terms_Use.cfm

the column of the polymer solutions inside the cylinder depending upon the rate of discharge through the injection holes. During the measurement of the pressure distribution along the surface of the cylinder, the height of the polymer solutions was kept approximately constant by adjusting the height of the head tank. Approximately 1200 cm^3 of the polymer solutions were consumed during individual measurements. Since the hydrostatic-pressure difference between the inner and outer sides of the cylinder can be assumed to be approximately constant along its span, polymer solutions will be injected into the boundary layer approximately at the same rate for all holes. This conjecture was qualitatively confirmed by the observation of the behavior of injected polymer solutions which were made visible by the addition of dye.

The aspect ratio of the test cylinder was 3.63 based on the dimension of the flat rear side. The cylinder occupied approximately 10 percent of the area of the flow passage and according to the blockage-correction method of Maskell [11] the corrected value of the base-pressure coefficient would be almost 23 percent lower than that measured. It is not clear *a priori*, however, that the correction method of Maskell can be applied to the case where the separated shear layers contain the polymer solutions. Therefore, it was decided to present the results uncorrected.

2.3 Polymers. The polymers used in the experiment were Alcox E-160, a polyethyleneoxide (PEO) manufactured by Meisei Chemical Works, Ltd. and Diaclear MA3000H, a polyacrylamide (PAM) manufactured by Mitsubishi Chemical Industries, Ltd. The weight-average molecular weight was nominally 4.0×10^6 for PEO and $(1.20 - 1.65) \times 10^7$ for PAM respectively. The polyacrylamide was strongly anionic.

The polymer solutions were prepared in a polyvinylchloride storage tank of capacity approximately 0.2 m^3 by mixing the dry powder in distilled water to a concentration desired. After being stirred gently for about half an hour, the solutions were aged for approximately 24 hours. The formation of large lumps of partially dissolved polymers was seldom encountered with this method. The polymer solutions thus prepared were transferred to the head tank just before individual experiments.

Since the polymer solutions were continually added to water recirculating in the channel during experiment, one might naturally suspect whether or not the concentration became appreciable at the end of each experiment. As will be seen in §3, the highest concentration of the polymer solutions tested was 700 ppm for PAM. If the whole volume of the polymer solutions contained in the storage tank, i.e. 0.2 m^3, was consumed, the concentration in the channel would be increased to become $700 \times (0.2/9.52) = 14.7$ ppm at most. The flow of PAM solution of this concentration was found to yield negligible change in the base pressure of the test cylinder as compared with the flow of pure water. The situation was almost the same in the case of PEO.

The base pressure was measured successively with and without the injection of the polymer solutions, the difference between the two readings yielding the effect of the polymer solutions added to the separated shear layers. Accordingly, one should examine an increase in the depth of water in the channel caused by the addition of the polymer solutions. It was estimated that, when the whole volume of the head tank was added, the depth of water in the channel increased by 0.02 cm approximately and this caused the error in the base pressure coefficient less than 1 percent.

3 Results and Discussion

The velocity profile in the passage measured at the section 0.35 m downstream of the end of the contraction and at the same time 0.30 m upstream of the location of the test cylinder is shown in Fig. 2 as a function of the vertical coordinate z nondimensionalized by the height of the passage H (= 14.5 cm). The coordinate system is defined in Fig. 1. The velocity is found to be uniform within the error of ±2.5 percent at worst over most portion of the passage. These data were taken at the average potential-core velocity of 0.76 m/s which was the velocity employed in the measurement of pressure. The potential-core velocity in the passage increased by 0.65 percent between the position of the measurement of the velocity profile and the position where the test cylinder was installed. The dynamic pressure in the potential core thus increased by 1.3 percent, the corresponding pressure drop being also 1.3 percent of the dynamic pressure. Since the velocity and static pressure were monitored during experiment at the position 0.30 m upstream of the test cylinder, these changes in the dynamic and static pressures were properly taken into account in the calculation of the base-pressure coefficient from the measured base pressure.

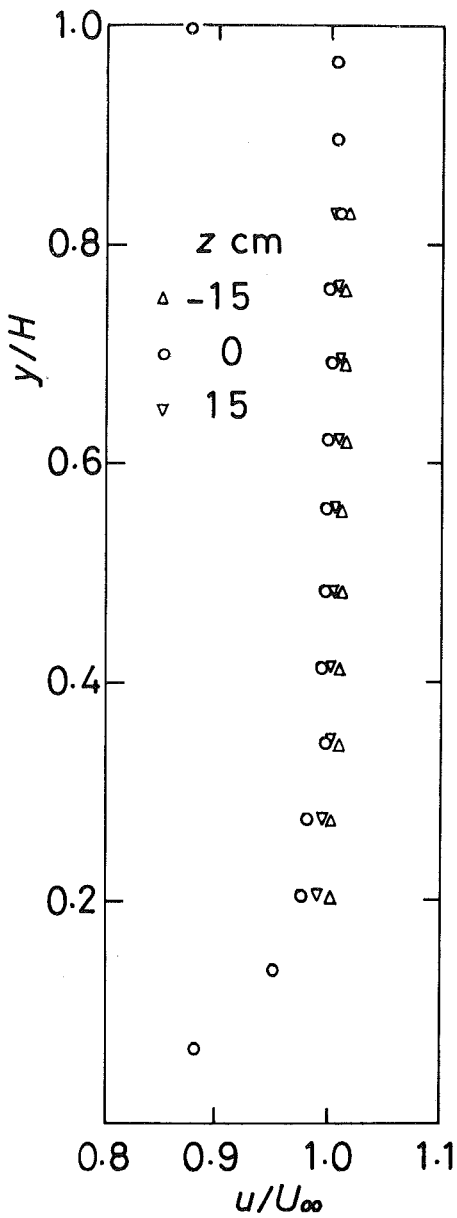

Fig. 2 Velocity distribution in flow passage. The uncertainty in y/H is ±0.03 and that in u/U_∞ is ±0.015.

Downloaded 02 Jun 2010 to 171.66.16.103. Redistribution subject to ASME license or copyright; see http://www.asme.org/terms/Terms_Use.cfm

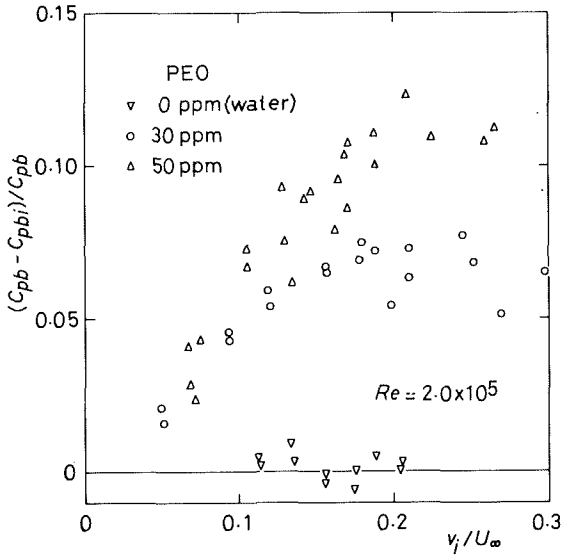

Fig. 3(a)

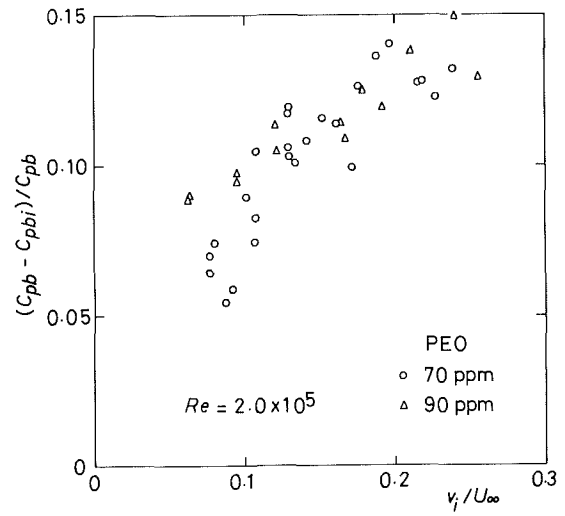

Fig. 3(b)

Fig. 3 Increase in base-pressure coefficient plotted against non-dimensional injection velocity of polymer solution (PEO). The uncertainty in the ordinate is ± 0.01 and that in the abscissa is ± 0.02.

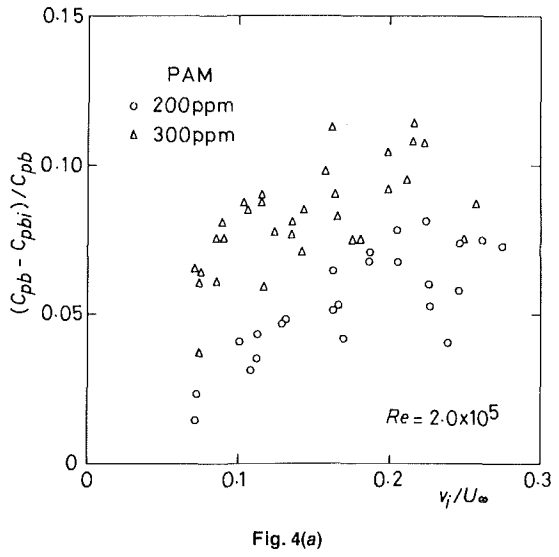

Fig. 4(a)

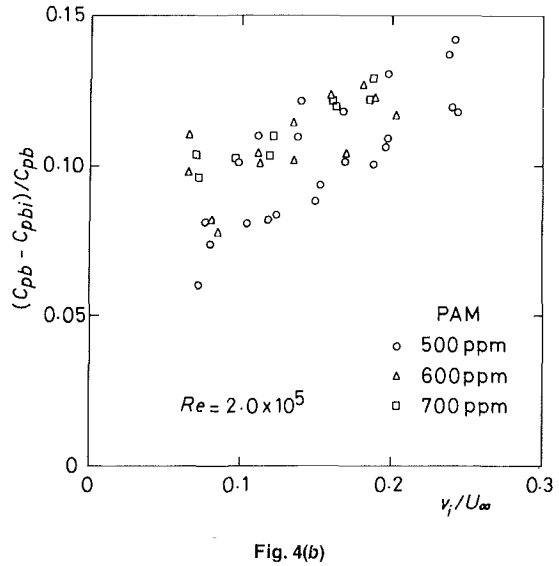

Fig. 4(b)

Fig. 4 Increase in base-pressure coefficient plotted against non-dimensional injection velocity of polymer solution (PAM). The uncertainty in the ordinate is ± 0.01 and that in the abscissa is ± 0.02.

The change of the base pressure by the injection of the polymer solutions will be presented as the ratio $(C_{pb} - C_{pbi})/C_{pb}$ plotted against v_i/U_∞. Here C_{pbi} and C_{pb} are the base-pressure coefficients with and without the injection of the polymer solutions, U_∞ the velocity of the approaching flow and v_i implies the average velocity of discharge of the polymer solutions through the injection holes. The base pressure was found to be almost constant over the rear side of the cylinder.

It is well established that the surface pressure measured by the pressure taps is in error owing to the viscoelastic nature of the polymer solutions. However, since no reliable methods of correction to be applicable to the present situation are not known to the authors, the measured pressure will be presented uncorrected.

The results for PEO are shown in Fig. 3. It is clear that the base pressure generally increases as the velocity of injection v_i or the concentration of the polymer solution c increases. Judged from the data for $c = 30$ ppm and 50 ppm, the increase in the base pressure seems to saturate at a certain value of v_i/U_∞ which may depend on the concentration. Moreover, the data for $c = 70$ ppm and 90 ppm suggest that the increase in the base pressure will become independent of the concentration if it is sufficiently high. To the extent of the present experiment in which the value of v_i/U_∞ is less than about 0.3, the maximum reduction in the base pressure is 14 percent at most for the solution of PEO. Unfortunately, in the present experiment, the value of v_i/U_∞ could not be taken to be wide enough to permit the determination of the saturated value of the base-pressure increase for higher concentration. In Fig. 3, the case of zero concentration ($c = 0$ ppm) corresponds to the injection of pure water. This measurement was performed in order to examine the extent to which the injection of pure water could change the base pressure of the semicircular cylinder. Any significant change of the base pressure with the ratio v_i/U_∞ does not seem to occur. Accordingly, the increase in the base pressure should be attributed to the effect of injection of the polymer solutions.

Figure 4 shows the results for PAM. The general trend of the change in the base pressure is almost the same to the case of PEO, including the saturation of the base pressure with

Downloaded 02 Jun 2010 to 171.66.16.103. Redistribution subject to ASME license or copyright; see http://www.asme.org/terms/Terms_Use.cfm

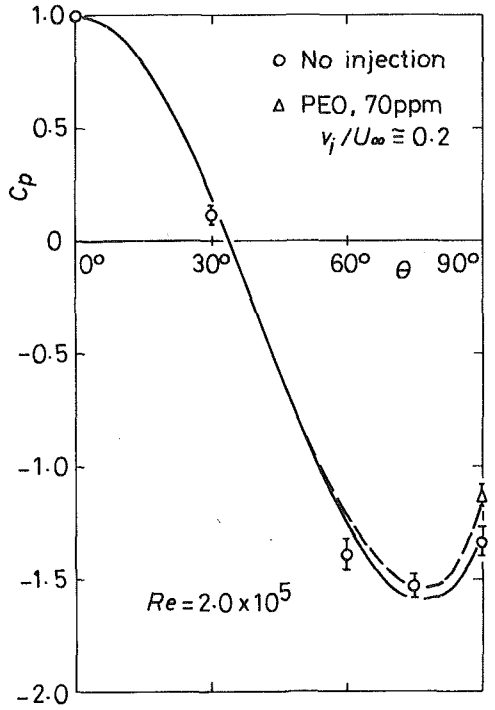

Fig. 5 Pressure distribution along surface of semicircular cylinder. —, Theory of Parkinson and Jandali [13], $\beta_S = 90$ deg, $C_{pb} = -1.34$ (no injection); – – –, Theory of Parkinson and Jandali [13], $\beta_S = 90$ deg, $C_{pbi} = -1.15$ (70 ppm solution of PAM, $v_j/U_\infty \simeq 0.2$). The uncertainty in the ordinate is shown by error flag and that in the abscissa is ±0.25 deg.

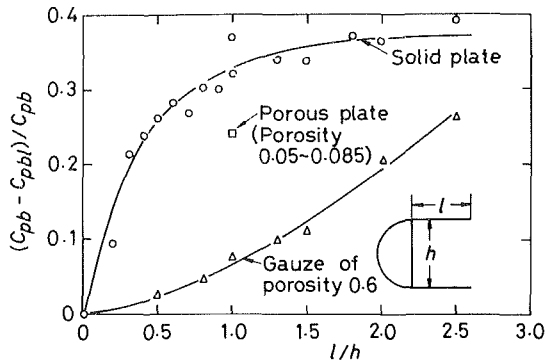

Fig. 6 Increase in base-pressure coefficient plotted against length of shoulder plates. The uncertainty in the ordinate is ±0.01 and that in the abscissa is ±0.013.

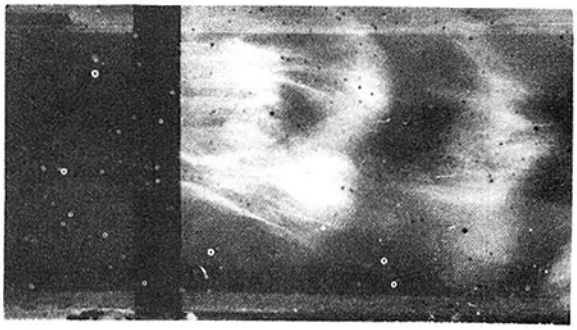

Fig. 7 Streaky structure of polymer solution in separated shear layers. Flow from left to right. Polymer solution was made visible by white dye. 500 ppm solution of PAM. $v_j/U_\infty \simeq 0.2$.

respect to the ratio v_j/U_∞ and the concentration. The maximum increase in the base pressure is again approximately 14 percent at most. However, the concentration of PAM required to produce the same amount of base-pressure increase is by an order higher than that of PEO.

Pressure distribution along the surface of the cylinder is shown in Fig. 5. The base pressure coefficient was plotted at the 90 deg position. The injection of the polymer solutions was found to change only insignificantly the pressure distribution along the round part of the cylinder, the deviation from that in the case of no injection being well within the error flag attached to the data points of Fig. 5. However, it should be remarked that the pressure on the round part of the cylinder slightly increased with an increase in the base pressure.

A possible mechanism by which the increase in the base pressure is brought about by the injection of the polymer solutions will now be considered. Since the aqueous solutions of PEO and PAM exhibit the viscoelastic property, the shear layers shed from the cylinder, which include the polymer solutions, will diminish the interaction between fluid inside and outside the base region. This will lead to an increase in the base pressure. In order to examine this hypothesis, an additional measurement of base pressure was performed by attaching thin plates of plexiglass 0.2 cm in thickness to the shoulder of the cylinder in the manner shown in Fig. 6. These plates will hereafter be referred to as the shoulder plates. The results obtained by changing the length l of the shoulder plates are shown in Fig. 6. The base pressure is found to increase first rapidly and then gradually with the increase in the length l. The problem is thus to estimate the length l which is appropriate to simulate the viscoelastic nature of the separated shear layers. The length of the formation region of the rolled-up vortices behind the cylinder (Gerrard [12]) can be taken as a possible choice. Although no measurement of the formation length was performed in the present experiment, visualization of flow in the near wake of the cylinder suggested that the end of the formation region was at the position very roughly one base height downstream of the base of the cylinder (see Fig. 8(*a*)). Here the end of the formation region was assumed to be the point at which the outside fluid first crossed the axis of the wake, as suggested by Gerrard [12]. From Fig. 6, the increase in the base pressure corresponding to $l/h = 1.0$ is seen to be 32 percent which is more than twice the maximum increase in the base pressure realized by the injection of the polymer solutions. (If the flow pattern of Fig. 8(*b*) is used to estimate the formation length, it will be very roughly 2.5 - 3.0 times the base height. Hence, from Fig. 6, the increase in the base pressure should be 37 percent.) These much larger increases in the base pressure than that actually measured suggest that the separated shear layers are porous in the sense that the polymer solutions have not yet attained a sufficient diffusion in the shear layers but exhibited streaky structure. The streaky structure of the polymer solutions may be clearly observed in the flow-visualization photograph shown in Fig. 7, in which the polymer solution was injected from the central half of the test cylinder. It should be noted that this streaky structure was brought about by the injection through the holes which were arranged with rather large intervals.

Another experiment was thus performed by replacing the shoulder plates by gauzes of porosity approximately 0.6. The results are included in Fig. 6. The increase in the base pressure is approximately 8 percent at $l/h = 1.0$, which, contrary to the solid shoulder plates, is considerably smaller than that obtained for the polymer solution. As also seen in Fig. 6, the increase in the base pressure was also measured to be 24 percent at $l/h = 1.0$ for porous shoulder plates of porosity 0.05 - 0.085. Although the measurements have not been made for a sufficiently wide range of the porosity, it is not unreasonable to assume that the increase in the base pressure comparable to that for the polymer solution will be obtained by employing the gauzes of appropriate porosity. The

Downloaded 02 Jun 2010 to 171.66.16.103. Redistribution subject to ASME license or copyright; see http://www.asme.org/terms/Terms_Use.cfm

(a) Pattern A

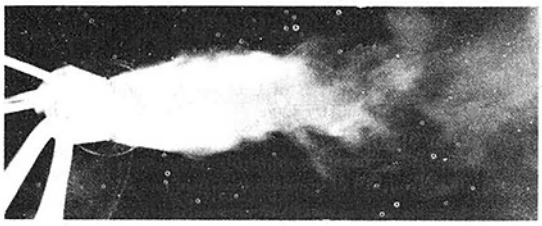

(b) Pattern B

Fig. 8 Two flow patterns behind semicircular cylinder. Flow from left to right. Polymer solution was made visible by white dye. 500 ppm solution of PAM. $v_i/U_\infty \simeq 0.2$.

foregoing results seem to lend support to the idea that the viscoelastic nature of the polymer solutions weakens the interaction of fluid inside and outside the base region and this increases the base pressure of the cylinder.

Visualization of flow revealed that two flow patterns shown in Fig. 8 existed in the wake of the cylinder. Fig. 8(*a*) will hereafter be denoted as pattern *A* and Fig. 8(*b*) as pattern B, respectively. These photographs of flow were taken for the 500 ppm solution of PAM at the injection velocity $v_i/U_\infty \simeq 0.20$, in which relatively large increase in the base pressure had been measured. Pattern A shows distinct vortex shedding from the cylinder while a large, approximately symmetrical separation bubble is formed in pattern *B*. Patterns *A* and *B* alternately changed one after another. Visual observation of the wake flow during about five minutes showed that pattern *A* occupied approximately 38 percent of the time of observation whereas pattern B occupied the remaining 62 percent of the time. It should be mentioned that patterns A and B also appeared in the wake of the cylinder even when pure water was injected at the velocity $v_i/U_\infty \simeq 0.2$. In this case, however, patterns *A* and *B* prevailed 70 and 30 percent of the time of observation, respectively. Accordingly it could safely be said that the injection of same or foreign liquid, if the injection velocity is sufficiently high, will give a change for pattern *B* to occur because pattern A is known to occur exclusively for the semicircular cylinder of this alignment without the injection. The important thing is that the polymer solutions greatly increase the duration of time of pattern *B*. This should be attributed to the viscoelastic nature of the polymer solutions added to the separated shear layers. It should be remarked here that patterns A and B also appeared in the 90 ppm solution of PEO at approximately the same velocity of injection as that of PAM, together with the durations of time for patterns A and B to occur. An interesting problem, which is left for the future, is to examine whether or not the similar switching of the wake pattern will appear when the body is immersed in the flow of the polymer solutions.

The switching of the two flow patterns suggests another way of interpretation of the increase in the base pressure. It would not be unrealistic to assume that pattern *B* corresponds to the wake flow which will be observed when the shoulder plates of appropriate length are attached to the cylinder, while pattern A is what is observed without any artificial device to modify the flow in the wake. The shape of the wake bubble shown in Fig. 8(*b*) seems to suggest that the equivalent length of the shoulder plates is 2.5 - 3.0 times the base height. On the other hand, Fig. 6 indicates that the increase in the base pressure becomes almost saturated for l/h more than about 1.5, the saturated increase in the base pressure being approximately 37 percent. If the fraction of time during which pattern A prevails is denoted by λ, the base-pressure coefficient $\tilde{C}_{pb}$ which will be measured when patterns *A* and *B* alternately occur can be estimated from

$$\tilde{C}_{pb} = \lambda C_{pbA} + (1-\lambda) C_{pbB}$$

where the suffixes *A* and *B* are referred to patterns *A* and *B*. This equation can also be written as

$$(C_{pbA} - \tilde{C}_{pb})/C_{pbA} = (1-\lambda)(C_{pbA} - C_{pbB})/C_{pbA}$$

Since $\lambda = 0.38$ and $(C_{pbA} - C_{pbB})/C_{pbA} = 0.37$, one obtains

$$(C_{pbA} - \tilde{C}_{pb})/C_{pbA} = 0.23$$

which is larger by about 60 percent than the maximum value (14 percent) obtained by the injection of the polymer solutions. As was previously mentioned, the authors are of the opinion that this difference should be attributed to the streaky structure of the polymer solutions in the shear layers. Accordingly, if the shear layers could completely be occupied by the polymer solutions by the injection through two-dimensional slits, say, the increase in the base pressure would become much larger than the data compiled in Figs. 3 and 4. Since the value of λ is expected to become smaller and smaller as more part of the shear layers is occupied by the polymer solutions, the base-pressure increase would amount to 37 percent at its maximum in view of the result of Fig. 6.

In passing, a comment will be made concerning the mechanism of the base-pressure change. Although the nature of the boundary layer along the front part of the body is changed by the injection of the polymer solution, it is the behavior of the separated free shear layers which are most important for the base-pressure change. Accordingly, the foregoing discussion concentrated on the properties of the free shear layers, excluding the changes of the boundary-layer properties. The boundary-layer properties are important in the sense that they yield an initial condition for the behavior of the shear layers.

The experimental results described heretofore have clearly demonstrated that the viscoelastic polymer solutions added to the separated shear layers can increase the base pressure of bluff bodies and thus reduce their pressure drag. Although the present experiments are of preliminary nature and not detailed enough, the results are sufficiently encouraging to recommend further investigations in this field.

4 Conclusions

The change in the base pressure of a semicircular cylinder was experimentally investigated when the polymer solutions of viscoelastic nature were added to the boundary layer which eventually separated from the surface of the cylinder. The experiments were performed at the Reynolds number of 2.0×10^5, based on the base height of the cylinder. The main results of the present investigation may be summarized as follows:

1 The base pressure of the semicircular cylinder can be increased by 14 percent at its maximum by injecting aqueous solutions of PEO and PAM to the boundary layer at the positions 30 deg downstream of the forward stagnation point.

2 PEO is more effective than PAM in the sense that the same amount of the base-pressure increase is obtained in PEO at concentrations of an order smaller than those in PAM.

Downloaded 02 Jun 2010 to 171.66.16.103. Redistribution subject to ASME license or copyright; see http://www.asme.org/terms/Terms_Use.cfm

3 Saturation of the base-pressure increase exists with regard to the concentration of the polymer solutions and their injection velocity.

4 Two different flow patterns exist in the wake of the cylinder at conditions where the maximum increase in the base pressure is obtained. The two flow patterns alternately change one after another with regard to time. The switching of the flow patterns can be used to approximately interpret the measured increase in the base pressure caused by the injection of the polymer solutions.

Acknowledgments

The authors express their sincere thanks to Mr. H. Tamura and Dr. Y. Suzuki for their discussion on the experimental results and to Mr. T. Yamazaki and Mr. T. Sampo for their skillful assistance in the construction of the experimental apparatus.

References

1 Lumley, J. L., "Drag Reduction by Additives," *Annual Review of Fluid Mechanics*, Vol. 1, 1969, p. 367.

2 Hoyt, J. W., "The Effect of Additives on Fluid Friction," ASME *Journal of Basic Engineering*, Vol. 94, No. 2, 1972, p. 259.

3 Landahl, M. T., "Drag Reduction by Polymer Addition," *Proceedings of the 13th International Congress of Applied Mechanics*, Moscow, 1973, p. 177.

4 Virk, P. S., "Drag Reduction Fundamentals," *AIChE Journal*, Vol. 21, No. 4, 1975, p. 625.

5 Berman, N. S., "Drag Reduction by Polymers," *Annual Review of Fluid Mechanics*, Vol. 10, 1978, p. 47.

6 Sarpkaya, T., Rainey, P. G., and Kell, R. E., "Flow of Dilute Polymer Solutions about Circular Cylinders," *Journal of Fluid Mechanics*, Vol. 57, Part 1, 1973, p. 177.

7 Vogel, W. M., and Patterson, A. M., "An Experimental Investigation of the Effects of Additives Injected into the Boundary Layers of an Underwater Body," *Proceedings of the 5th Symposium on Naval Hydrodynamics*, Bergen, ONR-ACR-112, 1964, p. 975.

8 Wu, J., and Tulin, M. P., "Drag Reduction by Ejecting Additive Solutions into Pure-Water Boundary Layer," ASME *Journal of Basic Engineering*, Vol. 94, No. 4, 1972, p. 749.

9 Thurston, S., and Jones, R. D., "Experimental Model Studies of Non-Newtonian Soluble Coatings for Drag Reduction," *Journal of Aircraft*, Vol. 2, No. 2, 1965, p. 122.

10 Wells, C. S., "An Analysis of Uniform Injection of a Drag-Reducing Fluid into a Turbulent Boundary Layer," *Viscous Drag Reduction*, Wells, C. S., ed., Plenum Press, 1969, p. 313.

11 Maskell, E. C., "A Theory of the Blockage Effects on Bluff Bodies and Stalled Wings in a Closed Wind Tunnel," Aeronautical Research Council Reports and Memoranda, No. 3400, 1965.

12 Gerrard, J. H., "The Mechanics of the Formation Region of Vortices behind Bluff Bodies," *Journal of Fluid Mechanics*, Vol. 25, Part 2, 1966, p. 401.

13 Parkinson, G. V., and Jandali, T., "A Wake Source Model for Bluff Body Potential Flow," *Journal of Fluid Mechanics*, Vol. 40, Part 3, 1970, p. 577.

Downloaded 02 Jun 2010 to 171.66.16.103. Redistribution subject to ASME license or copyright; see http://www.asme.org/terms/Terms_Use.cfm

3 Saturation of the base-pressure increase exists with regard to the concentration of the polymer solutions and their injection velocity.

4 Two different flow patterns exist in the wake of the cylinder at conditions where the maximum increase in the base pressure is obtained. The two flow patterns alternately change one after another with regard to time. The switching of the flow patterns can be used to approximately interpret the measured increase in the base pressure caused by the injection of the polymer solutions.

Acknowledgments

The authors express their sincere thanks to Mr. H. Tamura and Dr. Y. Suzuki for their discussion on the experimental results and to Mr. T. Yamazaki and Mr. T. Sampo for their skillful assistance in the construction of the experimental apparatus.

References

1 Lumley, J. L., "Drag Reduction by Additives," *Annual Review of Fluid Mechanics*, Vol. 1, 1969, p. 367.

2 Hoyt, J. W., "The Effect of Additives on Fluid Friction," ASME *Journal of Basic Engineering*, Vol. 94, No. 2, 1972, p. 259.

3 Landahl, M. T., "Drag Reduction by Polymer Addition," *Proceedings of the 13th International Congress of Applied Mechanics*, Moscow, 1973, p. 177.

4 Virk, P. S., "Drag Reduction Fundamentals," *AIChE Journal*, Vol. 21, No. 4, 1975, p. 625.

5 Berman, N. S., "Drag Reduction by Polymers," *Annual Review of Fluid Mechanics*, Vol. 10, 1978, p. 47.

6 Sarpkaya, T., Rainey, P. G., and Kell, R. E., "Flow of Dilute Polymer Solutions about Circular Cylinders," *Journal of Fluid Mechanics*, Vol. 57, Part 1, 1973, p. 177.

7 Vogel, W. M., and Patterson, A. M., "An Experimental Investigation of the Effects of Additives Injected into the Boundary Layers of an Underwater Body," *Proceedings of the 5th Symposium on Naval Hydrodynamics*, Bergen, ONR-ACR-112, 1964, p. 975.

8 Wu, J., and Tulin, M. P., "Drag Reduction by Ejecting Additive Solutions into Pure-Water Boundary Layer," ASME *Journal of Basic Engineering*, Vol. 94, No. 4, 1972, p. 749.

9 Thurston, S., and Jones, R. D., "Experimental Model Studies of Non-Newtonian Soluble Coatings for Drag Reduction," *Journal of Aircraft*, Vol. 2, No. 2, 1965, p. 122.

10 Wells, C. S., "An Analysis of Uniform Injection of a Drag-Reducing Fluid into a Turbulent Boundary Layer," *Viscous Drag Reduction*, Wells, C. S., ed., Plenum Press, 1969, p. 313.

11 Maskell, E. C., "A Theory of the Blockage Effects on Bluff Bodies and Stalled Wings in a Closed Wind Tunnel," Aeronautical Research Council Reports and Memoranda, No. 3400, 1965.

12 Gerrard, J. H., "The Mechanics of the Formation Region of Vortices behind Bluff Bodies," *Journal of Fluid Mechanics*, Vol. 25, Part 2, 1966, p. 401.

13 Parkinson, G. V., and Jandali, T., "A Wake Source Model for Bluff Body Potential Flow," *Journal of Fluid Mechanics*, Vol. 40, Part 3, 1970, p. 577.

DISCUSSION

S. Deutsch.[1] The effect of the addition of high molecular weight polymers on form drag is the general question motivating the paper, "An Increase in Base Pressure by Polymer Solutions Added to Separated Shear Layers," by Kiya, et al. [14]. The paper is a preliminary attempt to extend the measurements of Sarpkaya, et al. [15] to the more practical case in which the polymer additive is injected directly into the boundary layer. Kiya, et al. consider, rather than the cylinder of Sarpkaya, a half cylinder, rounded edge to the flow, presumably with the purpose of fixing the separation point. In the current study only one Reynolds number, that of 2×10^5 is considered. This is, perhaps unfortunately, near the middle of the transition regime for flow about a circular cylinder. Both Sarpkaya, et al. and the current study show, in fact, a reduction of form drag with polymer addition.

The current measurements should be considered preliminary for two reasons. First, they lack the detailed pressure distributions, Strouhal frequencies and particularly turbulence data that characterized the work of Sarpkaya. Moreover, they illustrate, all too clearly, the difficulties in making measurements in polymer solutions. For example, the blockage corrections of Maskell [16] could not be employed nor could surface pressure measurements be properly corrected for viscoelastic effects. In addition, we should note another possible source of error not considered by the authors; namely, the pitot static measurements of velocity. Berman, et al. [17] has reported pitot tube errors for dilute polymer solutions. They gave error estimates for solutions of 100 ppm at velocities of 3–10 m/s. They also report that the error can be significant at low speeds, with the measured velocity lower than the actual. One is forced to ask then whether exposing the pitot-static tubes to admittedly small concentrations (<14.5 ppm) but at quite low velocities (0.76 m/s) might not cause some additional errors. In particular, a lower measured than actual velocity could lead to the higher pressure coefficients observed on the upstream portion of the cylinder for the polymer runs.

Kiya, et al. go on to speculate that the reduced wake size (or rate of spread) is responsible for the larger base pressures in the polymer case. They further note a change in the character of the flow with polymers. Noting that the wake flow may either be of a vortex shedding nature or not, they observe that while both polymers and water exist in both regimes, the polymers spend less time in the shedding regime. Here it seems a shame that only a single Reynolds number and that in the middle of the transition region (where the details of the flow are no doubt quite sensitive to small upstream changes) was considered. Bearman [18] has previously observed that the loss of regular vortex shedding in the transition region is caused by the three-dimensionality of the flow due to upstream turbulence. Sarpkaya [15] has shown that vortex shedding for polymer solutions ceases at a lower Reynolds number than for solvent alone. Together they may explain the current observations.

We are still a long way from being able to predict or understand what the effects of additives will be in complex flows, such as the flow around the bluff body considered here. Clearly much more research is needed.

Additional References

14 Kiya, M., Arie, M., and Shoda, S., To appear in the *Journal of Fluids Engineering*.

15 Sarpkaya, T., Rainey, P. G., and Kell, R. E., *J.F.M.*, Vol. 51, 1973, p. 1977.

16 Maskell, E. C., Aero. Res. Counc. Rep. No. 3400, 1965.

17 Berman, N. S., Gurney, G. B., and George, W. K., *Physics of Fluids*, Vol. 16, No. 9, 1973.

18 Bearman, P. W., *J.F.M.*, Vol. 37, 1969, p. 577.

[1] Research Associate, The Pennsylvania State University, Applied Research Laboratory, State College, Pa. 16801.

Copyright © 1980 by ASME

Downloaded 02 Jun 2010 to 171.66.16.103. Redistribution subject to ASME license or copyright; see http://www.asme.org/terms/Terms_Use.cfm

Author's Closure

The authors are grateful to Dr. Deutsch for his valuable comments.

Since the point of separation is believed to be fixed at a point very close to the edges of the semicircular cylinder, the effects of Reynolds number on the wake flow may be less significant for the semicircular cylinder than for a circular cylinder. The data compiled by Hoerner [19] show that the drag coefficient of a semicircular cylinder in a uniform stream of Newtonian fluids is constant in the Reynolds-number range 10^4–10^6. This suggests that the present results obtained for one Reynolds number 2×10^5 may also valid in this rather wide range of Reynolds number.

The authors agree to Dr. Deutsch's comment that the present work is of preliminary nature because it does not include the measurement of the detailed pressure distributions, the Strouhal frequencies and the turbulence data. If these informations had been obtained, they would be helpful to our understanding of the mechanism of the base-pressure increase by the polymer injections. Dr. Deutsch's comment is also concerned with the errors in the measurement of the free-stream velocity by a Pitot-static tube in dilute polymer solutions. Unfortunately, any reliable method of correction of the errors does not seem to be established as yet. The authors can thus merely say that, since the concentrations of the recirculating fluids are very small (less than 14.5 ppm), the errors may not be significant enough to invalidate the present results of the base-pressure increase.

The authors are of the opinion that Dr. Deutsch's explanation of the change in the character of the wake flow with polymers may be taken as one of the possible mechanisms. It is worthwhile to mention that similar switchings of the flow patterns in the wake have recently been reported by Oba and Yasu [20] for cavitating flows (of pure water) around a circular cylinder. Certainly more work is needed to understand the effects of the additives on the unsteady separated flows past bluff bodies.

Additional References

19 Hoerner, S. F., Fluid-Dynamic Drag, published by the author, 1965.

20 Oba, R., and Yasu, Y., "Non-Linear, Low-Frequency Cavity Oscillations Behind a Circular Cylinder," Trans. of the JSME, Vol. 46, No. 402, 1980, pp. 206–212.

Downloaded 02 Jun 2010 to 171.66.16.103. Redistribution subject to ASME license or copyright; see http://www.asme.org/terms/Terms_Use.cfm

Journal of Fluids Engineering

Book Reviews

Laser Velocimetry and Particle Sizing, by H. D. Thompson and W. H. Stevenson, Hemisphere Publishing Co., 1979. Price: $49.50.

REVIEWED BY DENNIS K. McLAUGHLIN

The book *Laser Velocimetry and Particle Sizing* by H. D. Thompson and W. H. Stevenson is the *Proceedings of the Third International Workshop on Laser Velocimetry* held at Purdue University, July 11-13, 1978. It is a collection of papers by one hundred authors or co-authors on topics pertinent to laser velocimetry (anemometry). Despite the fact that laser velocimetry (LV) has developed into a practical instrument for research, it remains a relatively complicated and involved experimental technique. Consequently, a user of LV cannot afford to be without an adequate collection of literature including Thompson and Stevenson's book.

Laser Velocimetry and Particle Sizing is not a book for a novice. One cannot learn the principles and practical aspects of laser velocimetry from this book. Durst, Melling and Whitelaw's *Principles and Practice of Laser-Doppler Anemometry,* Academic Press, 1976, is much better suited for this purpose. However, for the serious user, Thompson and Stevenson's book contains a vast amount of information and references to even more information which will be of considerable use to those involved in making LV measurements. The workshop was divided into technical sessions on seven major topics: 1) Developments in instrumentation, 2) Data analysis 3) Combustion measurements, 4) Measurements in turbulent flows, 5) Measurements in internal combustion engines, 6) General applications, and 7) Particle diagnostics. Spread throughout these sessions is information on seeding and particle sizing techniques, optical systems, data reduction electronics and data analysis. Stevenson's historical review of laser velocimetry provides a useful introduction to the book.

This reviewer is impressed with the number of different flowfields in which the LV has been used with apparent success. Several of the applications include combustion and plasma flows, separated (reversing) flows, and two phase flows in which turbulence measurements were not possible before the LV. All of these experiments take advantage of the non-intrusive property of the laser velocimeter. In addition, several papers present comparisons between LV and pitot probe measurements for time mean velocity and LV and hot-wire measurements for turbulence properties. These works are useful in that they show quite good agreement in many cases and yet show enough disagreement (such as in the papers of Wiffen, Lau and Smith, and Dimotakis, Collins and Lang) to demonstrate that our understanding of all of the factors in the statistical data analysis is not complete. Further developments are needed in this area as they are needed in the area of novel optical systems such as the dual spot velocimeter.

Particle size information is important in almost all laser velocimeter applications so that it is not unusual to find experts in particle sizing among the LV users. The nine papers presented in this area show that reasonable estimates of particle size can be obtained with various configurations of laser beams with a minimum knowledge of refractive index properties and particle shape (if spherical). In many cases, precalibration with known particles is required in the techniques.

In summary, Thompson and Stevenson's book will be a welcome addition to the library of any experimentalist working with laser anemometry or contemplating doing so. As enormous amount of information is available under a single cover and hundreds of references are given for more in-depth reading.

Fluid Transients, by E. B. Wylie and V. L. Streeter, McGraw-Hill Book Company, 1978, 448 pp. Price: $34.50.

REVIEWED BY D. C. WIGGERT

This treatise is an extensively revised and updated version of the book *Hydraulic Transients*[1]; it is devoted to unsteady flows ranging from transient to periodic motions. Expanded subject matter includes treatment of boundary conditions, turbopump and turbine analysis, valve-stroking concepts, and open-channel flow. New topics are air release, liquid transmission and distribution systems, free vibration analysis, and gas pipeline transients. Special topics are presented which transcend traditional water hammer applications: porous-media flows, soil dynamics, and two- or three-dimensional flows. Emphasis is placed upon numerical solution of the one-dimensional hyperbolic wave equations, primarily making use of the method of characteristics. Linearization leads to closed-form impedance and modal analysis of piping systems. The implicit method of solution is emphasized in the chapter on open-channel flow.

Most of the techniques presented have been tested numerically, and where possible, are supported by laboratory or field data. The authors' thoroughness is especially evident in their coverage of pipeline transients, and in addition their broad background of experience is clearly transmitted to the reader. Much of the material is directly applicable to the practitioner; however, one should be aware that the emphasis is on numerical techniques.

To be more complete, the treatment of two-phase flows

[1] Copyright 1967 by McGraw-Hill, Inc.

Copyright © 1980 by ASME
Downloaded 02 Jun 2010 to 171.66.16.103. Redistribution subject to ASME license or copyright; see http://www.asme.org/terms/Terms_Use.cfm

could have drawn upon information available from recent studies related to nuclear reactor problems. Other numerical techniques—such as Law-Wendroff, finite elements, and two dimensional method of characteristics—could have been presented to show their strengths and weaknesses relative to the ones emphasized, and to present the reader with alternate formulations. The mathematics could perhaps be more cohesive and rigorously presented, for example, by making use of the matrix method to determine the characteristic roots and compatibility equations. These are not major issues, rather minor ones which relate to a preference of style as well as an understanding that constraints can limit the amount of material to be put forth. The book is a welcome addition to the fluid transient community's library.

Hydraulics in the United States 1776–1976, by Hunter Rouse, The Institute of Hydraulic Research of the University of Iowa, Iowa City, 1976, 238 pp. Price: $10.00.

REVIEWED BY FRANK M. WHITE

This little-publicized book is a delightful account of American contributions to hydraulics during the past two centuries and a worthy companion to the author's earlier book with S. Ince, *The History of Hydraulics.* Although the book was probably inspired by America's bicentennial celebration and is certainly one of the more lasting contributions to that effort, Professor Rouse in his preface actually cites guilt as the main motivation. He feels that the earlier history did not give American workers their full due respect, whereas his later speeches on the subject were much heavily oriented toward U.S. contributions.

Although "hydraulics" is not a favorite word among contemporary mechanical engineers, the author explains that, to him, it means scientific investigation into useful engineering applications of fluid flow, especially the original pioneering work rather than subsequent fine-tuning. Thus the book is filled with photographs, letters, and excerpts from the original manuscripts of the people who first developed the important ideas we now treat so routinely in textbooks. Naturally the author emphasizes the civil engineering aspects of hydraulics, but there is also a good treatment of the contributions of the ASME Hydraulics Division and its child, the Fluids Engineering Division.

After a Prologue on the European tradition, the book opens with a chapter on the first half-century of American work, primarily water supply and ship design problems. There is an account of a complete ship-resistance experiment conducted in 1768 by Benjamin Franklin. Two chapters then follow on 19th century work, especially mining applications in the west and, in the east, the famous Merrimack River industrial laboratory in Lowell, Massachusetts, operated from 1845–1884 by James B. Francis, for whom the mixed-flow turbine is named.

Chapter 4 describes the university hydraulic laboratories founded near the turn of this century at Worcester Polytechnic Institute, Cornell, Iowa, Berkeley, and subsequently many others. Chapter 5 details the monumental leadership exerted by John R. Freeman, a New Englander who established scholarships and professorships and generally inspired hydraulic research throughout the country and, in 1930, successfully overcame the opposition of the Army Corps of Engineers to the establishment of a National Hydraulics Laboratory.

The rise of fluid mechanics in 1930–1950 is outlined in Chapter 6, as Prandtl's scientific approach spread to America through the work of von Kārmān, Bakhmeteff, Ippen, Knapp, and the author himself, among others. Chapters 7 and 8 then detail the war and postwar years, respectively. There is a final chapter on the period 1965–1975, followed by an Epilogue in which the author expresses the belief that "the (hydraulics) profession will undoubtedly continue to flourish in the centuries to come." The reviewer certainly agrees.

The book is very readable throughout, with well-reproduced photographs and sketches, and the reviewer's interest never flagged. There are so many items which will be new to almost any fluids engineer: who wrote the first fluid mechanics textbook in 1771, who perfected the hurdy-gurdy wheel, who really developed the Francis turbine, who really derived the Buckingham Pi Theorem. It is invigorating to learn the background of one's chosen profession and the results cannot help but inspire our present efforts. An additional bittersweet benefit for middle-aged reviewers like myself is a history book which contains many photographs of one's own friends.

Copyright © 1980 by ASME

Downloaded 02 Jun 2010 to 171.66.16.103. Redistribution subject to ASME license or copyright; see http://www.asme.org/terms/Terms_Use.cfm

Journal of Fluids Engineering

Discussion

[Turbulent Flow in Axially Rotating Pipes[1]

Edward Silberman.[2] Readers of this paper may be interested to know that a very similar helical flow to that described in the paper occurs when fluid flows through a helically corrugated pipe. The discusser's work on helical pipe flow is summarized in references [10] and [11]. The wall helixes force the fluid to rotate in patterns like those shown in Figs. 5 and 6. The major difference is that in a boundary layer comparable with the depth of the helical grooves, the circumferential velocity drops from its maximum value to zero at the bottom of the grooves; one could visualize the flow as being established by an imaginary rotating sheath located at approximately the tops of the pipe ridges.

The discusser's work was all done in large commercial pipes, 1 ft (0.3 m) to 4 ft (1.2 m) in diameter, using both water and air as fluids at Reynolds numbers ranging from 3×10^5 to 5×10^6. The values of N, using maximum circumferential velocity in place of the circumferential speed of the pipe wall, was in the range of 0.33 to 0.5, depending on the helix angle (which depended, in turn, on pipe size because of the method of manufacturing helical pipe). Maximum V_z/V_m was in the range of 1.25 to 1.45 for comparison with Figs. 5 and 6.

In the discusser's work, data was taken at $1/D \sim 70$ or more where the velocity profiles are fully developed. This means that in a figure like Fig. 7, the pressure drop at the wall is the same as that along the center (as for $N = 0.25$ in the figure) and may be measured readily with suitably placed wall taps. Such pressure drop measuremetns were made and τ_{rz} and friction factor were obtained from them. It may be noted from equation (7) that for fully developed, axisymmetric flow, τ_{rz} depends only on the pressure drop and varies linearly with r, while from equation (6), $\tau_{r\theta} = 0$ everywhere! The measurements (some of which were made in air using split hot film anemometers) showed that there were periodic fluctuations in the mean flow so that $\tau_{r\theta} \neq 0$; with the aid of turbulence measurements, it was found that $\tau_{r\theta}$ increases from just outside the helical grooves toward the center of the pipe.

Friction factors showed a marked reduction from values for non-helical corrugated pipe at the same Reynolds number [10], the reduction being greater for the smaller pipes which induce larger N. Friction factors are independent of pipe length as long as the developing region is excluded from pressure measurements.

Turbulence intensity and correlation measurements were also made [11] and they provided an independent check on τ_{rz} at the wall. They also showed that the intensity of the radial turbulent component, especially, is dramatically reduced from what it is in a nonrotating flow between mid-radius and the wall; the effect on the other two components is not so great. Turbulence measurements also supplied a measure of the turbulent normal stresses which have been omitted from equations (6) and (7). The normal stresses almost balance the radial accelerative force in the central third of the pipe, but are much less important than pressure gradient in the remainder of the cross section.

Additional References

10 Silberman, E., "Effect of Helix Angle on Flow in Corrugated Pipes," *Journal of the Hydraulics Division*, ASCE, Vol. 96, No. HY11, Nov. 1970, pp. 2253-63. Also, closing discussion, Vol. 98, No. HY8, Aug. 1972, p. 1449.

11 Silberman, E., "Turbulence in Helically Corrugated Pipe Flow," *Journal of the Engineering Mechanics Division*, ASCE, Vol. 106, No. EM4, Aug. 1980.

Authors' Closure

The authors wish to express gratitude to Professor E. Silberman for offering his interesting experimental results and giving a comparison of flows in a rotating pipe and a helically corrugated one. He showed that in the corrugated pipe the change of velocity profiles and a decrease in pressure loss were caused by an increase in the helix angle. These changes bear some resemblance in character to those in the flow through the rotating pipe, but there exists an intrinsic difference between them in wall region: in the corrugated pipe the tangential velocity tends to be zero on the wall, but in the rotating pipe it takes the same value with the circumferential speed of the rotating pipe.

According to Rayleigh's stability criterion for a two-dimensional flow, the flow near the wall becomes unstable in the corrugated pipe, but it becomes stable in the rotating one. In the data by Professor Silberman, a suppression of turbulence can be seen only in the mid-radius part of the pipe, not in the wall region. In a rotating pipe, however, the flow is stabilized near the wall, which was confirmed by a flow visualization in the experiment of Cannon and Kays [5].[3]

In deriving the relationship of equations (5) and (6), the contribution of turbulent velocity components to the shear stresses is assumed to be negligibly small compared with that of the stresses caused by momentum change due to the deformation of time averaged velocity profiles along the pipe

[1] By M. Murakami and K. Kikuyama, published in the March, 1980 issue of the ASME JOURNAL OF FLUIDS ENGINEERING, Vol. 102, No. 1, p. 97.

[2] Professor, St. Anthony Falls Hydraulic Laboratory, University of Minnesota, Minneapolis, Minn.

[3] Number correspond to reference in the manuscript.

Copyright © 1980 by ASME

Downloaded 02 Jun 2010 to 171.66.16.103. Redistribution subject to ASME license or copyright; see http://www.asme.org/terms/Terms_Use.cfm

axis. This assumption, however, will be available only in the upstream region in the rotating pipe, and in the far downstream region where the flow is in a fully developed state, the assumption will not be valid.

As is seen in the velocity profiles at the sections of $l/D >$ 100 in the rotating pipe, where a fully developed flow is almost established, a velocity profile different from a solid body rotation type is maintained in the circumferential component. In this case, it may be considered that a tangential stress will be present between fluid layers and hence, some energy must be supplied to the flow by the rotating pipe wall.

The preservation of this concave velocity profile in the tangential component will allude to an existence of a longitudinal vortices in the rotating pipe. Cannon and Kays have observed them in the mid-radius region of the rotating pipe. Detailed measurements of the turbulence in the rotating pipe are now being prepared.

Vortex Motions Induced by V-Groove Rotating Cylinders and Their Effect on Mixing Performance[1]

C. L. Tucker.[2] The authors are to be congratulated for taking on a difficult task, that of correlating fluid mechanics and mixing in a complex flow geometry, and for doing an excellent job. It has long been the goal of workers in this field to predict the performance of mixing devices without resorting to empiricism, and this paper marks an important advance towards that goal.

In their introduction, the authors state that one question they hoped to answer was "whether the effect of the grooves was to increase the total amount of shear deformation imparted to the fluids or to overcome the adverse effects of interface orientation." This is a critical question, for if interface orientation effects can be overcome, it should be possible to create laminar mixers which are orders of magnitude more efficient than conventional devices. For example, Erwin [1] has pointed out that so-called mixing sections in single screw extruders increase mixing efficiency by reorienting fluid interfaces with respect to the shear deformation in the rest of the extruder. The authors conclude their paper by stating that V-grooved cylinders enhance mixing primarily by providing increased deformation, but that interface reorientation may be present as well. Since the time when this work was done, some progress has been made in mixing theory and in relating experimental measures of mixing to the type of measures usually employed by theoreticians. When the experimental evidence in this paper is examined in the light of these developments, I believe it is possible to show that there are no reorientation effects present in these particular mixers, and that as a result, the efficiency of V-grooved mixers must be due to increased deformation.

First, assume that the degree of mixing imparted to the fluid can be characterized by a striation thickness, λ. Laminar mixers tend to produce layered mixtures, and the striation thickness is simply the thickness of the repeating unit in a regularly layered mixture [2]. When the fluid enters the mixer, it has some initial striation thickness, λ_0, determined by the geometry of the inlet manifold. Erwin [1] has compared laminar shear mixing without reorientation of interfaces to laminar shear mixing with periodic interface reorientation. If the initial orientation of fluid interfaces is random and there is no reorientation, one gets the familiar result

$$\lambda/\lambda_0 = 2\gamma \tag{1}$$

where γ is to total shear strain imparted to the fluid. Equation (1) is the limiting form for large values of γ. If the shearing is broken down into N identical sections, and if the orientation of the fluid interfaces is randomized between each shearing section, then mixing proceeds as

$$\lambda/\lambda_0 = (2N/\gamma)^N \tag{2}$$

once again, provided that (γ/N) is large compared to unity. Slightly different equations result when the shear strains are not large or, in the reorienting mixer, when the amounts of shear between reorientations are not equal [2], but the equations retain the important character of $(1/\gamma)$ and $(1/\gamma)^N$ for simple and reorienting mixers, respectively.

Now, the experimental technique used to measure degree of mixing involves taking a number of small samples from the mixture, measuring the concentration of one component in each sample, and computing the variance among the concentrations. This sample variance technique is related to a well-defined statistical measure of mixing quality, the volumetric scale of segregation [3], by the equation

$$S_V = v_s[s^2/2\sigma_a{}^2] \tag{3}$$

where S_V is the volumetric scale of segregation, v_s the volume of the samples used in the mixing quality determination, s^2 the variance in concentration among samples, and $\sigma_a{}^2$ the variance in concentration among all points in the mixture. The value of $\sigma_a{}^2$ is easily computed provided that very little molecular diffusion has occurred by the time of the measurement. The effects of diffusion and of other errors on the accuracy of equation (3) has been studied [4], and the equation is accurate as long as S_V is small compared to v_s. This usually requires that the standard deviation, s, be less than about 0.05. The striation thickness and the volume scale of segregation both characterize the mixture, so they must be related in some way. Since λ is a length and S_V is a volume, on dimensional grounds we must have

$$S_V \propto (\lambda)^3 \tag{4}$$

The constant of proportionality depends on the exact geometry of the mixture, and could be worked out from the definition of the volumetric scale of segregation. This will not be done here, since the argument does not require a knowledge of this factor. Equations (3) and (4) now show how to relate the standard deviation measure used in experiments to the striation thickness measure used in theory. Provided that the other quantities are held constant,

$$s \propto (\lambda)^{3/2} \tag{5}$$

With this result, some of the theoretical predictions can now be related more closely to experimental results.

For a concentric cylinder mixer of a given geometry, the total strain imparted to the fluid is proportional to the angular velocity of the inner cylinder (ω) multiplied by the fluid residence time,

$$\gamma \propto (\omega M_T/Q) \tag{6}$$

where M_T is the total volume of the mixer and Q the total flow rate. Combining this with equation (5) and either equation (1) or equation (2) gives the type of experimental results to be expected from different types of mixers. For a mixer which imparts large shear deformations with no reorientation of

[1] By C. A. Rotz and N. P. Suh, published in the June, 1979 issue of the ASME JOURNAL OF FLUIDS ENGINEERS, Vol. 100, pp. 186–192.

[2] Assistant Professor of Mechanical and Industrial Engineering, University of Illinois, Urbana, Ill. 61801.

Downloaded 02 Jun 2010 to 171.66.16.103. Redistribution subject to ASME license or copyright; see http://www.asme.org/terms/Terms_Use.cfm

axis. This assumption, however, will be available only in the upstream region in the rotating pipe, and in the far downstream region where the flow is in a fully developed state, the assumption will not be valid.

As is seen in the velocity profiles at the sections of $l/D >$ 100 in the rotating pipe, where a fully developed flow is almost established, a velocity profile different from a solid body rotation type is maintained in the circumferential component. In this case, it may be considered that a tangential stress will be present between fluid layers and hence, some energy must be supplied to the flow by the rotating pipe wall.

The preservation of this concave velocity profile in the tangential component will allude to an existence of a longitudinal vortices in the rotating pipe. Cannon and Kays have observed them in the mid-radius region of the rotating pipe. Detailed measurements of the turbulence in the rotating pipe are now being prepared.

Vortex Motions Induced by V-Groove Rotating Cylinders and Their Effect on Mixing Performance[1]

C. L. Tucker.[2] The authors are to be congratulated for taking on a difficult task, that of correlating fluid mechanics and mixing in a complex flow geometry, and for doing an excellent job. It has long been the goal of workers in this field to predict the performance of mixing devices without resorting to empiricism, and this paper marks an important advance towards that goal.

In their introduction, the authors state that one question they hoped to answer was "whether the effect of the grooves was to increase the total amount of shear deformation imparted to the fluids or to overcome the adverse effects of interface orientation." This is a critical question, for if interface orientation effects can be overcome, it should be possible to create laminar mixers which are orders of magnitude more efficient than conventional devices. For example, Erwin [1] has pointed out that so-called mixing sections in single screw extruders increase mixing efficiency by reorienting fluid interfaces with respect to the shear deformation in the rest of the extruder. The authors conclude their paper by stating that V-grooved cylinders enhance mixing primarily by providing increased deformation, but that interface reorientation may be present as well. Since the time when this work was done, some progress has been made in mixing theory and in relating experimental measures of mixing to the type of measures usually employed by theoreticians. When the experimental evidence in this paper is examined in the light of these developments, I believe it is possible to show that there are no reorientation effects present in these particular mixers, and that as a result, the efficiency of V-grooved mixers must be due to increased deformation.

First, assume that the degree of mixing imparted to the fluid can be characterized by a striation thickness, λ. Laminar mixers tend to produce layered mixtures, and the striation thickness is simply the thickness of the repeating unit in a regularly layered mixture [2]. When the fluid enters the mixer, it has some initial striation thickness, λ_0, determined by the geometry of the inlet manifold. Erwin [1] has compared laminar shear mixing without reorientation of interfaces to laminar shear mixing with periodic interface reorientation. If the initial orientation of fluid interfaces is random and there is no reorientation, one gets the familiar result

$$\lambda/\lambda_0 = 2\gamma \tag{1}$$

where γ is to total shear strain imparted to the fluid. Equation (1) is the limiting form for large values of γ. If the shearing is broken down into N identical sections, and if the orientation of the fluid interfaces is randomized between each shearing section, then mixing proceeds as

$$\lambda/\lambda_0 = (2N/\gamma)^N \tag{2}$$

once again, provided that (γ/N) is large compared to unity. Slightly different equations result when the shear strains are not large or, in the reorienting mixer, when the amounts of shear between reorientations are not equal [2], but the equations retain the important character of $(1/\gamma)$ and $(1/\gamma)^N$ for simple and reorienting mixers, respectively.

Now, the experimental technique used to measure degree of mixing involves taking a number of small samples from the mixture, measuring the concentration of one component in each sample, and computing the variance among the concentrations. This sample variance technique is related to a well-defined statistical measure of mixing quality, the volumetric scale of segregation [3], by the equation

$$S_V = v_s[s^2/2\sigma_a{}^2] \tag{3}$$

where S_V is the volumetric scale of segregation, v_s the volume of the samples used in the mixing quality determination, s^2 the variance in concentration among samples, and $\sigma_a{}^2$ the variance in concentration among all points in the mixture. The value of $\sigma_a{}^2$ is easily computed provided that very little molecular diffusion has occurred by the time of the measurement. The effects of diffusion and of other errors on the accuracy of equation (3) has been studied [4], and the equation is accurate as long as S_V is small compared to v_s. This usually requires that the standard deviation, s, be less than about 0.05. The striation thickness and the volume scale of segregation both characterize the mixture, so they must be related in some way. Since λ is a length and S_V is a volume, on dimensional grounds we must have

$$S_V \propto (\lambda)^3 \tag{4}$$

The constant of proportionality depends on the exact geometry of the mixture, and could be worked out from the definition of the volumetric scale of segregation. This will not be done here, since the argument does not require a knowledge of this factor. Equations (3) and (4) now show how to relate the standard deviation measure used in experiments to the striation thickness measure used in theory. Provided that the other quantities are held constant,

$$s \propto (\lambda)^{3/2} \tag{5}$$

With this result, some of the theoretical predictions can now be related more closely to experimental results.

For a concentric cylinder mixer of a given geometry, the total strain imparted to the fluid is proportional to the angular velocity of the inner cylinder (ω) multiplied by the fluid residence time,

$$\gamma \propto (\omega M_T/Q) \tag{6}$$

where M_T is the total volume of the mixer and Q the total flow rate. Combining this with equation (5) and either equation (1) or equation (2) gives the type of experimental results to be expected from different types of mixers. For a mixer which imparts large shear deformations with no reorientation of

[1] By C. A. Rotz and N. P. Suh, published in the June, 1979 issue of the ASME JOURNAL OF FLUIDS ENGINEERS, Vol. 100, pp. 186–192.

[2] Assistant Professor of Mechanical and Industrial Engineering, University of Illinois, Urbana, Ill. 61801.

Copyright © 1980 by ASME

Downloaded 02 Jun 2010 to 171.66.16.103. Redistribution subject to ASME license or copyright; see http://www.asme.org/terms/Terms_Use.cfm

interfaces, one would expect

$$s \propto (\omega M_T/Q)^{-3/2} \tag{7}$$

while for a mixer with N shearing sections and reorientation of fluid interfaces between sections one would expect

$$s \propto (\omega M_T/Q)^{-3N/2} \tag{8}$$

If s is plotted as a function of $(\omega M_T/Q)$ on log-log paper, the slope of the resulting line corresponds to the exponent in equation (7) or (8), and indicates whether the mixer reorients interfaces or not.

Figure 5(*a*) in the paper is just such a plot, and an examination of this figure shows that the data have a slope of $-3/2$. The authors have fitted their data with curves instead of the straight lines that would be indicated by equation (7), but the curves flatten away from a $-3/2$ slope only at their upper ends where S is greater than 0.05 and equation (3) becomes inaccurate. Also, the 90 percent statistical confidence limits for the data extend up from each point by a factor of 1.64 and down from each point by a factor of 0.73 [4]. When this is taken into consideration, it can be seen that the observed scatter in the data is reasonable and that in the region of s less than 0.05 the straight line of $-3/2$ slope predicted by equation (7) is a reasonable fit for the data.

If there were some reorientation of interfaces as the fluid traveled from groove to groove, then one would expect a model like equation (2) to apply, with the number of shearing sections being equal to the number of grooves in the cylinder. The grooved cylinders used in this study had from six to eighteen grooves. Substituting these numbers for N in equation (8) shows that if the mixers were reorienting, then the slope of the log(s) versus log $(\omega M_T/Q)$ plots would range from minus nine to minus twenty-seven. The data do not show such step slopes, but do show good agreement with predictions based on no reorientation. Therefore, it seems that there are no interface reorientation effects in the grooved cylinder mixers of this study.

Given that interface reorientation is not a factor in these mixers, one would expect that total strain (or equivalent strain) would be a good predictor of mixing performance, and that better mixing would result from those designs that provide more deformation to the fluid. The authors' calculations of equivalent strain do rank-order the different grooved inner cylinders properly, but the smooth inner cylinder shows the highest value of total strain and the worst actual mixing performance. If, as suggested here, this effect cannot be explained by interface reorientation, then one is led to suspect that there are other factors which need to be considered when predicting mixer performance.

The first refinement which might be added to future calculations is a consideration of the strain distribution function. In the grooved cylinder mixers there is significant radial flow, and it seems reasonable that any particular bit of fluid would visit most parts of the flow field. As a result, the strain imparted to the fluid should be nearly uniform, as the authors have assumed. However, the same cannot be said about the mixer with a smooth inner cylinder. In this geometry there is no radial flow, and there is a distribution of axial velocity which leads to a distribution in fluid residence time and a distribution in the strain imparted to the fluid. At the outlet of a smooth cylinder mixer there is some fluid which has a strain of only two thirds of the average value, and almost half of the fluid has a strain less than 75 percent of the average value. (These particular numbers are for a small gap to radius ratio. The calculations for large gaps are more complicated, but give similar results.) This factor helps to bring the calculation for the smooth cylinder more in line with experimental results, but alone it cannot account for all of the discrepancy.

A second refinement for future calculations might be to consider residence time of fluid particles at various points in the mixer when computing the average strain. The volume averaged equivalent strain used by the authors assumes that fluid particles occupy each region of the mixer for a time proportional to the volume of that region. The strain rates might average out differently if one also accounted for the velocity of the fluid through each of those regions; certainly, the residence time should be lower where the velocity is higher. It seems that all of the information necessary to do this calculation is present in the type of numerical results presented in the paper. The question is whether the extra effort and computation would be worthwhile in terms of more accurate predictions.

In conlcusion, let me once again compliment the authors on a difficult job well done. They have made a significant contribution to the science of mixing.

Additional References

1 Erwin, L., "Theory of Mixing Sections in Single Screw Extruders," *Polymer Engineering and Science,* Vol. 18, No. 7, May 1978, pp. 573-576.

2 Rotz, C. A., "A Generalized Approach to Increased Mixing Efficiency for Viscous Liquids," S.M. thesis, Department of Mechanical Engineering, MIT, Jan. 1976.

3 Danckwerts, P. V., "The Definition and Measurement of Some Characteristics of Mixtures," *Applied Scientific Research*, Vol. 3, Series A, 1952, pp. 279-296.

4 Tucker, C. L., "Reaction Injection Molding of Reinforced Polymeric Parts," Ph.D. thesis, Department of Mechanical Engineering, MIT, Sept. 1978.

Lewis Erwin.[3] This paper presents a valuable combination of fluids mechanics analysis and experimental data in the study of a mixer. The author's discussion points out that an important further need in the analysis is the calculation of the effects of the mixture orientation. This has been accomplished in the past only in Lagrangian analysis of very simple flow systems [1,2]. A factor not discussed by the author is that the grooved cylinder mixers would be expected to exhibit a narrower strain distribution function [3]. This would also improve mixing. Determination of the relative importance of the orientation of the flow or distribution of the strain in improving mixing must await more precise mathematical analysis.

The standard deviation as a measure of mix has serious limitations because it is not straightforwardly related to other measures of mix such as scale and degree of segregation or striation thickness. This limits the value of the experimental results since an analytical relationship with the fluid mechanics cannot be derived. However, the comparative results presented show that the measure is useful.

Additional References

1 Erwin, L., *Poly. Eng. Science.*, Vol. 18, 1978, p. 1048.

2 Ranz, W. E., *AIChE J.*, Vol. 25, 1979, p. 41.

3 Lidor, G., and Tadmor, Z., *Poly. Eng. Science*, Vol. 16, 1976, p. 450.

Authors' Closure

We sincerely thank Drs. Erwin and Tucker for their comments concerning our paper. They have quite correctly pointed out that the determination of the strain distribution function might help explain this difference in mixing performance between the grooved and ungrooved cylinders. This

[3] Assistant Professor, Department of Mechanical Engineering, University of Wisconsin, Madison, Wis. 53706.

Downloaded 02 Jun 2010 to 171.66.16.103. Redistribution subject to ASME license or copyright; see http://www.asme.org/terms/Terms_Use.cfm

was not done in our study because we were trying to use a very simple analytical approach to better understand the design of laminar flow mixing equipment. To add the refinements suggested would have complicated the problem considerably, since the effects of an overall axial flow through the mixer would have to have been included. The simple model used did yield some surprising good correlations with experimental results. It is hoped that our work can be extended to include the refinements suggested by Erwin and Tucker. In addition, we would like to point out that increased accuracy in satisfying the boundary conditions can be achieved by mapping the irregular quadrilateral-shaped region of interest into a unit square and then discretizing and solving the transformed equations.

Turbulent Length Scales and the Turbulent Transport Number for Isotropic Turbulence[1]

R. G. Adbel-Gayed and D. Bradley.[2] In a recent paper [1] we surveyed experimental data on mass, momentum and energy transport for isotropic turbulence at the axis of pipes, in order to relate the ratio of turbulent diffusivity to kinematic viscosity, or turbulent transport number, ϵ/ν, to the flow Reynolds number, Re. Measurements of turbulent parameters also were surveyed and these related to Re. The two sets of results were combined to give a correlation between ϵ/ν and the turbulent Reynolds number, R_l, based on the integral length scale, l.

The accuracy of the proposed correlation was limited by that of the experimental data, particularly of the integral scale and the Taylor microscale for the radial direction, λ_y. In discussion of the paper Lawn [2] suggested that the exponent of R_{ly} in the correlation should be unity, not 0.56, and that, contrary to the interpretation in reference [1], the ratio of integral scale, l_y, to pipe diameter, d, was invariant with Re. Additional channel flow data lend support to the suggestions of Lawn.

The experimental integral length scale measurements of Laufer [3] at the centre of a channel, where the turbulence was isotropic, show the ratio of the integral length scale in the radial direction to the channel width to be independent of flow Reynolds number and equal to 0.1. The measurements of Comte-Bellot [4] at a flow Reynolds number of 6×10^4 give a value of this ratio of 0.04. The pipe flow data of reference [1] are reproduced in Fig. 1 and here also a macroscale which is invariant with Reynolds number is not inconsistent with the data.

On the assumption that l_y/d is invariant with Re then,

$$\frac{l_y}{d} = 0.08 \tag{1}$$

shown by the full line.

Application to this relationship of the equations of reference [1] which relate both r.m.s. turbulent radial velocity and ϵ_y/ν to Re yield

$$\frac{\epsilon_y}{\nu} = 0.62\, R_{ly}^{0.95} \tag{2}$$

This is closer to the relationship suggested by Lawn [2]. He also suggested that λ_y/d should vary as $\mathrm{Re}^{-0.45}$. An examination of the original [1] and additional [5,6] data

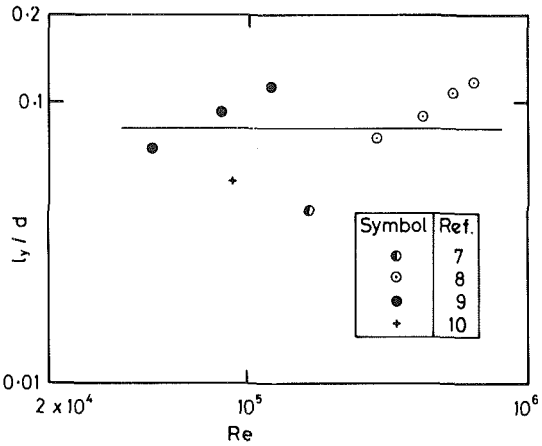

Fig. 1 Variation of radial macroscale at axis with pipe flow Reynolds number (log. scale).

relating the two length scales suggests the relationship

$$6.36\frac{l_y}{\lambda_y} = R_{ly}^{0.5} \tag{3}$$

Equations (1) and (3) together with equation (4) of reference [1] show λ_y/d to vary as $\mathrm{Re}^{-.46}$. However, such is the scatter of the experimental measurements of microscale, that an equally acceptable correlation of experimental data is

$$\frac{\lambda_y}{d} = 4.615\ \mathrm{Re}^{-0.45} \tag{4}$$

Equations (1), (3), and (4), together with equation (1) of reference [1], yield

$$\frac{\epsilon_y}{\nu} = 0.49\, R_{ly}^{0.97} \tag{5}$$

Both equations (2) and (5) give a better fit of the experimental data than does the relationship given in reference [1]. They appear to be satisfactory in the regime $70 < R_{ly} < 3{,}000$, but it is difficult to assign accuracy bounds.

Additional References

1 Abdel-Gayed, R.G., and Bradley, D., "Derivation of Turbulent Transport Coefficients from Turbulent Parameters in Isotropic Turbulence," ASME JOURNAL OF FLUIDS ENGINEERING, Vol. 99, Dec. 1977, pp. 732–736.

2 Lawn, C.J., "Discussion on Derivation of Turbulent Transport Coefficients from Turbulent Parameters in Isotropic Turbulence," ASME JOURNAL OF FLUIDS ENGINEERING, Vol. 100, Mar. 1978, pp. 139–140.

3 Laufer, J., "Investigation of Turbulent Flow in a Two-Dimensional Channel," NACA Report No. 1053, 1951 (supersedes NACA Tech. Note 2123, 1950).

4 Comte-Bellot, G., "Ecoulement turbulent entre deux parois-parallèles," Publ. Scientiques et Techniques du Ministére de l'Aire, no. 419 (1965). Translated as Aero.Res.Counc.31 609, FM4102 (1969).

5 Rotta, J., "Statistische Theorie nichthomogener Turbulenz, 1. Mitteilung," *Zeitschrift für Physik*, Vol. 129, 1951, pp. 547–572.

6 Comte-Bellot, G., and Corrsin, S., "Simple Eulerian Time Correlation of Full - and Narrow-Band Velocity Signals in Grid-Generated 'Isotropic' Turbulence," *Journal of Fluid Mechanics*, Vol. 48, Part 2, 1971, pp. 273–337.

7 Powe, R.E., and Townes, H.W., "Turbulence Structure for Fully Developed Flow in Rough Pipes," ASME JOURNAL OF FLUIDS ENGINEERING, Vol. 95, June 1973, pp. 255–262.

8 Baldwin, L.V., and Walsh, T.J., "Turbulent Diffusion in the Core of Fully Developed Pipe Flow," *AIChE Journal*, Vol. 7, No. 1, Mar. 1961, pp. 53–61.

9 Robertson, J.M., Burkhart, J.H., and Martin, J.D., "Study of Turbulent Flow in Rough Pipes," University of Illiois, Theoretical and Applied Mechanics Report No. 279, Urbana, 1965.

10 Lawn, C.J., "The Determination of the Rate of Dissipation in Turbulent Pipe Flow," *Journal of Fluid Mechanics*, Vol. 48, Part 3, 1971, pp. 477–505.

[1] By Ramzy G. Adbel-Gayed and Derek Bradley, published in the December, 1977, issue of the JOURNAL OF FLUIDS ENGINEERING, Vol. 99, pp. 732–736.

[2] Department of Mechanical Engineering, The University of Leeds, Leeds, England.

Downloaded 02 Jun 2010 to 171.66.16.103. Redistribution subject to ASME license or copyright; see http://www.asme.org/terms/Terms_Use.cfm

was not done in our study because we were trying to use a very simple analytical approach to better understand the design of laminar flow mixing equipment. To add the refinements suggested would have complicated the problem considerably, since the effects of an overall axial flow through the mixer would have to have been included. The simple model used did yield some surprising good correlations with experimental results. It is hoped that our work can be extended to include the refinements suggested by Erwin and Tucker. In addition, we would like to point out that increased accuracy in satisfying the boundary conditions can be achieved by mapping the irregular quadrilateral-shaped region of interest into a unit square and then discretizing and solving the transformed equations.

Turbulent Length Scales and the Turbulent Transport Number for Isotropic Turbulence[1]

R. G. Adbel-Gayed and D. Bradley.[2] In a recent paper [1] we surveyed experimental data on mass, momentum and energy transport for isotropic turbulence at the axis of pipes, in order to relate the ratio of turbulent diffusivity to kinematic viscosity, or turbulent transport number, ϵ/ν, to the flow Reynolds number, Re. Measurements of turbulent parameters also were surveyed and these related to Re. The two sets of results were combined to give a correlation between ϵ/ν and the turbulent Reynolds number, R_l, based on the integral length scale, l.

The accuracy of the proposed correlation was limited by that of the experimental data, particularly of the integral scale and the Taylor microscale for the radial direction, λ_y. In discussion of the paper Lawn [2] suggested that the exponent of R_{ly} in the correlation should be unity, not 0.56, and that, contrary to the interpretation in reference [1], the ratio of integral scale, l_y, to pipe diameter, d, was invariant with Re. Additional channel flow data lend support to the suggestions of Lawn.

The experimental integral length scale measurements of Laufer [3] at the centre of a channel, where the turbulence was isotropic, show the ratio of the integral length scale in the radial direction to the channel width to be independent of flow Reynolds number and equal to 0.1. The measurements of Comte-Bellot [4] at a flow Reynolds number of 6×10^4 give a value of this ratio of 0.04. The pipe flow data of reference [1] are reproduced in Fig. 1 and here also a macroscale which is invariant with Reynolds number is not inconsistent with the data.

On the assumption that l_y/d is invariant with Re then,

$$\frac{l_y}{d} = 0.08 \tag{1}$$

shown by the full line.

Application to this relationship of the equations of reference [1] which relate both r.m.s. turbulent radial velocity and ϵ_y/ν to Re yield

$$\frac{\epsilon_y}{\nu} = 0.62\, R_{ly}^{0.95} \tag{2}$$

This is closer to the relationship suggested by Lawn [2]. He also suggested that λ_y/d should vary as $\mathrm{Re}^{-0.45}$. An examination of the original [1] and additional [5,6] data

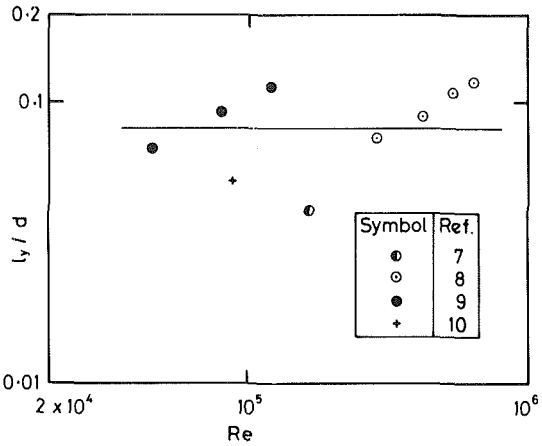

Fig. 1 Variation of radial macroscale at axis with pipe flow Reynolds number (log. scale).

relating the two length scales suggests the relationship

$$6.36\frac{l_y}{\lambda_y} = R_{ly}^{0.5} \tag{3}$$

Equations (1) and (3) together with equation (4) of reference [1] show λ_y/d to vary as $\mathrm{Re}^{-.46}$. However, such is the scatter of the experimental measurements of microscale, that an equally acceptable correlation of experimental data is

$$\frac{\lambda_y}{d} = 4.615\ \mathrm{Re}^{-0.45} \tag{4}$$

Equations (1), (3), and (4), together with equation (1) of reference [1], yield

$$\frac{\epsilon_y}{\nu} = 0.49\, R_{ly}^{0.97} \tag{5}$$

Both equations (2) and (5) give a better fit of the experimental data than does the relationship given in reference [1]. They appear to be satisfactory in the regime $70 < R_{ly} < 3{,}000$, but it is difficult to assign accuracy bounds.

Additional References

1 Abdel-Gayed, R.G., and Bradley, D., "Derivation of Turbulent Transport Coefficients from Turbulent Parameters in Isotropic Turbulence," ASME JOURNAL OF FLUIDS ENGINEERING, Vol. 99, Dec. 1977, pp. 732–736.

2 Lawn, C.J., "Discussion on Derivation of Turbulent Transport Coefficients from Turbulent Parameters in Isotropic Turbulence," ASME JOURNAL OF FLUIDS ENGINEERING, Vol. 100, Mar. 1978, pp. 139–140.

3 Laufer, J., "Investigation of Turbulent Flow in a Two-Dimensional Channel," NACA Report No. 1053, 1951 (supersedes NACA Tech. Note 2123, 1950).

4 Comte-Bellot, G., "Ecoulement turbulent entre deux parois-parallèles," Publ. Scientiques et Techniques du Ministére de l'Aire, no. 419 (1965). Translated as Aero.Res.Counc.31 609, FM4102 (1969).

5 Rotta, J., "Statistische Theorie nichthomogener Turbulenz, 1. Mitteilung," *Zeitschrift für Physik*, Vol. 129, 1951, pp. 547–572.

6 Comte-Bellot, G., and Corrsin, S., "Simple Eulerian Time Correlation of Full - and Narrow-Band Velocity Signals in Grid-Generated 'Isotropic' Turbulence," *Journal of Fluid Mechanics*, Vol. 48, Part 2, 1971, pp. 273–337.

7 Powe, R.E., and Townes, H.W., "Turbulence Structure for Fully Developed Flow in Rough Pipes," ASME JOURNAL OF FLUIDS ENGINEERING, Vol. 95, June 1973, pp. 255–262.

8 Baldwin, L.V., and Walsh, T.J., "Turbulent Diffusion in the Core of Fully Developed Pipe Flow," *AIChE Journal*, Vol. 7, No. 1, Mar. 1961, pp. 53–61.

9 Robertson, J.M., Burkhart, J.H., and Martin, J.D., "Study of Turbulent Flow in Rough Pipes," University of Illiois, Theoretical and Applied Mechanics Report No. 279, Urbana, 1965.

10 Lawn, C.J., "The Determination of the Rate of Dissipation in Turbulent Pipe Flow," *Journal of Fluid Mechanics*, Vol. 48, Part 3, 1971, pp. 477–505.

[1] By Ramzy G. Adbel-Gayed and Derek Bradley, published in the December, 1977, issue of the JOURNAL OF FLUIDS ENGINEERING, Vol. 99, pp. 732–736.

[2] Department of Mechanical Engineering, The University of Leeds, Leeds, England.

Copyright © 1980 by ASME

Downloaded 02 Jun 2010 to 171.66.16.103. Redistribution subject to ASME license or copyright; see http://www.asme.org/terms/Terms_Use.cfm